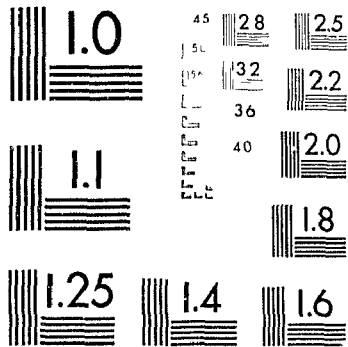


# 1

PM-1 3½"x4" PHOTOGRAPHIC MICROCOPY TARGET  
NBS 1010a ANSI/ISO #2 EQUIVALENT



PRECISION<sup>SM</sup> RESOLUTION TARGETS



National Library  
of Canada

Acquisitions and  
Bibliographic Services Branch

395 Wellington Street  
Ottawa, Ontario  
K1A 0N4

Bibliothèque nationale  
du Canada

Direction des acquisitions et  
des services bibliographiques

395, rue Wellington  
Ottawa (Ontario)  
K1A 0N4

*Your file - Votre référence*

*Our file - Notre référence*

## NOTICE

The quality of this microform is heavily dependent upon the quality of the original thesis submitted for microfilming. Every effort has been made to ensure the highest quality of reproduction possible.

If pages are missing, contact the university which granted the degree.

Some pages may have indistinct print especially if the original pages were typed with a poor typewriter ribbon or if the university sent us an inferior photocopy.

Reproduction in full or in part of this microform is governed by the Canadian Copyright Act, R.S.C. 1970, c. C-30, and subsequent amendments.

## AVIS

La qualité de cette microforme dépend grandement de la qualité de la thèse soumise au microfilmage. Nous avons tout fait pour assurer une qualité supérieure de reproduction.

S'il manque des pages, veuillez communiquer avec l'université qui a conféré le grade.

La qualité d'impression de certaines pages peut laisser à désirer, surtout si les pages originales ont été dactylographiées à l'aide d'un ruban usé ou si l'université nous a fait parvenir une photocopie de qualité inférieure.

La reproduction, même partielle, de cette microforme est soumise à la Loi canadienne sur le droit d'auteur, SRC 1970, c. C-30, et ses amendements subséquents.

**The Conjugate Margins of the Labrador Sea:  
Crustal Structure from Refraction Profiles  
and Their Tectonic Implications**

by

**Deping Chian**

Submitted in partial fulfilment of the requirements for the degree

of Doctor of Philosophy

at

Dalhousie University

Halifax, Nova Scotia

June, 1994

© Copyright by Deping Chian, 1994



National Library  
of Canada

Acquisitions and  
Bibliographic Services Branch

395 Wellington Street  
Ottawa, Ontario  
K1A 0N4

Bibliothèque nationale  
du Canada

Direction des acquisitions et  
des services bibliographiques

395, rue Wellington  
Ottawa (Ontario)  
K1A 0N4

*Your file* *Votre référence*

*Our file* *Notre référence*

THE AUTHOR HAS GRANTED AN IRREVOCABLE NON-EXCLUSIVE LICENCE ALLOWING THE NATIONAL LIBRARY OF CANADA TO REPRODUCE, LOAN, DISTRIBUTE OR SELL COPIES OF HIS/HER THESIS BY ANY MEANS AND IN ANY FORM OR FORMAT, MAKING THIS THESIS AVAILABLE TO INTERESTED PERSONS.

L'AUTEUR A ACCORDE UNE LICENCE IRREVOCABLE ET NON EXCLUSIVE PERMETTANT A LA BIBLIOTHEQUE NATIONALE DU CANADA DE REPRODUIRE, PRETER, DISTRIBUER OU VENDRE DES COPIES DE SA THESE DE QUELQUE MANIERE ET SOUS QUELQUE FORME QUE CE SOIT POUR METTRE DES EXEMPLAIRES DE CETTE THESE A LA DISPOSITION DES PERSONNE INTERESSEES.

THE AUTHOR RETAINS OWNERSHIP OF THE COPYRIGHT IN HIS/HER THESIS. NEITHER THE THESIS NOR SUBSTANTIAL EXTRACTS FROM IT MAY BE PRINTED OR OTHERWISE REPRODUCED WITHOUT HIS/HER PERMISSION.

L'AUTEUR CONSERVE LA PROPRIETE DU DROIT D'AUTEUR QUI PROTEGE SA THESE. NI LA THESE NI DES EXTRAITS SUBSTANTIELS DE CELLE-CI NE DOIVENT ETRE IMPRIMES OU AUTREMENT REPRODUITS SANS SON AUTORISATION.

ISBN 0-612-05155-2

Canada

Name Jeping Chian

Dissertation Abstracts International is arranged by broad, general subject categories. Please select the one subject which most nearly describes the content of your dissertation. Enter the corresponding four-digit code in the spaces provided.

0373

0373

**U·M·I**

SUBJECT TERM

SUBJECT CODE

**Subject Categories**

**THE HUMANITIES AND SOCIAL SCIENCES**

**COMMUNICATIONS AND THE ARTS**

Architecture 0729  
 Art History 0377  
 Cinema 0901  
 Dance 0478  
 Fine Arts 0357  
 Information Science 0723  
 Journalism 0391  
 Library Science 0399  
 Mass Communications 0708  
 Music 0413  
 Speech Communication 0459  
 Theater 0465

**EDUCATION**

General 0515  
 Administration 0514  
 Adult and Continuing 0516  
 Agricultural 0517  
 Art 0273  
 Bilingual and Multicultural 0282  
 Business 0688  
 Community College 0275  
 Curriculum and Instruction 0727  
 Early Childhood 0518  
 Elementary 0524  
 Finance 0277  
 Guidance and Counseling 0519  
 Health 0680  
 Higher 0745  
 History of 0520  
 Home Economics 0278  
 Industrial 0521  
 Language and Literature 0279  
 Mathematics 0280  
 Music 0522  
 Philosophy of 0998  
 Physical 0523

Psychology 0525  
 Reading 0535  
 Religious 0527  
 Sciences 0714  
 Secondary 0533  
 Social Sciences 0534  
 Sociology of 0340  
 Spectra 0529  
 Teacher Training 0530  
 Technology 0710  
 Tests and Measurements 0288  
 Vocational 0747

**LANGUAGE, LITERATURE AND LINGUISTICS**

Language  
 General 0679  
 Ancient 0289  
 Linguistics 0290  
 Modern 0291  
 Literature  
 General 0401  
 Classical 0294  
 Comparative 0295  
 Medieval 0297  
 Modern 0298  
 African 0316  
 American 0591  
 Asian 0305  
 Canadian (English) 0352  
 Canadian (French) 0355  
 English 0593  
 Germanic 0311  
 Latin American 0312  
 Middle Eastern 0315  
 Romance 0313  
 Slavic and East European 0314

**PHILOSOPHY, RELIGION AND THEOLOGY**

Philosophy 0422  
 Religion  
 General 0318  
 Biblical Studies 0321  
 Clergy 0319  
 History of 0320  
 Philosophy of 0322  
 Theology 0469

**SOCIAL SCIENCES**

American Studies 0323  
 Anthropology  
 Archaeology 0324  
 Cultural 0326  
 Physical 0327  
 Business Administration  
 General 0310  
 Accounting 0272  
 Banking 0770  
 Management 0454  
 Marketing 0338  
 Canadian Studies 0385  
 Economics  
 General 0501  
 Agricultural 0503  
 Commerce Business 0505  
 Finance 0508  
 History 0509  
 Labor 0510  
 Theory 0511  
 Folklore 0358  
 Geography 0366  
 Gerontology 0351  
 History  
 General 0578

Ancient 0579  
 Medieval 0581  
 Modern 0582  
 Black 0328  
 African 0331  
 Asia Australia and Oceania 0332  
 Canadian 0334  
 European 0335  
 Latin American 0336  
 Middle Eastern 0333  
 United States 0337  
 History of Science 0585  
 Law 0398  
 Political Science  
 General 0615  
 International Law and Relations 0616  
 Public Administration 0617  
 Recreation 0814  
 Social Work 0452  
 Sociology  
 General 0626  
 Criminology and Penology 0627  
 Demography 0938  
 Ethnic and Racial Studies 0631  
 Individual and Family Studies 0628  
 Industrial and Labor Relations 0629  
 Public and Social Welfare 0630  
 Social Structure and Development 0700  
 Theory and Methods 0344  
 Transportation 0709  
 Urban and Regional Planning 0999  
 Women's Studies 0453

**THE SCIENCES AND ENGINEERING**

**BIOLOGICAL SCIENCES**

Agriculture  
 General 0473  
 Agronomy 0285  
 Animal Culture and Nutrition 0475  
 Animal Pathology 0476  
 Food Science and Technology 0359  
 Forestry and Wildlife 0478  
 Plant Culture 0479  
 Plant Pathology 0480  
 Plant Physiology 0817  
 Range Management 0777  
 Wood Technology 0746  
 Biology  
 General 0306  
 Anatomy 0287  
 Biostatistics 0308  
 Botany 0309  
 Cell 0309  
 Ecology 0329  
 Entomology 0353  
 Genetics 0369  
 Immunology 0793  
 Microbiology 0410  
 Molecular 0307  
 Neuroscience 0317  
 Oceanography 0416  
 Physiology 0433  
 Radiation 0821  
 Veterinary Science 0778  
 Zoology 0472  
 Biophysics  
 General 0786  
 Medical 0760

**EARTH SCIENCES**

Biogeochemistry 0425  
 Geochemistry 0496

Geodesy 0370  
 Geology 0372  
 Geophysics 0373  
 Hydrology 0388  
 Mineralogy 0411  
 Paleobotany 0345  
 Paleocology 0426  
 Paleontology 0418  
 Paleozoology 0985  
 Palynology 0427  
 Physical Geography 0368  
 Physical Oceanography 0415

**HEALTH AND ENVIRONMENTAL SCIENCES**

Environmental Sciences 0768  
 Health Sciences  
 General 0566  
 Audiology 0300  
 Chemotherapy 0992  
 Dentistry 0567  
 Education 0350  
 Hospital Management 0769  
 Human Development 0758  
 Immunology 0982  
 Medicine and Surgery 0564  
 Mental Health 0347  
 Nursing 0569  
 Nutrition 0570  
 Obstetrics and Gynecology 0380  
 Occupational Health and Therapy 0354  
 Ophthalmology 0381  
 Pathology 0571  
 Pharmacology 0419  
 Pharmacy 0572  
 Physical Therapy 0382  
 Public Health 0573  
 Radiology 0574  
 Recreation 0575

Speech Pathology 0460  
 Toxicology 0383  
 Home Economics 0386

**PHYSICAL SCIENCES**

**Pure Sciences**  
 Chemistry  
 General 0485  
 Agricultural 0749  
 Analytical 0486  
 Biochemistry 0487  
 Inorganic 0488  
 Nuclear 0738  
 Organic 0490  
 Pharmaceutical 0491  
 Physical 0494  
 Polymer 0495  
 Radiation 0754  
 Mathematics 0405  
 Physics  
 General 0605  
 Acoustics 0986  
 Astronomy and Astrophysics 0606  
 Atmospheric Science 0608  
 Atomic 0748  
 Electronics and Electricity 0607  
 Elementary Particles and High Energy 0798  
 Fluid and Plasma 0757  
 Molecular 0609  
 Nuclear 0610  
 Optics 0752  
 Radiation 0756  
 Solid State 0611  
 Statistics 0463  
**Applied Sciences**  
 Applied Mechanics 0346  
 Computer Science 0984

Engineering  
 General 0537  
 Aerospace 0538  
 Agricultural 0539  
 Automotive 0540  
 Biomedical 0541  
 Chemical 0542  
 Civil 0543  
 Electronics and Electrical 0544  
 Heat and Thermodynamics 0348  
 Hydraulic 0545  
 Industrial 0546  
 Marine 0547  
 Materials Science 0794  
 Mechanical 0548  
 Metallurgy 0743  
 Mining 0551  
 Nuclear 0552  
 Packaging 0549  
 Petroleum 0765  
 Sanitary and Municipal System Science 0554  
 Geotechnological Operations Research 0796  
 Plastics Technology 0795  
 Textile Technology 0994

**PSYCHOLOGY**

General 0621  
 Behavioral 0384  
 Clinical 0622  
 Developmental 0620  
 Experimental 0623  
 Industrial 0624  
 Personality 0625  
 Physiological 0989  
 Psychobiology 0349  
 Psychometrics 0632  
 Social 0451



DALHOUSIE UNIVERSITY

FACULTY OF GRADUATE STUDIES

The undersigned hereby certify that they have read and recommend to the Faculty of Graduate Studies for acceptance a thesis entitled "The Conjugate Margins of the Labrador Sea: Crustal Structure from Refraction Profiles and Their Tectonic Implications"

by Deping Chian

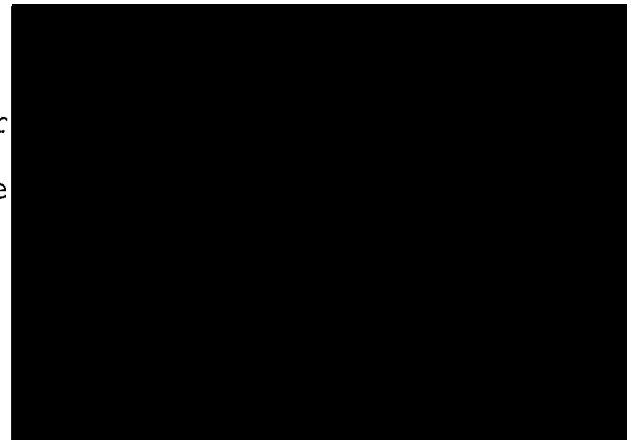
in partial fulfillment of the requirements for the degree of Doctor of Philosophy.

Dated June 16, 1994

External Examiner

Research Supervisor

Examining Committee



DALHOUSIE UNIVERSITY

DATE: June 29, 1994

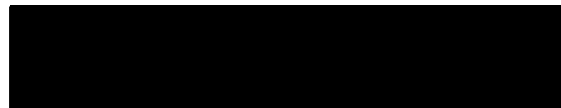
AUTHOR: Deping Chian

TITLE: The Conjugate Margins of the Labrador Sea: Crustal Structure from  
Refraction Profiles and Their Tectonic Implications

DEPARTMENT OR SCHOOL: Oceanography

DEGREE: Ph.D. CONVOCATION: October YEAR: 1994

Permission is herewith granted to Dalhousie University to circulate and to have copied for non-commercial purposes, at its discretion, the above title upon the request of individuals or institutions.



Signature of Author

THE AUTHOR RESERVES OTHER PUBLICATION RIGHTS, AND NEITHER THE THESIS NOR EXTENSIVE EXTRACTS FROM IT MAY BE PRINTED OR OTHERWISE REPRODUCED WITHOUT THE AUTHOR'S WRITTEN PERMISSION.

THE AUTHOR ATTESTS THAT PERMISSION HAS BEEN OBTAINED FOR THE USE OF ANY COPYRIGHTED MATERIAL APPEARING IN THIS THESIS (OTHER THAN BRIEF EXCERPTS REQUIRING ONLY PROPER ACKNOWLEDGEMENT IN SCHOLARLY WRITING) AND THAT ALL SUCH USE IS CLEARLY ACKNOWLEDGED.

For Tracy

數年寒壁

苦羽滿豐

天生我材

壯志未卜



## Table of Contents

<b>TABLE OF CONTENTS .....</b>	<b>V</b>
<b>LIST OF TABLES.....</b>	<b>IX</b>
<b>LIST OF FIGURES.....</b>	<b>X</b>
<b>ABSTRACT.....</b>	<b>XV</b>
<b>LIST OF ABBREVIATIONS AND SYMBOLS .....</b>	<b>XVI</b>
<b>ACKNOWLEDGMENTS.....</b>	<b>XVIII</b>
<b>CHAPTER 1. INTRODUCTION .....</b>	<b>1</b>
<b>1.1 Continental Stretching .....</b>	<b>1</b>
<b>1.2 Volcanism on Rifted Continental Margins .....</b>	<b>3</b>
<b>1.3 Seismic Measurements on Rifted Continental Margins.....</b>	<b>5</b>
<b>1.4 Conjugate Margins of the Labrador Sea.....</b>	<b>7</b>
<b>1.5 Methodology and Data.....</b>	<b>12</b>
<b>1.6 About This Thesis.....</b>	<b>15</b>
<b>CHAPTER 2. GEOLOGY AND PREVIOUS GEOPHYSICAL DATA.....</b>	<b>17</b>
<b>2.1 The Labrador Sea.....</b>	<b>17</b>
<b>2.2 Precambrian Geology .....</b>	<b>18</b>
<b>2.3 Phanerozoic Geology and Previous Geophysical Data .....</b>	<b>18</b>
<b>CHAPTER 3. ARCHEAN/KETILIDIAN CRUST ALONG THE CONTINENTAL SHELF OF SW GREENLAND FROM A SEISMIC REFRACTION PROFILE.....</b>	<b>27</b>
<b>3.1 Introduction.....</b>	<b>27</b>
<b>3.2 Data Acquisition and Processing.....</b>	<b>29</b>
<b>3.3 Seismic Modeling.....</b>	<b>33</b>
Sediments .....	34
Upper and Intermediate Crust .....	35
Lower Crust and Upper Mantle.....	36
Along-Strike Variations .....	37

3.4 Interpretation.....	39
3.5 Conclusions .....	49
<b>CHAPTER 4. THE CONTINENT-OCEAN CRUSTAL TRANSITION ACROSS</b>	
<b>THE SW GREENLAND MARGIN.....</b>	<b>51</b>
4.1 Introduction .....	51
4.2 Reflection Profile.....	52
4.3 Wide-Angle Seismic Data and Modeling .....	56
4.3.1 Data.....	56
4.3.2 One-Dimensional Reflectivity Modeling of Sonobuoy F.....	57
4.3.3 Two-Dimensional Modeling of OBS Data .....	61
4.3.4 Determining <i>S</i> Waves .....	69
4.3.5 Error Analysis .....	75
4.4 Gravity and Magnetic Modeling.....	76
4.5 Discussion.....	80
4.5.1 The Seismic Model.....	80
4.5.2 Undercrusted Serpentinite or Magmatic Underplating? .....	82
4.5.3 Processes of Crustal Thinning.....	85
4.6 Conclusions .....	86
<b>CHAPTER 5. THE CONTINENT-OCEAN CRUSTAL TRANSITION ACROSS</b>	
<b>THE LABRADOR MARGIN .....</b>	<b>88</b>
5.1 Introduction .....	88
5.2 Seismic Data.....	91
5.2.1 Wide-Angle OBS Data .....	91
5.2.2 Modeling Procedures for Wide-Angle Data .....	92
5.3 Two-dimensional Seismic Modeling.....	95
5.3.1 Line 90R3: On the Continental Shelf .....	95
5.3.2 Line 90R2: On the Deep Sediments .....	97
5.3.3 Line 90R1: The Wide Crustal Transition from Continent to Ocean Across the Labrador Margin .....	98
Seismic Phases .....	107
OBS B .....	108
OBS H.....	108
OBS Q.....	111
OBS C .....	113
OBS D.....	113

OBS P.....	116
OBS G.....	118
OBS A.....	118
OBS M.....	121
OBS K and I.....	121
<b>5.4 Interpretation.....</b>	<b>126</b>
<b>5.5 Resolution of Results .....</b>	<b>129</b>
5.5.1 Error Analysis .....	129
5.5.2 Comparison with Reflection Data .....	131
Deep Multi-Channel Reflection Profile .....	132
Combined View of Reflection and Refraction Results .....	134
5.5.3 Constraints From Two-dimensional Gravity Modeling .....	135
<b>5.6 Correlation with Magnetic Anomalies.....</b>	<b>137</b>
<b>5.7 Conclusion.....</b>	<b>139</b>
<b>CHAPTER 6. RECONSTRUCTION OF RIFT-STAGE CRUST ACROSS THE</b>	
<b>CONJUGATE MARGINS OF LABRADOR SEA .....</b>	<b>140</b>
<b>6.1 Location of Continent-Ocean Boundary .....</b>	<b>140</b>
<b>6.2 Origin of Transitional Crust .....</b>	<b>146</b>
<b>6.3 Nature of the Thinned Upper Crust.....</b>	<b>153</b>
<b>6.4 Reconstruction of Pre-breakup Crust and Rifting Model.....</b>	<b>156</b>
<b>6.5 Comparison with Other Models.....</b>	<b>165</b>
<b>6.6 Conclusions .....</b>	<b>170</b>
<b>CHAPTER 7. SUMMARY AND FUTURE WORK.....</b>	<b>172</b>
<b>7.1 Summary.....</b>	<b>172</b>
<b>7.2 Major Contribution.....</b>	<b>174</b>
<b>7.3 Future Work .....</b>	<b>175</b>
<b>APPENDIX A. ERROR ANALYSIS OF THE SEISMIC VELOCITY MODEL ..</b>	<b>179</b>
<b>APPENDIX B. SUPPRESSION OF TIME CODE CROSS-TALK DISTURBANCES</b>	
<b>IN SIGNAL CHANNELS OF OCEAN BOTTOM SEISMOMETERS IN SEISMIC</b>	
<b>REFRACTIONS.....</b>	<b>184</b>

<b>B1 Introduction .....</b>	<b>184</b>
<b>B2 Brief Description of Data.....</b>	<b>186</b>
<b>B3 Spectral Analysis.....</b>	<b>187</b>
<b>B4 Time code suppression in T-X space .....</b>	<b>189</b>
B4.1 Computing Time Lags .....	190
B4.2 Time Code Suppression to Field Data.....	191
B4.3 Improving Time Lag Estimates .....	192
B4.4 Time Windows .....	192
<b>B5 Conclusions .....</b>	<b>193</b>
<b>B6 Acknowledgements for Appendix B .....</b>	<b>194</b>
<b>APPENDIX C. OBS LOCATIONS .....</b>	<b>224</b>
<b>BIBLIOGRAPHY .....</b>	<b>225</b>

## List of Tables

Table 3. 1 OBS positions along southwestern Greenland shelf.....	34
Table 4. 1 OBS Positions and Water Depths Along Refraction Line 88R2.....	60
Table 4. 2 One-Dimensional Velocity Model for Sonobuoy F.....	60
Table 6. 1 Comparison Between Observations and Predictions of Melt and Serpentine Models.....	152
Table 6. 2 Supporting Refraction Observations for the Upper-Continental Termination on the Labrador Margin .....	157
Table C. 1 OBS Locations for the 1990 refraction lines 90R1, 90R2, and 90R3 .....	224

## List of Figures

1.1 Map of basement age and magnetic-anomaly lineations in the North Atlantic.....	8
1.2 Map of the Labrador Sea .....	9
1.3 Schematic diagram showing the ray paths during a wide-angle seismic field experiment using ocean bottom seismometers (OBS). .....	13
2.1 Correlation of various Precambrian provinces in the North Atlantic .....	19
2.2 Sediment thickness map of the Labrador Sea.....	21
2.3 Interpreted geological cross-section across Greenland (top) and Labrador (bottom) based on reprocessing of BGR-17. ....	22
2.4 Density and velocity model, and gravity and magnetic anomaly profiles across the Labrador margin, after Van der Linden (1975) and Hinz et al. (1979).....	25
2.5 The structural cross-section of Stergiopolous (1984) across the southwestern Greenland margin.....	26
3.1 Simplified geology, isobaths and major geological units of the continental crust of southwestern Greenland .....	28
3.2 Vertical geophone record sections of OBS N .....	31
3.3 Hydrophone record sections of OBS J.....	32
3.4 Compilation of near range profiles of <i>P</i> waves (left) and <i>S</i> waves (right) from the three OBS M, L and K.....	40
3.5 Compilation of <i>P</i> wave profiles for the five OBS, emphasizing the features of the lower crustal arrivals, PcP (or Pc) and PmP.....	41
3.6 <i>P</i> and <i>S</i> wave velocity-depth models for each OBS.....	45
3.7 Final two-dimensional <i>P</i> and <i>S</i> wave velocity model along the southwestern Greenland margin.....	46
4.1 Location map of the Labrador Sea, showing refraction lines 88R <sub>2</sub> and 88R <sub>1</sub> , bathymetric contours, numbered magnetic anomalies, fracture zones, and an extinct rift axis.....	53
4.2 (top) Single-channel reflection data along line 88R <sub>2</sub> with interpretations .....	55
4.3 Example of coherency mixing.....	58
4.4 Profile from sonobuoy F hydrophone with 1-D modeling.....	62
4.5 Profile from OBS B hydrophone with 2-D modeling .....	64
4.6 Profile from OBS C horizontal geophone with 2-D modeling .....	65
4.7 Profile from OBS D horizontal geophone with 2-D modeling .....	66

4 8 Profile from OBS E vertical geophone with 2-D modeling	70
4 9 Profile from OBS G vertical geophone with 2-D modeling	71
4 10 (a) Two-dimensional velocity model showing contours of $V_p$ (in km/s) across the SW Greenland margin (b) Selected ray paths for OBS B, C, D, and E	72
4 11 (a) Crustal $S$ phases for OBS B and (b) a combination of hydrophone and vertical geophone channels of OBS C	74
4 12 The modeling of magnetic and gravity data across the SW Greenland continent margin	78
4 13 Compressional wave velocity versus shear wave velocity showing fields for various rock types	83
5 1 Map of the Labrador Sea, showing zones of refraction measurements	89
5 2 Line drawings from coincident multi-channel reflection line 90-1 (Keen et al 1994b) Horizontal distance is consistent with what is used for wide-angle modeling	94
5 3 Crustal velocity model for refraction line 90R3	96
5 4 Single-channel reflection profile along refraction line 90R2 with interpretations	99
5 5 Top Refraction profile at OBS K, 90R2 Bottom Ray-tracing on velocity model	101
5 6 Top Refraction profile at OBS I, 90R2 Bottom Ray-tracing on velocity model	102
5 7 Top Refraction profile at OBS Q, 90R2 Bottom Ray-tracing on velocity model	103
5 8 Top Refraction profile at OBS C, 90R2 Bottom Ray-tracing on velocity model	104
5 9 2-D velocity modeling of line 90R2, showing contours of $V_p$ every 0.2 km/s	105
5 10 Top Refraction profile at OBS B, 90R1 Bottom Ray-tracing on velocity model	109
5 11 Top Refraction profile at OBS H, 90R1 Bottom Ray-tracing on velocity model	110
5 12 Top Refraction profile at OBS Q, 90R1 Bottom Ray-tracing on velocity model	112
5 13 Top Refraction profile at OBS C, 90R1 Bottom Ray-tracing on velocity model	114
5 14 Top Refraction profile at OBS D, 90R1 Bottom Ray-tracing on velocity model	115
5 15 Top Refraction profile at OBS P, 90R1 Bottom Ray-tracing on velocity model	117
5 16 Top Refraction profile at OBS G, 90R1 Bottom Ray-tracing on velocity model	119
5 17 Top Refraction profile at OBS A, 90R1 Bottom Ray-tracing on velocity model	120
5 18 Top Refraction profile at OBS M, 90R1 Bottom Ray-tracing on velocity model	122
5 19 Top Refraction profile at OBS K, 90R1 Bottom Ray-tracing on velocity model	123
5 20 Top Refraction profile at OBS I, 90R1 Bottom Ray-tracing on velocity model	124
5 21 Refraction profile from OBS K and I on line 90R1, emphasizing crustal $S$ waves	125

5 22	Two-dimensional velocity model showing contours of $V_p$ across Labrador	127
5 23	Velocity/depth error analysis for the seismic phase P3 west of OBS A on 90R1	130
5 24	Time-domain comparison of refraction and reflection results	133
5 25	The modeling of magnetic and gravity data across the Labrador margin	138
6 1	Map of the Labrador Sea, showing the distribution of the high-velocity material on both margins	141
6 2	Compilation of magnetic (top), gravity (middle), and seismic velocity (bottom) results across the SW Greenland continent margin	143
6 3	Compilation of magnetic (top), gravity (middle), and seismic velocity (bottom) results across the Labrador continent margin	144
6 4	Time domain line drawings of coincident reflection line 90-3 for SW Greenland and line 90-1 for Labrador overlain with refraction results	Back Pocket
6 5	Reconstruction to chron 27 for velocity contour profiles for crust across the conjugate margins of the Labrador Sea	158
6 6	Reconstruction of balanced crust from both margins (a) Crustal reconstruction to chron 31 (68 Ma) (b) The same cross-section as (a) but with the high-velocity crust removed, (c) Seaward ends of lower crust for both margins are joined to show the balanced cross-section at the time of the final breakup	161
6 7	(a) Pre-stretching crust of the Labrador-Greenland continent (b) Restored cross-section with the asymmetry close to the point of lower crustal breakup removed (c) Rift zone crust at the time of rifting according to Figure 6 6c	164
6 8	(left) Sibuet's rifting model, (right) Boillot's rifting model	169
A1	$\chi^2$ contour plot of velocity-depth for seismic phase P3 west of OBS C (Figure 4 6)	182
A2	$\chi^2$ contour plot of $V_p/V_s$ ratios in lower crust and topmost sediment	183
B1 1	Cruise line positions of the Hudson 88R1 and 88R2	196
B1 2	Channel 2 (hydrophone) data of OBS R1J, mixed with time code cross-talks	197
B1 3	Channel 1 time codes of OBS R1J	198
B2 1	16 traces from channel 2 of OBS R1J at 45 km from OBS position	199
B2 2	16 traces from channel 1 of OBS R1J at 45 km from OBS position	200
B3 1	Power spectrums of channels 2 and 1 of OBS R1J at 45 km from OBS position Also shown are the coherency and phase spectrums of the two channels	201
B3 2	Power spectrum of channel 4 of OBS R1J at 50 km from OBS position	202
B3 3	Channel 2 data of OBS R1J Frequencies above 7 75 Hz are rejected by an 8-point Butterworth regression filter Time code disturbances are mostly suppressed, while signals are also attenuated	203



B3 4 Channel 1 in f-k domain	204
B3 5 Channel 2 in f-k domain	205
B3 6 Contour map of channel 2 in f-k domain	206
B3 7 Mesh display of channel 2 data in f-k domain with the first and the third quadrants removed of their energy (c f Figure B3 5)	207
B3 8 Seismograms generated by inverse Fourier transforming the modified f-k response function as shown in Figure B3 7	208
B3 9 Seismograms generated by inverse Fourier transforming the f-k response function of channel 2 after removing all the numbered energy concentrations in Figure B3 6 While time codes are highly suppressed, signals are also attenuated	209
B3 10 Seismograms generated by inverse Fourier transform the f-k response function that includes only the energy concentrations numbered 9 and 10 in Figure B3 6 These are purely time codes	210
B4 1 Estimating time lags by matching the maximum correlation between channel 2 and channel 1	211
B4 2 After time code line-up, the time codes in channel 2 is better lined up than the original traces as shown in Figure B2 1	212
B4 3 Before time code line-up the estimated time code in channel 2 (by averaging along straight lines across different traces) is less resolved Subtracting the estimates from the data gives the lower left diagram	213
B4 4 After time code line-up the estimated time code in channel 2 (by averaging along curved lines across different traces defined by the estimated time lags) is better resolved Subtracting the estimates from the data gives the lower left diagram	214
B4 5 First iteration of time code removing processing	215
B4 6 7th iteration of time code removing processing	216
B4 7 First iteration of time code removing processing with correlation performed at a narrow frequency band from 7.75 to 12 Hz	217
B4 8 third iteration of time code removing processing with correlation performed at a narrow frequency band from 7.75 to 12 Hz	218
B4 9 Time code removing processing with correlation performed at a narrow frequency band from 7.75 to 12 Hz 5 time windows were used	219
B4 10 Time code removing with correlation performed at a narrow frequency band from 7.75 to 12 Hz 5 time windows were used with half of each overlapped	220
B4 11 3rd iteration of time code removing processing with correlation performed at a narrow frequency band from 7.75 to 12 Hz 5 time windows were used with half of each overlapped	221

B4.12 3rd iteration of time code removing processing with correlation performed at a narrow frequency band from 7.75 to 12 Hz. 5 time windows were used with half of each overlapped. The resulting traces are stacked by 12 .....	222
B4.13 First iteration of time code removing processing with correlation performed at a narrow frequency band from 7.75 to 12 Hz. 5 time windows were used with half of each overlapped. The resulting traces are stacked by 12 and every one trace is displayed.....	223

## Abstract

When continental lithosphere is stretched, it thins, subsides, and ruptures, followed by formation of a new oceanic basin between the continental margins. The processes that govern the evolution of rifted continental margins have been controversially addressed, especially in the construction of rifting models (pure or simple shear) and in the interpretation of an anomalous high-velocity lower crustal layer that is commonly observed on both (conjugate) sides.

This thesis presents the first conjugate margin studies based on crustal seismic velocity structure. The study area is the Labrador Sea conjugate margins: southwestern Greenland and Labrador margins. Data include wide-angle seismic records from two 230-km-long profiles along and across the southwestern Greenland margin, and a 150-km-long profile and a 350-km-long profile along and across the Labrador margin. Coincident deep multi-channel and single-channel reflection data are used during wide-angle modeling and final interpretations. Modeling of observed gravity and magnetic data is also performed and used in the interpretations.

The results indicate three distinct zones across each margin. From the continent seaward, Zone I represents thinned continental crust, Zone II the transitional crust, and Zone III the true oceanic crust. The landward end of the cross-section in Zone I represents 27-30 km thick preexisting continental crust whose middle to lower crust has velocity of 6.2-6.9 km/s and whole upper crust has velocity of 5.5-5.6 km/s. This crust is thinned gradually seaward over a distance of ~100 km in Zone I on the Labrador margin while on the SW Greenland margin it is thinned sharply over a distance of only 20 km. Zone II is characterized by a distinct lower crust with a high-velocity of 7.0-7.6 km/s. This layer is 4-5 km thick, extends for a horizontal distance of 70-80 km, and is located seaward of Chron 31 on both margins. Combined interpretation for this lower crustal block favors an origin of serpentinization rather than magmatic underplating. Comparison with the seafloor spreading magnetic anomaly data suggests that true oceanic crust started to form between Chrons 27 and 31, with the first clear magnetic anomaly occurring at Chron 27.

The crustal cross-sections are used as a starting point in reconstruction of the rifting history. Results suggest that the initial continental stretching started symmetrically. At a later stage of stretching, more thinning occurred at the eastern side of the rift zone, leading to a lower crustal separation near the seaward end of the continental slope on western Greenland. A composite pure and simple shear model is favored in which all the lower crust in the rift zone moves with Labrador and most of the upper crust in the rift zone moves with Greenland. Serpentinization of upper mantle materials started after the crustal separation, forming undercrusting beneath the thinned upper crust on the southwestern Greenland margin and seaward of the lower crust on the Labrador margin. This proposed model explains all the new data presented in this thesis, as well as other observations that have been controversially addressed on similar margins.

## List of Abbreviations and Symbols

1-D	One-dimensional
2-D	Two-dimensional
88R1	Refraction line along western Greenland, shot in 1988
88R2	Refraction line across western Greenland, shot in 1988
90R1	Refraction line across Labrador margin, shot in 1990
90R2	Refraction line on the continental slope of Labrador margin, shot in 1990
90R3	Refraction line on the shelf of Labrador margin, shot in 1990
90-1	MCS reflection line across the Labrador margin, shot in 1990
90-3	MCS reflection line across west Greenland, shot in 1990
Hz	Frequency unit in Hertz
MCS	Multi-channel seismic profiles
OBS	Ocean bottom seismometers
P	Compressional wave
P1	P wave Refraction in oceanic sediment
P2	P wave Refraction in oceanic upper crust
P3	P wave Refraction in oceanic lower crust
Pc	P wave Refraction in continental lower crust
PcP	Wide-angle reflection from continental upper/lower crustal boundary (Conrad boundary)
Pg(1)	P wave Refraction in continental upper crust
Pg(2)	P wave Refraction in continental middle crust
PmP	Wide-angle reflection from the Moho discontinuity
Pn	P wave Refraction in upper mantle
Ps	P wave in sediment
Pw	P wave in water
S	Shear wave

S/B	Sonobuoy
Sg(1)	S wave Refraction in continental upper crust
Sg(2)	S wave Refraction in continental middle crust
$\sigma$	Poisson's ratio
S/N	Signal to noise ratio
$\rho$	Density
T.C.	Time codes
$T_c, T_o$	Computed and observed travel-time
$T_{rms}$	Root-mean-square travel-time misfit
dZ, dV, dg	Perturbation of depth, velocity, and gradient
V, $V_p$	Compressional velocity
$V_a$	Apparent velocity
$V_s$	Shear velocity

## Acknowledgments

I am indebted to many individuals and organizations for their support during the preparation and completion of this thesis. Special appreciation is to the members of my thesis committee. Among them are Ian Reid who provided necessary hardware and software support for processing and modeling the wide-angle seismic data on the Labrador margin, and Charlotte E. Keen whose valuable comments and criticisms on the final interpretations of cross margin seismic profiles helped greatly to improve the writing of Chapters 5-7. In addition, Barry Clark's editorial comments and many suggestions on geological interpretations were valuable for improving the thesis. Constructive inputs from Chris Beaumont, Shirri Srivastava and Owen Hertzman have also been very helpful. Finally, Keith E. Loudon, my thesis supervisor, merits a special word of appreciation. I am grateful for his open ideas exhibited in interpreting seismic data and his patience in reading and commenting all kinds of versions of documents I handed to him. I am also grateful for the graduate fellowship he offered and the opportunities he provided for attending various academic conferences.

I have enjoyed working with the people and the stimulating scientific and social environment in the Department of Oceanography at Dalhousie University, and in the Atlantic Geoscience Center. Frequent consultation with John Osler in computer skills were very beneficiary and many of the computer programs I used at Dalhousie were written by him. Every day friendly greeting and help from Susan, David, Jim, and many other uncounted colleagues and friends leave me happy memories.

My special appreciation is devoted to my wife, Tracy (Cuining) whose persistent support and encouragement are essential for my going through the long-lasting thesis period at Dalhousie. Her distinctive personality and talent have proved to be a great asset to me and my family.

## **Chapter 1. Introduction**

This thesis is aimed at a better understanding of initial rifting mechanisms for Atlantic-type continental margins. The data that will be used primarily include crustal-scale wide-angle seismic measurements, coupled with coincident multi-channel or single-channel reflection, and gravity and magnetic data across the conjugate margins of the Labrador Sea. The resulting crustal structure for both margins is used for a reconstruction of pre-breakup crust, which leads to a continental stretching and rifting model that is consistent with existing observations for the Labrador Sea margins as well as for similar continental margins worldwide.

### **1.1 Continental Stretching**

When continental lithosphere is stretched, it thins and subsides with sediments accumulating atop the thinned crust (McKenzie 1978). Continued stretching causes the continental lithosphere to break, allowing asthenosphere to upwell to the surface and a new ocean basin to form.

Two contrasting end-member styles are believed to exist for continental stretching: pure shear and simple shear. In the most basic pure shear model (McKenzie 1978), thinning takes place uniformly within the crust and the upper mantle. This model predicts a phase of tectonic subsidence due to crustal thinning and lithospheric heating, followed by a phase of thermal subsidence due to lithospheric cooling. In addition to subsidence, the pure shear model predicts time- and space-domain variations in heat flow and thickness of



continental crust that have been tested in basins such as the North Sea continental basin (Sclater and Christie 1980), the northern Bay of Biscay continental margin (Le Pichon and Sibuet 1981; Chenet et al. 1983), and the Baltimore Canyon Trough and Georges Bank Basin (Sawyer et al. 1982). For some regions, such as the margins of the Labrador Sea and of Nova Scotia, a depth-dependent model which allows crustal and sub-crustal (mantle) material to extend differentially can account for major observations (Royden and Keen 1980; Beaumont et al. 1982; Issler and Beaumont 1987).

Although the pure shear model can explain many observations in extensional basins, it does not address the asymmetry that is observed on many continental margins. This asymmetry is manifested in a variety of ways, such as the volume and history of sedimentation, the extent of crustal thinning, and the patterns of basin-forming listric normal faults.

The alternative end-member type simple shear model suggests that this asymmetry may be a product of detachment faulting (Wernicke 1981) or delamination (Lister, et al. 1986; Wernicke and Tilke 1989) of the whole lithosphere. This model invokes a low-angle detachment fault that cuts through the continental crust and separates the resulting margins into asymmetric, upper and lower conjugate plates. The upper plate margin records more thinning of the lower crust and less syn-rift subsidence than does its conjugate, lower plate margin. Quantitative modeling of simple shear extension predicts asymmetry in subsidence and thermal evolution for the upper and lower plates (Voorhoeve and Houseman 1988; Issler et al. 1989). On rifted continental margins such as the Bay of

Biscay (Le Pichon and Barbier 1987) and Galicia Bank (Boillot et al. 1989b, 1992), the simple shear model has been supported by the observation of an S-reflector, interpreted as the trace of the detachment fault, and a smaller amount of upper crustal stretching as compared to total crustal thinning.

An alternative explanation of the asymmetry observed on rifted continental margins is that the continent was rifted symmetrically by pure shear but resulted in asymmetric conjugate margins because rupturing was close to one side of the rift zone. This explanation was proposed by Keen et al. (1989) in reconstructing rifting between Canada and Europe based on deep seismic profiles across the Flemish Cap margin and its conjugate Goban Spur margin (Peddy et al. 1989). Offsets between preexisting weak zones within the continental crust and the location of a hot ascending mantle plume may result in this process (Dunbar and Sawyer 1989; Braun and Beaumont 1989). In this model, rifting may occur by pure shear, or by a composite pure and simple shear mechanism in which the lower crust deforms by a pure shear mechanism while the upper crust detaches along a low-angle fault (Braun and Beaumont 1984; Keen et al. 1989; Sibuet 1992).

## **1.2 Volcanism on Rifted Continental Margins**

As summarized by White and McKenzie (1989), volcanism may significantly modify the shape and thermal history of rifted continental margins. These margins are called volcanic to contrast with nonvolcanic margins which are devoid of surface volcanic activity.

Typical volcanic rifted conjugate margins exhibit major zones of extrusive and intrusive volcanic material on each side. The existence of these extrusives has been observed on reflection profiles as seaward-dipping reflectors, such as in Rockall and Voring Plateaus (Hinz et al. 1987), and has been confirmed by drilling (Eldholm et al. 1986). In addition, an even larger amount of melt products are underplated immediately beneath the thinned continental crust and seaward-dipping reflectors, bearing a high velocity of 7.2-7.6 km/s as observed from wide-angle seismic data (e.g. Mutter et al. 1984; White et al. 1987). One explanation for this is that these volcanics were formed as a result of upwelling of anomalously hot asthenosphere beneath thinned continental crust. As shown by White and McKenzie (1989), the observed magmatic material in the Hatton Bank margin could be generated if the potential temperature of the asthenosphere under the rifted margin was  $\sim 100\text{-}150^{\circ}\text{C}$  hotter during the rift stage than the mean potential temperature of normal oceanic spreading centers. The load of the extrusives makes the margin subside, while the addition of intruded material in the lower crust, together with the dynamic uplift caused by mantle convection and lithospheric heating, elevates the crust (White et al. 1987). Horizontal transport of the extrusives forms a group of seaward dipping sequences typically 4-7 km thick (Hinz et al. 1987) with a significant velocity increase of 3.5-6.5 km/s from top to bottom. This velocity gradient is probably caused by increasing crack closure with depth (Whitmarsh and Miles 1987; White et al. 1987). The addition of igneous material into the ductile lower crust forms the underplating layer which is typically 15 km thick with a well-defined velocity of 7.2-7.5 km/s. This velocity

coincides with the predicted velocity range of 7.0-7.8 km/s for the mantle-derived underplate based on thermo-petrologic models and initial and equilibrium pressure/temperature conditions (Furlong and Fountain 1986).

The problem with this model is that not all volcanic margins show a clear association with a thermal anomaly (e.g. Holbrook and Keleman 1993) and that the high-velocity lower crust is also observed, at a much smaller thickness, in many nonvolcanic margins (e.g. Whitmarsh et al. 1990; Reid 1994). These phenomena can be partly explained by an alternative convective partial melting model (Buck 1986; Mutter et al. 1988) in which mantle rocks are advected upward to a new depth depending on the amount of stretching. This model does not require a thermal anomaly in the asthenosphere and yet can result in the formation of underplating in the crust, a feature especially useful for nonvolcanic rifted margins such as those along eastern Canadian coast (Keen et al. 1994a). A disadvantage with this model is that currently there is no obvious mechanism other than the high asthenospheric temperature for the underplates to have a velocity higher than 7.2 km/s.

### **1.3 Seismic Measurements on Rifted Continental Margins**

Given the various complications involved in determining the initial continental stretching mechanisms, it has been difficult to discriminate convincingly between competing stretching models, especially between pure and simple shear models. As Steckler and Watts (1982) noted:

**“Seismic studies (refraction and reflection) with large aperture arrays in combination with biostratigraphic data from deep wells in the continental shelf, appear to hold the most promise of addressing these problems during the next decade.”**

While abundant MCS reflection and refraction data on rifted continental margins have been collected and interpreted, a complete understanding of the formation of these margins does not yet exist. In fact, indisputable evidence suggesting any dominance of either of the existing rifting models has not been observed. This is partly because (1) the margins are wide and with one exception (Keen et al. 1989), existing deep seismic profiles do not cover the complete conjugate margins from the continent to the ocean; (2) no combined studies of coincident refraction and reflection profiling have been made for crust on the complete conjugate pairs; (3) a thick pile of sediment frequently exists which prevents clear seismic signals from deep crustal layers from being recorded.

Seismic refraction methods have been used to define crustal affinities on rifted continental margins, but mainly for volcanic passive margins where refraction experiments reveal the existence of the high-velocity (7.2-7.5 km/s) lower crust (e.g., Mutter et al. 1984; Holbrook et al. 1994). The initial rifting mechanism, however, is probably best preserved on nonvolcanic margins, where the preexisting velocity signature of the continental crust has not been altered by subsequent volcanic activity. For investigating the nature of rifting mechanisms, refraction methods must delineate the detailed velocity structure from unstretched continent to normal oceanic crust. An example is the Goban

Spur margin where the cross-margin velocity contours from refraction profiling suggest a uniform, gradual thinning of both the upper and lower crust (i.e., pure shear) across the margin (Horsefield et al. 1994), which is in agreement with reflection data for the conjugate margins (Keen et al. 1989; Peddy et al. 1989). On the other hand, the wide zone of thin crust off the Iberia margin bears a velocity structure which is different from normal oceanic crust and therefore is interpreted to represent thinned continental crust (Ginzburg et al. 1985; Whitmarsh et al. 1986, 1990). The existence of a thin lower crustal layer bearing a high velocity of 7.2-7.6 km/s in nonvolcanic margins is interpreted to be either underplate igneous rocks (Todd and Reid 1989; Reid and Keen 1990; Whitmarsh et al. 1990) or serpentinized mantle (Pinheiro et al. 1992; Reid 1994).

#### **1.4 Conjugate Margins of the Labrador Sea**

The Labrador Sea is one of the best areas for a detailed study of the structure of rifted continental margin. This small basin, about 900 km wide (Figures 1.1-2), includes almost all the major tectonic elements appearing in the much larger Atlantic Ocean. This allows us a good opportunity to study with limited resources the geological and geophysical signatures of continent-ocean crustal changes. Although already well studied in terms of sedimentary sequences (Balkwill 1987; Rolle 1985) and magnetic anomaly and seafloor spreading history (Srivastava and Tapscott 1986; Roest and Srivastava 1989), the detailed structures of the continental and oceanic crust and the transitional region in between are still unclear. Our understanding of the basin-forming mechanisms of the

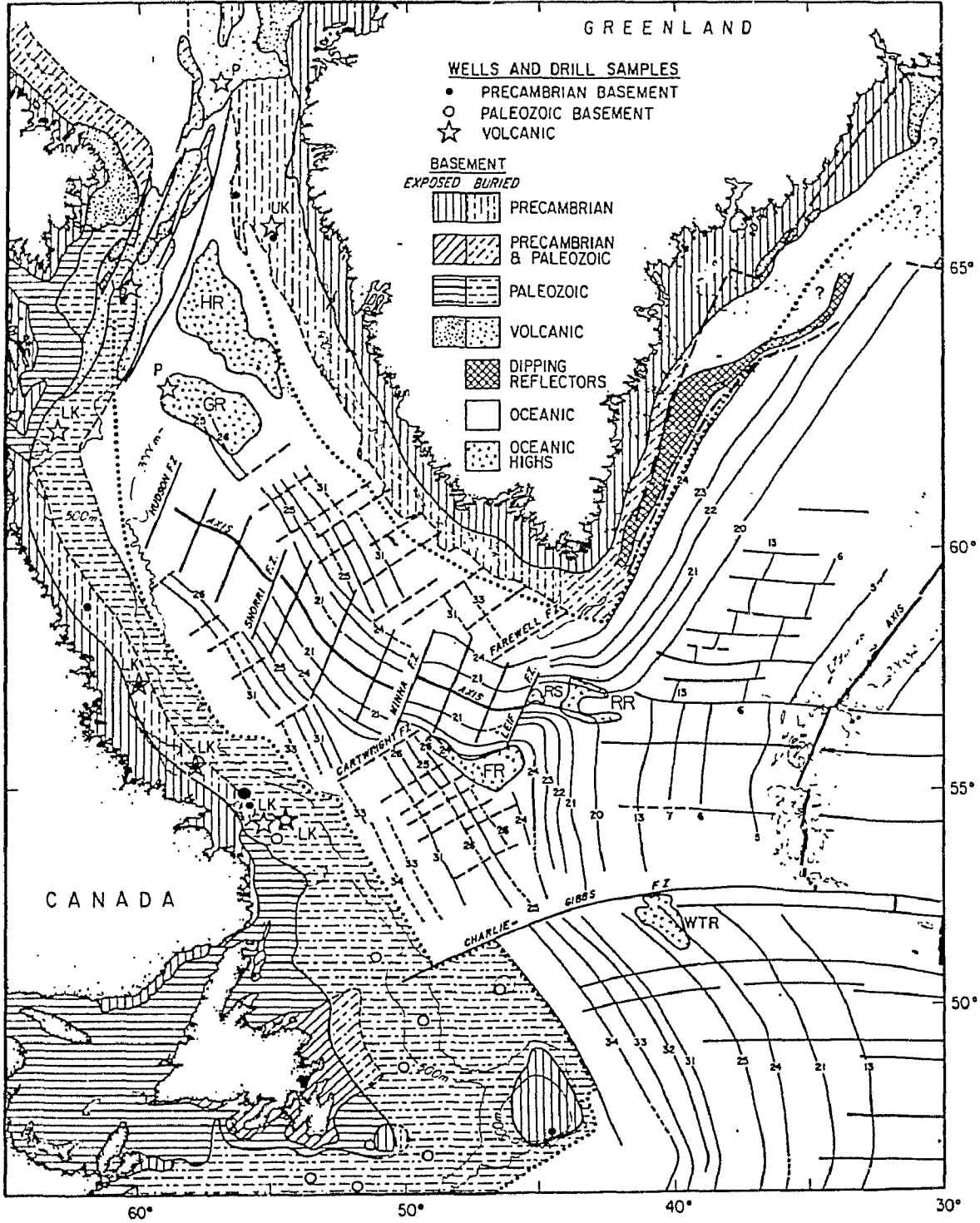


Figure 1.1. Summary of basement age and magnetic-anomaly lineations in the North Atlantic. Solid lines that cross the magnetic lineations are reasonably well determined fracture zones; dashed lines are more poorly determined fracture zones in the Upper Cretaceous and Paleocene crust. Significant basement highs on oceanic crust are shaded by a "v" pattern: HR = Hecla Rise; GR = Gjoa Rise; RS = Runa Seamount; RR = Ran Ridge; FR = Fury Rise; and WTR = West Thulean Rise. The dashed line in the West Greenland margin is the minimum seaward limit of Continent Ocean Boundary (COB); the nearby dotted line is probably the maximum seaward limit of COB. From Tucholke and Fry (1985).

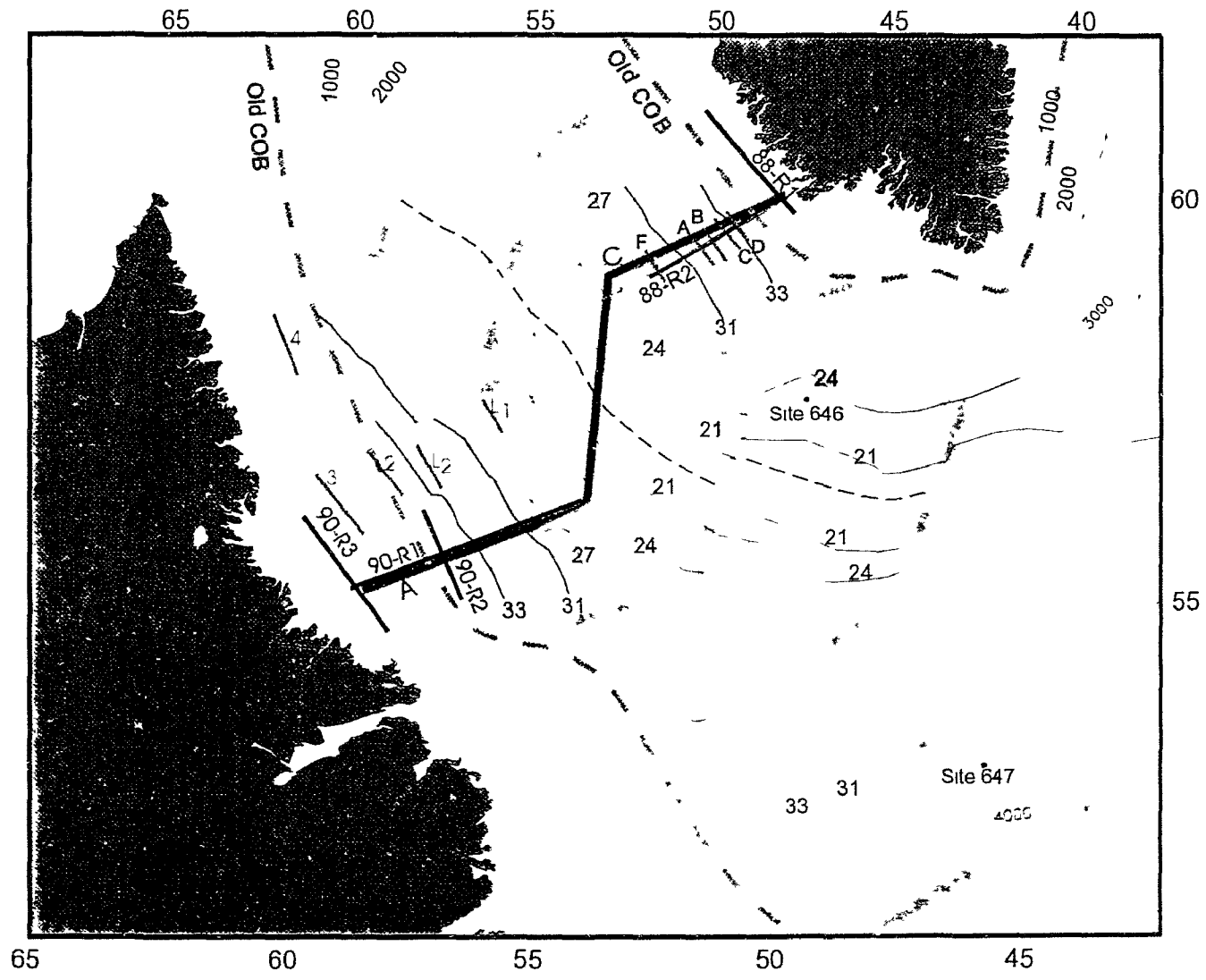


Figure 1 2 Map of the Labrador Sea, showing zones with refraction lines (thin solid lines), cross-basin MCS reflection line (thick solid lines), bathymetric contours (thin dotted curves numbered in meters), chrons (thin solid lines), fracture zones (thick grey), and extinct rift axis (thin broken)



Labrador Sea conjugate margins is still confused by the combined occurrence of features typical of both volcanic and nonvolcanic margins.

Both the Labrador and southwestern (SW) Greenland margins are classified as nonvolcanic, due to the lack of thick syn-rift extrusive basalts (Balkwill 1987; Rolle 1985). Cross-basin seismic reflection sections show a clear Atlantic-type margin asymmetry both in shelf/slope morphology and sedimentology. The southwestern Greenland margin is sediment-starved while the conjugate margin of the Labrador side has accumulated up to 11 km thick sediments underneath the shelf (Tucholke 1988). Seaward-dipping reflectors are not observed on either margin along available multi-channel reflection lines (Balkwill 1987). However, some features characteristic of volcanic margins are observed. Shallow marine to non-marine environments during deposition of syn-rift mid-Cretaceous sediments in the Labrador margin (Balkwill 1987) and southwestern Greenland margin (Rolle 1985) indicate little or no subsidence accompanying initial rifting. Seismic refraction studies reveal that a thin (<5 km thickness) layer with velocity of ~7.2 km/s in the lower crust seems to be sporadically present in the following areas: (a) in some oceanic areas, as shown by sonobuoy data at ODP site 646 (Srivastava et al. 1989), and near magnetic Chron 24 (Osler and Loudon 1992); (b) offshore on both sides of the basin, as shown by several previous refraction lines for the southwestern Greenland side (Stergiopoulos 1984) and earlier refraction lines for the Labrador side (Van Der Linden 1975); (c) underneath the Greenland shelf of the northern Labrador Sea (Gohl and Smithson 1993). The latter area exhibits a high-velocity (~7.5 km/s) lower crust

thickening northward to ~10 km towards Davis Strait, interpreted as magmatic underplating into the lower continental crust during the initial rifting. It is likely that this underplating is related to extensive hotspot activity in Davis Strait at Chrons 25-56 time (~58 Ma; Clark and Upton 1971). However, by this time the central and southern Labrador Sea was already opened and it is unclear whether the high-velocity lower crust in the central and southern areas is a result of underplating or other processes such as serpentinization.

The following topics are of particular interest to the refraction studies to be presented in this thesis:

- (1) No seismic determination of the Precambrian continental crust has previously been made on either side of the Labrador Sea. The crustal structural models constructed for the Labrador margin (Hinz et al. 1979) and used for geodynamic modeling (Issler 1987) are based on old refraction data under the Superior and Grenville Cratons to the west of Labrador (Berry and Fuchs 1973), as well as on the non-unique interpretation of gravity data (Hinz et al. 1979).
- (2) The nature of the continent-ocean boundary (COB) remains unclear. The position of the COB is normally set close to Chrons 33-34 (75-84 Ma), which are the oldest magnetic anomalies identified for the Labrador Sea (Srivastava and Tapscott 1986; Roest and Srivastava 1989). However, this COB position has been challenged by Chalmers (1991), who proposed that the COB occurs much farther seaward at Chron 27.
- (3) The high-velocity (7.2-7.5 km/s) lower crustal layer seems to be present under some places of the Labrador Sea but disappears under others, as revealed by existing refraction data (Van Der

Linden 1975; Stergiopoulos 1984; Srivastava et al. 1989; Gohl and Smithson 1993; Osler and Loudon 1992). The most puzzling fact is that some of these high velocities appear to lie in oceanic areas, unlike volcanic margins, where underplating appears beneath the continental slope. I would like to define the distribution of this layer and to determine if it exists on both conjugate margins, and represents underplate igneous rocks or serpentinitized peridotite.

- (4) Refraction profiling should be able to help determine whether the observed asymmetry in sediment thickness and shelf/slope morphology also exists in the deeper crust, and whether there is a clear separation between upper and lower plates in the pre-breakup crust, as predicted by a simple shear rifting model, or the pre-breakup crust was stretched uniformly, as predicted by a pure shear model.

### **1.5 Methodology and Data**

In this thesis I use wide-angle seismic reflection and refraction techniques to study crustal structure. Ocean bottom seismometers (OBS) are used for recording seismic signals shot from large airgun arrays at the sea surface. During a field experiment (Figure 1.3), a number of OBS are deployed to the seafloor along a pre-defined seismic line. Shots are fired from the beginning to the end of the line, with a dense shot interval of 100-200 meters. The seismic rays of each shot travel in all directions. Only a limited portion of these rays are recorded together with noise by the OBS receivers. The primary component of the recorded seismic energy includes direct water wave, and wide-angle reflections and

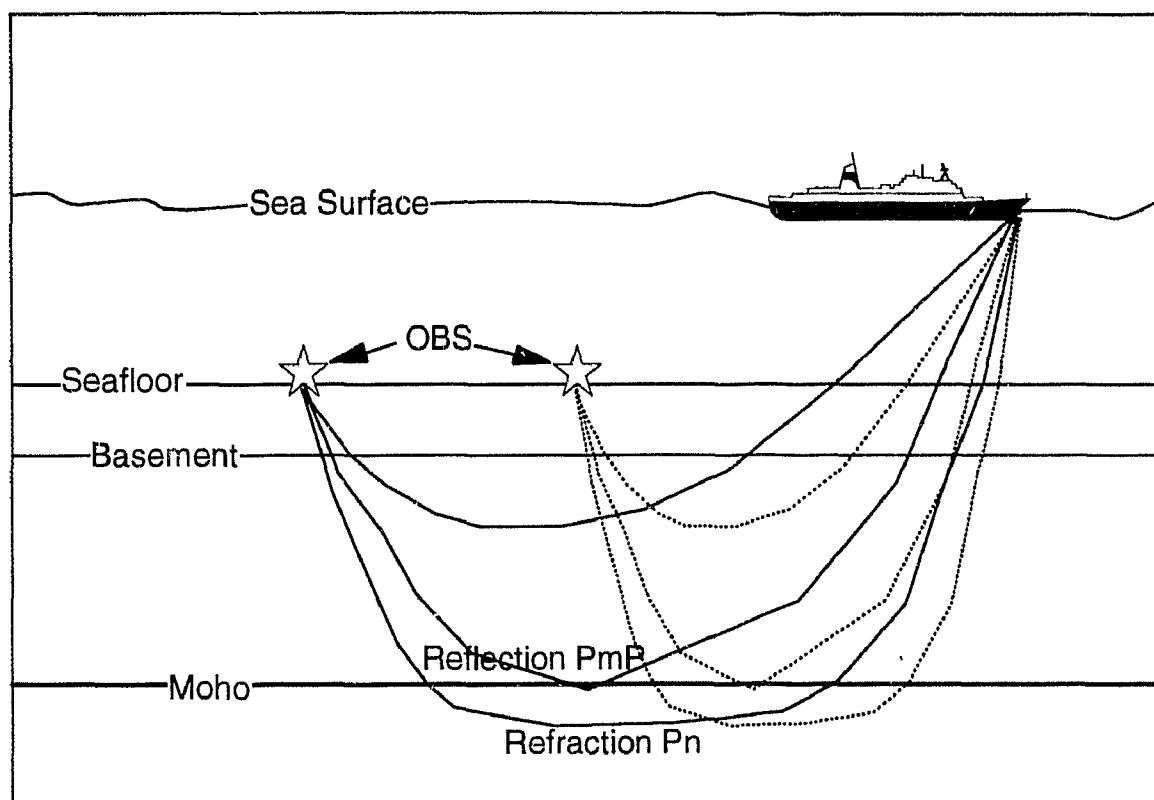


Figure 1.3 Schematic diagram showing the ray paths during a wide-angle seismic field experiment using ocean bottom seismometers (OBS).

refractions from the sediment, crust, and upper mantle. Refractions are the best indicator of velocity values, while reflections are most efficient in defining velocity discontinuities or reflectors. The direct water wave can be used for correcting possible errors associated with the OBS positioning and shot timing. To obtain the velocity structure, I use forward modeling techniques to match the observed travel-time and amplitude. This includes methods of one-dimensional reflectivity, WKBJ (Chapman 1978), and two-dimensional ray tracing (Cerveny et al. 1977). In the simple one-dimensional modeling, velocity is only a function of depth. This can be a valid approximation to simple structures with small lateral variation, such as along-strike on the continent. For complicated structures such as across continental margins, the two-dimensional approach should be used, in which velocity is a function of both depth and horizontal distance. Because of the introduction of an extra variable, many more complications are added to the modeling processes, especially in ways of parameterization and updating of the velocity model.

In 1988 and 1990, five wide-angle seismic reflection/refraction lines were shot to study the conjugate margins of the Labrador Sea (Figure 1.2). Among these profiles are two 230-km long refraction profiles (lines 88R<sub>1</sub> and 88R<sub>2</sub>) shot in 1988 along and across the southwestern Greenland margin. Profile 88R<sub>1</sub> is situated on the Precambrian craton of the West Greenland and profile 88R<sub>2</sub> extends from this craton seaward to the basin profile 87R<sub>2</sub> (Osler and Loudon 1994). The data and results of five unpublished sonobouy lines (Stergiopolous 1984) which are in the area close to 87R<sub>2</sub> are referenced during the wide-angle modeling. A coincident single-channel reflection profile was recorded along 88R<sub>2</sub>,

and is used to constrain sediment layers and basement topography. A recent MCS reflection profile (90-3; Keen et al. 1994b) runs close to line 87R<sub>2</sub> (Figure 1.2) and is referenced in the final interpretation of crustal structures across the margin.

Three refraction lines were shot in 1990 along and across the conjugate Labrador margin. The transect line 90R<sub>1</sub> is 350 km long, intersecting with the other shorter line 90R<sub>2</sub>, which is along-strike atop the thick sediments, and with another refraction line 90R<sub>3</sub>, (Reid 1994) which constrains the velocity structures of the preexisting Labrador continental crust. Line 90R<sub>1</sub> was complemented by a coincident multi-channel reflection line (Keen et al. 1994b). A combined analysis of these seismic data and their wide-angle modeling provides a clear picture of velocity structures across the wide continental shelf and slope of the Labrador margin. When this cross-section is interpreted in combination with that across the conjugate southwestern Greenland margin, it will be possible, for the first time, to reconnect the two-dimensional velocity structure of pre-breakup crust, from which to construct an initial rifting model for a nonvolcanic conjugate margin pair.

## **1.6 About This Thesis**

Chapter 1 gives a general introduction to our current knowledge and remaining problems associated with studying rifted continental margins and introduces the seismic techniques that will be used in this thesis to tackle these problems. Chapter 2 provides a general geological and geophysical background for the area surrounding the Labrador Sea, which will be useful in the geological interpretation of the refraction results. Chapter 3 presents the results and interpretation for the Precambrian crust along the shelf of

southwestern Greenland, the contents of which have been published in the *Canadian Journal of Earth Sciences* (Chian and Loudon 1992). Chapter 4 analyzes the refraction data along 88R<sub>2</sub> across the Greenland margin, the contents of which have been published in the *Journal of Geophysical Research* (Chian and Loudon 1994). Chapter 5 analyzes wide-angle data from fifteen OBS on two seismic lines on the Labrador margin. The combined interpretation of all these data on both margins, including refraction, reflection, gravity and magnetic data, appears in Chapter 6. This Chapter restores the crustal structure across the conjugate margins during rifting, and compares the results with those on several other nonvolcanic rifted margins, including the position of the continent-ocean boundary, the origin of the observed high-velocity lower crust, the nature of the upper continental crust, and the initial rifting mechanisms. Finally, Chapter 7 summarizes the major observations and interpretations of this thesis and presents some possible implications from the new results that may lead to future work for studying rifted continental margins.

The major contribution of this thesis is that it presents the first detailed seismic velocity cross-sections for crust across a complete conjugate pair of nonvolcanic rifted continental margins. Based on these cross-sections, the pre-breakup stretched continental crust is reconstructed, and a new rifting model is proposed. This model is compatible with existing data and overcomes the difficulties encountered by existing rifting models.

## **Chapter 2. Geology and Previous Geophysical Data**

In this Chapter, I will briefly review the regional geology and tectonic setting of the Labrador Sea. Geology of two different eras is involved: Precambrian and Phanerozoic. Precambrian rocks span a time period of about 1700-1900 Ma. Refraction lines 88R<sub>1</sub> and 90R<sub>3</sub> were deployed over these rocks to constrain their crustal structure. Phanerozoic geological events took place after ~150 Ma. The primary interests of this thesis will be in the latter geological period, whose crustal structure is constrained by refraction lines 88R<sub>2</sub>, 90R<sub>1</sub>, and 90R<sub>2</sub>, as well as by reflection, gravity and magnetic data.

### **2.1 The Labrador Sea**

The Labrador Sea forms a northwestward extension of the North Atlantic Ocean, with the main basin about 900 km wide, bounded in the west by Labrador, in the east by SW Greenland, and in the north by Davis Strait (Figure 1.1). Its coast lines span a length of ~1300 km from its southern limit to Davis Strait in the north. The continental shelf and slope are much narrower on the western Greenland margin than on the Labrador margin (Figure 1.2; Srivastava et al. 1981). About 4 million cubic kilometers of Cretaceous, Tertiary, and Quaternary clastic sediments have been deposited into the basin (Balkwill 1987). Half of this material comprises terrace prisms on the Canadian and Greenland margins, most of which is along the Canadian margin. The other half forms a thick blanket on the basin floor. The crust is deeply subsided under the Labrador shelf, partly due to sediment loading, whereas little or no subsidence has occurred under the western Greenland shelf (Rolle 1985).



## **2.2 Precambrian Geology**

Both sides of the Labrador Sea are occupied by several Precambrian metamorphic complexes (Figure 2.1). To the west side, the rocks of eastern Labrador comprise two distinct crustal blocks: Middle Proterozoic block (<1710 Ma) in the south (Grenville Craton), and Archean to Lower Proterozoic craton (Nain Province) in the north, which was affected by the Makkovikian Orogeny between 1860-1760 (Scharer et al. 1988). On the eastern side of the Labrador Sea, the rocks of West Greenland comprise three distinct groups: the Archean Block, Ketilidian Mobile Belt, and Nagssagtoqidian Mobile Belt (Srivastava 1978). While the Nain province corresponds to the Archean Block in Greenland, the Makkovik Orogen is possibly a trans-Labrador-Sea extension of the Ketilidian Mobile Belt in southern Greenland. The Nagssagtoqidian Mobile Belt in northern Greenland received northward-progressive deformation and metamorphism until ~1700 Ma. Dating of surface Precambrian rocks show younger ages in southern Labrador than in northern Labrador. Two possible models to explain this age difference are the southward tilting of continental crust or the progressive southward accretion of the crust (Scharer and Gower 1988). The latter resembles the determination that southwestern Greenland was formed through the late Archean juxtaposition of several separately-evolved terrains (Friend et al. 1988).

## **2.3 Phanerozoic Geology and Previous Geophysical Data**

The rift-related Mesozoic extension of the Canada-Greenland continent possibly started at ~160 Ma, as evidenced from the dating of coast parallel dike swarms in SW

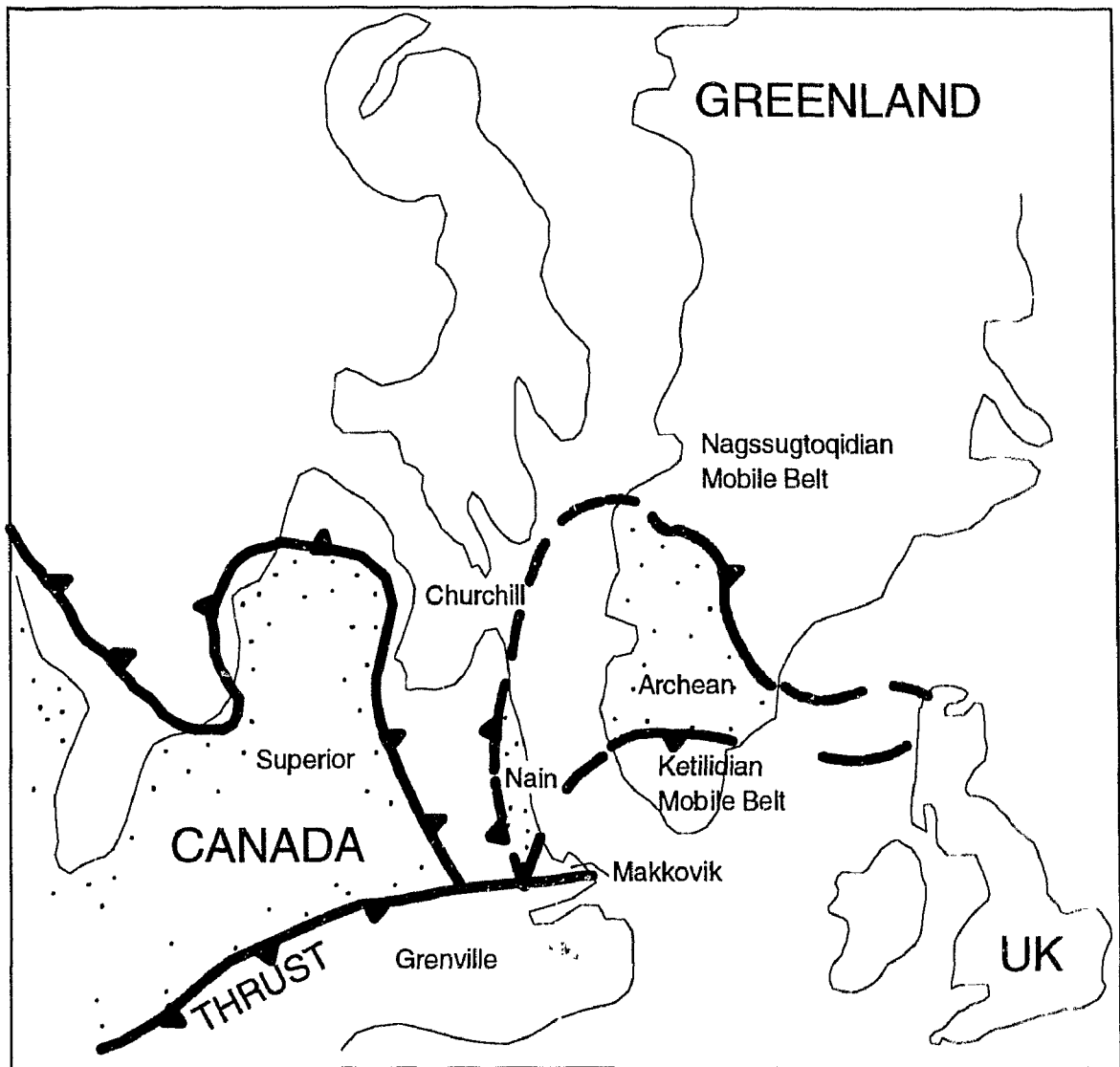


Figure 2.1 Correlation of various Precambrian provinces that were part of the North Atlantic Craton before the Mesozoic opening of the Atlantic Ocean. Areas shaded with dots represent oldest rocks in Archean time. After Korstgard et al. (1987).

Greenland (Watt 1969). Propagating from south to north, the Atlantic rifting event arrived at the Grand Banks by the early Cretaceous, first split the Greenland-Europe continent from Canada during the mid-Cretaceous, and then separated Europe from Greenland in the late Paleocene. The first of these two rifting phases allowed active seafloor spreading produced in the Labrador Sea. This rifting occurred with minimal volcanic activity, leaving less than 800 m of syn-rift extrusive basalts on the Labrador margin (Balkwill 1987). Unlike the continental breakup in other parts of the North Atlantic where the rift axes are superimposed to a large extent on Phanerozoic megasutures of different cratons, the rift between Labrador and Greenland developed entirely within Precambrian basement and cross-cut the structural grain (Ziegler 1989).

Little or no subsidence accompanied the rifting, as suggested from the depositional environment of syn-rift sediments under both margins (Balkwill 1987; Rolle 1985). Features typical for Atlantic-type passive margins are present, including asymmetry in shelf/slope morphology and sediment distribution. Less than 4 km of sediments are deposited near the western Greenland margin while the Labrador margin has accumulated up to 11 km of sediments under the shelf (Tucholke 1988; Figure 2.2).

The seafloor spreading history of the Labrador Sea is documented by magnetic anomaly lineations, with well-defined anomalies observed between Chrons 21 and 27 (48-62 Ma) (Srivastava 1978; Rcest and Srivastava 1989). Anomaly lineations older than Chrons 24-25 (54-57 Ma) are broken by several fracture zones (Figure 1.1), which are associated with a NW rotation of the spreading axis at anomalies 24-25 when Eurasia

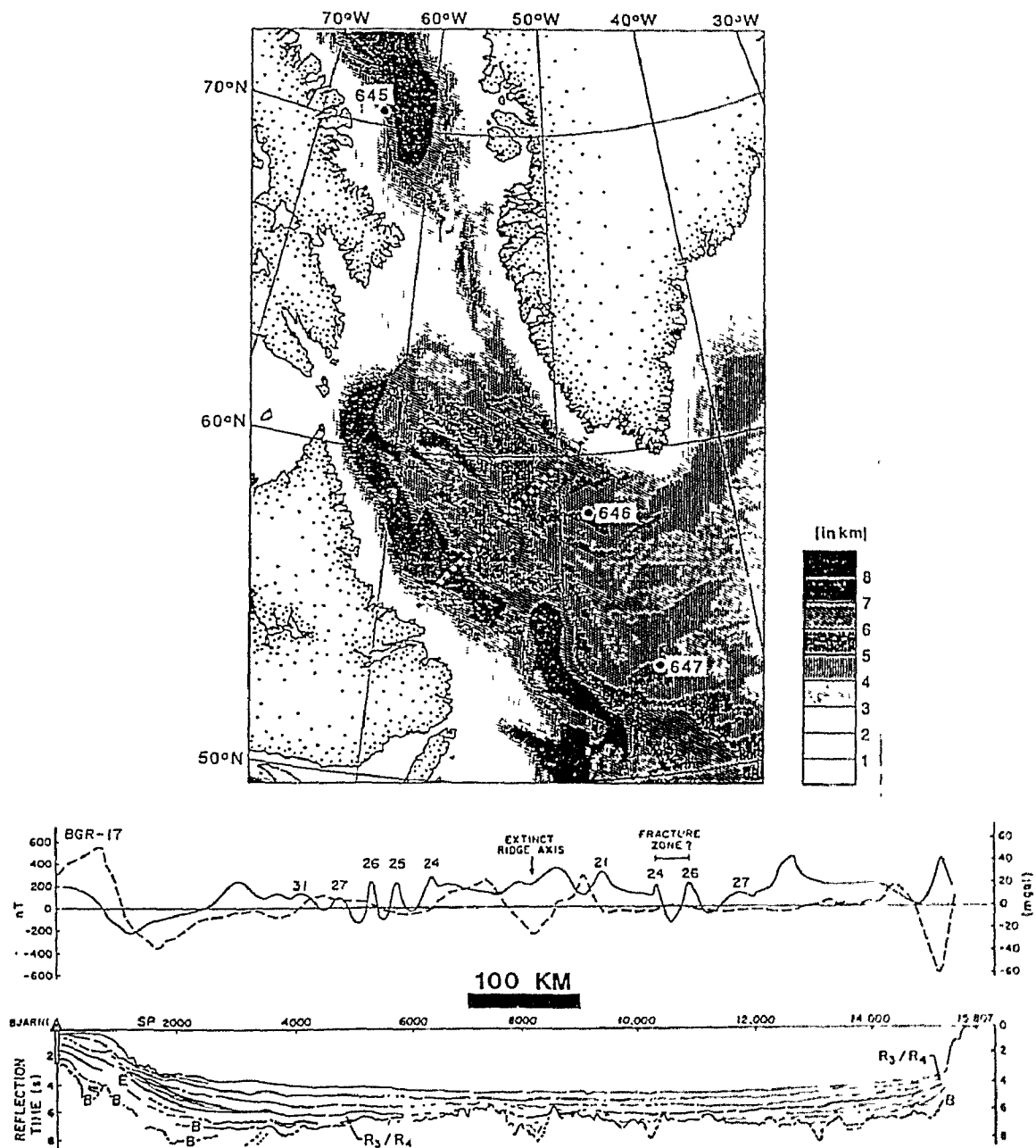


Figure 2.2 Sediment thickness map of the Labrador Sea. Also shown are gravity (dotted line) and magnetic anomalies (solid line) in the middle diagram and line drawings of BGR multichannel line 17 in the bottom diagram. Modified from Srivastava and Arthur (1989).

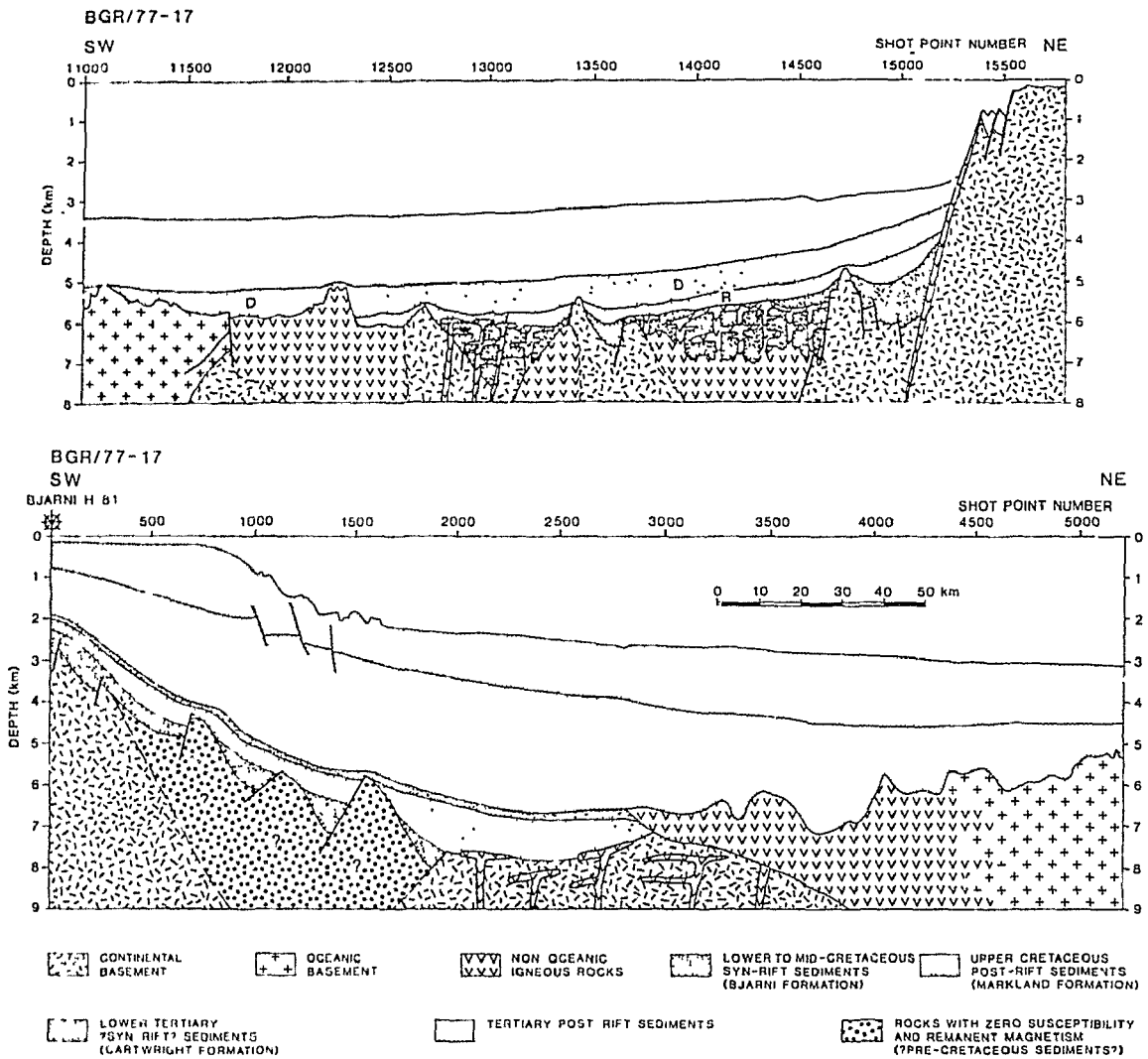


Figure 2.3 Interpreted geological cross-section across the margins of Greenland (top) and Labrador (bottom) based on reprocessing of BGR-17. After Chalmers et al. (1993).

separated from Greenland. The less clearly defined, low amplitude anomalies in areas older than Chron 27 have been interpreted by Roest and Srivastava (1989) as Chrons 31 and 33. This has been challenged recently by Chalmers (1991) who, on the basis of reprocessing of MCS reflection data BGR-21 (the Federal Institute for Geosciences and Natural Resources), suggested an initiation of seafloor spreading at Chron 27 (62 Ma; Figure 2.3). His interpretation places the continent-ocean boundary (COB) ~120 km farther seaward of the previously suggested position.

The sediment-corrected oceanic basement depths across the whole basin are approximately 1 km too shallow compared with the world average depth for crust of the same age, which is similar to what is observed in the Norwegian-Greenland Sea (Hyndman 1973; Srivastava and Arthur 1989). The progressive northward shoaling of bathymetry from southern Labrador Sea to Davis Strait lead Hyndman to suggest that the rifting was caused by a hotspot, which was activated at Davis Strait in the late Cretaceous and then moved through Greenland to its current position under Iceland. Surface and borehole measurements of heat flow at site 646 are 20-25% higher than predicted by a standard lithospheric thermal model (Louden et al. 1989). Therefore a significant amount of this depth anomaly may be due to elevated temperatures from the hot-spot activity in the Davis Strait during late Cretaceous-Paleocene time. Geochemical studies of the large volume of basalts onshore and offshore Baffin Island and the west Greenland coast suggests that they are products of intraplate volcanism as opposed to MORB (mid-ocean ridge basalts; Clarke et al. 1988). The geochemical relationship between the basalts of

Davis Strait and Site 647 in the Labrador Sea appears to be similar to that between the basalts of the Iceland hot-spot and Rockall margin which also suggests a hot-spot origin for the elevation and thermal anomalies (Srivastava and Arthur 1989).

Recent refraction studies on the Greenland margin of the northern Labrador Sea show the existence of a high-velocity ( $\sim 7.5$  km/s) lower crust thickening toward Davis Strait, interpreted as magmatic underplating into the lower continental crust during initial rifting (Gohl and Smithson 1993). It is likely that this underplating is related to hotspot activity in Davis Strait at Chrons 25-26, by which time the central and southern Labrador Sea was already opened. Deep crustal structure for the Labrador basin is partly shown by some scattered, old refraction lines on the northern Labrador margin (Van der Linden 1975; Figure 2.4), on the SW Greenland margin (Stergiopolous 1984; Figure 2.5), and some newer sonobuoy data near ODP site 646 (Srivastava et al. 1989) and OBS data in the center of the basin (Osler and Louden 1992; 1994). Some of these data show the existence of a high-velocity lower crust with a small thickness of  $< 5$  km in the oceanic regions. A proper interpretation for the high-velocity layer awaits further data.

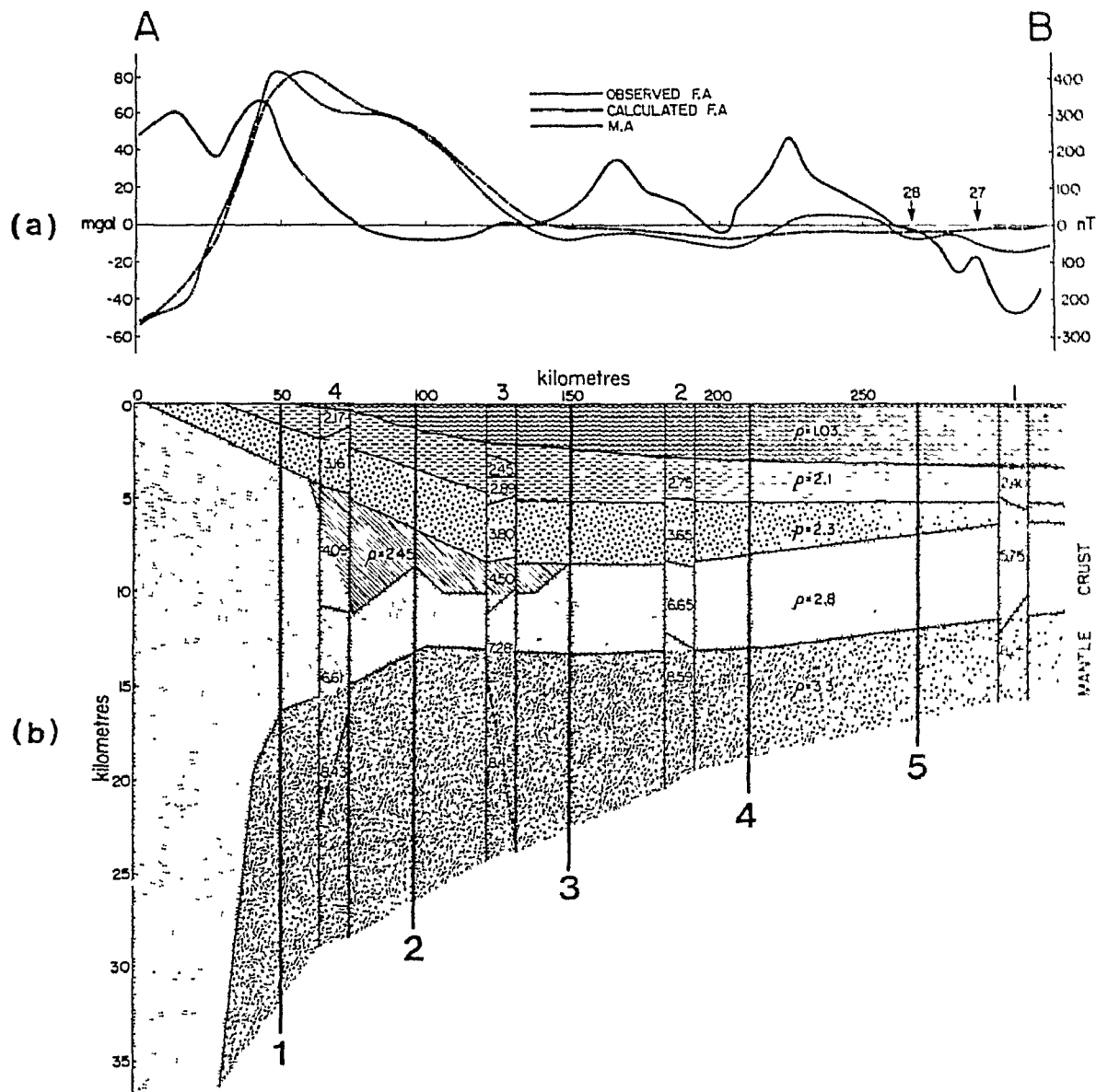


Figure 2.4 (a) The fit between the observed (dotted) and the calculated (dashed) free-air anomalies across the Labrador margin. Magnetic anomaly along profile is also shown (solid). The corresponding density and velocity model is shown in (b). Velocity and density values are given in km/s and gr/cm<sup>3</sup>, respectively. After Van der Linden (1975) and Hinz et al. (1979).



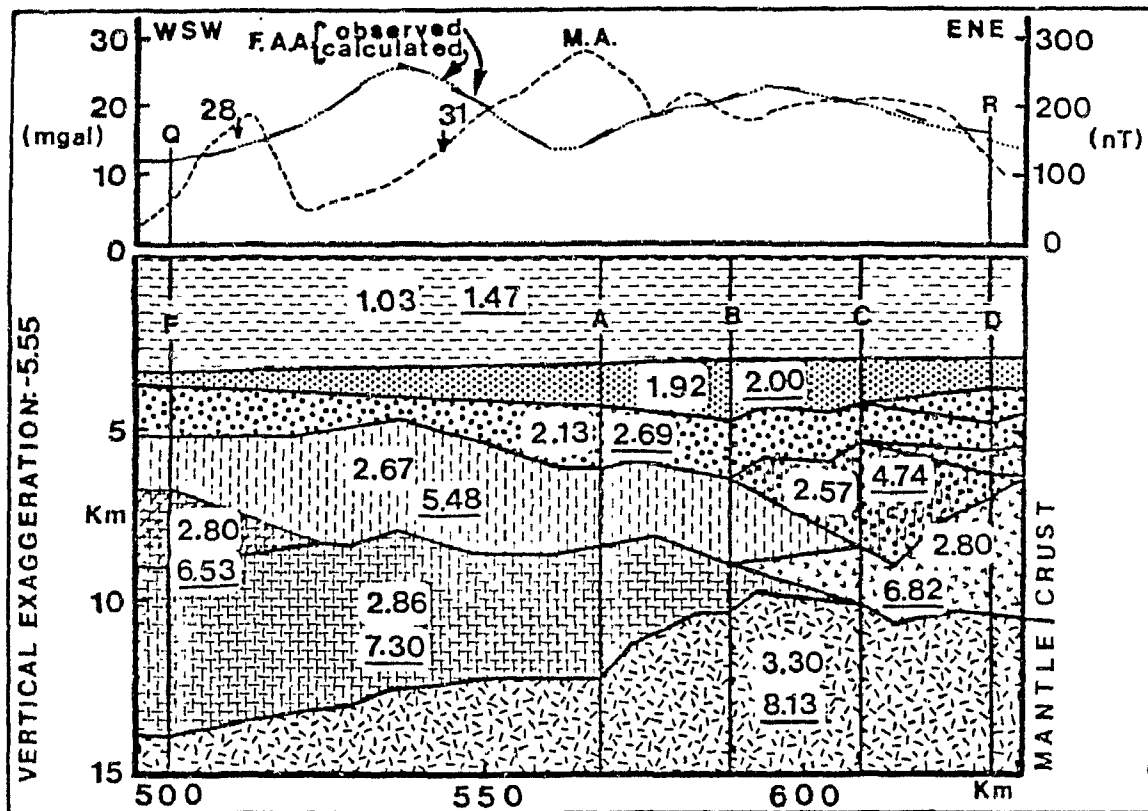


Figure 2.5 The structural cross-section of Stergiopolous (1984) starting from lines F to D in the Labrador Sea map (Figure 1.2). Number in parentheses are density values in  $\text{g}/\text{cm}^3$ , while the other numbers inside each layer denotes P wave velocities in  $\text{km}/\text{s}$ .

## **Chapter 3. Archean/Ketilidian crust Along the Continental Shelf of SW Greenland**

### **From a Seismic Refraction Profile**

#### **3.1 Introduction**

In the summer of 1988, two 230-km-long seismic refraction profiles were shot along and across the southwestern Greenland continental margin. This chapter presents the interpretation of the line shot along the shelf of southwestern Greenland parallel to the ocean-continent boundary. The purpose of this investigation is two-fold: to study the crustal velocity structure of the Archean/Proterozoic boundary of the southwestern Greenland continental crust and to determine if this part of the continental crust has been affected by the Mesozoic rifting which produced the Labrador Sea.

The location of the refraction profile with respect to major geological boundaries is shown in Figure 3.1. About half of the refraction line lies in the Archean gneiss complex; the other half crosses the border zone and extends into the Ketilidian granite mobile belt. Geochemical studies indicate that the southern border of the Archean craton in Greenland is a Proterozoic continental margin (Van Breemen et al. 1974; Patchett and Bridgwater 1984; Kalsbeek and Taylor 1985a, b). Surface geological and geochemical studies suggest that the formation of the various tectonic units in this North Atlantic craton was dominated either by successive late Archean to Proterozoic intrusions (Schärer and Gower 1988), or by late Archean juxtaposition of several separately-evolved terrains (Friend et al. 1988). One of the most important questions is whether the Archean/Proterozoic boundary is a predominantly vertical feature, as suggested by surface geology, or whether it

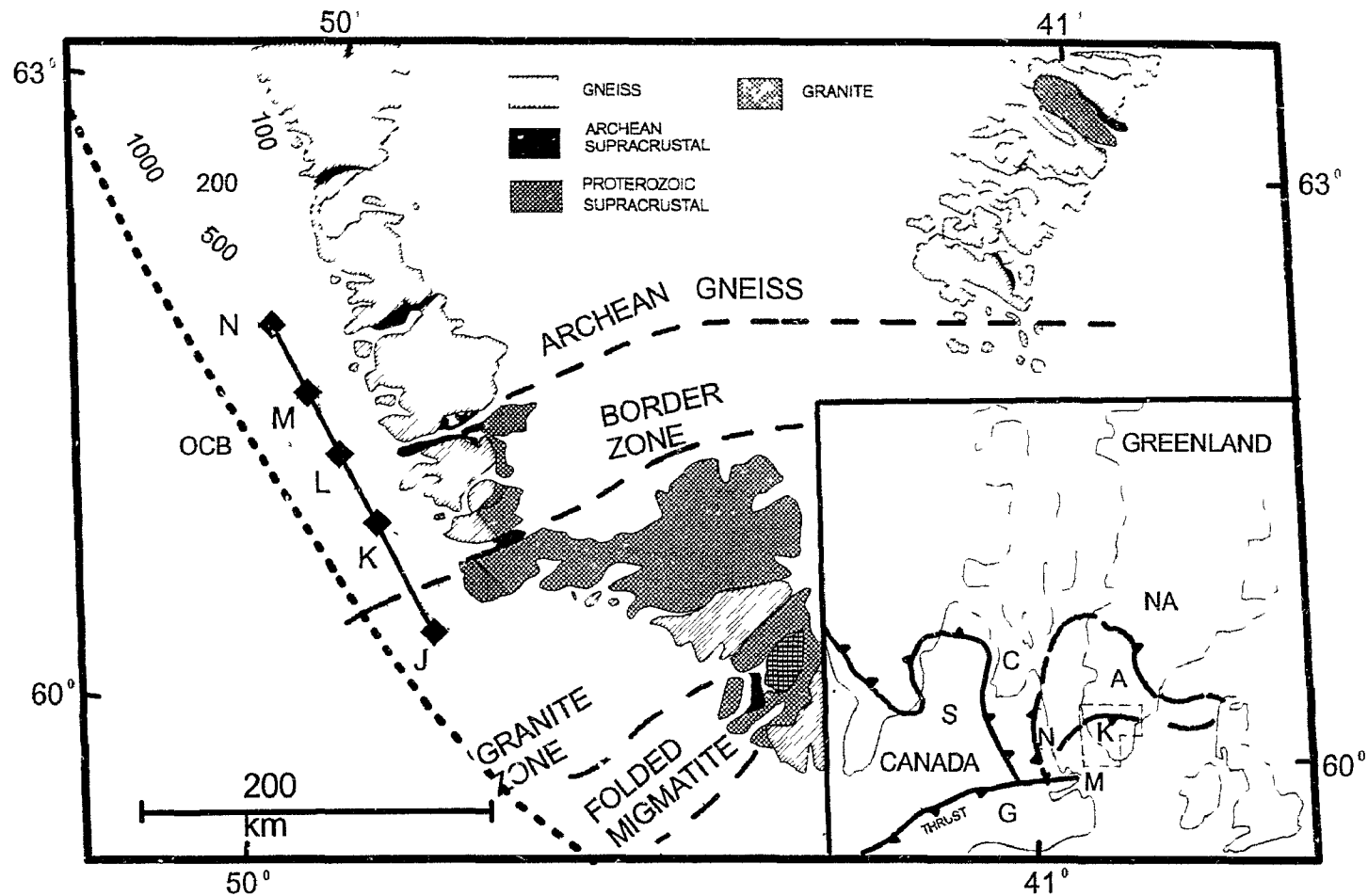


Figure 3.1. Simplified geology, isobaths (in metres) and major geological units of the continental crust of southwestern Greenland. Thick solid line locates the 230 km seismic refraction line. Filled rectangles show the location and identification of OBS receivers. GNEISS: Archean gneisses and gneisses within the Ketilidian mobile belt; GRANITE: predominantly granodiorite with some diorite and granite, early Proterozoic age; ARCHEAN and PROTEROZOIC SUPRACRUSTAL: metasediments and metavolcanic rocks. OCB denotes the ocean-continent boundary from Roest and Srivastava (1989). Identification of geological features in the inset is as follows: A=Archean block; K=Ketilidian mobile belt; NA=Nagssugtoqidian mobile belt, N=Nain Province; M=Makkovik Province; C=Churchill Province; S=Superior Craton; G=Grenville Province. Dotted areas delineate the Archean cratons; white continental areas indicate early Proterozoic orogenic belts; arrowed lines locate thrust margins; thin dashed line delineates boundaries of larger map. Modified from Bridgwater et al. (1976) and Korstgård et al. (1987).

shallows at depth. Although magnetic and gravity modelling tend to favour a vertical contact (Woodside and Verhoef 1989), no crustal seismic data have been obtained in this area to constrain the geological models.

Following the formation of the continental crust in the Precambrian, Greenland separated from North America by rifting and subsequent sea-floor spreading in the Labrador Sea between mid-Cretaceous and Oligocene times (Srivastava et al. 1981). Hyndman (1973) and Srivastava et al. (1981) suggested that this area was possibly affected by a hotspot which was activated in Davis Strait in the Paleocene. Although the margins of Davis Strait show extensive outpourings of lavas during the initial opening, the maximum thickness of the syn-rift basalts found so far along the Labrador margin is only 800 m (Balkwill 1987). However, seismic refraction data in some offshore and other oceanic areas of the Labrador Sea reveal sporadic occurrences of a high velocity ( $\sim 7.5$  km/s) lower crustal layer which possibly represents lower crustal magmatic underplating resulting from the hotspot activity (Van Der Linden 1975; Stergiopoulos 1984; Srivastava et al. 1989). It is, therefore, important to define the nature of the lower crust of the Precambrian continent to determine if it also has been affected by underplating.

### **3.2 Data Acquisition and Processing**

The seismic data lie on a 230-km-long profile along the outer shelf of the southwestern Greenland margin (Figure 3.1). Seven ocean bottom seismometers (OBS) were deployed roughly uniformly along the line, five of them (OBS N, M, L, K and J) giving useful information (Table 3.1). The seismic source was an array of six 1000 cu. in

(16.4 l) air guns firing every minute (~150 m between adjacent shots). Slow-speed analog cassette tapes continuously recorded 4 channels of data, including internal clock pulses and seismic signals from hydrophone, and vertical and horizontal geophones. The data were digitized and interpolated to a fixed sampling rate (80 or 72 samples per second). Subsequent processing included zero mean, bandpass filtering (2-8 Hz) and clipping of high amplitudes. A variable gain scales the amplitude of seismograms in order to compensate for dissipation of the wave energy. Two examples of full record sections from OBS N and J at opposite ends of the line are shown in Figures 3.2 and 3.3. Because the data along the southwestern Greenland margin are noisy (except from OBS K), a stack or semblance stack of 5 or 7 adjacent shots is applied to every displayed trace for most of the profiles. The semblance stack is defined as a stack of a number of traces along an optimal phase velocity, which produces the maximum semblance within a moving time window of 0.015 sec, followed by weighting with the normalized semblance (0-1). The semblance stack is especially useful in displaying *S* wave records because of interference from *P* wave reverberations.

Several factors may have affected the signal-to-noise ratio (S/N). It is clear that the semi-diurnal tides shook the shallow OBS instruments during ebb and flood, which is most clearly observed at OBS J (Figure 3.3). The roughness of the seafloor (the average water depth is 130 m with a maximum relief of ~200 m) and the lack of sediments overlying basement may have scattered the incident sound energy. Smaller-scale structural complexities in the upper crust under OBS M and L may also have diffracted the seismic

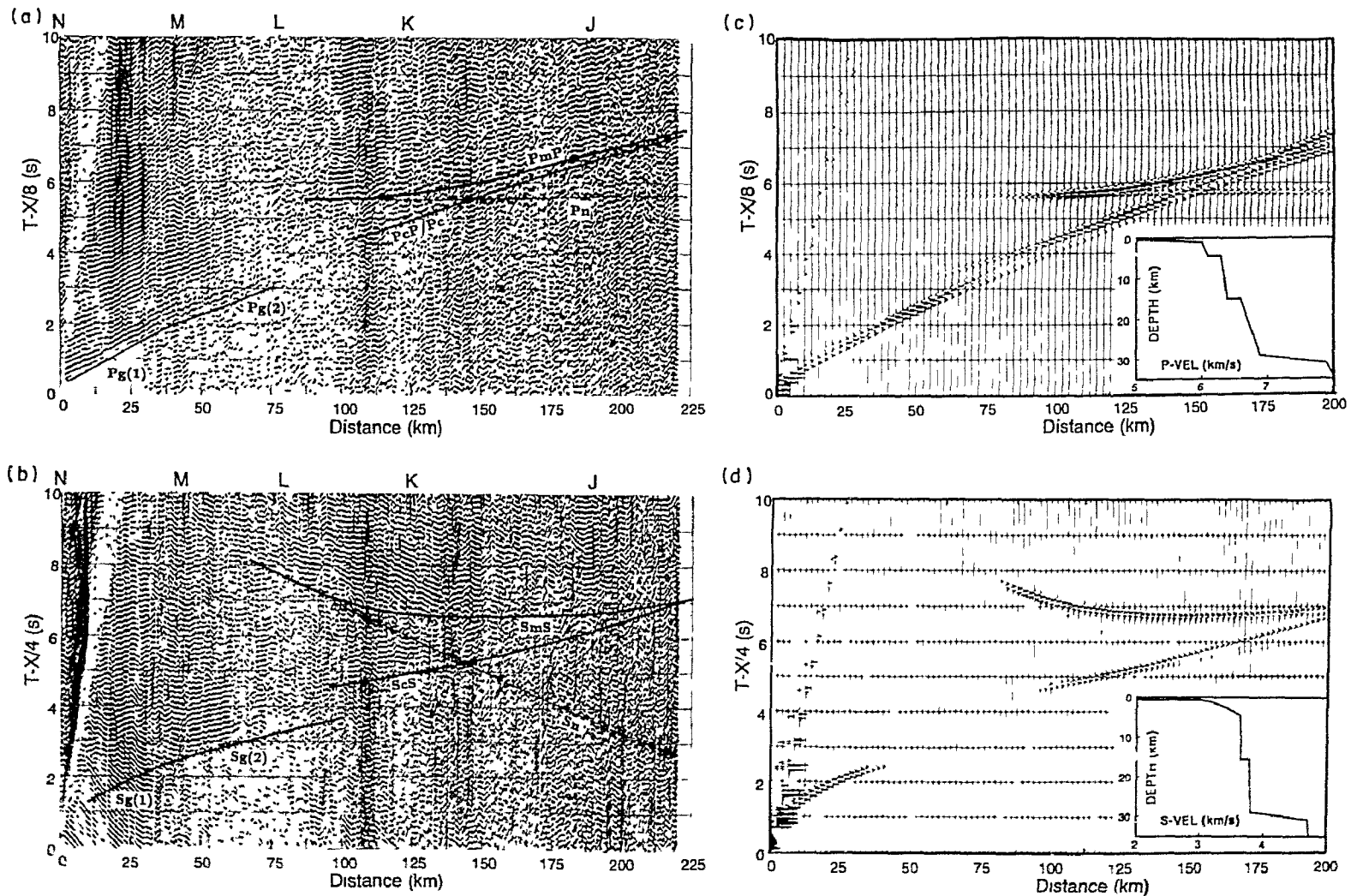


Figure 3.2. Vertical geophone record sections of OBS N, plotted with a reduction velocity of 8.0 km/s (a) and 4.0 km/s (b). Overlain solid lines are travel-time curves from the WKBJ synthetic seismograms (c, d) computed from the inserted crustal models. Every shot is displayed for both field sections. OBS positions are shown on top of each profile. Processing steps applied are: i) 7-trace semblance stacking (see text for definition); ii) Butterworth filtering from 2 to 8 Hz; iii) amplitude scaling by a factor of  $X/8$  for  $X > 8$  and 1 otherwise; iv) timing corrections for tape skew, OBS clock offset and drift, and airgun firing delay.

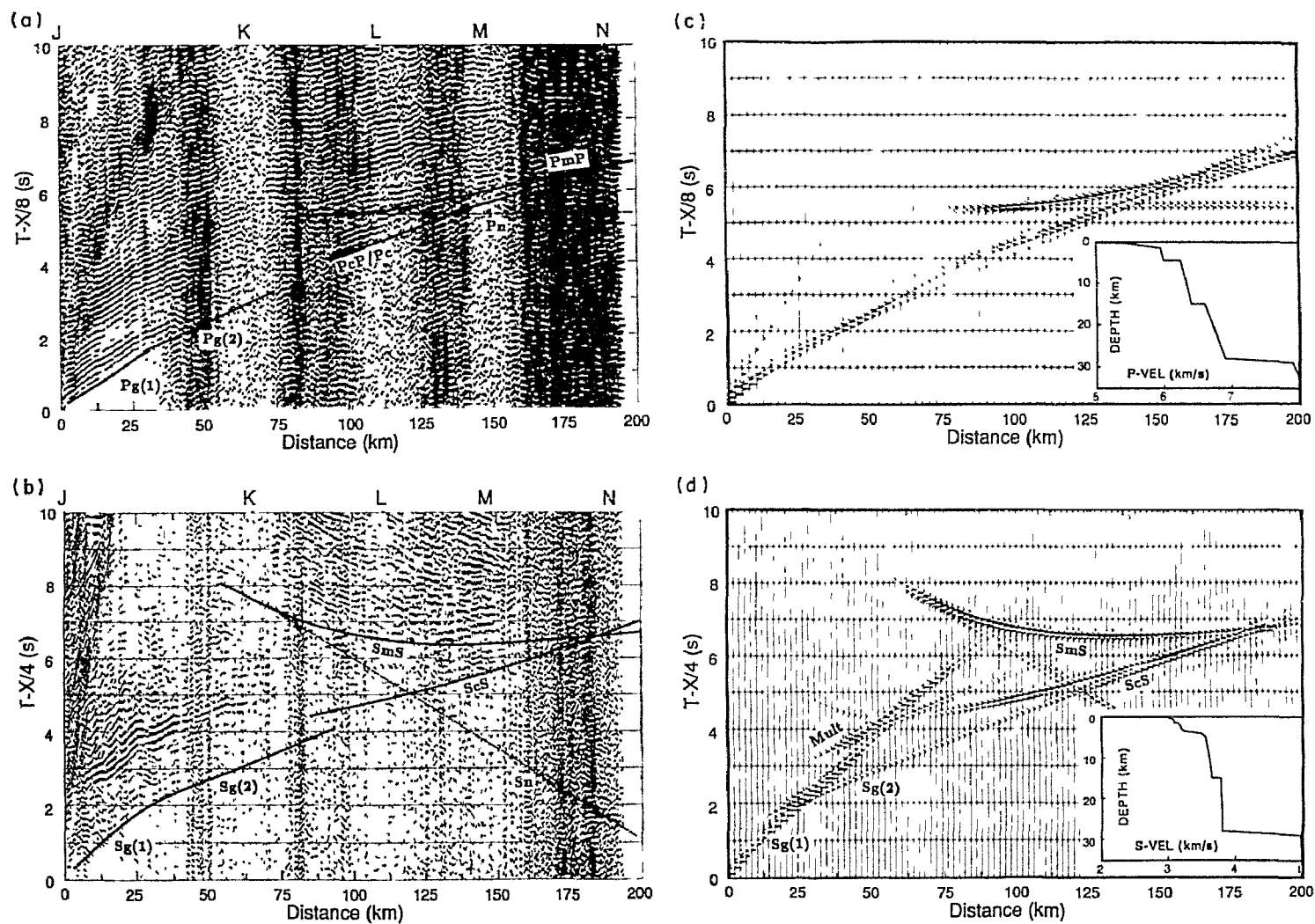


Figure 3.3. (a) Hydrophone record sections of OBS J, plotted with a reduction velocity of 8 km/s and 5-shot semblance stacking; (b) horizontal geophone record section of OBS J, plotted with a reduction velocity of 4.0 km/s and 9-shot semblance stacking; (c, d) corresponding crustal model and synthetic seismograms. Every two shots are displayed. OBS positions are shown on top of each field profile. Overlain solid lines are travel-time curves drawn from the WKB synthetic seismograms. For other processing steps see caption of Fig. 3.2.

energy and thus weakened or complicated the coherent seismic events. The association of multiples with almost every seismic event, together with the reverberations, create a complex pattern in the profiles. The OBS in the middle of the line (K) has the highest S/N ratio and the best defined upper and intermediate crustal refractions Pg(1) and Pg(2), but their maximum horizontal range is only 125 km, which is not long enough to sample the entire suite of lower crustal and Moho arrivals.

In determining the velocity structure for both  $P$  and  $S$  wave profiles, plane layer solutions from T-X travel-time curves were constructed for each OBS data set in order to get a rough idea of the crustal  $P$  and  $S$  wave velocity model. This model was then modified by comparing the amplitudes and travel-times of the observed seismic record sections and synthetic seismograms produced by the one-dimensional WKB algorithm (Chapman 1978; Chapman and Drummond 1982). In most cases,  $S$  wave phases are also observed (e.g. Figures 3.2-3). However, the later-arrival,  $S$  wave travel-times are usually more difficult to pick than the first-arrival  $P$  waves, and therefore the thickness of each layer was primarily obtained from  $P$  waves arrivals. These thicknesses were then used as a starting point in modelling the  $S$  waves.

### **3.3 Seismic Modeling**

The similarity in travel-time curves among the five useful OBS profiles enables us to arrive at a single, one-dimensional, first-order interpretation. Relatively consistent  $P$  and  $S$  wide-angle reflections and/or refractions travel from the upper crust (Pg(1), Sg(1)), the intermediate crust (Pg(2), Sg(2)), the lower crust (PcP, Pc, ScS, Sc) and the Moho



boundary (PmP, Sn ). I will show how to relate these seismic phases to the crustal structure and velocities and will present one-dimensional modelling results for the

**Table 3. 1 OBS positions along southwestern Greenland shelf**

	N	M	L	K	J
Latitude ( $^{\circ}$ N)	61.8845	61.5943	61.3322	61.0118	60.5376
Longitude ( $^{\circ}$ W)	50.4750	49.9990	49.5552	49.0482	48.2981

seismograms recorded by OBS N and J (Figures 3.2-3). These two OBS profiles represent the general crustal structure along the refraction line. The other OBS profiles show features similar to the general structure but record some lateral changes and will be discussed at the end of this section.

### **Sediments**

The *P* wave arrival Ps, refracted in the thin sediment layer, is identified only in OBS N and J as a small initial segment for ranges less than 10 km (not shown in this paper). It represents a thin sediment layer which is ~400 m thick with a velocity of ~2.8-4.2 km/s under OBS N and ~50 m thick with a velocity of ~3.9 km/s under OBS J. This sediment layer and the overlying water column generate multiples and reverberations that sometimes mask other arrivals. In addition, the thickening of this thin layer under OBS N

makes Pg(1) and Pg(2) arrive slightly later on profile N (Figure 3.2) than on profile J (Figure 3.3).

### **Upper and Intermediate Crust**

The refracted arrivals Pg and Sg from the upper and intermediate crust mainly include two linked segments (Pg(1), Pg(2), and Sg(1), Sg(2)) which form a change in slope at ranges of 25-40 km (Figures 3.2-3). Pg(1) is slightly curved at near ranges, representing a rapid velocity increase from ~5.5 to 6.0 km/s within the first ~1.5 km depth. Below this depth the velocity stays nearly constant, eventually producing a constant slope for Pg(1). The slope jump from Pg(1) to Pg(2) is caused by a sudden velocity increase from 6.0 to ~6.3 km/s for *P* wave and ~3.4 to ~3.6 km/s for *S* wave at a depth of 3-5 km under OBS N and J. This velocity discontinuity represents the boundary between the upper and intermediate layers. It was originally thought that between this velocity discontinuity and the seafloor are generated *S* wave multiples which accompany every arrival in the *P* and *S* wave profiles of OBS N and J at a nearly constant travel-time delay (~2 seconds). Modelling shows, however, that the main energy for such multiples occurs only at horizontal ranges greater than 25 km (e.g. Figure 3.3d), while on field profiles the multiples have strong energy even at ranges close to zero. I deduce that these multiples must be *S* waves bounded within the thin upper sediment whose *S* wave velocity may reach as low as 200 m/sec, similar to arrivals observed by Lewis and McClain (1977).

### Lower Crust and Upper Mantle

The lower crustal arrivals include both wide-angle reflections (PcP and ScS) from the Conrad boundary and refractions (Pc and Sc) from within the upper part of the lower crust (Figures 3.2-3). The Conrad boundary for *P* waves appears to be relatively sharp since PcP arrivals usually carry strong amplitudes. Around the critical point (between ranges of 100 and 130 km), the amplitudes of PcP and Pc overlap and hence are most visible. Modelling shows that the depth of the Conrad discontinuity is 15.5 km in both profiles N and J. The Pc segment at ranges of 100-140 km on profile N and at ranges of 95-155 km on profile J defines the *P* wave velocity in the upper part of the lower crust to be consistently 6.6 km/s. The velocity for the lower part of the lower crust cannot be measured directly from the field data. However, modelling shows that a slight change of this velocity will change the curvature and timing of the wide-angle reflection PmP. Since PmP can be well traced on profile J (Figure 3.3), I was able to estimate the *P* wave velocity above the Moho by matching the curvature of PmP between synthetic seismograms and profile J. The best matching velocity for the lower crust above the Moho is 6.9 km/s. A similar value is also estimated for profile N (Figure 3.2). Modelling shows that the *S* wave velocity in the upper part of the lower crust is 3.8 km/s for both OBS N and J (Figures 3.2-3). In the lower part of the lower crust, this same *S* wave velocity (3.8 km/s) has to be used in order to match the curvature of SmS and its travel-time.

The transition zone from the bottom of the lower crust to the upper mantle is best seen on profile N. A slope change of  $P_c$  at a range of  $\sim 150$  km is probably caused by an increased velocity gradient in the transition zone from 6.9 km/s at 29 km depth to 8.0 km/s at 31 km depth.  $P_mP$  on profile J arrives  $<0.2$  seconds earlier at a range of 100 km than on profile N at the same range, indicating a slightly shallower (1-2 km) Moho depth under OBS J.

### **Along-Strike Variations**

The  $P$  and  $S$  wave data recorded by the five OBS (N, M, L, K, and J) (Figures 3.2-5) enable us to investigate crustal velocity variations along the strike of the refraction line. I used one-dimensional WKBJ seismic modelling to deduce the velocity-depth structure for each individual OBS profile since large lateral variations are not apparent in the data. The modelling results are shown in Figure 3.6. Seismograms at either side of each OBS were modelled separately. Each modelled velocity value was horizontally positioned approximately at the centre of the offset from the OBS to the major energy of the seismic event. The results were then combined to give an approximate two-dimensional (2D) crustal structure (Figure 3.7), which subsequently was checked with a full 2D ray-tracing algorithm (Cerveny et al. 1977).

The  $P$  and  $S$  wave velocities for the upper and intermediate zones as shown in Figure 3.7 are obtained from least-squares fitting of the  $P_g(1)$  and  $P_g(2)$  arrivals on all the useful T-X OBS profiles (Figures 3.2-5). The corresponding error in the calculation of the slope of these phases is estimated to be within  $\pm 0.05$  km/s. It should be noted,

however, that this error estimate is valid only for a plane layer solution. Additional errors may arise when a wide-angle reflection is picked instead of a refraction, which may happen in the Border Zone (velocities with a question mark in Figure 3.7) where the structure becomes more complicated. The lower crustal velocities are mainly derived from one-dimensional WKBJ modelling. Although precise error bounds cannot be calculated, velocity variations in excess of 0.1 km/s will significantly degrade the match of the synthetic seismograms to the data.

Figure 3.4 shows a comparison of the recorded upper and intermediate crustal phases in profiles M, L and K. For OBS N (Figure 3.2), M, L and K, positive ranges represent shots to the south of OBS locations while for OBS J (Figure 3.3) the records are displayed in a reverse direction. These profiles show that the slope of the Pg(1) phase at OBS N and M represents a velocity of 6.0 km/s which decreases to 5.6 km/s at OBS J. Similarly, Pg(2) represents a velocity of 6.4 km/s at OBS N and M which decreases to 6.3 km/s at OBS J. The slope jump from Pg(1) to Pg(2) and from Sg(1) to Sg(2) is at a similar position on T-X profiles for positive ranges of profile N, negative ranges of profile K and positive ranges of profile J. This indicates that the boundary between the upper and intermediate zones is at a similar depth (~5 km) south of OBS N and north of OBS K and J. However, the boundary is deeper (~9 km) under OBS M and L, as inferred from the lateral shift of the junction point of Pg(1) and Pg(2) to 55 km for the positive range of profile M and the negative range of profile L (shown in Figure 3.4). This junction point shifts to 40 km for the positive range of profile L, where the boundary is modelled at a

depth of ~7 km. The phases of Pg and Sg become complicated for positive ranges of profile K, indicating interruptions in the upper crust within a region about 30 km wide south of OBS K. These lateral variations of upper and intermediate crustal velocity structure are summarized in Figure 3.7.

Figure 3.5 shows a comparison among the various profiles of PcP (or Pc), the lower crustal arrival, and PmP, the wide-angle reflection from the Moho. Although PcP shows strong amplitudes for profiles N, J and K, it is less clear for the other two profiles, M and L. 2D modelling shows that some of the rays that generate the apparent PcP in profiles N and J actually turn below the thickened upper crust, producing an extended Pg(2) arrival (denoted as Pg<sup>+</sup>(2) in Figure 3.5) between ranges of 100 and 140 km in profiles L. Pg<sup>+</sup>(2) has slightly earlier arrival times than Pc, masking the weaker Pc arrival. The PcP on profile K (Figure 3.5) suffers a travel-time distortion and amplitude build-up. This amplitude enhancing appears on all record sections at the same horizontal position along the line, indicating a shallow complexity which is not modelled. However, the travel-time curves are similar, indicating little changes in the depth of the Moho along the refraction line. There are varying amplitude features among different profiles for PmP, but the limited data quality and coverage prevent us from further detailing lower crustal variations along the strike.

### **3.4 Interpretation**

The continental crust of southwestern Greenland is separated into upper, intermediate, and lower zones according to velocity values (Figures 3.6-7). The boundary

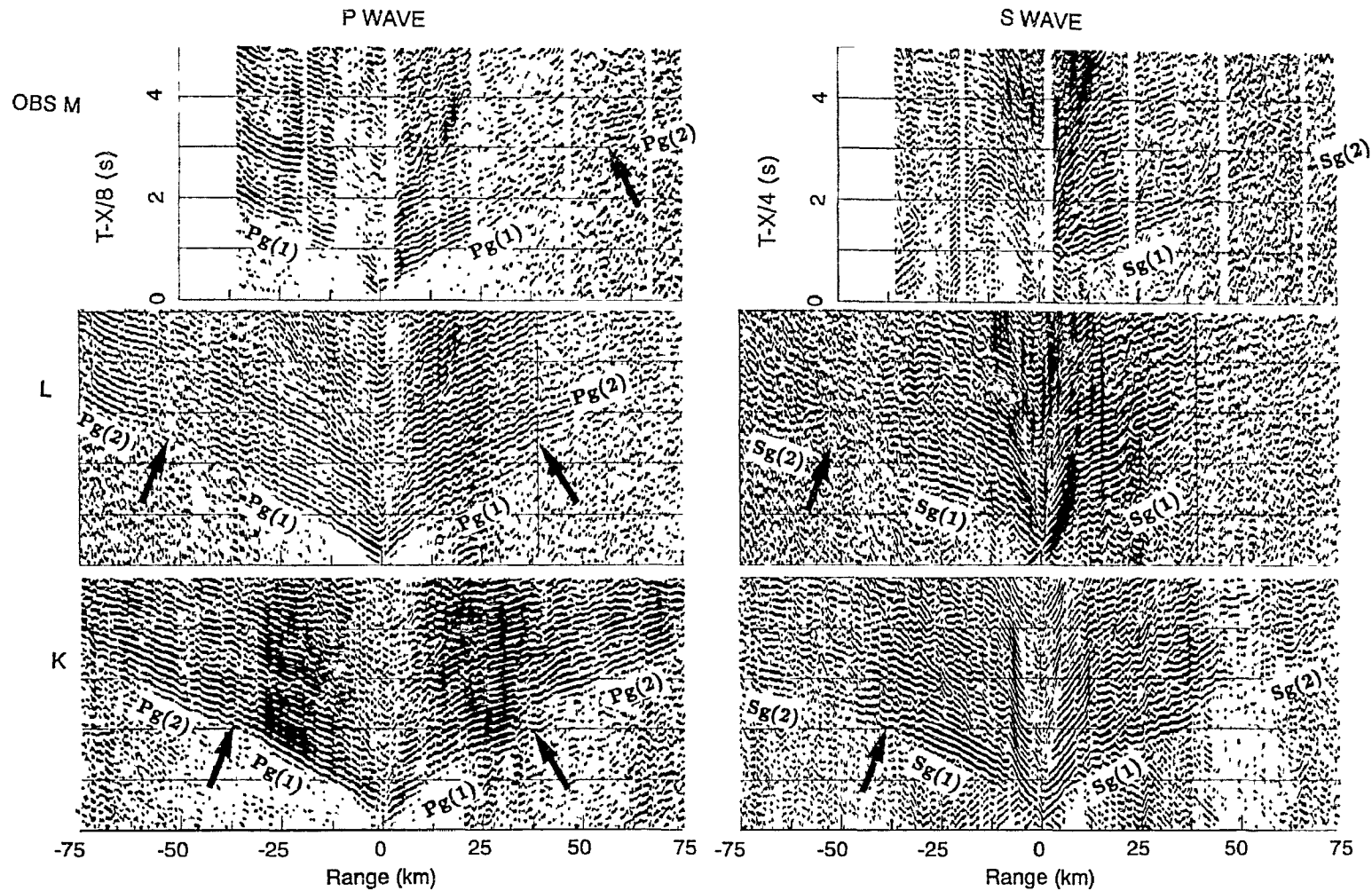


Figure 3.4. Compilation of near range profiles of P waves (left) and S waves (right) from the three OBS M, L and K which are listed from top to bottom. The profiles are plotted with their positive horizontal axes toward the south. The reducing velocity for the plotting is 8 km/s for P waves and 4 km/s for S waves. The junction point between Pg(1) and Pg(2) is denoted by an arrow. Note that the shifting of this point represents a change of the depth for the bottom of the upper crust.

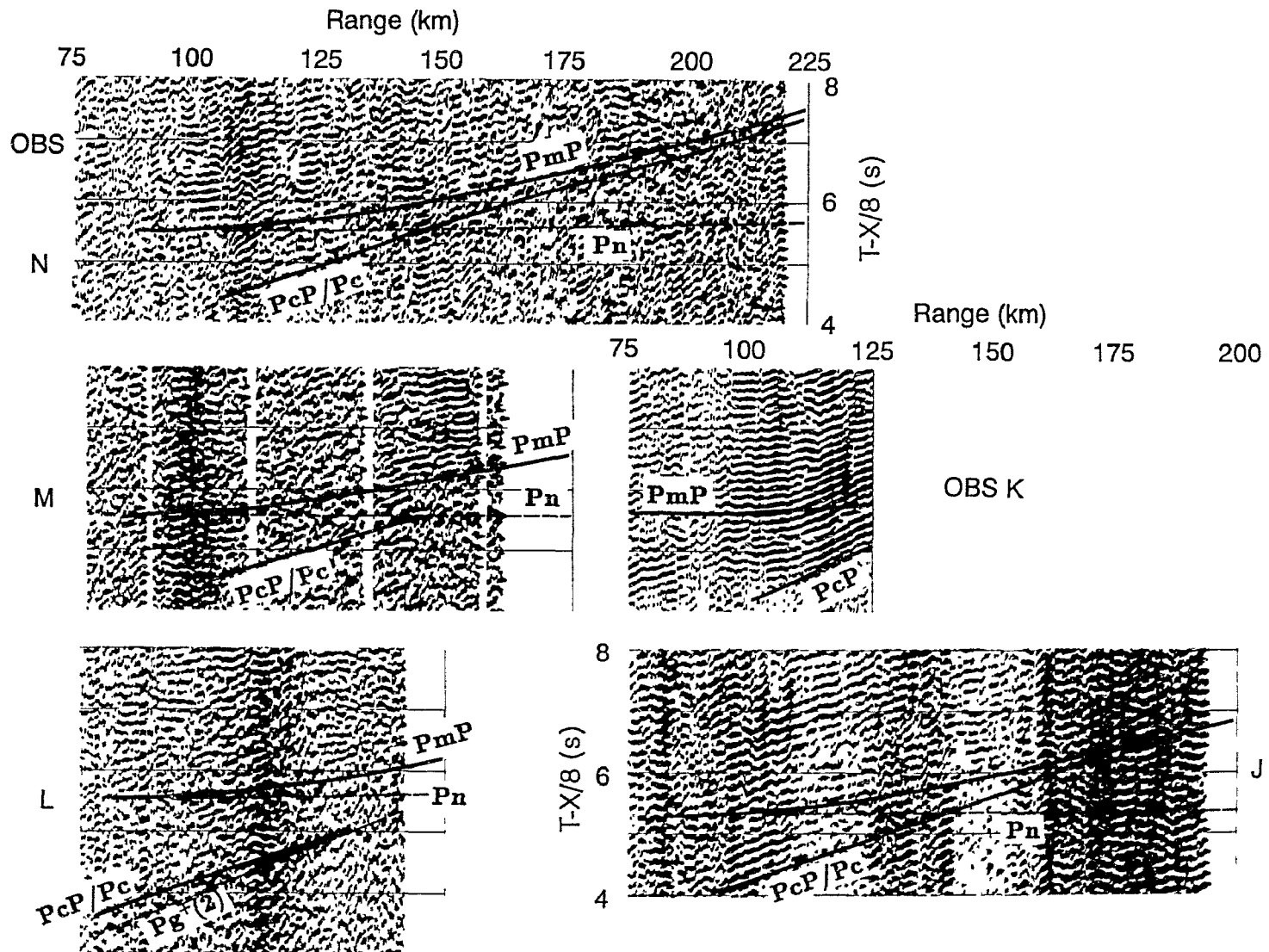


Figure 3.5. Compilation of P-wave profiles for the five OBS, emphasizing the features of the lower crustal arrivals, PcP (or Pc) and PmP. Solid and dotted lines are travel-time curves calculated from 1D modelling, except for OBS L whose travel-time curves are from 2D modelling. Pg+(2) in profile L represents rays which turn over below the thickened upper crust (see text for detail).



that divides the intermediate crust from the upper crust lies at ~5 km depth in the north (OBS N) and the south (OBS J), and deepens up to ~9 km in the middle (OBS M), producing a change in slope of arrivals from Pg(1) to Pg(2). The near-range curvature of Pg(1) indicates that within the top 1.5 km of crust, there is a velocity gradient from ~5.5 to 6.0 km/s for *P* waves, and from ~3.2 to 3.5 for *S* waves. This velocity gradient is probably caused by increasing crack closure with depth (Christensen 1978). Horizontally, *P* wave velocities in the upper crust in general decrease from 6.0 km/s in the north to 5.6 km/s in the south. In the intermediate crust, *P* wave velocities show a similar trend from 6.4 km/s in the north to 6.3 km/s in the south. *S* wave velocities show smaller and unsystematic lateral variations around values of 3.4 km/s within the upper crust and 3.6 km/s within the intermediate crust.

Since thick syn-rift extrusive basalts occur as seaward-dipping reflectors on the shelf of central east Greenland (Hinz et al. 1987), as well as on the margins of Davis Strait (Srivastava 1983), by analogy it is natural to consider the uppermost 5 km thick layer under the shelf of southwestern Greenland as Mesozoic extrusive volcanics. However, the fact that velocities in general decrease from north to south and that the Proterozoic structural trends cut through the top of the upper crust appears to preclude this possibility. In addition, the *P* and *S* wave velocities do not seem to correspond to the velocity range (3.5-6.0 km/s for *P* waves and 2.7-3.0 km/s for *S* waves) within the Mesozoic seaward-dipping reflectors southwest of Rockall Plateau (Whitmarsh and Miles 1987). Hence I suggest that the top crustal layer is of Precambrian origin. Syn-rift basalts, if they exist,

should be much thinner and comparable with those (<400 m thick) of the conjugate Labrador margin (Balkwill 1987).

Lateral changes in structural boundaries and velocity values within the upper crust partly match the divisions of the Archean block, the Border Zone, and the Ketilidian mobile belt, which are based on surface isotopic and petrological measurements (Figure 3.7). The boundary between the Archean block and the Border Zone is matched by a thickening of the upper crust northwards from the Border Zone to the Archean block. The velocity discontinuity between the upper and intermediate zones shallows relatively abruptly under OBS M, possibly due to normal faulting (Figure 3.7).

The  $P$  and  $S$  wave velocities from refraction surveys provide much information on the bulk composition of rocks which can be determined when compared with laboratory velocity measurements (e.g. Hall 1987; Holbrook *et al.* 1988). Since laboratory measurements of  $P$  and  $S$  wave velocities are not available in adjacent areas, I compare the results of the field velocity measurements (Figure 3.7) with laboratory measurements of  $P$  and  $S$  wave velocity for Lewisian metamorphic rocks (Hall and Simmons 1979; Hall and Al-Haddad 1979), and  $P$  wave velocity for rock samples from the Grenville Front Tectonic Zone (Burke 1990). Surface geological observations (Allaart 1976; Bridgwater *et al.* 1976) are also used in constructing bulk rock types for upper crust. Since laboratory velocity measurements are made at various confining pressures (at room temperature), it is necessary to establish the relationship between depth of crust and its confining pressure. I estimate the overburden pressure at each depth level from a vertical distribution of

densities ( $\rho$ ) inferred solely from  $P$  wave velocities ( $V_p$ ) by  $\rho=0.252+0.3788 V_p$ . The estimated pressures, as well as temperatures (Issler 1987) at various depths are shown at the right side of Figure 3.7. I find that the upper crust of the Archean block in southwestern Greenland most likely matches a quartz-feldspar gneiss composition, whose  $P$  wave velocity at a pressure of 0.5 kbar is 5.99 km/s. The bulk of the intermediate crust is likely amphibolitized pyroxene granulite, whose  $P$  and  $S$  wave velocities at 2 kbar are measured to be 6.41 and 3.54 km/s, respectively. The upper crust in the Ketilidian mobile belt bears a  $P$  wave velocity value much lower (5.6 km/s) than in the Archean (6.0 km/s), and is matched by quartz granite. A unique match for the composition of the intermediate layer in the Ketilidian is not obtained because of the lack of  $S$  wave laboratory data. However, this layer is consistent with a granite and granitic gneiss composition (Holbrook et al. 1988). South of OBS K and within the Border Zone there appears to be some high velocity (6.6 km/s ?) material that forms a complicated pattern for the southern ranges of profile K (Figure 3.4). This may be a manifestation of uplift of lower crustal rocks.

The lower crust is characterized by a small velocity gradient from 6.6 to 6.9 km/s for  $P$  waves and a nearly constant velocity of 3.8 km/s for  $S$  waves (Figure 3.6). Considering the effects of temperature and pressure on the velocity values, I suggest that the most likely rocks for the lower crust of southwestern Greenland are gabbroic and hornblende granulites. This is consistent with the experimental velocity studies of Christensen and Fountain (1975) and the petrological modelling of wide-angle seismic

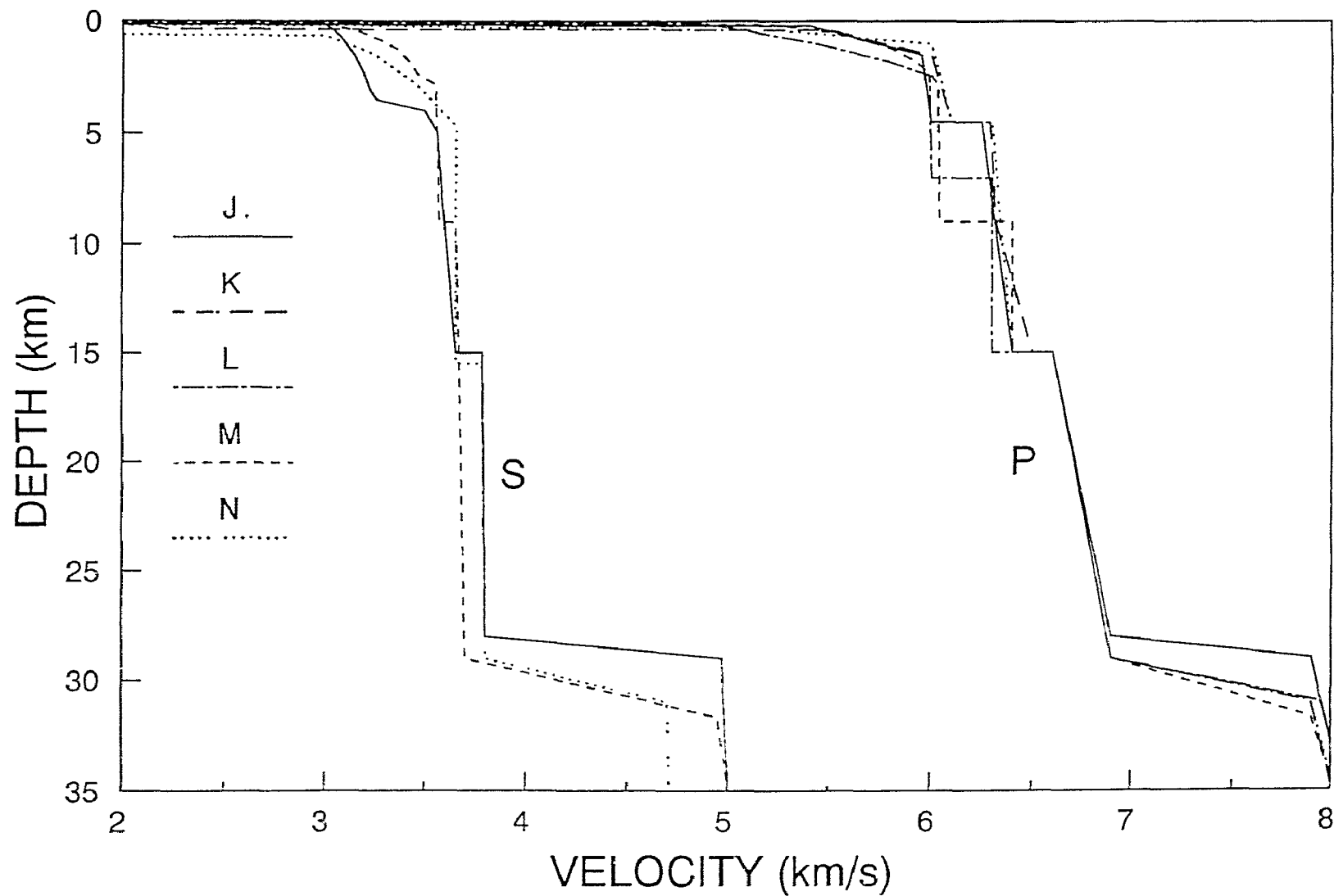


Figure 3.6. P- and S-wave velocity-depth models used for generating synthetic amplitudes that match field data from OBS N (Fig. 3.2) and J (Fig. 3.3), and M, L and K (Figs. 3.4-5).

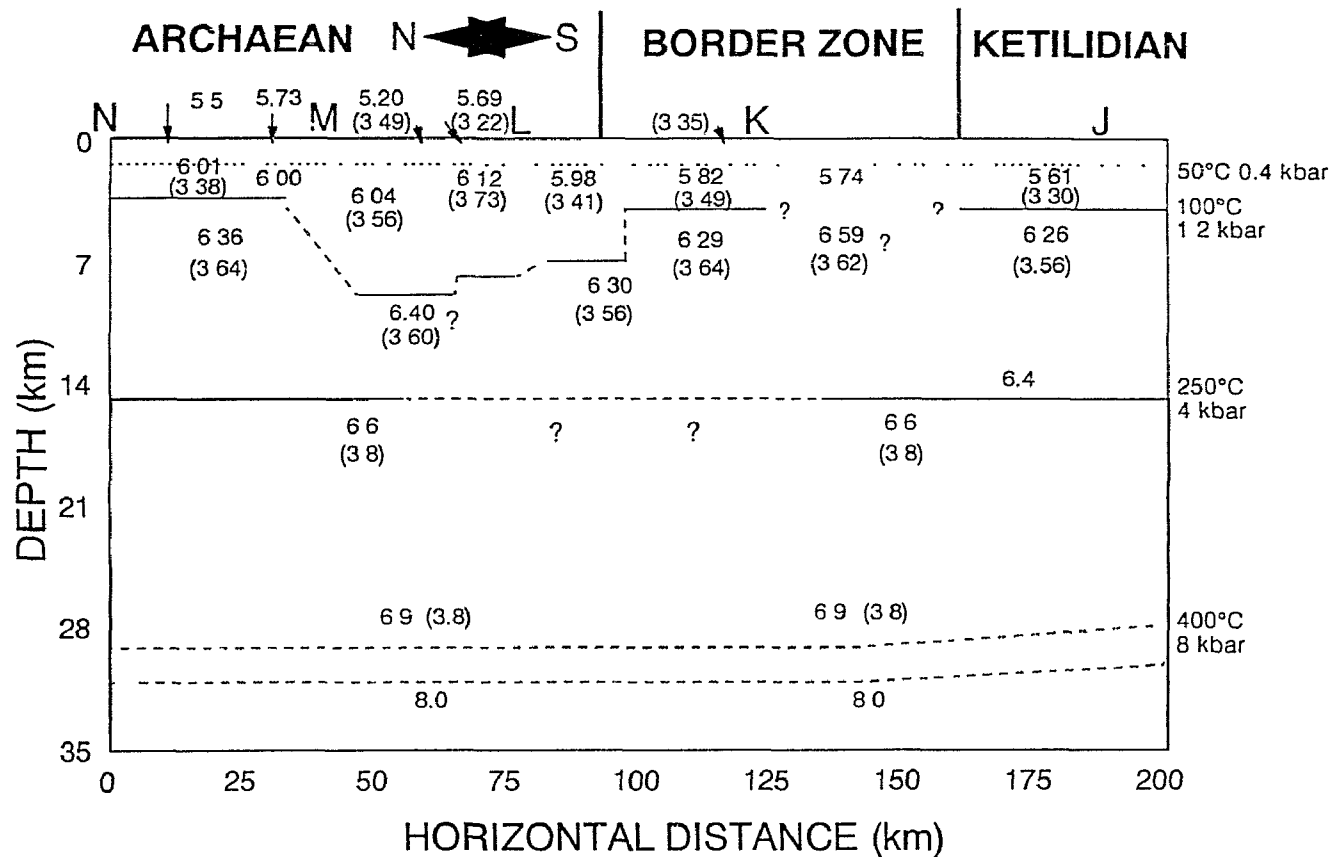


Figure 3.7. Final two dimensional velocity model along the southwestern Greenland margin. P- and S-wave velocity values are shown at their approximate positions on the two dimensional crustal model. The bracketed numbers are S-wave velocities. The varying velocity values shown in the upper crust are mainly derived by measuring the slope of Pg(1) and Pg(2) on T-X profiles on each side of the five OBS N, M, L, K, and J located from north to south as shown on top of the diagram. The accuracy for these velocity values is better than  $\pm 0.05$  km/s assuming a plane layer solution, except for those with a question mark, where uncertainties are caused by complicated or less clear patterns of arrivals. The velocities in the lower crust are mainly derived from interactive 1D modelling, with an estimated accuracy of  $\pm 0.1$  km/s. The temperature values shown on the right side of the model are from the thermal model of Issler (1987). The overburden pressure at each depth level is calculated from a vertical distribution of densities (\*) inferred solely from P-wave velocities by  $* = 0.252 + 0.3788 V_p$ .

data in southwestern Germany by Holbrook et al. (1988). Consistent Moho wide-angle reflections are observed from both ends of the refraction line, suggesting an approximately equal thickness for the lower crust within both the Archean block and the Ketilidian mobile belt (Figure 3.7). The Moho discontinuity is characterized by a transition zone less than 2 km thick between the crust and the upper mantle. The Moho is 1-2 km shallower in the Ketilidian mobile belt than at the southern edge of the Archean block.

Van Breemen et al. (1974), Patchett and Bridgwater (1984), and Kalsbeck and Taylor (1985a; 1985b) used Sr, Nd, and Pb isotope systematics, respectively, to show that the Ketilidian crust has a large component of mantle-derived material with short residence time in the mid-Proterozoic, and that only the Border Zone is underlain by older Archean basement. The orientations of ductile overthrusts and dyke swarms in some areas of the North Atlantic craton (Figure 3.1) tend to favour a collisional model in which a rigid continental plate (including the Ketilidian mobile belt) pushed north against the North Atlantic craton (Bridgwater et al. 1973; Watterson 1978; Korstgård et al. 1987). Some supporting geological evidence includes thrusting of the Ketilidian sediments and volcanics over Archean gneisses in Grønland and Midtøstlandet inside the Border Zone (Allaart 1976). Although the details of deeper crustal changes in the Border Zone are not revealed from the refraction data, the significant thickening of the upper crust in the southern part of the Archean block (Figure 3.7) is consistent with the mechanism of Precambrian plate collision between the Archean crust and the Ketilidian mobile belt. The gravity anomaly (Woodside 1989) along the southwestern Greenland continental margin shows a

significant low around OBS L, which is consistent with the thickening of a low velocity/density upper crust. Good wide-angle reflections from the Moho are observed from most of the OBS instruments (Figures 3.2-5), the modelling of which suggests an approximately equal thickness (15 km) and composition for the lower crust and a Moho boundary at ~30 km (Figure 3.7). However, a ductile lower crust could have been re-equilibrated during the post-orogenic period, eliminating the remnants of an earlier crustal root (Meissner *et al.* 1991).

The 30-km-thick crust along the shelf of southwestern Greenland (Figure 3.7) obtained from the wide-angle seismic data, is thinner than the 34-39 km thick crust obtained from earlier wide-angle seismic data under the Precambrian shield to the southwest of Labrador (Berry and Fuchs 1973), which has commonly been used in geodynamic modelling of the Labrador Sea (Royden and Keen 1980; Issler and Beaumont 1987). Apart from its lesser thickness, the continental crust under the refraction line has a velocity structure typical of Precambrian crust, with no evidence for a high-velocity, lower crustal, underplated layer caused by the Mesozoic opening of the Labrador Sea. Since the sediment thickness (<400 m) and water depth (<500 m) are negligible compared to the total crustal thickness in southwestern Greenland, the principle of isostasy requires little or no thinning (<2 km) of the pre-existing continental crust. However, it is possible that crustal thickness increases to 40 km north of the study area, possibly as an effect of gradual northward thickening of a syn-rift lower crustal underplating (Gohl and Smithson 1993).

### 3.5 Conclusions

1) The continental crust of southwestern Greenland is composed of upper, intermediate, and lower crust with distinct *P* and *S* wave velocity values. The boundary between the upper and intermediate crust is at ~5 km depth for the Archean block and the Ketilidian mobile belt, and deepens to ~9 km in the southern end of the Archean. In the Archean block, the velocities of the upper and intermediate zones are 6.0 and 6.4 km/s for *P* waves and 3.4 and 3.6 km/s for *S* waves. These velocities match a composition of quartz-feldspar gneiss for the upper crust and amphibolitized pyroxene granulite for the lower crust. In the Ketilidian mobile belt, the corresponding velocities are 5.6 and 6.3 km/s for *P* waves and 3.3 and 3.6 km/s for *S* waves. These velocities match a composition of quartz granite for the upper crust and granite and granitic gneiss for the intermediate crust.

2) The boundary between the intermediate and lower crust is a prominent seismic discontinuity at 15-16 km depth in both the Archean block and Ketilidian mobile belt. *P* wave velocity in the lower crust shows a small vertical gradient from 6.6 km/s at the boundary to 6.9 km/s at the Moho. *S* wave velocity, however, shows little vertical variation in the lower crust and averages 3.8 km/s. This velocity structure shows a typical continental-type crust with no evidence of Mesozoic magmatic underplating in the lower crust nor extrusive basaltic emplacement on top of the upper crust. According to the observed velocities, the most likely rocks for the lower crust of the Archean/Ketilidian units are gabbroic and hornblende granulites.



3) The refraction data support a mechanism for a Precambrian collisional boundary between the Archean and the Ketilidian mobile belt.

## **Chapter 4. The Continent-Ocean Crustal Transition Across the SW Greenland**

### **Margin**

#### **4.1 Introduction**

A major goal of studying the structure of Atlantic-type, passive continental margins has been to discriminate between different rifting models, especially between pure (McKenzie 1978) and simple (Wernicke 1985; Lister et al. 1986) shear mechanisms. A simple shear model invokes a low-angle detachment fault that cuts through the continental crust and separates the resulting margins into asymmetric, upper and lower conjugate plates. The upper plate margin records more thinning in the lower crust and less syn-rift subsidence than does its conjugate, lower plate margin. This model has been supported by the existence of an S-reflector, interpreted as the detachment fault, and a smaller amount of upper crustal stretching as compared to total crustal thinning in the Bay of Biscay (Le Pichon and Barbier 1987) and Galicia Bank (Boillot et al. 1989b, 1992). On the other hand, the observed overall symmetry of crustal thinning across the restored rift zone for the conjugate margins of Flemish Cap (Keen and de Voogd 1988) and Goban Spur (Peddy et al. 1989) suggests a pure shear, symmetric extension with final breakup closer to one side of the rift zone (Keen et al. 1989). Finally, it is possible to interpret the rifting of some margins using a mixture of pure shear for the lower crust and lithosphere and simple shear for the upper crust (e.g., Galicia Bank; Sibuet 1992).

The conjugate margins of the Labrador Sea are ideal for the investigation of passive margin formation. Reconstructed positions of the margins can be well constrained

from the seafloor spreading history of the basin, given its small overall width (Srivastava 1978; Roest and Srivastava 1989). The margins are nonvolcanic and exhibit an apparent asymmetry in the shelf/slope morphology, sediment thickness (Balkwill 1987; Rolle 1985), and gravity anomalies (Woodside 1989). This chapter presents detailed seismic velocity variations and their lithologic and tectonic interpretation for the complete transition from continent to ocean crust across the SW Greenland margin of the Labrador Sea (Figure 4.1). *P* and *S* waves from dense airgun shots penetrating the crust and upper mantle are observed on ocean bottom seismometers along a 230-km-long profile. These data are used to construct a two-dimensional (2-D) seismic model. This model contains a 50-80-km wide transitional zone with a low-velocity upper layer interpreted as thinned upper continental crust and a high-velocity lower crustal layer interpreted as serpentinized mantle. The data suggest that Chron 27 marks the initiation of seafloor spreading in the Labrador Sea. More detailed constraints on the rifting mechanism, however, must await a seismic model for the conjugate margin, east of Labrador (Chapter 5).

## 4.2 Reflection Profile

The seismic data to be presented in this chapter include wide-angle refraction and coincident single-channel reflection profiles along a 230-km-long line (88R<sub>2</sub>) that covers the complete transition from preexisting continental to oceanic crust across the SW Greenland margin (Figure 4.1). The seismic source for both data sets is an array of six, 1000 in<sup>3</sup> (16.4 l) air guns firing every 90 s with an approximate spacing of 200 m. The reflection data were recorded primarily for constraining the sediment thickness and

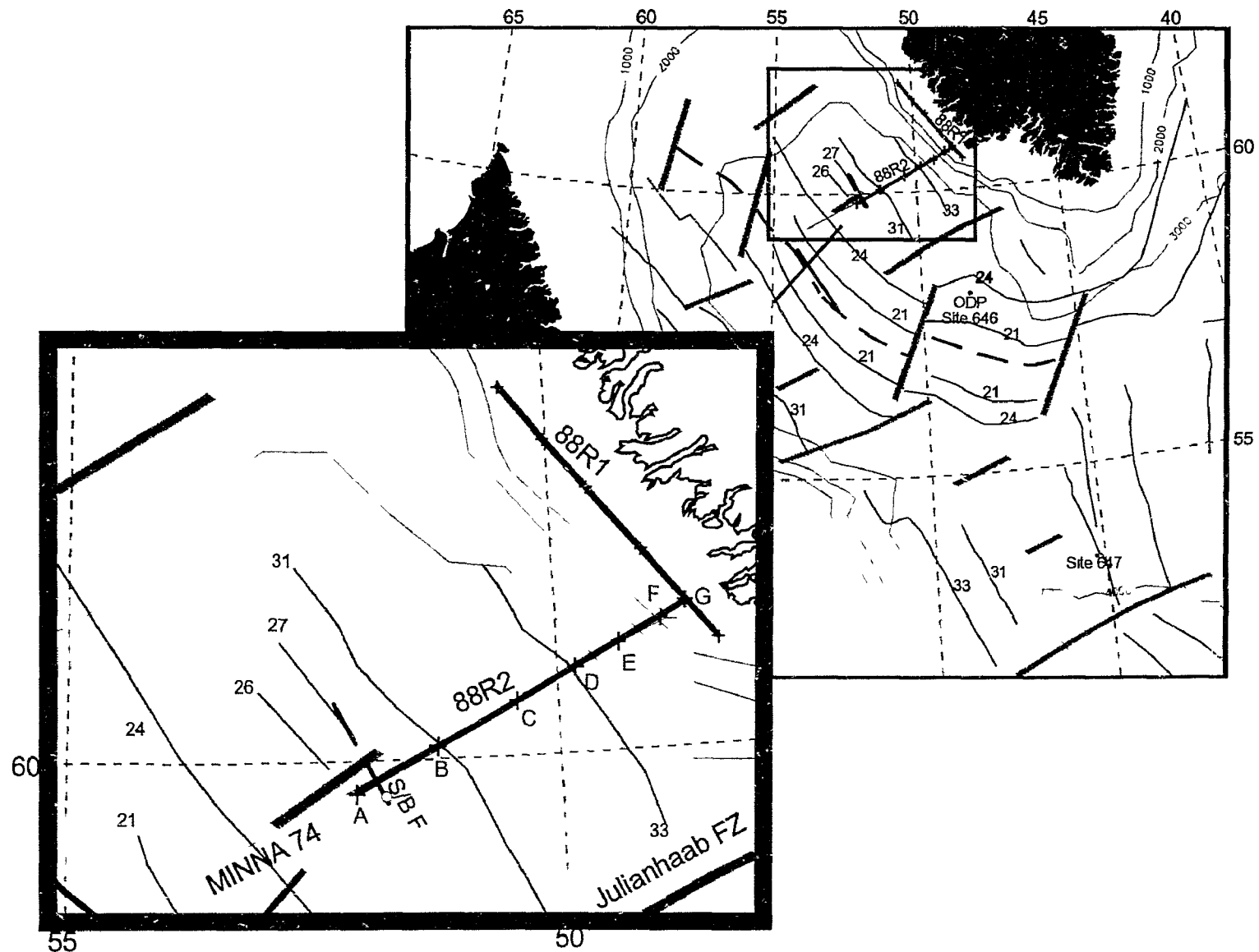


Figure 4.1 Location map of the Labrador Sea, including bathymetric contours plotted every 1,000 m (dotted lines), numbered magnetic anomalies (thin lines), fracture zones (thick grey lines), and an extinct rift axis (thick broken lines). Refraction lines (thick lines) include 88R2 (Chapter 4), 88R1 (Chapter 3), and two lines along and across the extinct ridge axis [Osler and Loudon, 1992; Osler, 1993]. Labeled crosses are OBS instrument locations A-G (Table 4.1); circle is sonobuoy F [Stergiopoulos, 1984]. R/V MINNA 74 gravity and magnetic profile is nearly coincident with line 88R2.

basement morphology.

The pattern of reflectivity on the single-channel profile (Figure 4.2) enables a gross definition of three primary seismic sequences within the sedimentary section. The first and second layers are characterized by high-amplitude reflectors on top and low-amplitude reflectors below. A group of continuous seismic phases forms the boundary between the second and third (bottom) layers. This boundary can be traced continuously from the margin to the east and may correspond to boundary  $R_{3/4}$  at Ocean Drilling Program (ODP) Site 646 (Srivastava et al. 1989). The layer beneath this boundary contains the syn-rift sediments, which are adjacent to the shelf and characterized as strongly folded and faulted seismic sequences (Figure 4.2).

The most significant feature of the profile is the topography of the basement. In general, the profile shows three zones of distinct basement topography, separated by two basement highs. From the shelf seaward, Zone I with large tilted basement blocks probably represents stretched continental crust. At the seaward end of the line (Zone III), where magnetic anomalies 26 and 27 are located, reflection hyperbola from the basement are typical of oceanic crust. Zone II in between is characterized by a number of smaller tilted blocks and is interpreted as transitional crust.

As a first-order approximation, the stretching factor ( $\beta$ ) for the upper crust is calculated based on the geometry of the tilted blocks in Zones I and II following the method of Chenet et al. (1983) (Figure 4.2). In order to convert two-way travel times into depth, I measured  $P$  wave velocities for each sediment layer from sediment- corrected

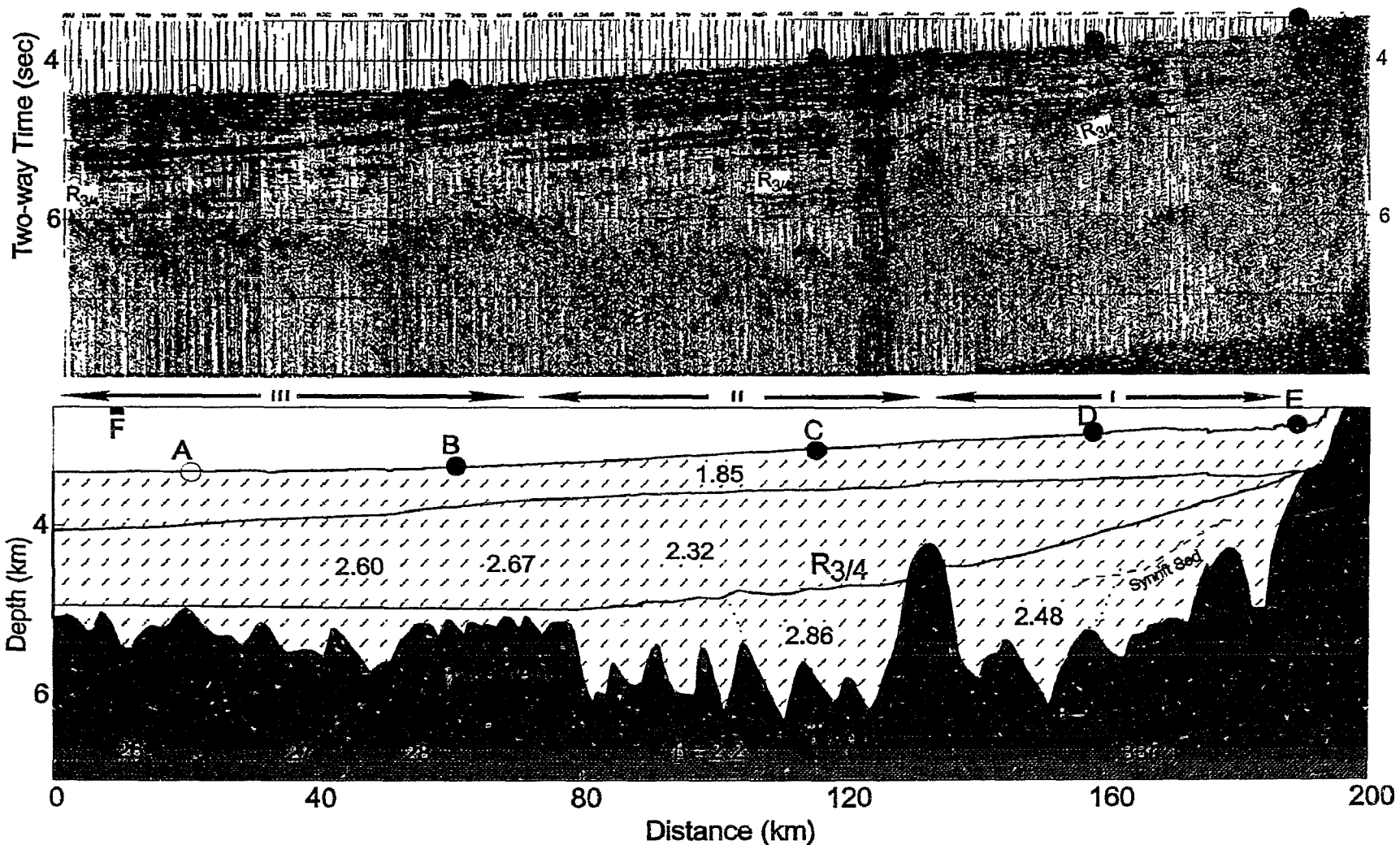


Figure 4.2. (top) Single-channel reflection data along line R2 band-pass filtered at 4-40 Hz. R3/4 boundary is tentatively interpreted following Srivastava et al. (1989). (bottom) Depth-converted sediment layers and basement topography (see text for details of interpretation). Numbers within sediment layers (hatched pattern) are velocities (in km/s) obtained from OBS profiles along line R2. Extension factors are calculated from the tilted blocks following Chenet et al. (1983). Magnetic chrons are located and numbered beneath short vertical lines following Roest and Srivastava (1989).

ocean bottom seismometers (OBS) profiles, with reference to the one-dimensional (1-D) modeling results from sonobuoy data around ODP Site 646 (Srivastava et al. 1989). A  $\beta$  value of 2.2-3.0 is obtained in transition Zone II which is slightly higher than the  $\beta$  value of 2.0 in Zone I. The amount of stretching determined in this manner is typically less than the stretching of the crust as a whole. It is likely to represent only the extension in the most brittle layers of the upper crust (Le Pichon and Barbier 1987). The remaining extension may be accommodated by creep in the lower crust for depth-dependent pure shear models or low-angle faulting for simple shear models.

### **4.3 Wide-Angle Seismic Data and Modeling**

#### **4.3.1 Data**

Seven OBS were deployed along line 88R2, six of them (OBS B, C, D, F, and G) giving useful information. The OBS used along line 88R2 recorded seismic signals from hydrophone and vertical and horizontal 4.5 Hz geophones on cassette tapes. These analog data were digitized and interpolated to a fixed sampling rate of 80 samples per second. Subsequent processing includes band-pass filtering (4-9 Hz for *P* waves and 2-8 Hz for *S* waves), clipping of high amplitudes, and gain that increases linearly with horizontal distance.

Since different recording channels sometimes respond differently to various seismic phases, I find that a sum of several channels is a useful way to present seismograms that demonstrate all prominent phases with just one figure. Before the summation, however, careful correction for the relative time difference between channels is necessary to

maintain or enhance the coherency of major seismic phases. In addition, a coherency filter is applied to some of the profiles. This algorithm (Chapter 3) is defined as a stack of a number of traces along an optimal phase velocity, which produces the maximum semblance within a moving time window of 0.15 s, followed by weighting with the normalized semblance (0-1). The coherency filtering thus defined can be used to enhance certain phases, particularly *S* waves, which are frequently entangled with *P* wave reverberations and multiples (Figure 4.3).

Major constraints on the crustal velocity structure come from OBS B, C, and D, which provide the best data quality. The data from OBS E are of poorer quality, possibly due to increased noise from deepwater currents. OBS F and G, situated under shallow water (~200 m; Table 4.1), also give good seismic signals, but the seismic rays are severely distorted by the sharp shelf break and/or the Moho relief, making it difficult to extract crustal information. Because of the failure of OBS A, data from an older sonobuoy profile (Stergiopolous 1984) are used to help constrain the oceanic crustal structure.

#### **4.3.2 One-Dimensional Reflectivity Modeling of Sonobuoy F**

The wide-angle profile from sonobuoy F (Figure 4.4), shot along strike during Hudson 79-013 (Figure 4.1), is used to constrain the crustal velocity structure at the western end of line 88R2. An additional sonobuoy, but with poorer data quality was also deployed at the opposite end of the same profile. Previous slope-intercept analysis of the reversed travel times (Stergiopolous 1984) yielded similar velocity models, indicating a



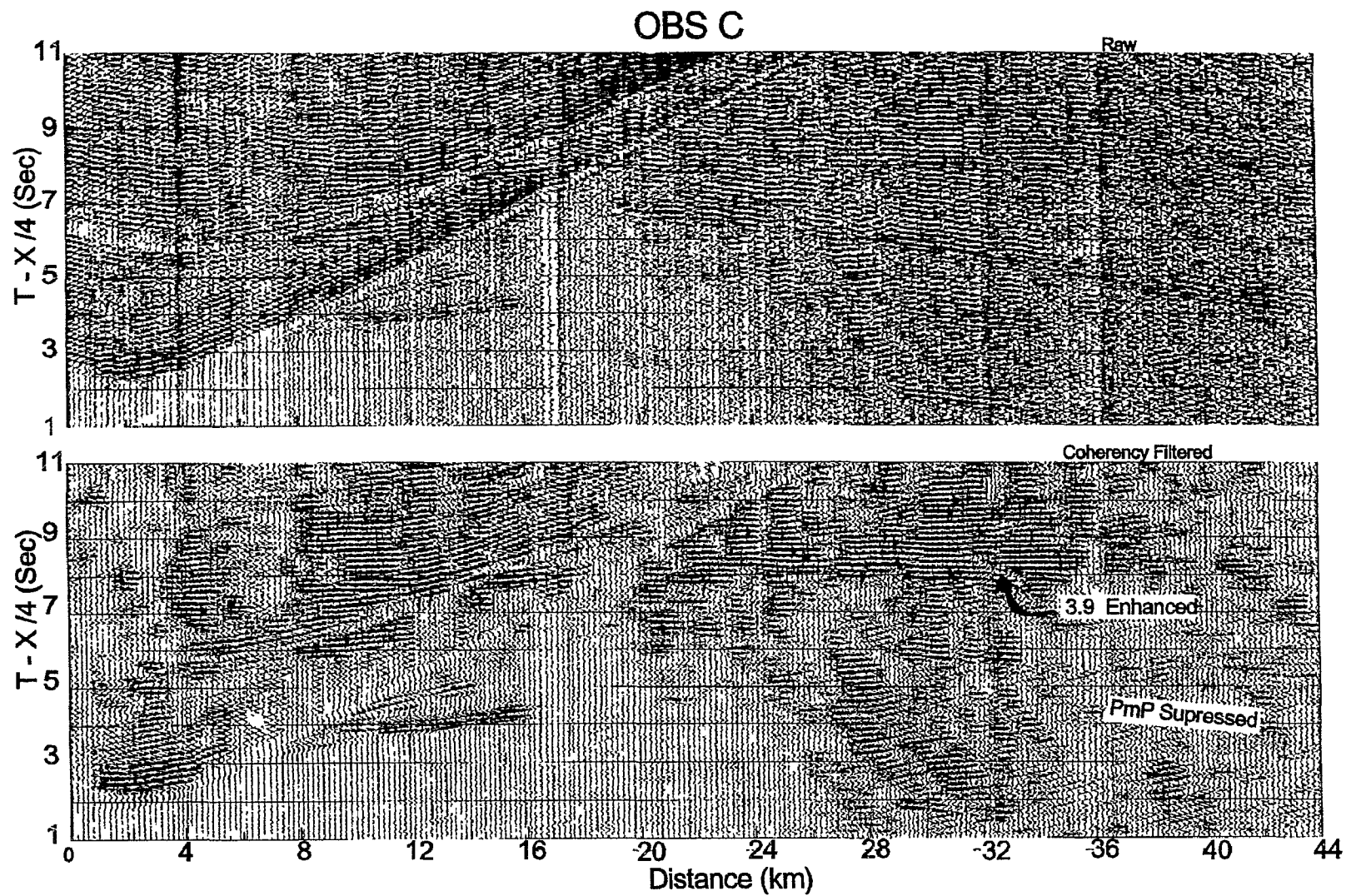


Figure 4.3. (top) Sediment-corrected vertical geophone channel from OBS C, band-pass filtered (2-8 Hz) with gain increasing linearly with distance. (bottom) Same data with coherency mixing of five adjacent traces. The mixing velocity is scanned between 2.5 and 4.5 km/s at a step of 0.5 km/s.

homogeneous structure along the line. In the reanalysis of sonobuoy F, a full waveform record section (Figure 4.4a) was produced by digitizing the original shipboard FM tape recording. Horizontal ranges were calculated from direct or reflected water waves using an average water velocity of 1.486 km/s. Determination of the  $P$  and  $S$  wave velocity-depth structure is based on forward modeling of the observed record section using 1-D ray tracing and full reflectivity synthetic seismograms (Figure 4.4b).

Crustal  $P$  phases contain two separate amplitude maxima centered at 13-16 and 17-23 km, with relatively abrupt changes in phase velocity. To fit this pattern requires a layered structure for the crust, with thicker units of low velocity gradient at velocities of 5.5, 6.5, and 7.2 km/s, separated by higher gradient zones with variable thicknesses. The initial velocity gradient from 4.8 to 5.5 km/s is not well constrained, apart from the total travel time, on account of the interference of the water reflection with the ground wave. The linear gradient of  $1.3 \text{ s}^{-1}$  from 5.5 to 6.5 km/s creates the initial amplitude buildup in the refracted wave ( $P_2$ ), although at ranges slightly less than observed. The sharp discontinuity from 6.5 to 7.2 km/s creates the second amplitude maximum from the wide-angle reflection ( $P_3P$ ), although it is not as abrupt or as strong as observed. The depth and velocity transition at the base of the crust is poorly constrained by modeling a third set of phases as  $P_mP$  with increasing amplitudes at ranges 27-30 km.

$S$  waves show a similar although less well-developed pattern of amplitudes and phase velocities. The one exception is that the uppermost crustal layer (with  $V_p=5.5$  km/s) must represent a gradient zone (with  $V_s=3.0$  to 3.2 km/s), primarily in order to fit the  $S$

**Table 4. 1 OBS Positions and Water Depths Along Refraction Line 88R2**

OBS	Latitude, °N	Longitude, °W	Water Depth, m
A	59.8408	52.1033	3368
B	60.0517	51.2900	3303
C	60.2767	50.4233	3076
D	60.4442	49.7767	2916
E	60.5516	49.3514	2823
F	60.6633	48.9100	136
G	60.7400	48.6133	175

**Table 4. 2 One-Dimensional Velocity Model for Sonobuoy F**

Thickness, km	$V_p$ , km/s	$V_s$ , km/s
3.335	1.485	
0.10	1.90	0.58
0.58	2.10	0.64
1.21	2.50	0.85
0.10	4.80	2.70
0.20	5.10	2.90
0.40	5.50	3.00
0.50	5.50	3.15
0.15	5.60	3.20
0.15	5.80	3.30
0.15	5.95	3.45
0.15	6.10	3.50
0.15	6.30	3.55
1.20	6.45	3.60
0.10	6.80	3.85
1.80	7.15	4.10
1.80	7.25	4.15
8.00	4.70	

wave travel times. The two deeper constant velocity layers are modeled with  $V_s$  of 3.6 and 4.1 km/s, giving Poisson's ratios of 0.28 and 0.26 for the mid and lower crust, respectively.

Figure 4.4b compares velocity models of sonobuoy F with results of 2-D synthetic modeling for a separate profile (Osler and Loudon 1992; Osler 1993) which terminates 70 km to the southwest, as located in Figure 4.1. This comparison indicates that at sonobuoy F: (1) The upper crust is thicker and contains a more complex structure, and (2) The lower crust is of similar thickness but contains a smaller velocity gradient.

### **4.3.3 Two-Dimensional Modeling of OBS Data**

Since significant lateral variations in seismic velocity are expected across the continent-ocean transition, I use 2-D dynamic ray tracing (Cerveny et al. 1977) for modeling the observed OBS data. The sedimentary structure and basement relief used in the modeling are derived from the coincident reflection data (see previous section). I tried two methods for describing the crustal structure. The first one divided the crust into several homogeneous layers using velocities obtained from sediment-corrected sections. The depth of each boundary was varied along the profile to match the observed travel times of crustal and mantle arrivals. This method generated strong wide-angle reflected energy which does not produce an acceptable fit to the observed amplitudes. Small misfits in travel times also existed. A second approach therefore represented most structural variations by lateral and horizontal velocity gradients. Velocities on a regular grid are obtained by bilinear interpolation of values at arbitrary points.

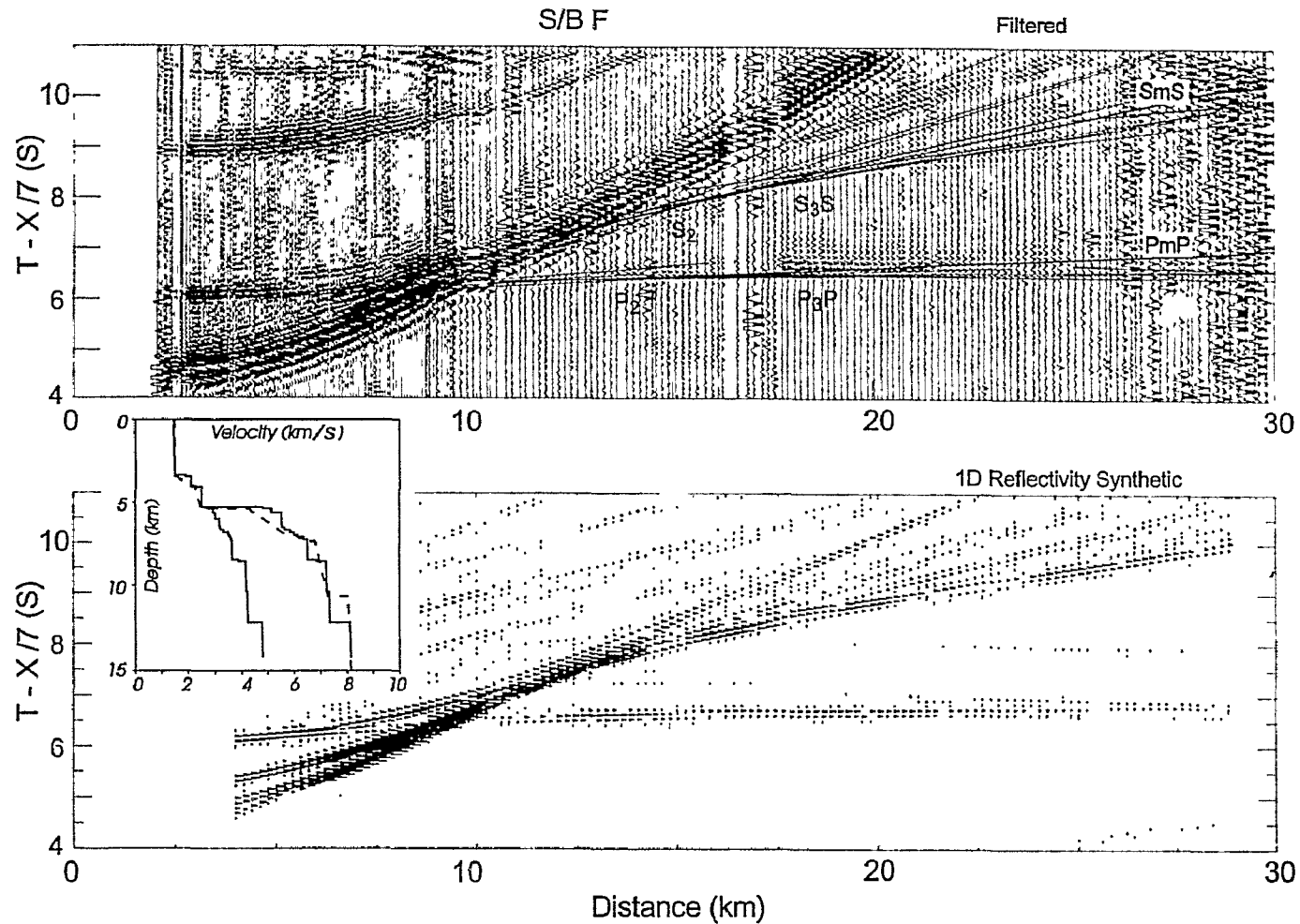


Figure 4.4. (top) Sonobuoy F hydrophone filtered at 4-10 Hz. Overlain lines are travel time curves computed from one-dimensional reflectivity modeling. Ranges are calculated from direct water wave (not shown) at 0-10 km and from water bottom reflection at 10-30 km, assuming an average water velocity of 1.486 km/s. (bottom) One-dimensional reflectivity synthetic seismograms generated from the P and S velocity model (solid line) in the upper left corner. Complete velocity-depth values for this model are given in Table 4.2. Dotted line in the inset shows the P velocity structure 70 km southwest of sonobuoy F [Osler, 1993]. P2 and S2 are refractions from upper crust; P3P and S3S are reflections from lower crust; PmP and SmS are reflections from upper mantle. S waves are doubly converted from and to P waves at the sediment-basement interface.

The seismograms generated from the final, 2-D velocity model with this second method are compared to individual recorded sections for OBS B, C, D, E, and G in Figures 4.4-8. The strong seismic phases that are crucial in determining the  $P$  velocity model include refractions from the sediment layers ( $P_{\text{sed}}$ ), refractions from the upper and the lower crust ( $P_2$ ,  $P_3$ ), and reflections and refractions from the upper mantle ( $P_mP$ ,  $P_n$ ). In addition, two sets of strong multiples are sometimes useful. The water column multiple ( $P_mP_2$ ) is frequently strong. Its curvature can constrain the velocity of the lower crust and its travel time the depth of the Moho when the first arrival cannot be recognized (e.g., OBS B; Figure 4.5). Another prominent multiple ( $P_mP'$ ) is produced between the seafloor and the sediment/basement interface. This multiple is strongest in the hydrophone channel of both OBS B (Figure 4.5) and OBS C but is minimal, for example, in the horizontal geophone of OBS C (Figure 4.6).

**OBS B.** The velocity-depth structure of crust from the model of sonobuoy F (Figure 4.4) is used as a control for the western end of the 2-D model. The upper crustal structure is smoothed laterally to provide an overall fit to the western profile of OBS B (Figure 4.5). The velocity (7.15-7.25 km/s) of the lower crust and the depth (12 km) of the Moho determined from modeling the curvature of  $P_mP_2$  to the west of OBS B are similar to the model of sonobuoy F. The lower crustal velocity east of OBS B is less well constrained because of distortion caused by the sharp change in depth of the basement.

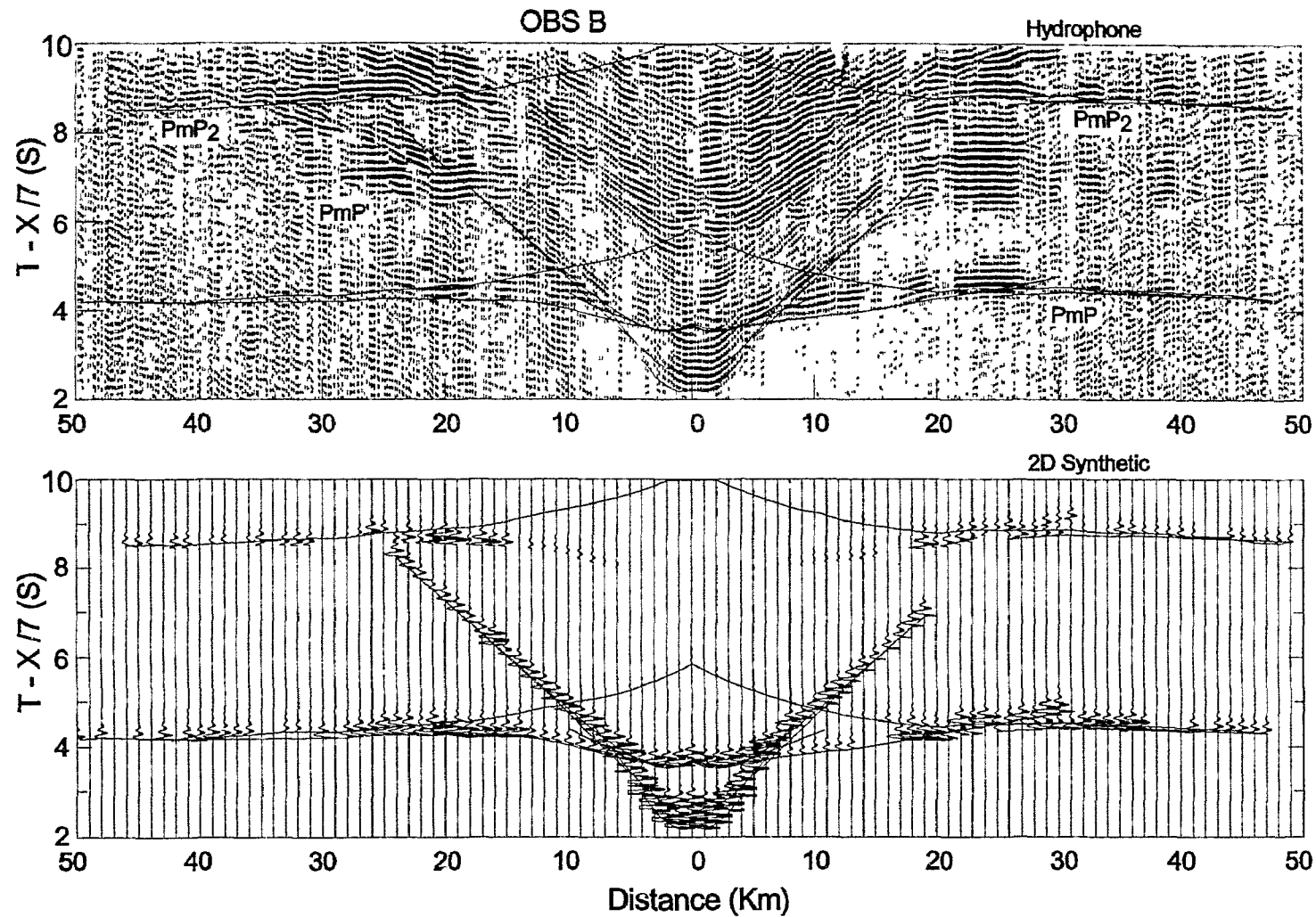


Figure 4.5. (top) OBS B hydrophone coherency filtered using five traces. Calculated travel time curves from two-dimensional dynamic ray tracing are superimposed.  $PmP$  is the wide-angle reflection from the Moho.  $PmP_2$  and  $PmP'$  are water and sediment multiples of  $PmP$ . (bottom) Synthetic seismograms and travel time curves generated by two-dimensional dynamic ray tracing from the seismic model of Figure 4.10a.

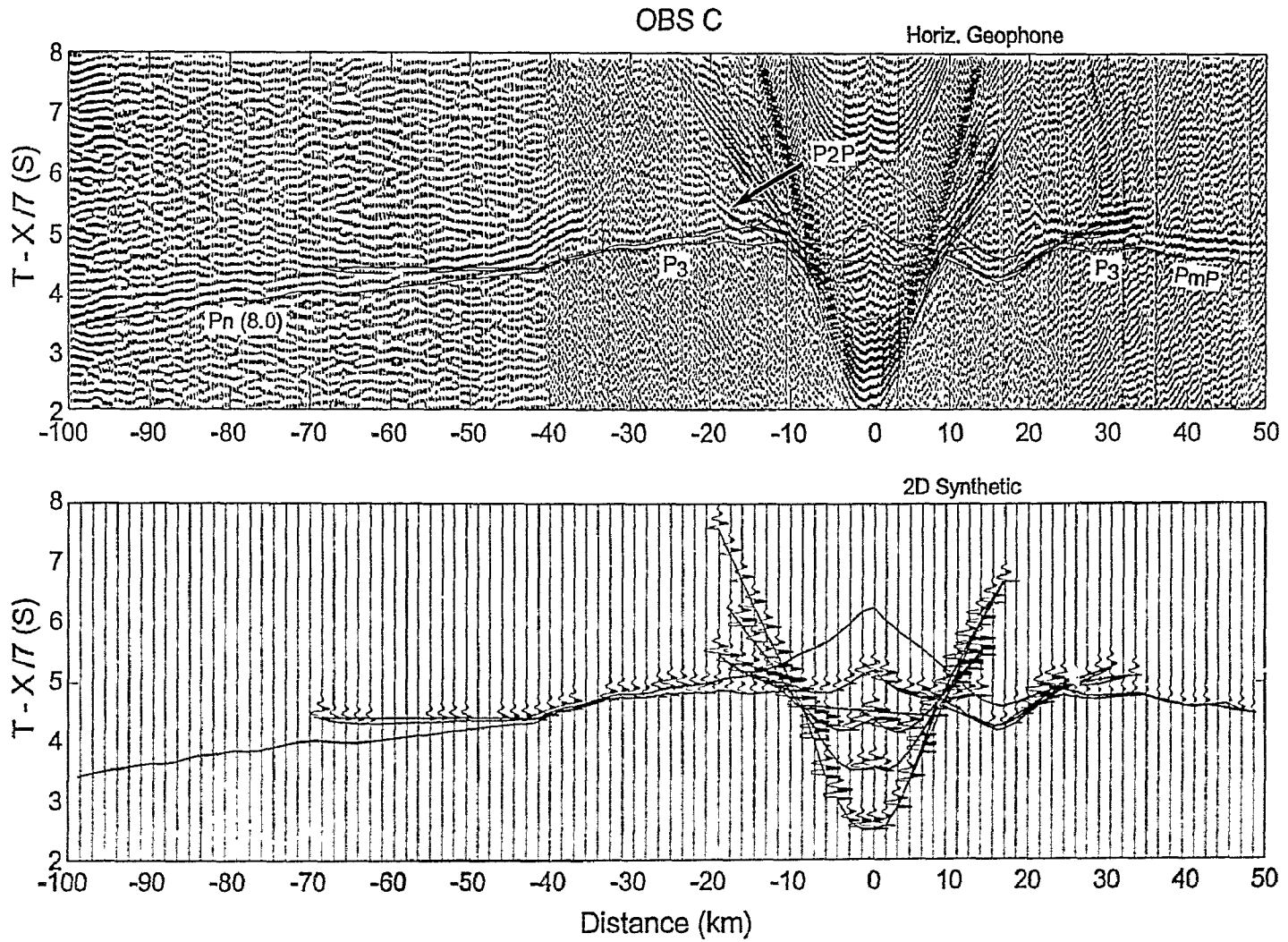


Figure 4.6. (top) OBS C horizontal geophone with traces between ranges of -100 to -40 km coherency filtered using five traces. Calculated travel time curves from two-dimensional dynamic ray tracing are superimposed. (bottom) Synthetic seismograms and travel time curves generated by two-dimensional dynamic ray tracing from the seismic model of Figure 10a.



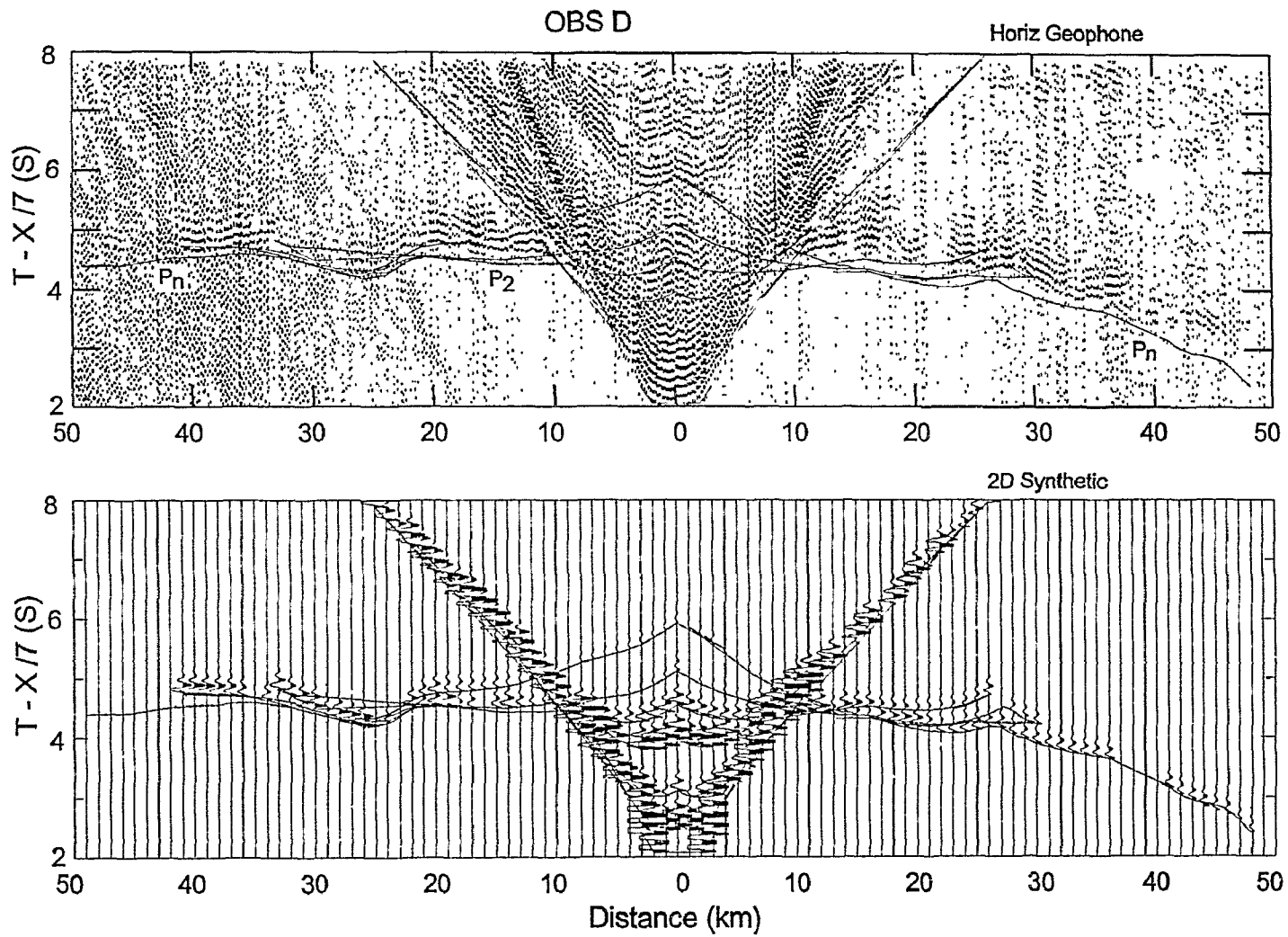


Figure 4.7. (top) OBS D horizontal geophone. Calculated travel time curves from two-dimensional dynamic ray tracing are superimposed. (bottom) Synthetic seismograms and travel time curves generated by two-dimensional dynamic ray tracing from the seismic model of Figure 10a.

**OBS C.** The seismograms of OBS C (Figure 4.6) are characterized by significant differences on either side of the OBS. On the western side, the velocity of the upper crust is about 4.0-5.0 km/s. This low-velocity forms a strong velocity contrast with the layers below, producing a distinct reflection phase ( $P_2P$ ). The lower crust is represented by a clear phase  $P_3$ , which is refracted by a gradient layer of high velocity (7.0-7.6 km/s), with the bulk of the lower crust at 7.4-7.6 km/s. On the eastern side of OBS C, there is a significant travel time pull-down (by 1 s) of upper crustal arrivals between ranges of 12 and 20 km which cannot be fit unless a velocity of  $\sim 6.5$  km/s is introduced beneath the elevated basement. The high amplitudes of the lower crustal arrival  $P_3$  (at eastern ranges of  $\sim 30$  km) are produced by the large velocity gradient under this elevated basement. The lower crust under this basement high has a velocity of 6.8-7.4 km/s constrained by  $P_3$  with a phase velocity of  $\sim 7.0$  km/s. A higher velocity would incorrectly reduce the travel time of  $P_3$ . The Moho near the basement high is placed at a depth of 11.8 km which is the same as that westward. This provides a reasonable fit to the travel time of  $P_mP$  whose slope is distorted by the faulted basement block east of the basement high. A strong  $P_mP$  phase is not observed west of OBS C but is replaced by the clear appearance of  $P_n$  which can be traced to a horizontal range of 100 km. The steep tilting of the mantle arrival at a western range of 40 km is caused by the basement jump ( $>1$  km) adjacent to OBS B.

**OBS D.** The high velocity of the elevated basement is also expressed in the travel time pull-down of lower crustal arrivals of OBS D (Figure 4.7) at western ranges of 20-28 km.

The modeling of  $P_n$  for the western ranges of the OBS supports the velocity structures under the basement high as obtained from OBS C. On the eastern side of OBS D, the upper crustal arrival is well modeled and corresponds to an easterly increasing velocity of 5.3-5.6 km/s. First arrivals at ranges >28 km have travel times too early to be produced solely by shallowing the basement toward the continent. A reasonable fit can be produced by setting the Moho at a very shallow depth (~8.2 km) and the mantle underneath with a high velocity gradient (7.7-8.0 km/s). It should be noted that the calculated travel times are slightly earlier than observed. While a smaller velocity of 7.5-8.0 km/s produces a better fit, this would degrade both the calculated travel times for OBS E and the computed gravity anomaly. Therefore complications exist for this part of the seismic model which the data are not sufficient to resolve.

**OBS E.** Shots to the west of OBS E (Figure 4.8) give important information on the depth of the Moho. Between ranges of 22-30 km, a strong phase can only be modeled as a refraction from a layer with a velocity of ~7.7 km/s at 8-9 km depth, which is consistent with the modeling of OBS D. A slower velocity will cause an unacceptable travel time delay and will shift the major amplitude westward. To the east, the seismograms are noisy and mostly affected by basement relief across the continental slope.

**OBS G.** OBS G (Figure 4.9) is situated at the eastern end of refraction line 88R2.  $P$  and  $S$  waves from the upper continental crust are observed which give the same velocities as those from another refraction line  $R_1$  along strike (Chapter 3). Deeper arrivals are distorted by the sharp shelf break and hence give little information about crustal structure.

The final velocity model that produces all the synthetic seismograms and travel times in Figures 4.4-9 is shown in Figure 4.10a. To show the ray coverage for different regions of the model, I plot in Figure 4.10b the boundaries of the model overlain with ray paths from OBS B, C, D, and E.

#### 4.3.4 Determining *S* Waves

Here I present the first shear wave data for transitional crust and upper mantle across a nonvolcanic rifted margin. There are primarily two types of crustal *S* waves observed in the OBS data: PSP and PSS (Figure 4.11). PSP phases are formed by double *P-S* conversion at the sediment/basement boundary. The other prominent phase is PSS, which is only converted once. The energy of such converted *S* waves is especially strong when the *P* velocity in the bottom of sediments ( $V_{\text{sed}}$ ) is close to the *S* velocity ( $V_S$ ) in the crust (Spudich and Orcutt 1980b).

*S* waves can appear on all component sensors of the OBS. For example, the PSP phase at OBS B only appears on the horizontal geophone (Figure 4.11a), whereas the PSS phase in OBS C appears on both hydrophone and vertical geophone channels (Figure 4.11b). Reverberations of *P* phases frequently interfere with *S* waves, requiring coherency mixing to suppress phases with higher apparent velocities. In addition, when sediment phases are strong, they interfere with upper crustal *S* waves because of their similar velocities, making it more difficult to pick the correct *S* phases.

Once *S* phases are identified, their travel times are modeled by adjusting the  $V_P/V_S$  ratio for all layers of the *P* velocity model. For OBS B, a  $V_P/V_S$  ratio of 1.8 for both the

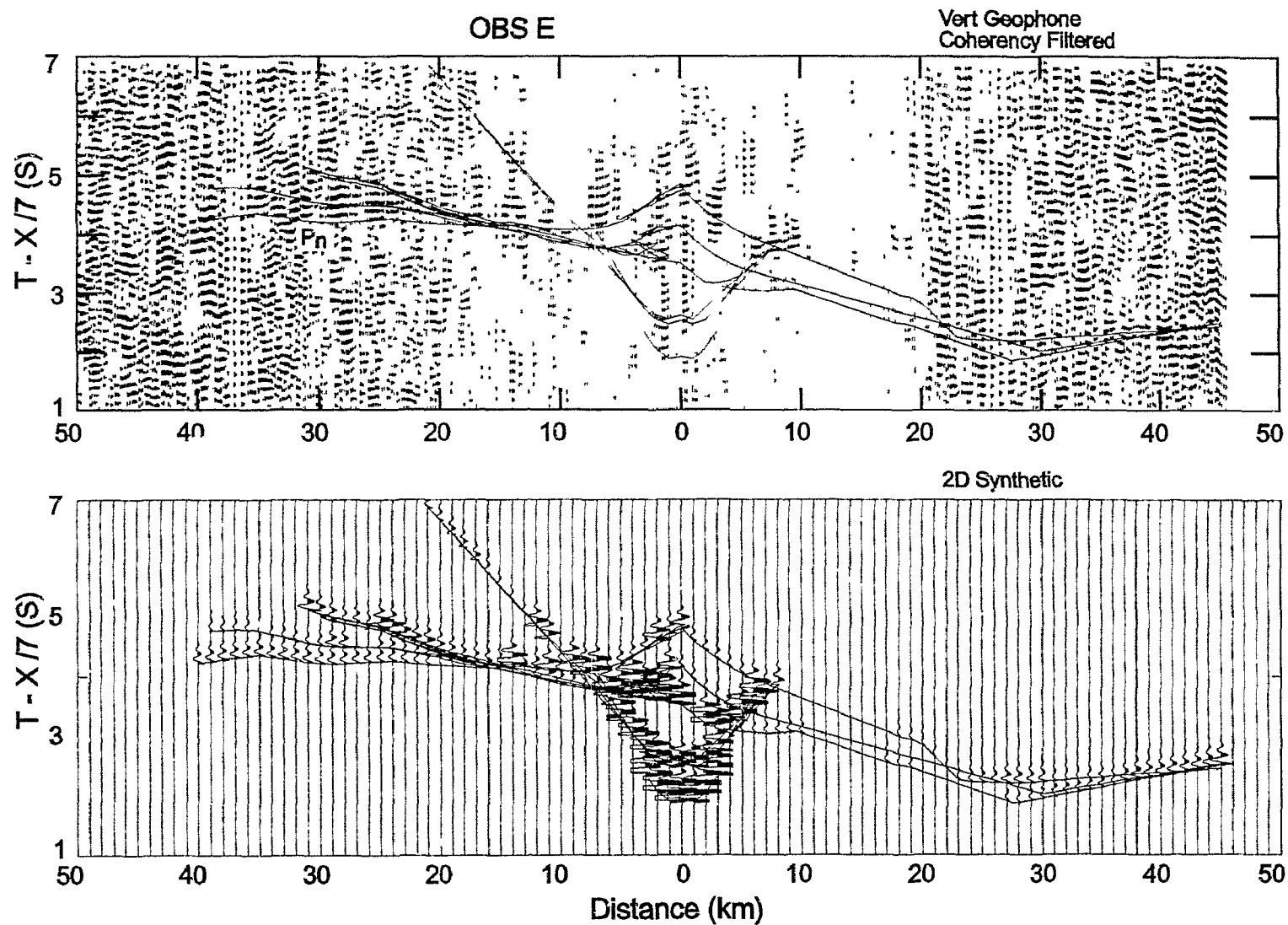


Figure 4.8. (a) Top: OBS E vertical geophone coherency filtered using five traces. Calculated travel time curves from two-dimensional dynamic ray tracing are superimposed. (bottom) Synthetic seismograms and travel time curves generated by two-dimensional dynamic ray tracing from the seismic model of Figure 4.10a.

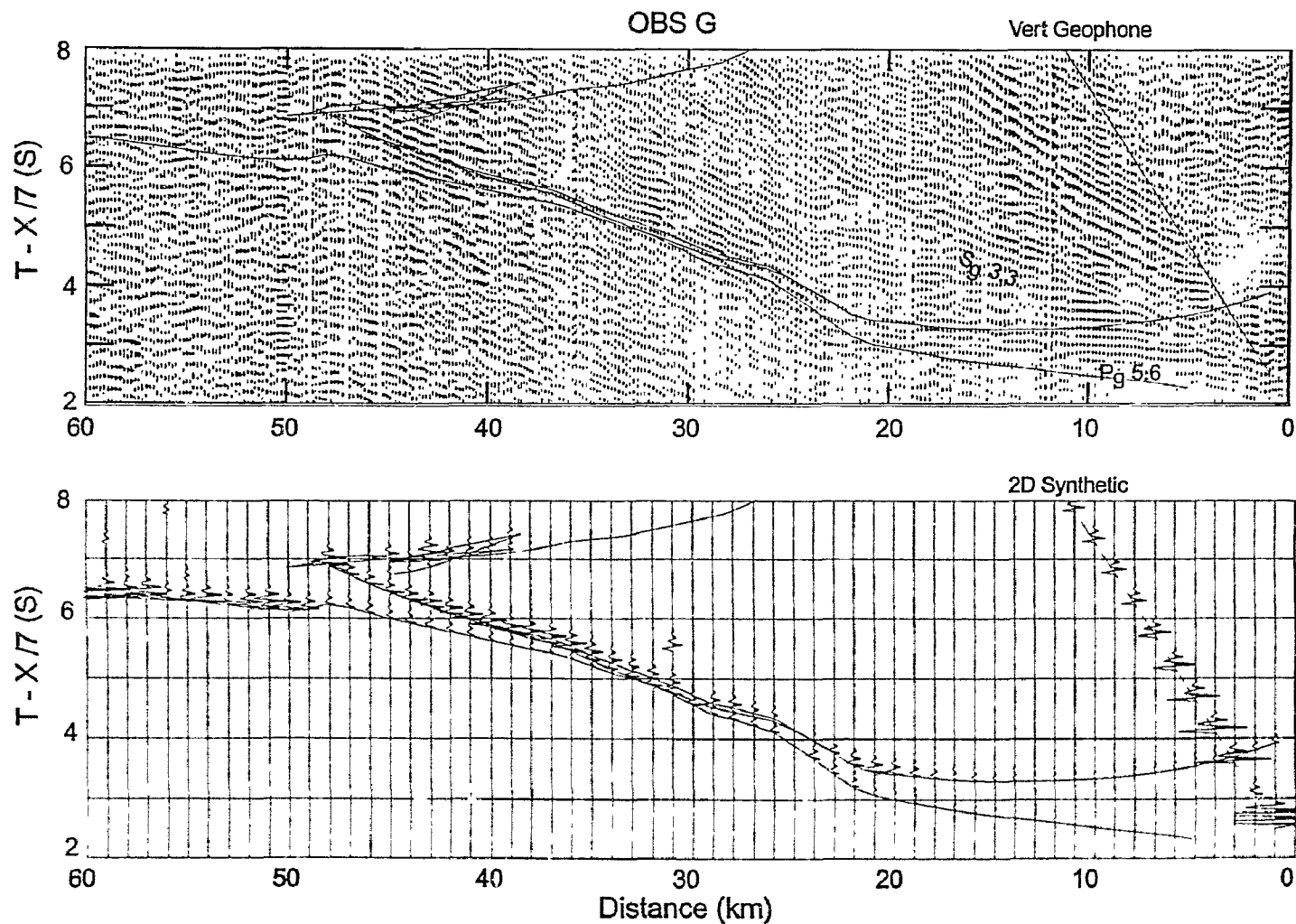


Figure 4.9. (top) OBS G vertical geophone coherency filtered using five traces. Calculated travel time curves from two-dimensional dynamic ray tracing are superimposed. Pg and Sg (with associated phase velocities in km/s) are P and S refractions from upper continental crust. (bottom) Synthetic seismograms and travel time curves generated by two-dimensional dynamic ray tracing from the seismic model of Figure 10a.

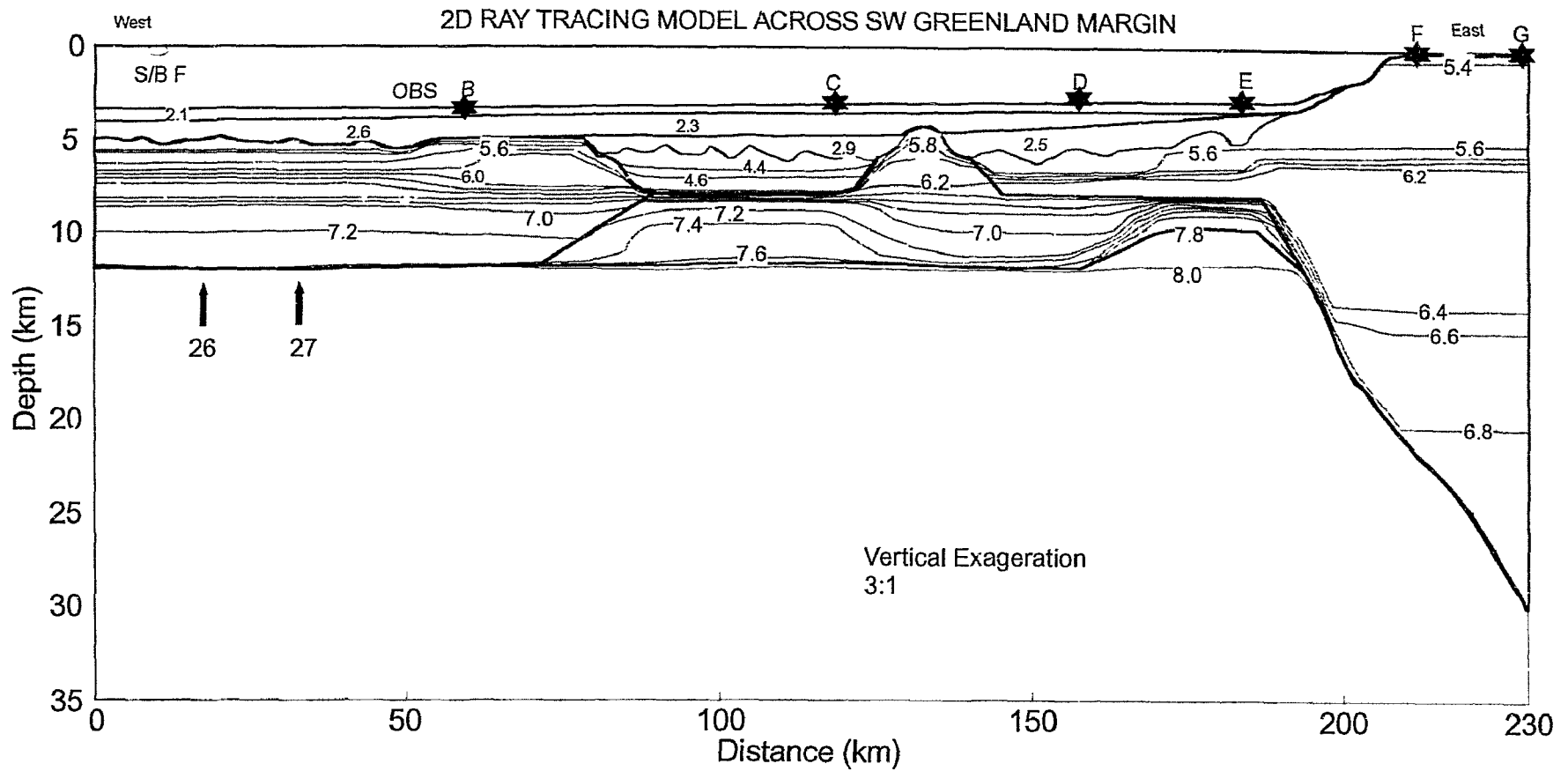


Figure 10a

Figure 4.10 (a) Two-dimensional velocity model showing contours of  $V_p$  (in km/s) across the SW Greenland margin. The contour interval is 0.2 km/s. At some significant velocity boundaries (thick lines) contour lines are terminated for clarity. Solid stars indicate positions of OBS; oval delineates the approximate position of sonobuoy F. Vertical exaggeration is 3:1. (b) Selected ray paths for OBS B, C, D, and E overlain by boundaries of the two-dimensional model shown above.

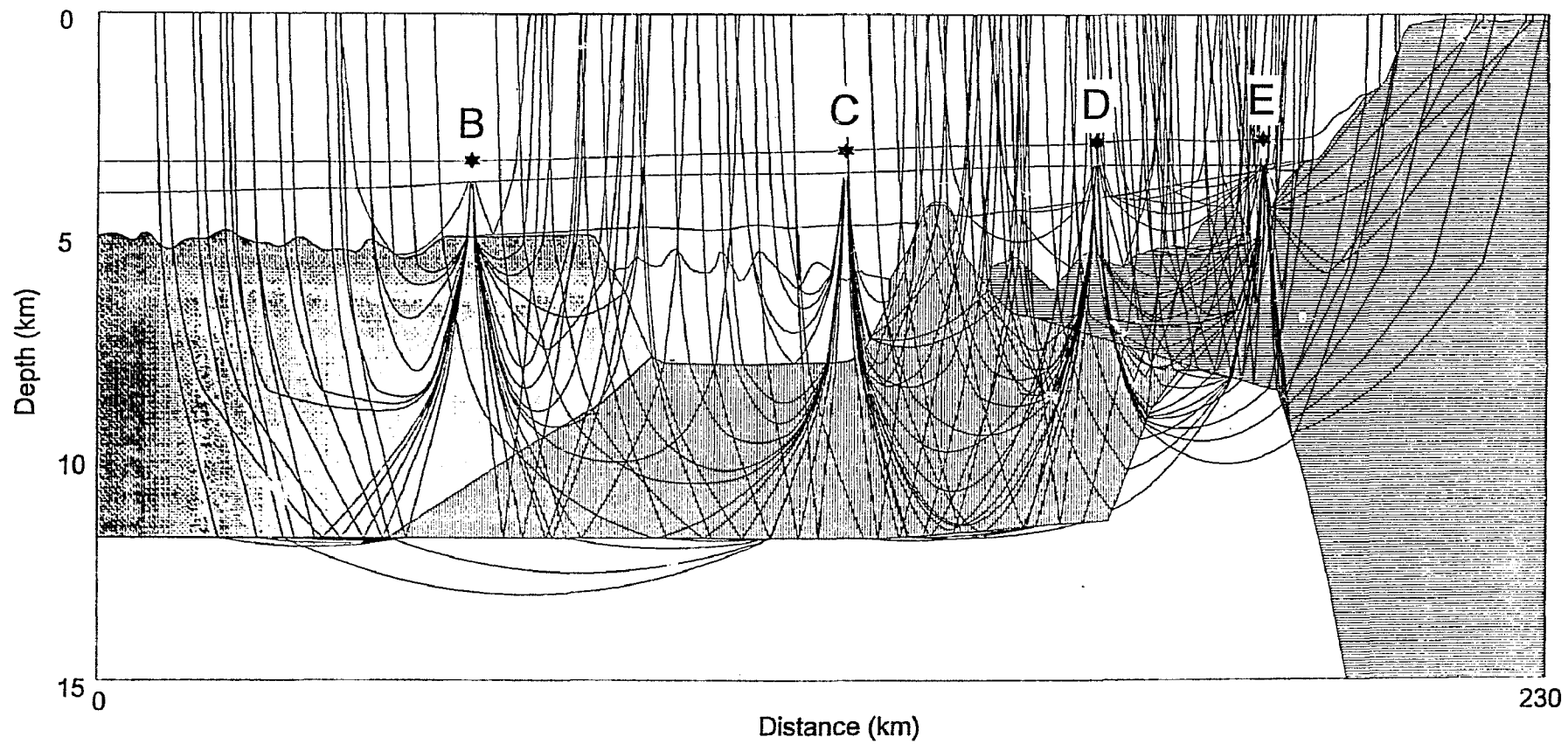


Figure 10b



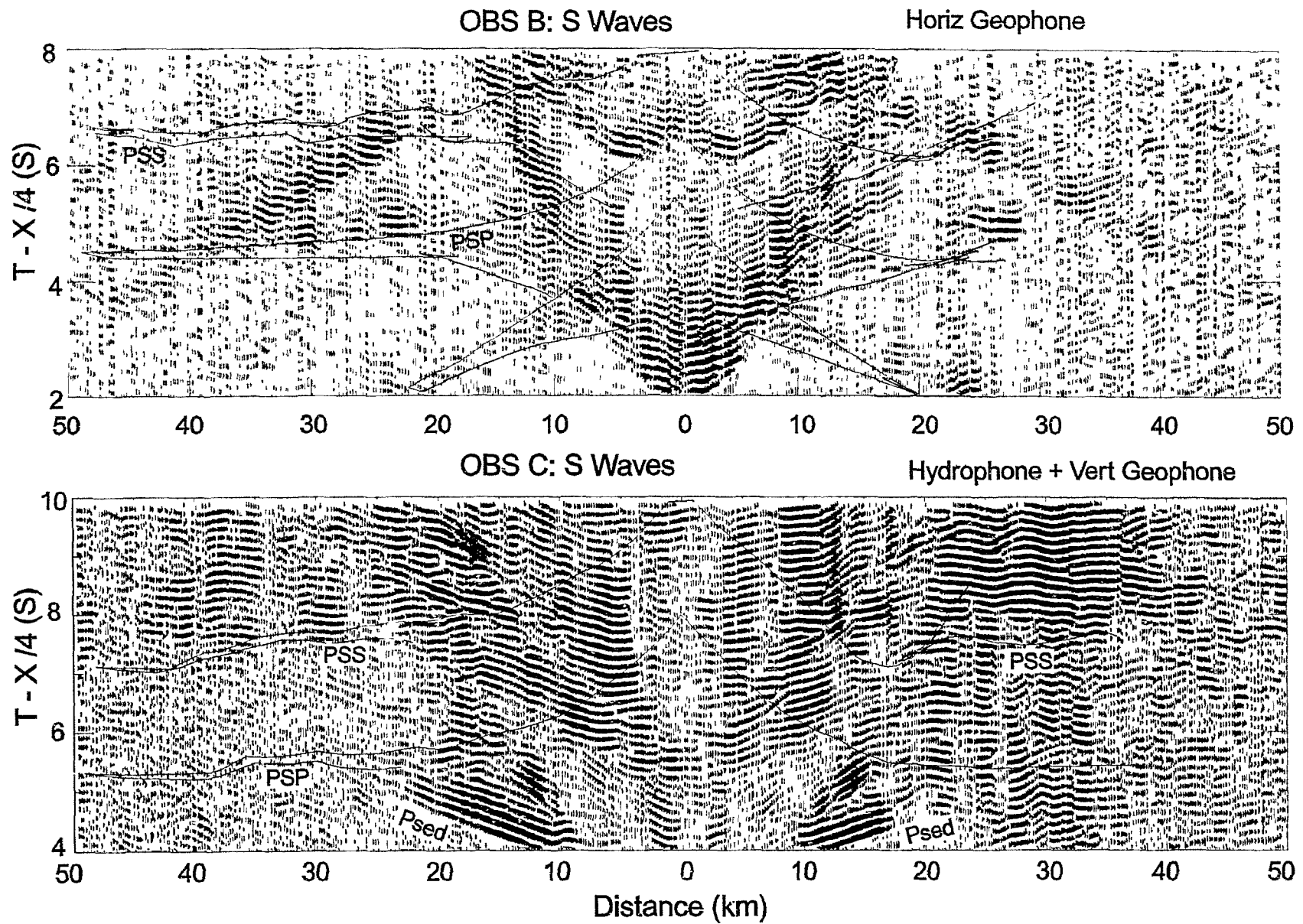


Figure 4.11 (a) Crustal S phases for the horizontal geophone channel of OBS B and (b) a combination of hydrophone and vertical geophone channels of OBS C. PSP is a crustal S refraction generated by double P-S conversion at the sediment/basement interface. PSS is converted only once at this interface.

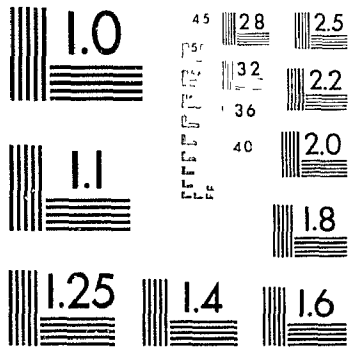
upper and lower crust enables a fit of travel times for PSP and PSS (Figure 4.11a). The modeling of the PSS phase at OBS C requires an additional unknown: the value of  $V_p/V_s$  ratio for the top sediment layer. This is determined by maximizing the overall travel time fit. The  $V_p/V_s$  ratios for the three sediment layers are 4.5, 2.7 and 1.7. For the high-velocity lower crust and upper mantle, they are 1.83 and 1.90, respectively. This method does not result in a totally satisfactory fit to the data, but it does provide a simple and reasonable estimate of Poisson's ratio for each layer with error estimates (see Appendix A). One advantage of this method is that all the structural variations from the better observed  $P$  waves are retained for the modeling of  $S$  phases, which in general are less complete and definitive.

#### 4.3.5 Error Analysis

Since the final velocity model includes strong lateral and vertical variations with variable seismic ray coverage (Figure 4.10b), analysis of the resolution of the model can only be investigated for one crustal unit at a time. I choose to perform error analysis for the lower crust but not for the upper crust primarily because the upper crust does not have sufficient ray coverage. Reflections and refractions are treated separately. For a refracted phase, the velocity and top interface depth of a layer are varied to determine their effect on the average travel time misfit. For a wide-angle reflected phase, the velocity gradient and the depth of the bottom interface of the layer are adjusted. When normalized to the misfit endurance (maximum travel time misfit acceptable), these become  $\chi^2$  plots where the

2

PM-1 3½"x4" PHOTOGRAPHIC MICROCOPY TARGET  
NBS 1010a ANSI/ISO #2 EQUIVALENT



PRECISION<sup>SM</sup> RESOLUTION TARGETS

bounds of acceptable parameters are delimited by the contour of  $\chi^2=1$ . The details of this method are discussed in Appendix A.

Figure A1 gives results of an error analysis for  $V_p$  of the lower crust west of OBS C. The contour levels are normalized to 40 ms, which includes the errors in first-arrival travel times. Errors are  $\pm 0.10$  km/s for  $V_p$  and  $\pm 0.3$  km for the top boundary depth. The same analysis is performed for the  $P_n$  phase, which indicates an error of  $\pm 0.05$  km/s for the upper mantle  $P$  velocity and  $\pm 1$  km for the Moho depth. For a PSS phase at OBS C, error analysis follows a similar approach (see Appendix A) which indicates an error of  $\pm 0.20$  km/s for the lower crustal  $S$  velocity (Figure A2).

The errors of  $P$  and  $S$  velocities for the lower crust west of OBS B are estimated by iterating the 2-D model for OBS B and 1-D reflectivity model for sonobuoy F. By this qualitative approach, I estimate that the errors are approximately  $\pm 0.15$  km/s for  $V_p$  and  $\pm 0.20$  km/s for  $V_s$ . These values are similar to the results of the previous, more quantitative approach.

#### 4.4 Gravity and Magnetic Modeling

The gravity and magnetic data used for modeling were extracted from a R/V MINNA 74 profile (Voppel et al. 1988; S. P. Srivastava, personal communication, 1993), which is almost exactly coincident with the refraction line 88R2 (Figure 4.1). Calculation of synthetic magnetic anomalies are based on the spreading rates of Roest and Srivastava (1989) and the time scale of Kent and Gradstein (1986). The observed magnetic data (Figure 4.12) show a clear change in pattern at Chron 28. While Chrons 25 and 26, and

possibly 27 and 28, correlate well with observed anomalies, Chrons 31-33 do not. Therefore it is possible that seafloor spreading with the generation of true oceanic crust did not start until Chron 28. This is compatible with the interpretation of Chalmers (1991).

The gravity map of the Labrador Sea (Woodside 1989) shows small along-strike variations adjacent to line 88R2, justifying two-dimensional gravity modeling. The contribution of the sediments is calculated using the drilling results at ODP Site 646 (Jarrard et al. 1989; see Figure 4.1 for location) to determine the velocity-density relationship for the top 1 km of sediments. These data are extrapolated downward to cover the entire sediment column. The contribution from the crust is calculated from the velocity grid obtained from the 2-D ray tracing model (Figure 4.10a), converted into density (in  $\text{g/cm}^3$ ) using the relationship  $\rho = -.6997 + 2.2302V_p - .598V_p^2 + .07036V_p^3 - .0028311V_p^4$  (Ludwig et al. 1971). I set the minimum crustal density as  $2.40 \text{ g/cm}^3$  and the maximum as  $3.30 \text{ g/cm}^3$ . I assume a uniform mantle density ( $3.30 \text{ g/cm}^3$ ) and calculate gravity from blocks above 35 km depth.

The final computed gravity curve fits the overall patterns of the observed data with a maximum misfit of 5 mGals (Figure 4.12), which is not significant considering the resolution of the observed gravity profile. Two important controls on the crustal structure result from this model:

1. The observed free air gravity anomaly along line 88R2 provides the only control over the shape of the deepening Moho east of OBS E. It is characterized by a positive peak (34

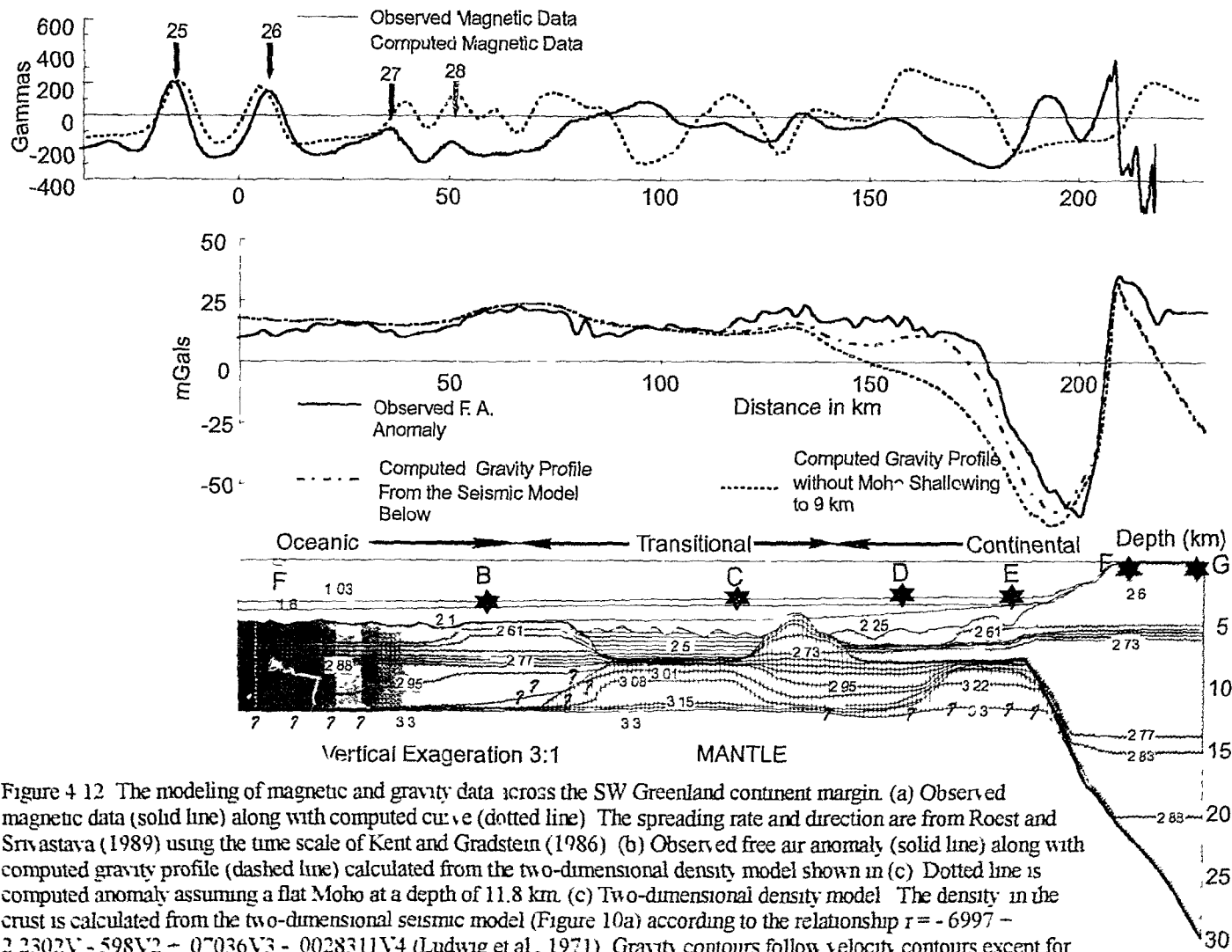


Figure 4.12 The modeling of magnetic and gravity data across the SW Greenland continent margin. (a) Observed magnetic data (solid line) along with computed curve (dotted line). The spreading rate and direction are from Roest and Srivastava (1989) using the time scale of Kent and Gradstein (1986). (b) Observed free air anomaly (solid line) along with computed gravity profile (dashed line) calculated from the two-dimensional density model shown in (c). Dotted line is computed anomaly assuming a flat Moho at a depth of 11.8 km. (c) Two-dimensional density model. The density in the crust is calculated from the two-dimensional seismic model (Figure 10a) according to the relationship  $\rho = -6997 - 2.2302V - 598V^2 - 0.036V^3 - 0.028311V^4$  (Ludwig et al., 1971). Gravity contours follow velocity contours except for the leftmost 50 km.

mGals) at the shelf break, followed at 10 km seaward by a large negative anomaly (-63 mGals). This sudden change is primarily due to the edge effect between the abrupt deepening of the basement and the steep slope of the Moho. The calculated gravity low between 180 and 200 km is particularly sensitive to the Moho relief under the continental slope.

2. The model provides important controls over the depth of the Moho at the base of the continental slope. The diagram in the middle of Figure 4.12 shows two computed gravity curves. The dotted curve results from a Moho which remains flat seaward of the continental slope. A Moho which shallows to 8.2 km at the bottom of the continental slope significantly improves the fit of the gravity (dashed line) and is more consistent with the 2-D seismic modeling, particularly for OBS E (Figure 4.8).

It can be seen from Figure 4.12 that the gravity contours follow velocity contours except for the leftmost 50 km of the profile. This exception is introduced because strict adherence to the velocity-density relationship used in the remainder of the model produces a calculated gravity curve for the leftmost 50 km which is ~20 mGal higher than observed. An alternative for avoiding this misfit is to deepen the Moho from 12 to 13 km west of OBS B. While this change of Moho is within the error bounds of the data, it is not supported by any other deep seismic data in the basin.

## 4.5 Discussion

### 4.5.1 The Seismic Model

The seismic model shown in Figure 4.10a represents the complete crustal transition across the SW Greenland continental margin. A gross feature of the model is that it can be divided into three distinct zones, similar to those previously identified from basement morphology. In Zone I, the 30-km-thick preexisting continental crust is thinned abruptly to a thickness of only ~3 km under OBS E. Further west, this layer terminates at a basement high where it joins Zone II, which has a low-velocity upper crust, underlain by an unusually high-velocity (~7.5 km/s), 4-5-km thick lower crust. This zone spans a length of ~50 km, terminating in the west at another basement high that separates Zone II from a 7-km thick crust bearing oceanic-type velocities (Zone III).

Remarkable vertical and lateral variations are observed both in the depths and velocities near the two basement highs that separate the three zones. Among these complexities, the structures around the basement high between Zones I and II are the most interesting and important. To the east, the  $V_p$  of the upper crust ranges from ~5.5 to ~6.2 km/s. The similarity of this value with that of the adjacent, preexisting, upper and middle continental crust under the shelf (Chapter 3, Figure 4.12) suggests that the crust east of OBS D is composed mainly of stretched, metamorphosed upper and middle continental crust.

To the west of the basement high, the upper crust in Zone II has critical importance in determining the position of the continent-ocean boundary (COB). An



evident feature of this upper crust is that the seismic velocity (4.0-5.0 km/s) is unusually low compared to both the continental crust to its east and oceanic crust to its west. Comparison with a recent multichannel reflection profile (Keen et al. 1994b), which is adjacent and parallel to line 88R2, indicates that the base of the upper crust in the transition zone is a strong reflective boundary. This reflector is similar to the *S* reflector in the Bay of Biscay (Le Pichon and Barbier 1987), and it can be traced 100 km westward from OBS E . Therefore the upper crust throughout Zone II possibly stems from a common origin.

The most surprising result of this work is the existence of a high-velocity (7.2-7.6 km/s) lower crust, which is 4-5 km thick within a 50-70 km-wide zone around OBS C. The bulk of this lower crust has a  $V_p$  of 7.4-7.6 km/s with an error bound of  $\pm 0.1$  km/s (Figure A1). The corresponding  $V_s$  is  $4.0 \pm 0.2$  km/s as determined from a PSS phase (Figure 4.11), which implies a Poisson's ratio of  $0.30 \pm 0.03$ . This high-velocity layer is restricted in its extent between OBS B and D. Its high velocity (7.4-7.6 km/s) cannot be found either in the continental crust to the east (Chapter 3) or in the oceanic crust to the west (sonobuoy F, Figure 4.4; OBS B, Figure 4.5).

To investigate the origin of the lower crust in Zones II and III, a  $V_p - V_s$  diagram (Figure 4.13) is used to compare reported seismic data for the crust and upper mantle (Christensen 1989) with laboratory data for serpentinites and pyroxene/olivine gabbros (Spudich and Orcutt 1980a; Christensen and Smewing 1981). In addition, included are results for the lower continental crust along the SW Greenland shelf determined in

Chapter 3. The observed  $V_p$  of the lower crust in Zone III is similar to values reported by Osler (1993), who shows that rather high velocities (<7.3 km/s) for layer three are typical of the oceanic crustal structure within the Labrador Sea to the east of the extinct rift axis. The even higher  $V_p$  for the lower crust of Zone II lies outside the region of normal gabbroic crust but is consistent with the  $V_p$  observed for the underplated lower crust on volcanic margins. It also intersects the theoretical curve (PSP) for serpentinized mantle (Christensen 1966). Therefore the velocities alone are not able to definitely distinguish between underplated mafic rocks (i.e., high-Mg mafic gabbro) and serpentinized upper mantle mineralogies.

#### **4.5.2 Undercrusted Serpentinite or Magmatic Underplating?**

High-velocity lower crust has been found on other nonvolcanic, rifted continental margins, but its lithology and mechanism of formation are similarly not clearly determined. For example, on the western margin of Iberia the lower crust near the proposed COB has anomalously high velocity (7.3-7.6 km/s) and a small thickness (2-3 km). This has been interpreted either as underplate (Whitmarsh et al. 1990) or as serpentinite (Boillot et al. 1992). Farther south in the Tagus Abyssal Plain, even higher velocities (7.6-7.9 km/s) for the lower crust are interpreted as serpentinites (Pinheiro et al. 1992). On the conjugate margin off Newfoundland, refraction data on the southern Grand Banks show a thin, high-velocity (7.2-7.7 km/s), lower crust interpreted as serpentinite (Reid 1994). A similar high-velocity, lower crust is observed on the southern (Todd and Reid 1989) and northern margins of Flemish Cap (Reid and Keen 1990), but it is interpreted as underplate.

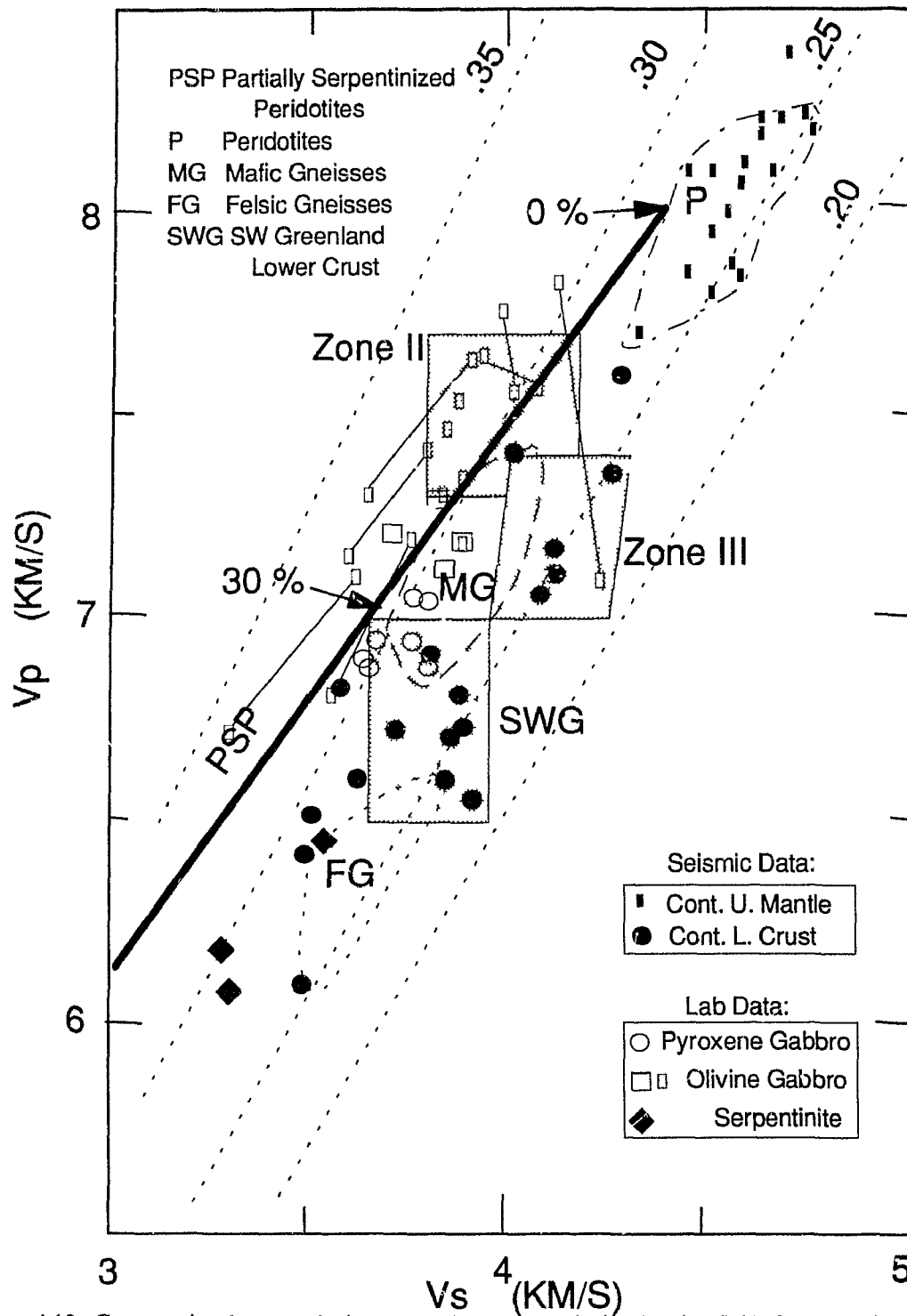


Figure 4.13. Compressional wave velocity versus shear wave velocity showing fields for peridotites (P); partially serpentinized peridotites (PSP) with 0 and 30 percent serpentine points marked; felsic gneisses (FG); mafic gneisses (MG); reported crustal seismic data for continental lower crust (solid circles) and upper mantle (vertical rectangles); and serpentinite data at 0.6 kbar from ophiolite samples (solid diamond) (Fountain and Christensen, 1989; Christensen, 1966, 1978, 1989). Field for SWG represents the continental lower crust of the SW Greenland margin (Chapter 3). Also shown are laboratory data for pyroxene gabbro (open circles) and olivine gabbro (open rectangles) (Spudich and Orcutt, 1980a; Christensen and Smewing, 1981). Fields for zones II and III are determined from the lower crustal seismic velocities and uncertainties (this chapter).

Of the two possible explanations for the origin of the high-velocity layer, the melt model is favored by the widely accepted existence of magmatic underplating immediately underneath the stretched lower continental crust of volcanic margins (White and McKenzie 1989). However, for a crystallized melt product to have a velocity as high as 7.5 km/s, a high asthenospheric temperature is required, which for a stretching factor of  $>5$  would have produced a minimum thickness of 20 km. Such a large thickness is not observed. A melt model may also produce volcanic flows (e.g., seaward-dipping reflectors), a feature absent from reflection profiles across the margins of the Labrador Sea (Balkwill 1987; Keen et al. 1994b). In addition, a melt model cannot explain why the observed high-velocity layer is offset seaward by 80 km from the continental slope, where underplating generally occurs.

For the above reasons, I suggest that the observed high-velocity lower crust more likely represents serpentinized mantle. The observed  $V_P - V_S$  for the lower crust of Zone II (Figure 4.13) is consistent with the theoretical curve for  $\sim 15\%$  serpentinization. Above the seismic Moho, the modified mantle has been "undercrusted" to form the high-velocity lower crust (Boillot et al. 1989a, b). A small amount of serpentinization also possibly exists within the upper mantle layer, increasing its vertical velocity gradient and producing a strong refracted arrival  $P_n$  (Figure 4.6). The basement high, bordering Zones I and II, may represent a serpentinite diapir. It lies on top of the most highly serpentinized lower crustal layer where the velocity is lower than on either side (Figure 4.10a). Compared with the serpentinized ridge off the Galicia margin (Boillot et al. 1992), however, greater

along-strike variations probably exist for the serpentinite diapir off SW Greenland, as evidenced by its reduced elevation on a nearby deep multichannel reflection profile (Keen et al. 1994b).

#### 4.5.3 Processes of Crustal Thinning

The major characteristics of the upper crust in Zone II are its low-velocity (4.0-5.0 km/s), its small thickness (~2.5 km), its block-faulted pattern, and the irregular magnetic anomalies it generates (Figure 4.12). It cannot be oceanic crust (i.e., extruded melt product) if the interpretation of the underlying layer as serpentized peridotite (as opposed to a plutonic intrusion) is correct. I suggest that the upper crust in Zone II is composed of thinned and faulted upper continental crust. An approximate calculation of the stretching factor  $\beta$  based on the surface geometry of the tilted blocks suggests  $\beta=2-3$  for this part of upper crust (Figure 4.2). From this value, the thickness of the preexisting continental crust is estimated to be 5-8 km. This is compatible with refraction data along the shelf of SW Greenland (Chapter 3) and the depth of a reflector across the SW Greenland shelf in a nearby deep multichannel reflection profile (Keen et al. 1994b).

If the above interpretations are correct, the lower continental crust has been removed from this margin and must presently exist under the conjugate margin of Labrador. In the most basic form, this result suggests a simple shear model for the initial rifting (Wernicke 1985; Lister et al. 1986; Wernicke and Tilke 1989), in which the SW Greenland margin acts as an upper plate and contains no associated magmatism. The very low-angle normal fault responsible for the final breakup might have followed the present

curvature of the Moho under the continental slope, turning almost horizontally at the base of the thinned continental crust for about 100 km (Figure 4.12). It is not known if the original lower continental crust beneath this fault was affected by syn-rift ductile creep, in addition to or instead of simple shear. To construct a complete rifting scenario, seismic data on the conjugate Labrador margin is required.

#### 4.6 Conclusions

Using wide-angle data and coincident normal-incidence seismic reflection data, I have obtained a detailed two-dimensional velocity model for the complete crustal transition of the sediment-starved, SW Greenland continental margin (Figure 4.10a). When converted to density values, this seismic model offers a reasonable fit to the gravity data (Figure 4.12). Interpretation of upper crustal structures is also compatible with the change in magnetic anomalies and character of basement structures.

The SW Greenland continental margin is characterized by three distinct zones:

1. In Zone I, the 30-km preexisting continental crust is thinned abruptly to a thickness of ~3 km. This thinned crust is faulted and extends seaward to intersect a basement high, interpreted as an elevated serpentized peridotite.
2. In the continent-ocean transition (Zone II), the 4-5 km lower crust extends for 50-80 km and exhibits a bulk  $V_p$  of  $7.5 \pm 0.1$  km/s and  $V_s$  of  $4.0 \pm 0.2$  km/s. This is interpreted as undercrusted serpentized peridotite. The faulted upper crust for this zone has a very low-velocity of 4.0-5.0 km/s and possibly represents block-faulted upper continental crust.

3. The lower crust in Zone III has  $V_p$  of  $\sim 7.2$  km/s and  $V_s$  of  $\sim 4.1$  km/s. Such velocities possibly extend seaward to the extinct ridge axis, and correspond to magnetic anomalies younger than Chron 28. Seafloor spreading likely did not start until Chron 28.
4. A simple shear model without magmatism is favored for the initial rifting of the Labrador Sea. The SW Greenland margin possibly acts as an upper plate margin, while the lower plate lies on the conjugate Labrador margin. Seismic data across the conjugate margin of Labrador are needed to further test the rifting model, which is the subject of Chapter 5.

## **Chapter 5. The Continent-Ocean Crustal Transition Across the Labrador Margin**

### **5.1 Introduction**

A unique determination of rifting mechanisms on nonvolcanic, passive continental margins has remained elusive. This is exhibited not only in the dispute over pure (McKenzie 1978) vs. simple shear (Wernecke 1985; Lister et al. 1986) models (e.g. Le Pichon and Barbier 1987; Boillot et al. 1989b, 1992; Keen et al. 1989, 1994b; Sibuet 1992), but also in the uncertainty over serpentinitized undercrusting vs. magmatic underplating for the formation of a thin, high-velocity lower crust offshore in many nonvolcanic, rifted continental margins (e.g. Whitmarsh et al. 1986, 1990; Reid and Keen 1990; Pinheiro et al. 1992; Reid 1992; Chapter 4).

The best way to determine the rifting mechanism is probably to examine the detailed resultant crustal structure across the complete transition from continent to ocean on conjugate margin pairs. This can be accomplished by deep multi-channel reflection profiling and wide-angle seismic refraction methods. Although multi-channel reflection profiles have been used to re-construct crustal layering on rifted conjugate margins (Keen et al. 1989; 1994b), refraction methods have not been used to study the details of seismic velocity variations across conjugate margins.

In 1990, a 350-km-long wide-angle seismic refraction line was shot across the entire Labrador margin (Figure 5.1). This line was complemented by a coincident multi-channel reflection line (Keen et al. 1994b), one intersecting refraction line along the shelf, and one along-strike refraction line on the slope. These lines were designed to be in a conjugate position to the two refraction lines of Chapters 4 on the S.W. Greenland margin. This will facilitate a reconstruction of crust, from which it will be possible, for the first time, to delineate the rifting stage with a detailed 2-D velocity profile for both rifted conjugate margins.



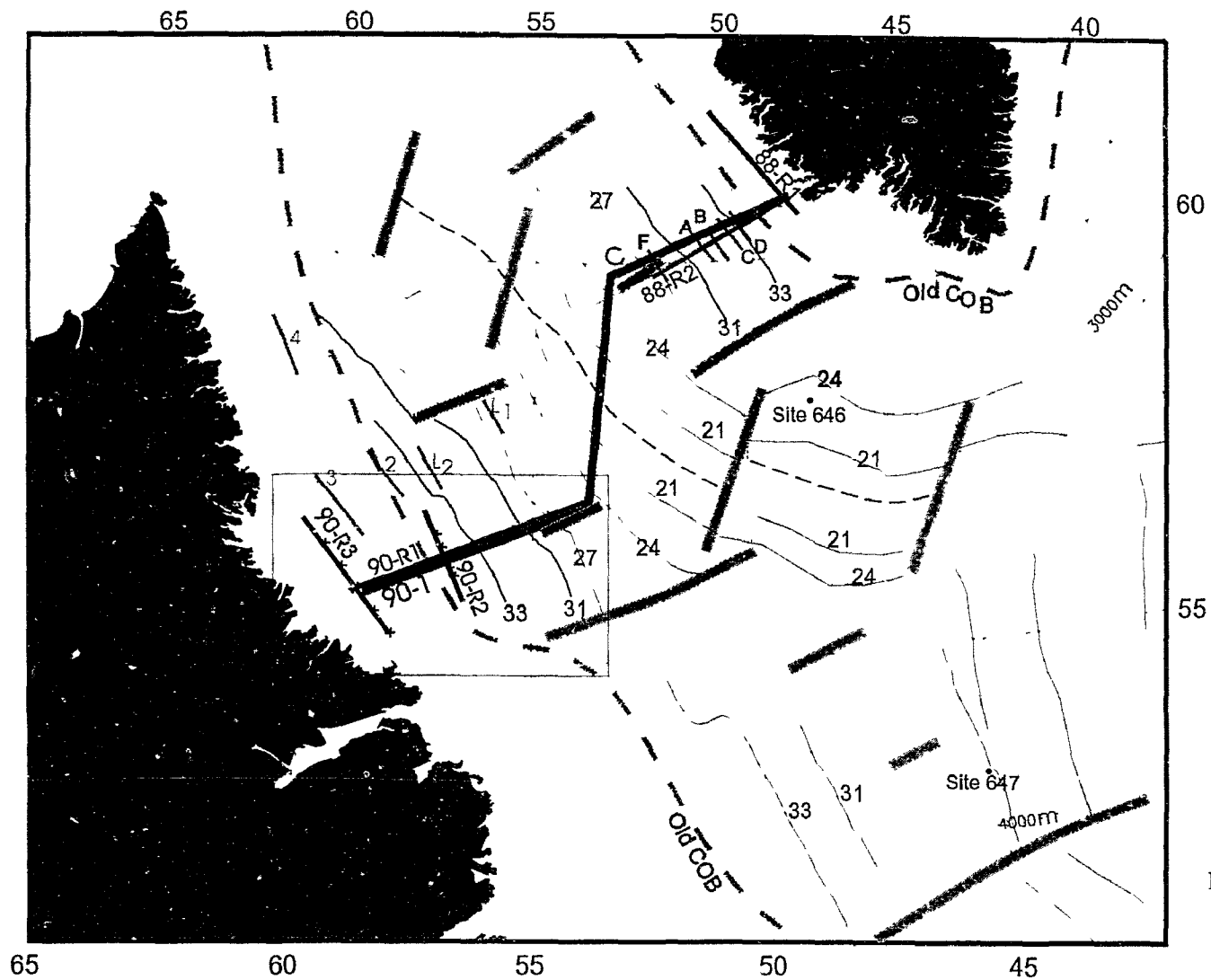


Figure 5.1a

Figure 5.1. Map of the Labrador Sea (a), showing zones with refraction lines (thick solid), bathymetry contours (in meters), chrons (solid), fracture zones (thick grey), extinct rift (thin broken), and previously defined COB (thick broken). The frame inside figure (a) shows the area zoomed in figure (b).

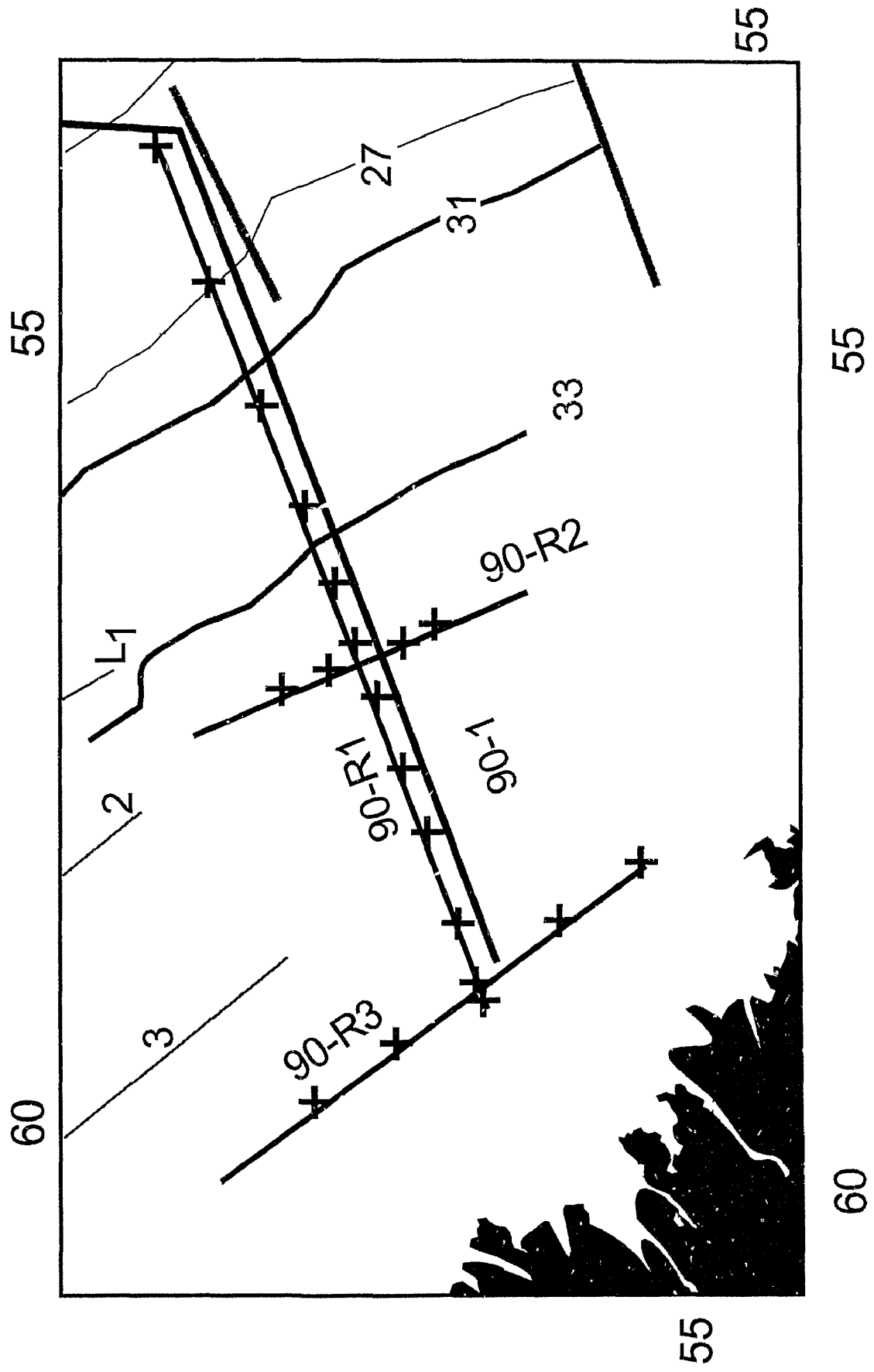


Figure 5 lb 2

Some of the major objectives of the refraction lines on the Labrador margin are:

1) To determine whether the crust under the Labrador shelf and slope represents stretched lower continental crust, as predicted by a simple shear rifting model, or is composed of both the upper and lower continental crust, which supports a pure shear model.

2) To determine if a thin layer of anomalously high-velocity lower crust, as observed in the conjugate SW Greenland margin, also exists in the Labrador margin. If so, does it represent serpentinized mantle or underplate?

In the remainder of this chapter, I will first introduce the seismic data, and then describe the details of the 2-D modeling (seismic, gravity and magnetic). This leads to a 2-D velocity and density profile for sediments and crust across the whole margin, which will facilitate a reconstruction of the full crustal section which will be discussed in the following chapter.

## **5.2 Seismic Data**

### **5.2.1 Wide-Angle OBS Data**

There are three refraction lines (90R1, 90R2, and 90R3) on the Labrador margin shot in 1990 during Hudson 90-013 cruise (see Table C.1 for OBS locations). The primary line is 90R1 which has 11 OBS, distributed over a 350 km distance across the entire Labrador margin, with a shooting interval of ~120 m. This refraction line is complemented by a recent coincident multi-channel reflection line which was analyzed independently (Keen et al. 1993). The deep velocity structures obtained from line 90R1 are tied to results from a 150-km refraction line 90R2, along-strike on the continental slope, and a 200-km refraction line 90R3 along the shelf (Reid 1994). A total of 21 OBS were used, recording on cassette tapes the time and seismic signals from hydrophone and 4.5 Hz vertical geophones. These analog data were digitized and interpolated to a fixed sampling rate of

100 samples per second. Corrections are made for OBS clock drift and shot delay. The corrections for the OBS mis-positioning (both lateral and off-line) and timing are performed by comparison with computed water wave. Before plotting of the data, further processing includes band-pass filtering of 4-8 Hz, clipping of high amplitudes, gain that increases linearly with horizontal distance, and coherency mixing (Chapter 4) of 5 adjacent shots scanned at velocities of 2.5-8.5 km/s for  $P$  waves and 2.5-4.5 km/s for  $S$  waves.

Refraction line 90R3 is along-strike on the continental shelf, showing good  $P$  and  $S$  waves and has been analyzed and modeled by Ian Reid at Bedford Institute of Oceanography (Reid 1984). In this thesis, I will only present the 2-D seismic model slightly modified from his original model. I will then present the other along-strike refraction line 90R2 which is on the continental slope. Given the controls from these two lines, I will present the wide-angle data from the 11 OBS of line 90R1, compared with their 2-D synthetic seismograms. In the modeling on line 90R1 I use the coincident multi-channel reflection profile (Figure 5.2) to control the sediment structure and basement topography.

### **5.2.2 Modeling Procedures for Wide-Angle Data**

I tried two methods for the 2-D modeling of the refraction data. The first incorporates an interactive modeling program developed by Ian Reid. Each layer is simply specified by its top boundary, one velocity value at this boundary and one gradient value within this layer. Running interactively on a workstation, the program simultaneously displays the observed seismic data overlain with computed travel-time curves, as well as the 2-D velocity model with selected ray paths. Adjusting the velocity/boundary will modify the computed travel-time curves and traced rays in nearly real time. All these properties of the program enable a fast manipulation and modeling of a large amount of wide-angle data as is the case on line 90R1.

After obtaining a semi-final 2-D model using Reid's program, the model is converted to the same format (SEIS83) as used in Chapter 4 for the wide-angle data across the SW Greenland margin. This approach has two main reasons, i.e. to better describe the complex 2-D structure with velocity contours and to image both conjugate margin structures using the same method. Unlike Reid's program, structural changes in SEIS83 programs are specified by layers with boundary relief and velocity values at user-specified node points. Therefore, almost any form of velocity structure can be included in the modeling.

Both programs have their pros and cons. The advantage of Reid's program is in its simplification of model input and interaction. The disadvantage of this program, however, is that it does not allow a single layer to have lateral velocity variations. In addition, vertical velocity changes can only be specified by a linear gradient with depth. Although these can be overcome by adding more layers into the model, for complicated structures, this would generate a block-like pattern which is not representative of the real situation. On the other hand, these problems do not exist in the SEIS83 programs, which are capable of generating smoothly varying velocity contours and abrupt boundaries. In addition, SEIS83 is designed for computing a variety of seismic rays, and therefore it is easy to include multiples and *S* waves in the computation. The disadvantage of SEIS83 is that many variables are required for inputting the velocity values at node points, which slows down the modeling process. In addition, because it uses two-point ray-tracing for selecting rays at each receiver, the ray-tracing program is slow. When running on a HP Appolo 700 workstation, it typically takes >3 CPU minutes to complete a full calculation for one OBS.

In the modeling of the wide-angle data for the Labrador margin, the travel-time of a specific seismic phase is used as the major constraint, rather than its amplitude. This is

## Time Section X-Labrador Margin

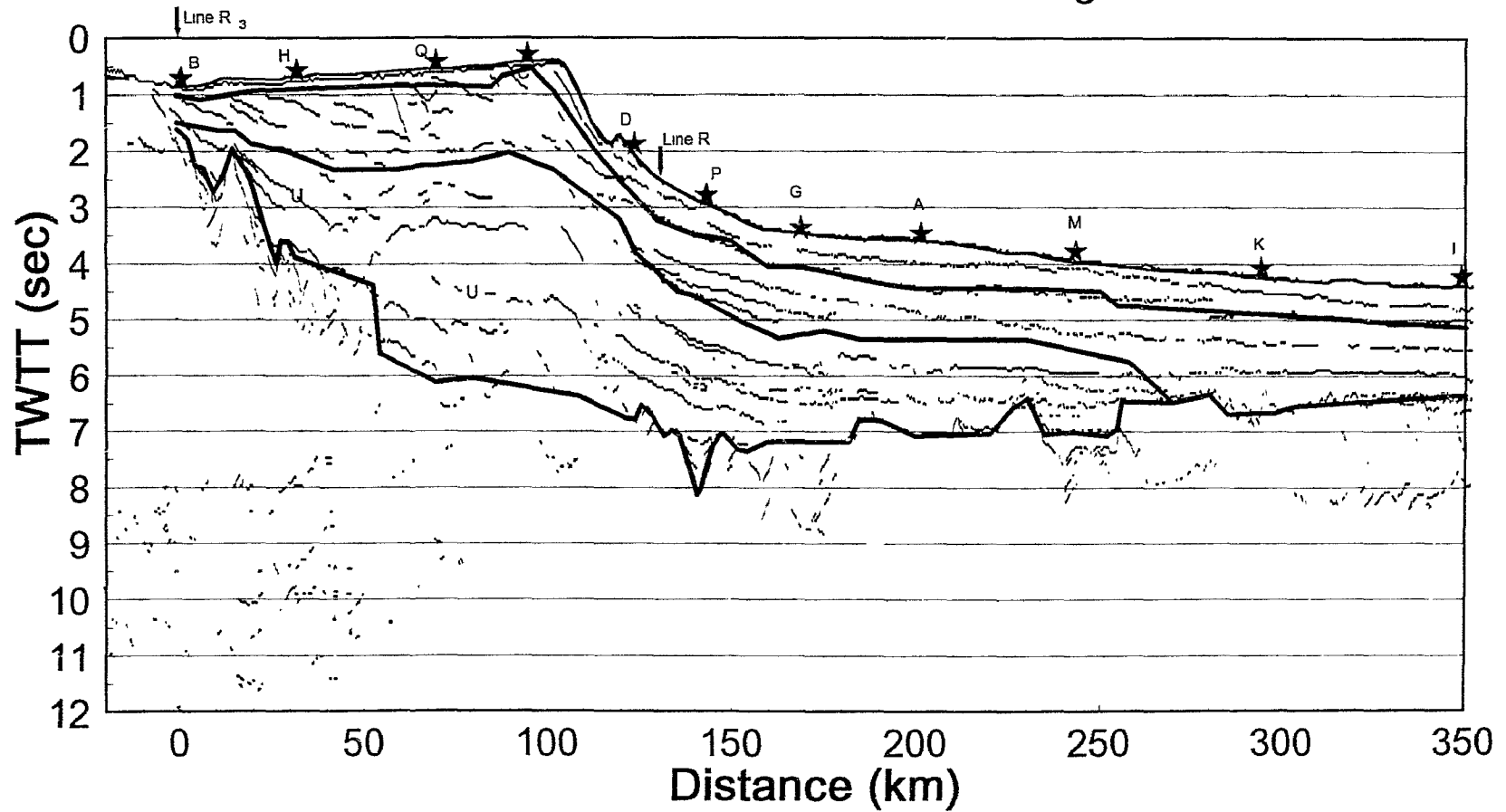


Figure 5.2. Line drawings from coincident multi-channel reflection line 90-1 (Keen et al. 1994b). Horizontal distance is consistent with what is used for wide-angle modeling.

because I am mainly interested in the gross crustal velocity structures rather than smaller details. To quantify this, let us imagine a wavelet whose frequency spectrum is centered at 5 Hz. When this wavelet is traveling through crust with a velocity of 6 km/s, its wavelength is 1.2 km. This means that small basement complications on the scale of 0.3-3 km will influence the shape of the amplitudes but have little effect on the computed travel-times for primary reflections and refractions. On the other hand, these small structural details are sometimes not resolvable by the coincident reflection profile because of the overlying thick sediments (Figure 5.2). Therefore, it is difficult to model the amplitudes of crustal phases on the Labrador margin. This is different from the SW Greenland margin where only thin sediments exist (Chapter 4). Therefore, in the Labrador margin I mainly use travel-time information to model each OBS rather than trying to minimize the amplitude misfit as done for the SW Greenland margin.

### **5.3 Two-dimensional Seismic Modeling**

In the following description of wide-angle modeling and accompanying figures (Figures 5.5-21), two horizontal scales are used. Ranges represent the distance between shots and a particular OBS, while distances refer to the positions of the OBS and shots on the 2-D model.

#### **5.3.1 Line 90R3: On the Continental Shelf**

The OBS data show a two-layer crustal structure underlying a thin sheet of sediments along the shelf (Figure 5.3). A clear velocity division at a distance of 80 km is evident in the upper crust. North of this point, the upper crust is described by a velocity of 6.3 km/s at the top (~0.9 km depth) with a downward gradient of  $0.05 \text{ s}^{-1}$ . To the south, the upper crust thins and velocity decreases to 6.0 km/s at the top (3-4 km depth) with the same gradient. This velocity division is compatible with the upper crustal structure on the SW Greenland shelf (Chian and Loudon 1992 or Chapter 4) and represents a tectonic

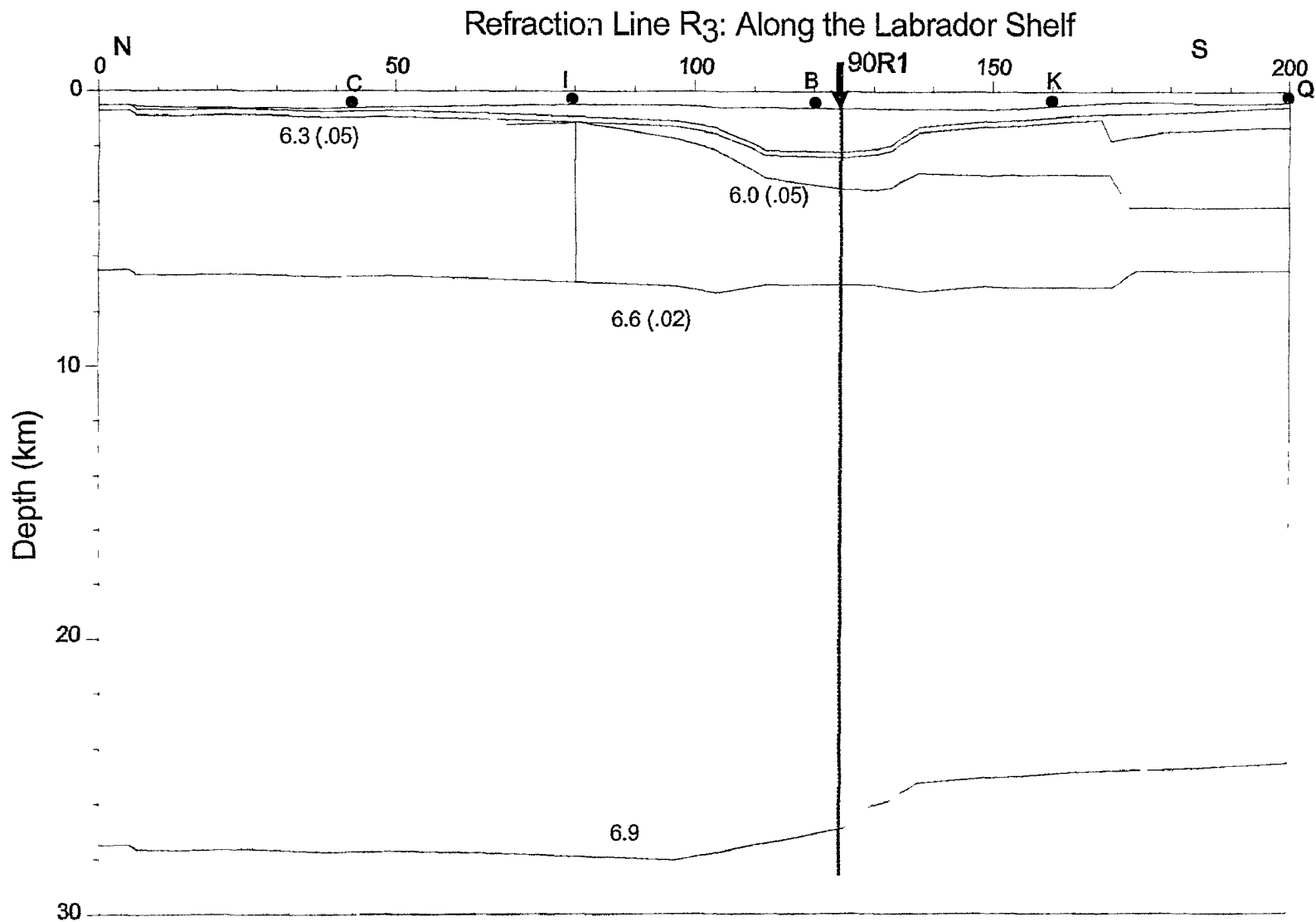


Figure 5.3. Crustal velocity model for refraction line R<sub>3</sub>, modified from I. Reid (unpublished data).



boundary between the Nain (Archean) and the Makkovik (Proterozoic) provinces. The difference across this tectonic boundary becomes minimal in the lower crust (below 6.5-7 km depth). The velocity of the lower crust is 6.6 km/s with a downward gradient of  $0.02 \text{ s}^{-1}$ . Unlike the lower crustal structure in the SW Greenland margin, there is no seismic evidence for any velocity boundary below 7 km within the lower crust. The Moho is situated at a depth of 29 km in the north and 27 km in the south. The cross-margin line 90R1 intersects line 90R3 at a distance of 123 km.

### **5.3.2 Line 90R2: On the Deep Sediments**

Refraction line 90R2 is oriented along strike on the continental slope of Labrador. The purpose of this line is to obtain a well-controlled velocity structure of the thick sediments and thinned continental or transitional crust, which will provide a constraint on the structure of the cross line 90R1. The available data include 4 OBS (K, Q, C and I) and a coincident single-channel reflection profile (Figure 5.4). The reflection profile contains useful data from only the top part of the sediments (TWTT of <4 sec; Figure 5.4), and is used for specifying the first three layers in the 2-D model. Deeper velocity structures are obtained from modeling the sediment and basement arrivals on the OBS. Since OBS Q and C are the closest to (17 and 12 km away, respectively) and on the opposite sides of line 90R1, these two OBS are most useful for 90R1 and are therefore most carefully modeled. The results from these two OBS also fit data for the other two more distant OBS (K and I; Figures 5.5-6) which are located farther away from 90R1 (~28 km), although slight local misfits exist for the shallow sediments (OBS K) and the depth of the basement (OBS I).

Velocity in the sediments is well-defined by a strong refracted phase (P1), and a wide-angle reflected phase (P2P) extending from a range of 10 km to more than 50 km at OBS I and Q (Figures 5.6-7) and to 30 km at OBS C (Figure 5.8). The water multiples

(P12 and P2P2) of these two phases are equally well-defined in OBS Q and I. This is best modeled by the existence of a thick sediment layer with a velocity of 3.0 km/s at 4.5 km increasing linearly with depth to 3.6 km/s at the sediment/basement boundary (8.0 km). Beneath the sediments, a two-layer structure is evident for the crust. Modeling requires that the upper crust has a relatively low-velocity of 4.8 km/s with a gradient of  $0.1 \text{ s}^{-1}$ . A higher velocity for this layer would cause the P2 phase to arrive too early between ranges of 22 and 28 km at OBS Q (Figure 5.7). For the lower crust, there are ambiguities as to whether the wide-angle reflection from the Moho is the discontinuous phase labeled PmP or the later phase labeled P3'. In the latter case, the PmP' can be fit but it is difficult to fit Pn with a reasonable crustal model which can be tied to line 90R1. In the first case, however, the modeled lower crust matches well with the cross line 90R1, starting with a velocity of 6.2 km/s at 10.5 km which increases to 6.7 km/s at 14 km (the Moho). Therefore, this first model is adopted. The final velocity model is shown in Figure 5.9.

### **5.3.3 Line 90R1: The Wide Crustal Transition from Continent to Ocean Across the Labrador Margin**

Refraction line 90R1 has 11 OBS deployed over a distance of 350 km across the Labrador margin. OBS B, H, Q, C are situated in sequence from the inner shelf to the shelf break (Figures 5.10-13). Major constraints on velocities are obtained from OBS H and Q, which show good data quality. Interpretation of data for OBS B is complicated by severe basement relief. OBS C lies in shallow water, close to the shelf break and is noisy, possibly due to water currents.

OBS D and P (Figures 5.14-15) lie on the continental slope and have good data quality. Although structures underneath these OBS are complicated, there is good control from the reflection profile (Figure 5.2) of Keen et al. (1994b) and from the crossing

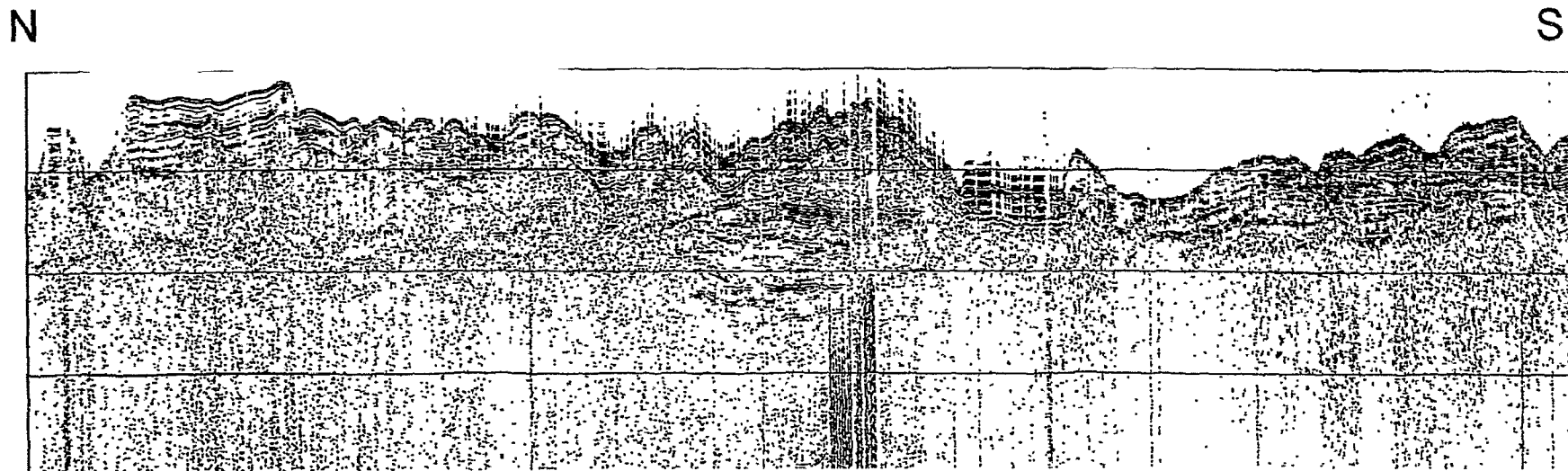


Figure 5.4a

Figure 5.4 (a) Single-channel reflection profile along refraction line 90R2. (b) Interpreted Depth section for this reflection line which is used in the subsequent wide-angle modeling.

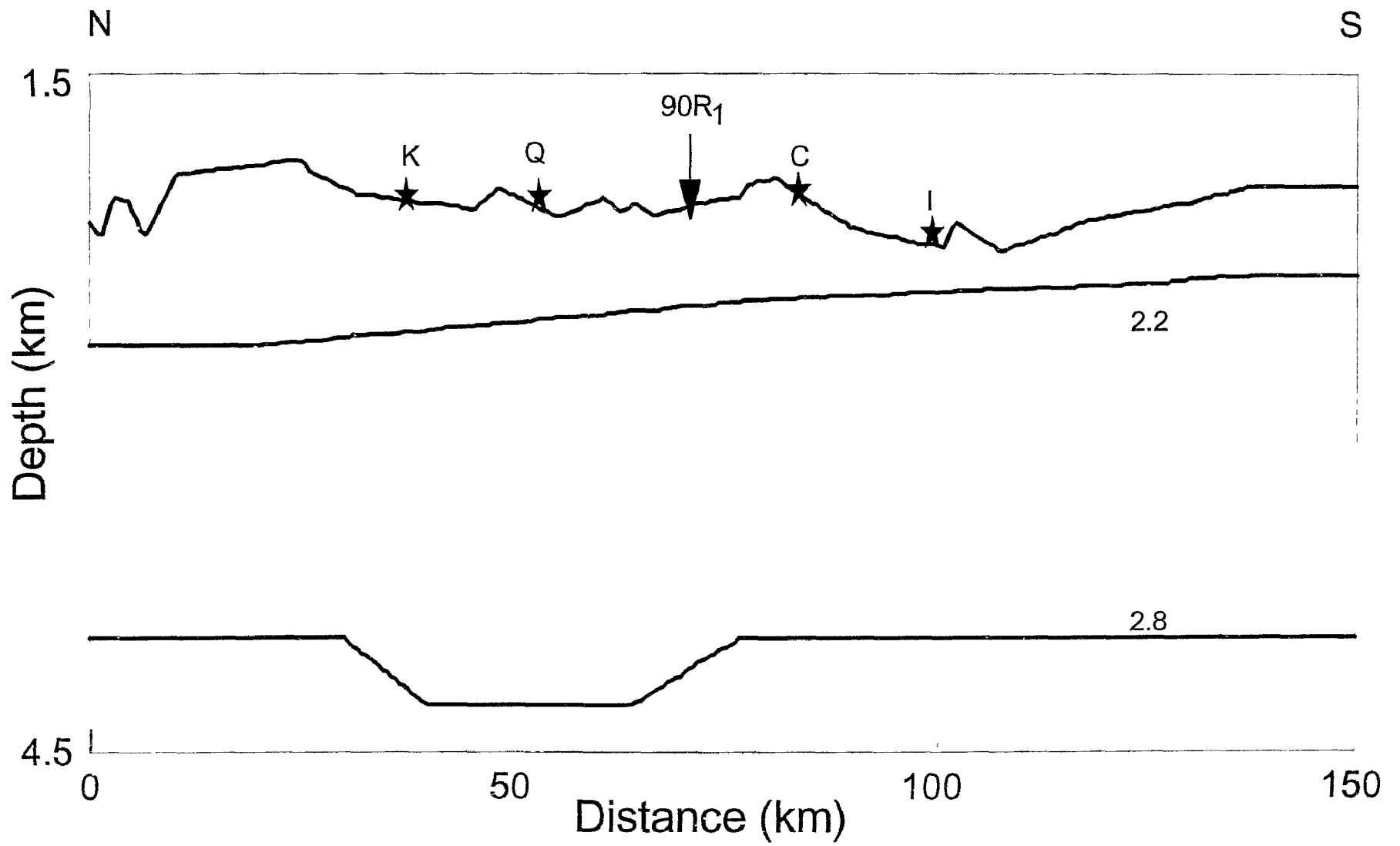


Figure 5 4b

Hud 90-013 R2: OBS K

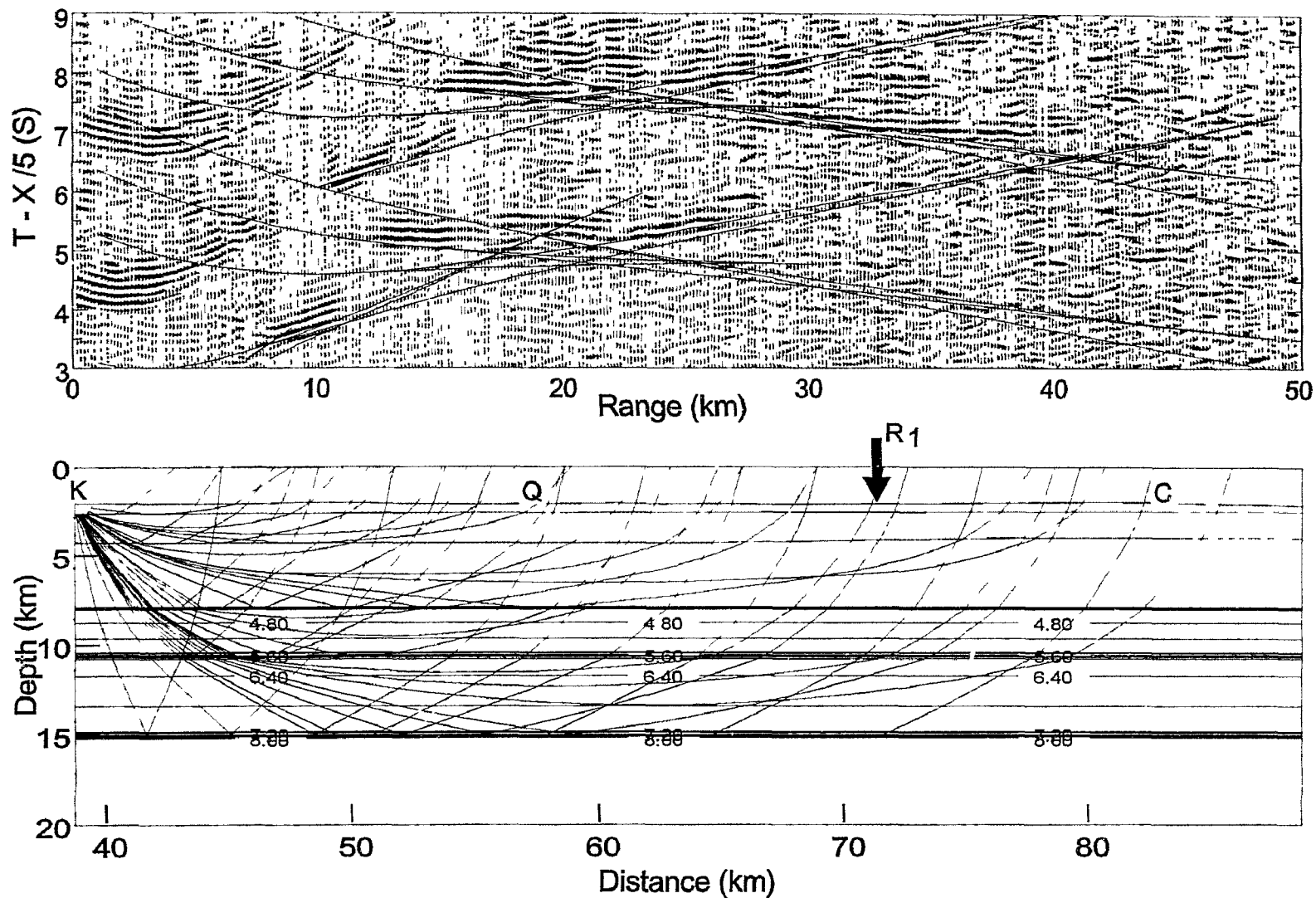


Figure 5.5. Top: wide-angle profile from OBS K on line 90R2. Bottom: traced rays overlain onto the velocity model

Hud 90-013 R2: OBS I

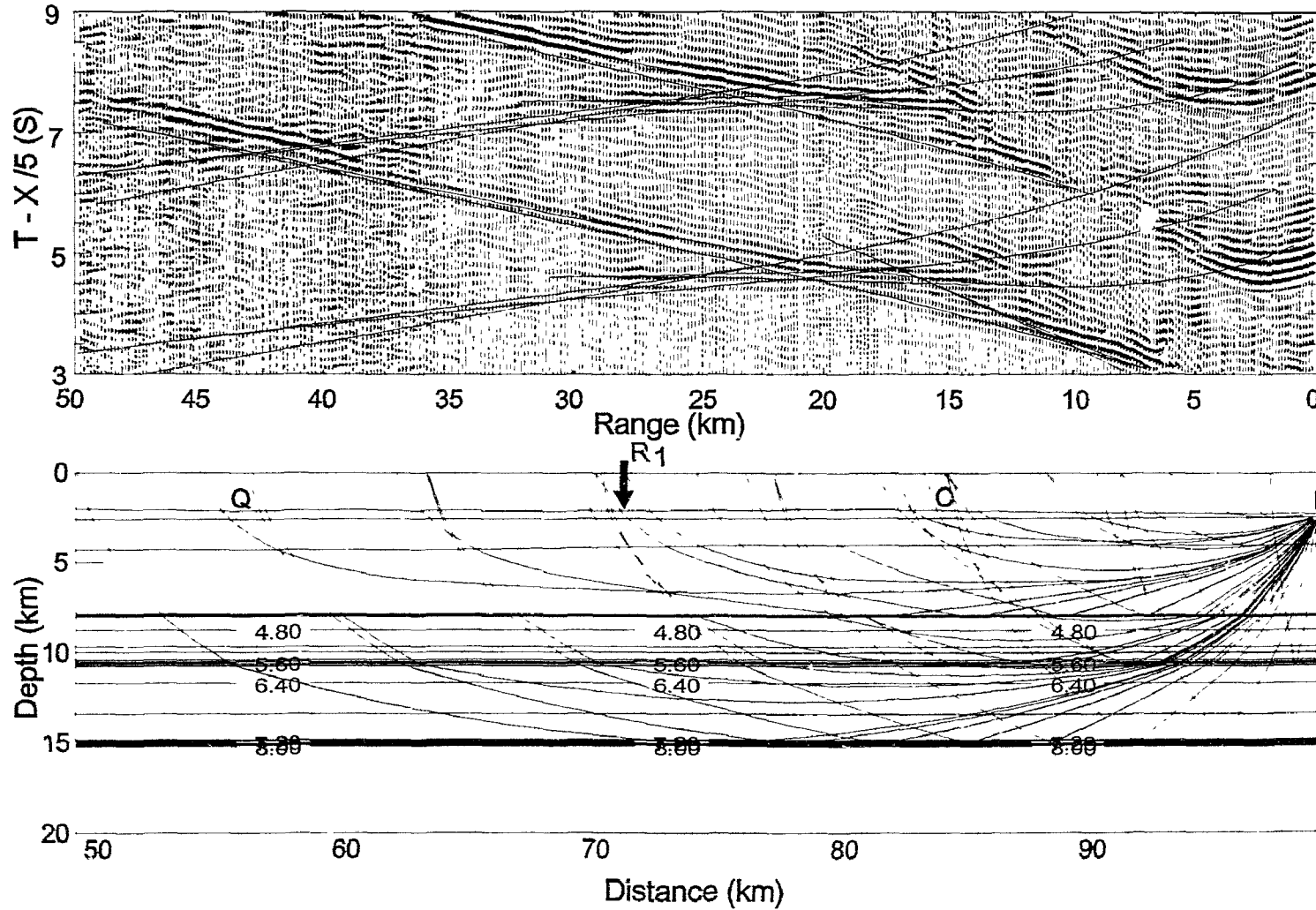


Figure 5.6. Top: wide-angle profile from OBS I on line 90R2. Bottom: traced rays overlain onto the velocity model.

Hud 90-013 R2: OBS Q

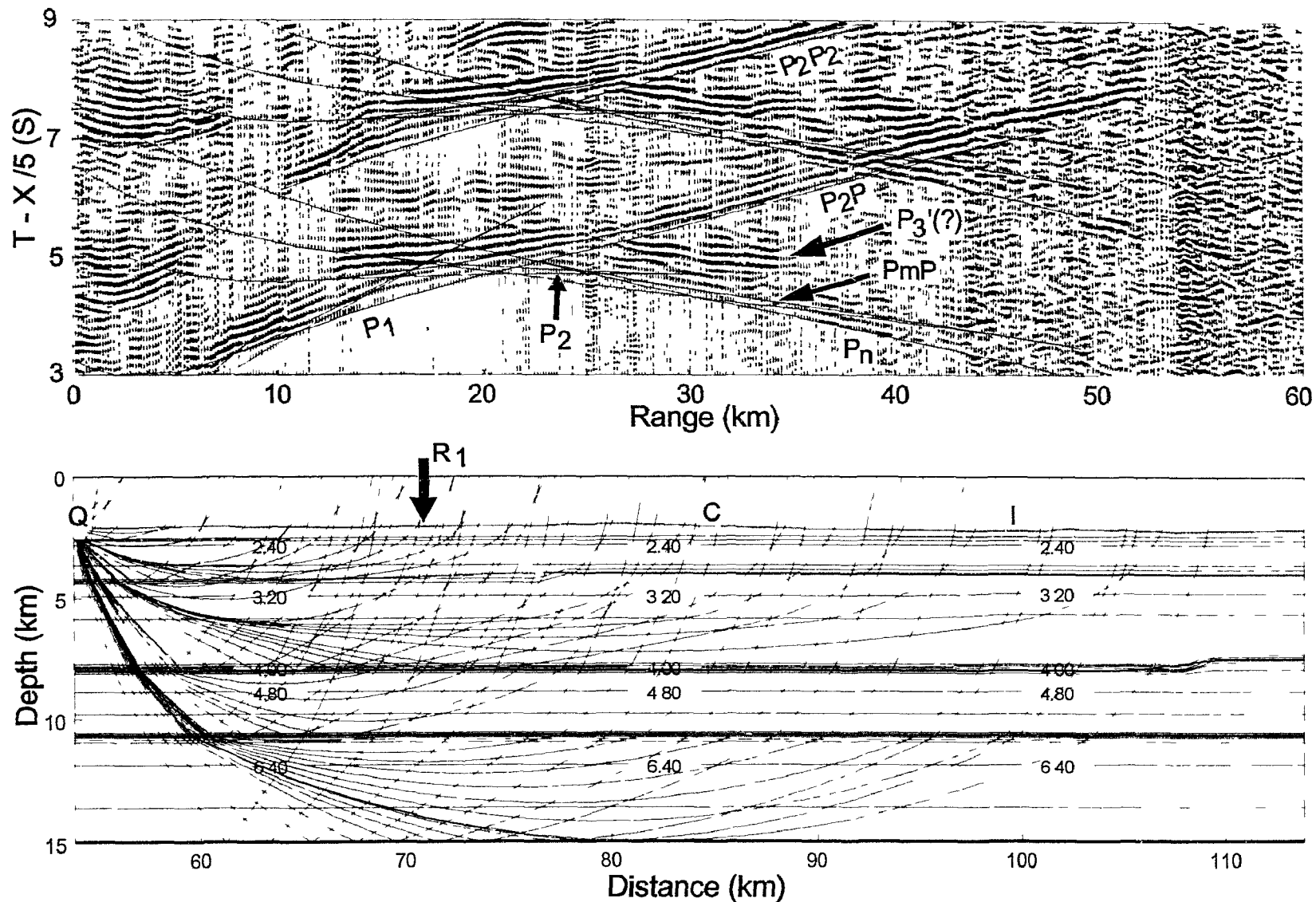


Figure 5.7 Top: Wide-angle profile from OBS Q on line 90R2. Bottom: Traced rays overlain onto the velocity model.

Hud 90-013 R2: OBS C

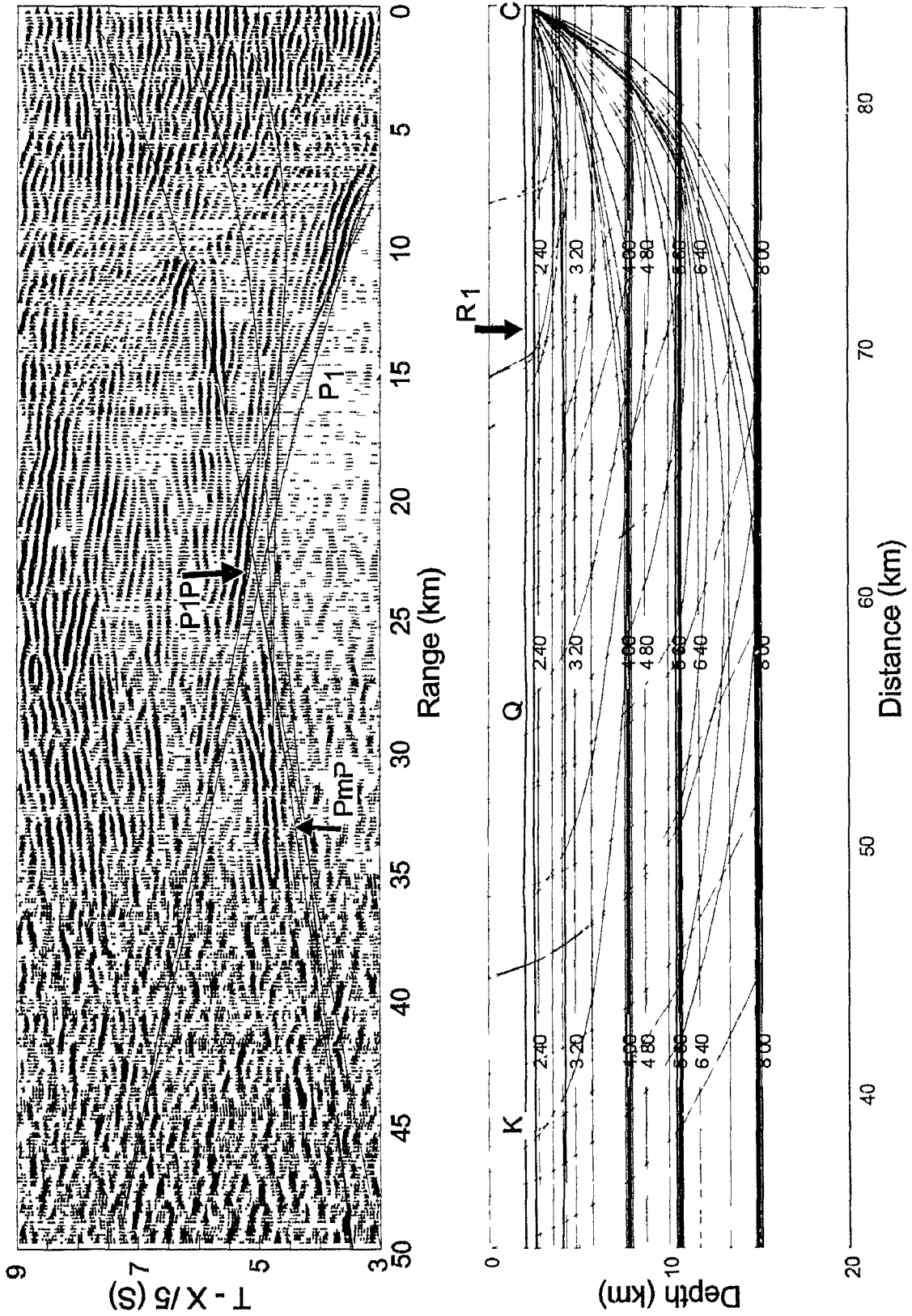


Figure 5.8 Top Wide-angle profile from OBS C on line 90R2 Bottom traced rays overlain onto the velocity model



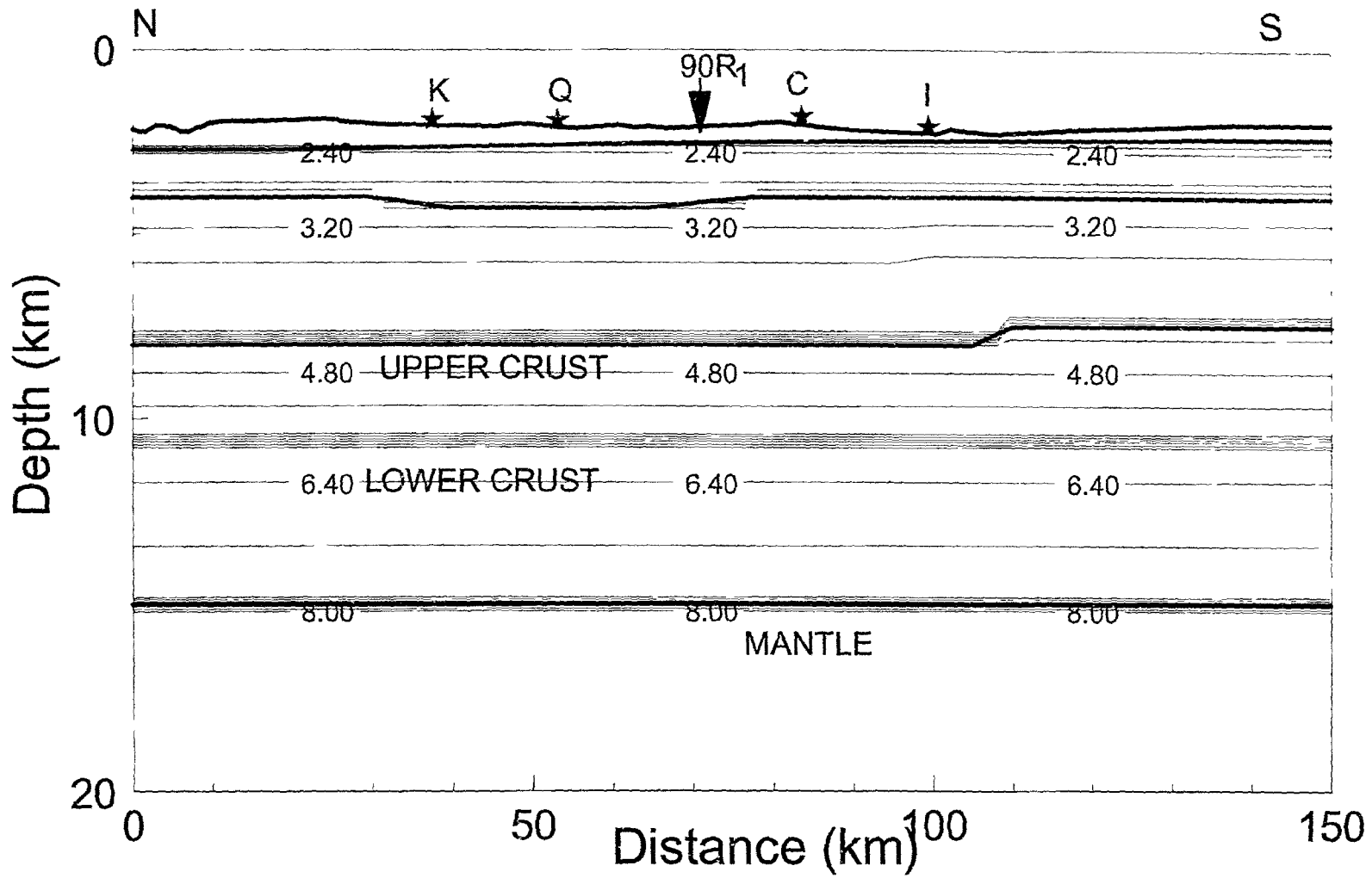


Figure 5.9. 2-D velocity modeling of line 90R2, showing contours of  $V_p$  every 0.2 km/s. Filled stars represent locations of OBS K, Q, C, and I. Vertical arrow indicates the point where line 90R1 intersects.

refraction line 90R2, which intersects line 90R1 between OBS D and P. Further seaward, where a "transparent" crust is found on reflection profile 90-1, OBS G (Figure 5.16) shows only the water multiple of the crustal arrivals, whereas OBS A (Figure 5.17) shows good crustal arrivals even at large ranges (<70 km). Adjacent to the 1-km basement jump at 250 km, OBS M (Figure 5.18) shows very poor data. On top of the smooth basement, the last two OBS (K and I; Figures 5.19-20) at the eastern end of the line show very good data quality, including clear water multiples and *S* waves.

The sedimentary line drawings of the reflection data (Figure 5.2) are used to construct a preliminary 2-D velocity model for modeling the OBS data. In doing this, the two-way travel-time (TWTT) is converted into depth using an assumed velocity-depth relationship. This relationship is later updated during the wide-angle modeling. This update is based on the assumption that the TWTT from reflection profiles is correct. Therefore, when a reasonable 2-D velocity model is obtained, the boundaries in the model are converted into TWTT and adjusted according to the misfit to the reflection data. In addition, the interpretation of basement reflections is also updated during the modeling, especially when they are unclear under the thick pile of sediments (9 km) on the shelf. The solid lines in Figure 5.2 are the sediment and basement boundary lines, converted from the final 2-D seismic model using the final velocity values for the sediments. It can be seen that the seafloor matches perfectly with the time section. The two sediment boundaries in the 2-D model follow closely with reflective events, with exceptions under the shelf where the events are more discontinuous, and in case of phase changes at 270-280 km.

In all the following plots of OBS data, minus ranges correspond to the distances from the OBS westward to shot points. Positive ranges represent shot points to the east of the OBS. For simplicity, only travel-time curves and ray paths are plotted together with observed seismic profiles in these figures.

### Seismic Phases

Useful wide-angle seismic phases observed in the OBS refraction experiment can be broadly divided into five categories, based on the different layers through which the waves travel. In doing this, I use the same labeling convention for all the data on line 90R1, regardless of the crustal type, to avoid ambiguity. The first is the direct water wave (Pw), traveling from the surface through the water column to the OBS on the seafloor. Pw is used for adjusting the OBS positions and for testing the correctness of the shot timing around each OBS. The second group consists of phases traveling through the sediments as refractions (P1) or wide-angle reflections (P1P) from the sediment/basement interface. Rays producing this phase may travel through several layers in the sediment column, especially under the shelf where up to 9 km of sediments are deposited. It is generally easy to distinguish sediment phases from the third group: upper crustal phases P2 (refractions) and P2P (reflections). This is because sediment arrivals are usually aligned at a much lower apparent velocity. The fourth group is P3, refracted from the lower crust, and PmP, reflected from the Moho. The last phase is the mantle refraction, Pn, which has the highest apparent velocity of ~8.0 km/s, and is commonly distinct from crustal phases.

Of the many multiples that are recorded, water and sediment multiples are usually the strongest. As usual, water multiples are denoted by appending a subscript "2" to the notations for corresponding first-arrivals, and sediment multiples are denoted by appending a prime (') to the end of the notations for first-arrivals. This convention follows the notation of White et al. (1976) and Chapter 4. While it is possible that water multiples can be formed either at the source or receiver positions, it is found that most of the observed water multiples on line 90R1 were formed at the OBS receivers. This is most evident from OBS D (Figure 5.14) at the continental slope where water depth for each shot varies dramatically. From the figure it can be seen that the water multiple from crust (P12) between ranges of -28 and -10 km is closely parallel to its first arrival. At these ranges, the shots were in shallow water. For ranges >10 km, shots have water depth of >2 km. The travel-time delay is, however, the same for both (1.8 sec).

#### OBS B

OBS B (Figure 5.10) is located at the crossing point between lines 90R1 and 90R3. The structure underneath the OBS is controlled by line 90R3. The amplitude profile shows clear upper crustal phase (P2) at ranges from 0 km to 60 km to the east of the OBS. Unfortunately, this phase is distorted by severe basement relief (Figure 5.10b) and therefore not able to be accurately modeled. Between ranges of 170 and 230 km, there is a strong Pn phase which may be related to the shape of the Moho at ~30 km.

#### OBS H

This OBS (Figure 5.11) records well-defined refracted phases P1, P2 and P3, and reflected phase PmP. Among them, crustal and mantle phases are all distorted by the

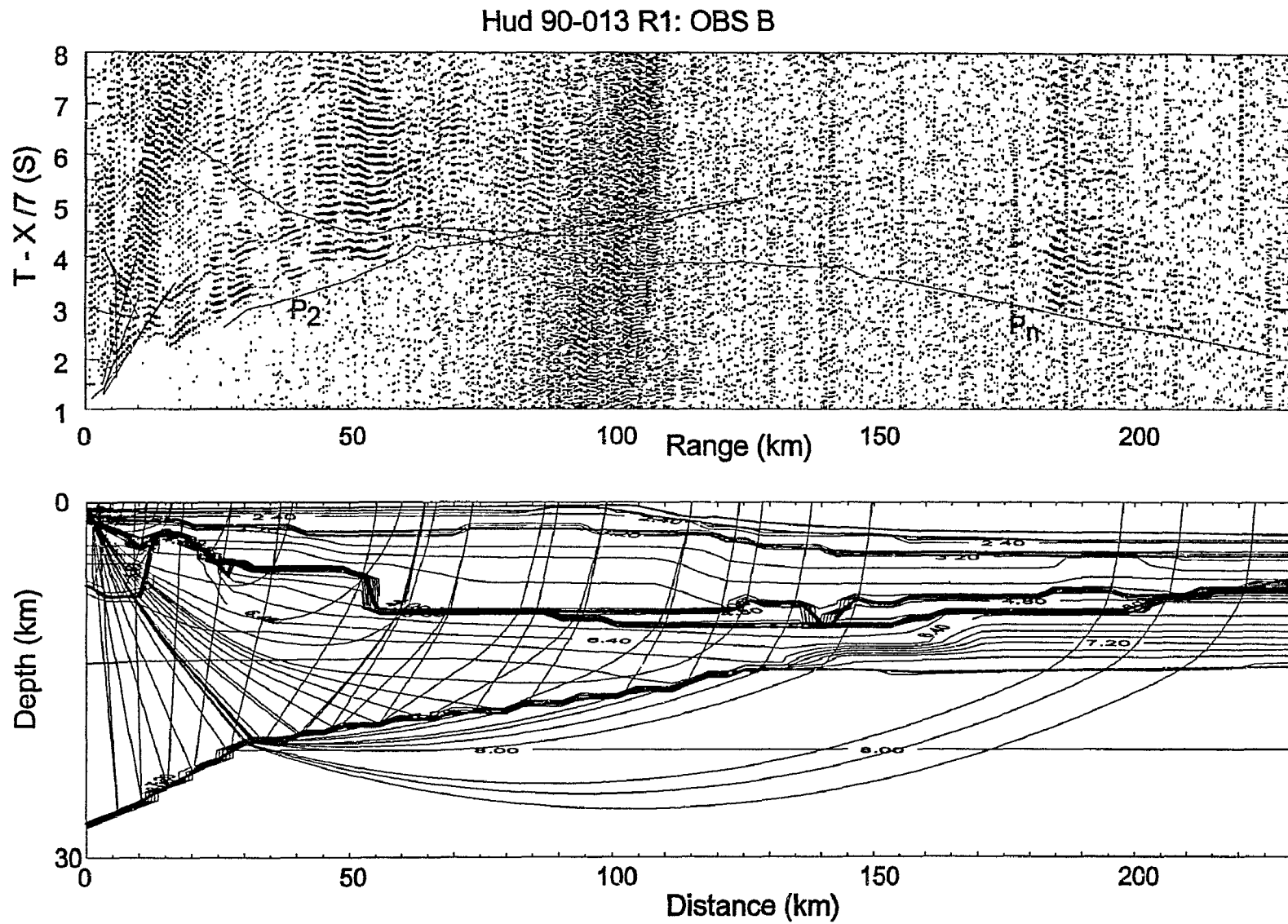


Figure 5.10. Top: Wide-angle profile from OBS B on line 90-R1. Bottom: traced rays overlain onto the velocity model.

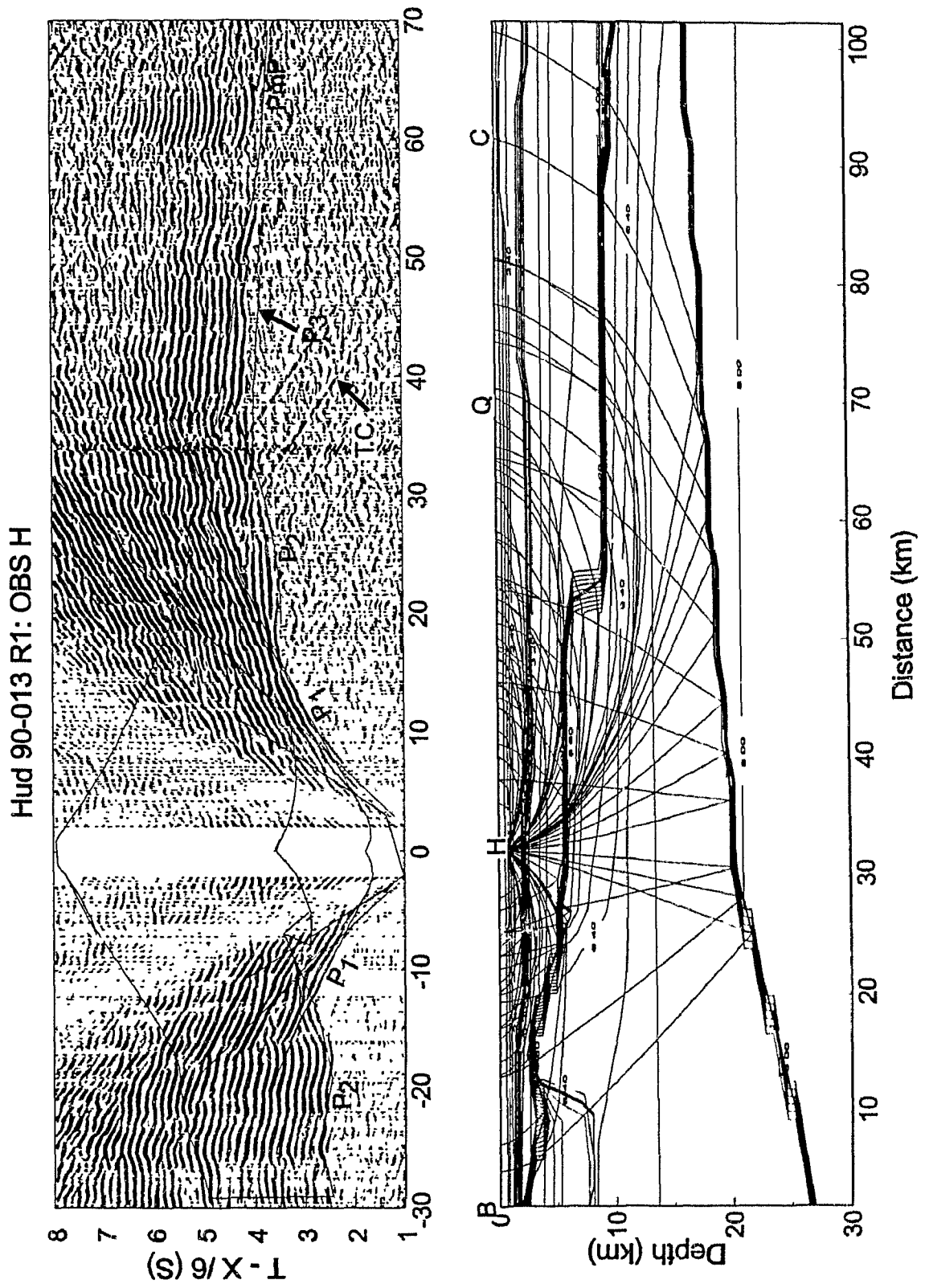


Figure 5 11 Top: Wide-angle profile from OBS H on line 90-R1. Bottom: traced rays overlain onto the velocity model.

complicated 2-D structure. Between -10 km and -30 km range, the curved phase (P2) is well modeled by the existence of a high-velocity (6.4 km/s) intrusion between distances of 15 and 20 km in the 2-D model. This feature is supported by the sub-crustal reflections in the reflection profile (Figure 5.2). To the east of the OBS, between 20 and 30 km range, the P2 phase again forms a concave shape, modeled by a sharp basement deepening of 3 km at 52 km in the model. This feature is supported by the reflection data which show a change of reflective pattern from faulting to continuous layering. Between 38 km and 50 km range, a strong and continuous phase P3 defines the crustal velocity as 6.2-6.9 km/s with varying vertical and horizontal gradients as described by the velocity contours in the final model (Figure 5.11b). PmP is mainly visible at 55-70 km range, modeled by a Moho at a depth of 18 km at a distance of 67-77 km in the structural model. For distance of <67 km, the Moho depth is determined by gravity modeling which will be discussed later.

#### OBS Q

The sharp basement deepening at 52 km of the model, as seen from OBS H and reflection profile, is also expressed in a time shift of 0.3-0.4 sec for ranges of -40 km to -22 km at OBS Q (Figure 5.12). Despite the crustal complexities to the west of OBS Q, the travel-time and slope of the lower crustal phase, P3, which is strong at ranges -30 km to -20 km, is well modeled. To the east, refractions from the thick (~9 km) sediments, P1, is not disturbed by crustal arrival (P1P) at positive ranges and is clearly recognizable at ranges up to 32 km. The modeling of this clear P1 phase, as well as the same phase at negative ranges, indicates that the velocity in the lower part of sediments has a gradient between 3.2 km/s at 2.5 km depth and 4.0 km/s at 9 km depth. The reflection from the sediment/basement interface (P1P) arrives much later than P1 due to the large sediment thickness. To model P1P, I referenced the coincident reflection profile which shows a few strong reflectors fading out below a TWTT of 5.5-6.0 sec (Figure 5.2). This gives a few

Hud 90-013 R1: OBS Q

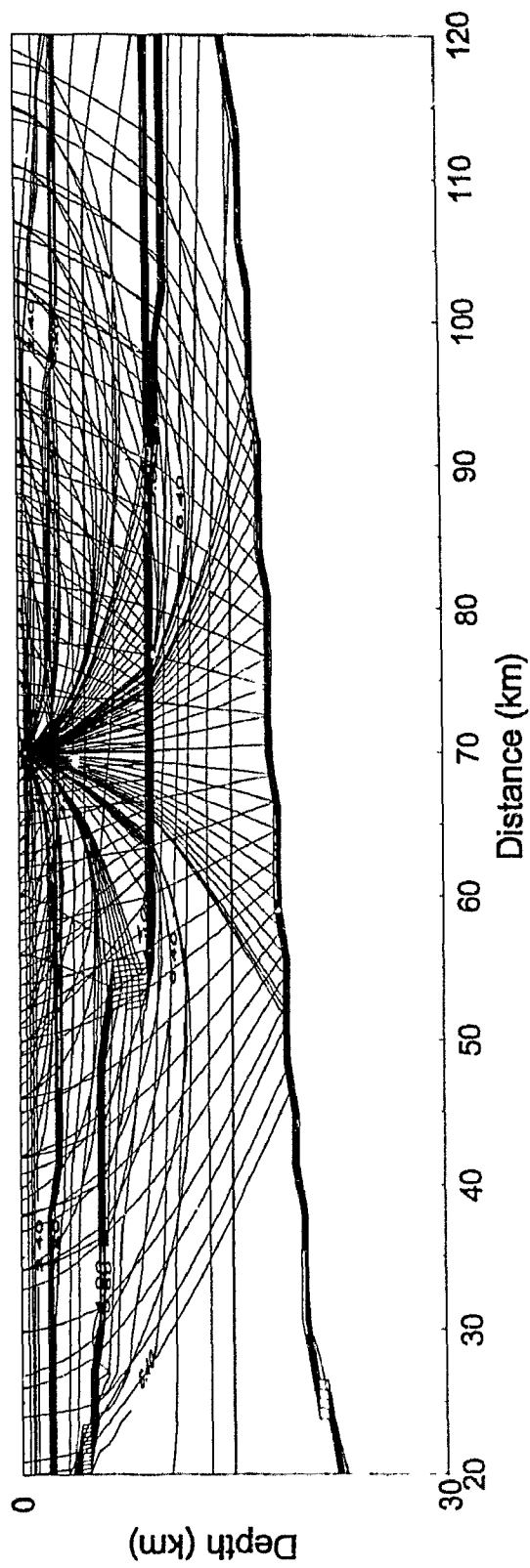
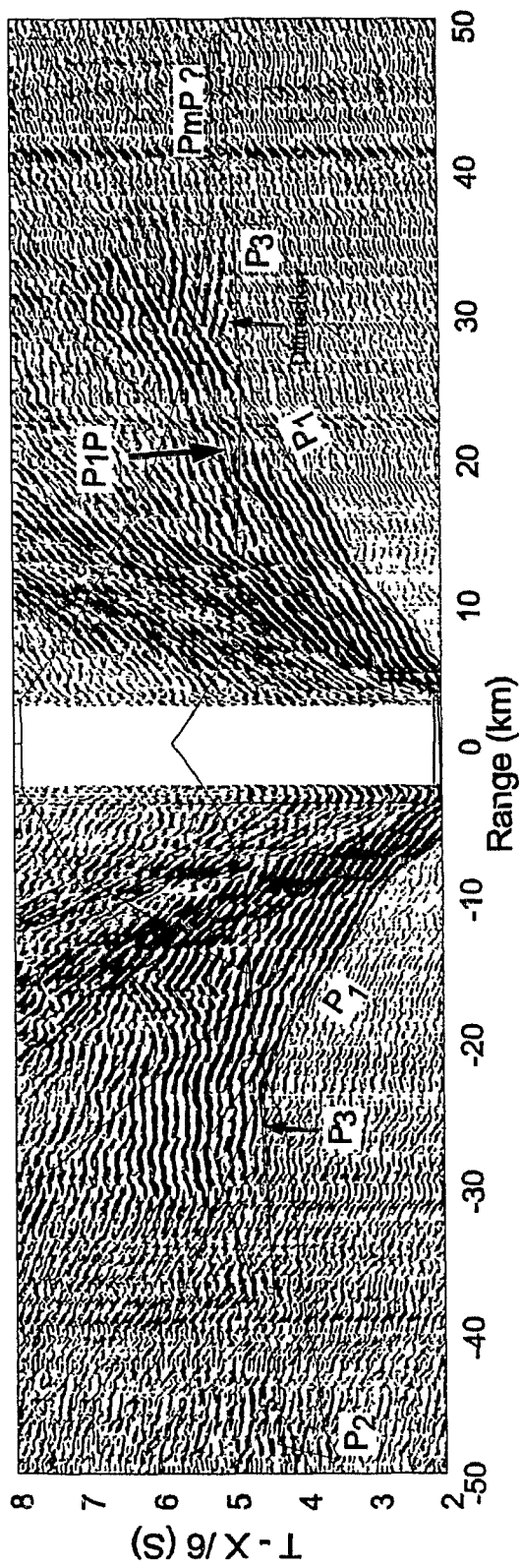


Figure 5 12. Top: Wide-angle profile from OBS Q on line 90R1. Bottom: traced rays overlain onto the velocity model.



options for choosing basement interface and the one that produces the best fit to the observed amplitude pattern of P1P is chosen for the final model. The chosen basement depth also produces a consistent travel-time for P1P2 on OBS D whose rays were reflected from an adjacent area on basement surface.

There is no evidence on the OBS profile to suggest more than one layer for the crystalline crust. A proper extension of lower-crustal velocity contours from both sides of the OBS produces a reasonable fit to P3 except the curvature of its hyperbola diffraction around a range of 30 km. This implies that the upper crust does not continue to the east of 52 km. There is no control on the depth of the Moho from this OBS, as PmP can not be convincingly determined.

#### OBS C

Sitting close to the shelf break, OBS C recorded no useful data on its hydrophone channel and the data of the geophone channel (Figure 5.13 ) are very noisy. This is possibly caused by bottom currents near the edge of the continental shelf (similar to OBS E and F on SW Greenland margin). However, P1 at negative ranges is well-defined. A strong amplitude at ranges of -30 km to -35 km is modeled as PmP, which extends to the west and undergoes a travel-time jump at a range of -45 km due to changes in the upper crust. To the east of the OBS, PmP appears at 30-50 km range, consistent with the modeled seismograms, and is reflected from the base of a single-layered crust with velocity gradients from 6.2 to 6.8 km/s.

#### OBS D

OBS D (Figure 5.14) records clear phases of very high quality, including P1, P2P, and PmP/Pn, as well as water multiples of P12, P2P2. As can be seen from Figure 5.14b, a large lateral change in velocity for both the sediments and crust starts to emerge. It is

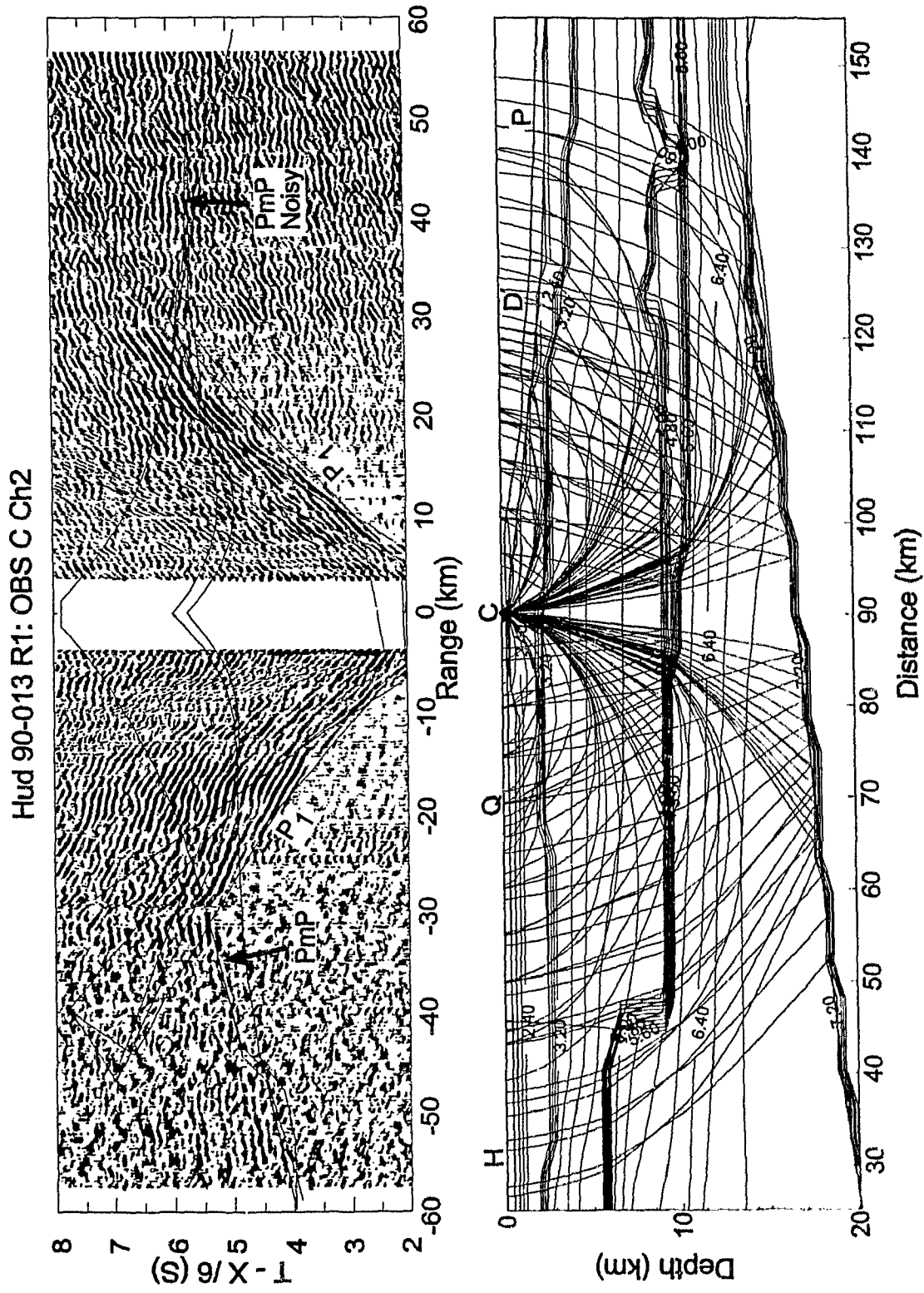


Figure 5.13. Top: Wide-angle profile from OBS C on line 90R1. Bottom: traced rays overlain onto the velocity model.

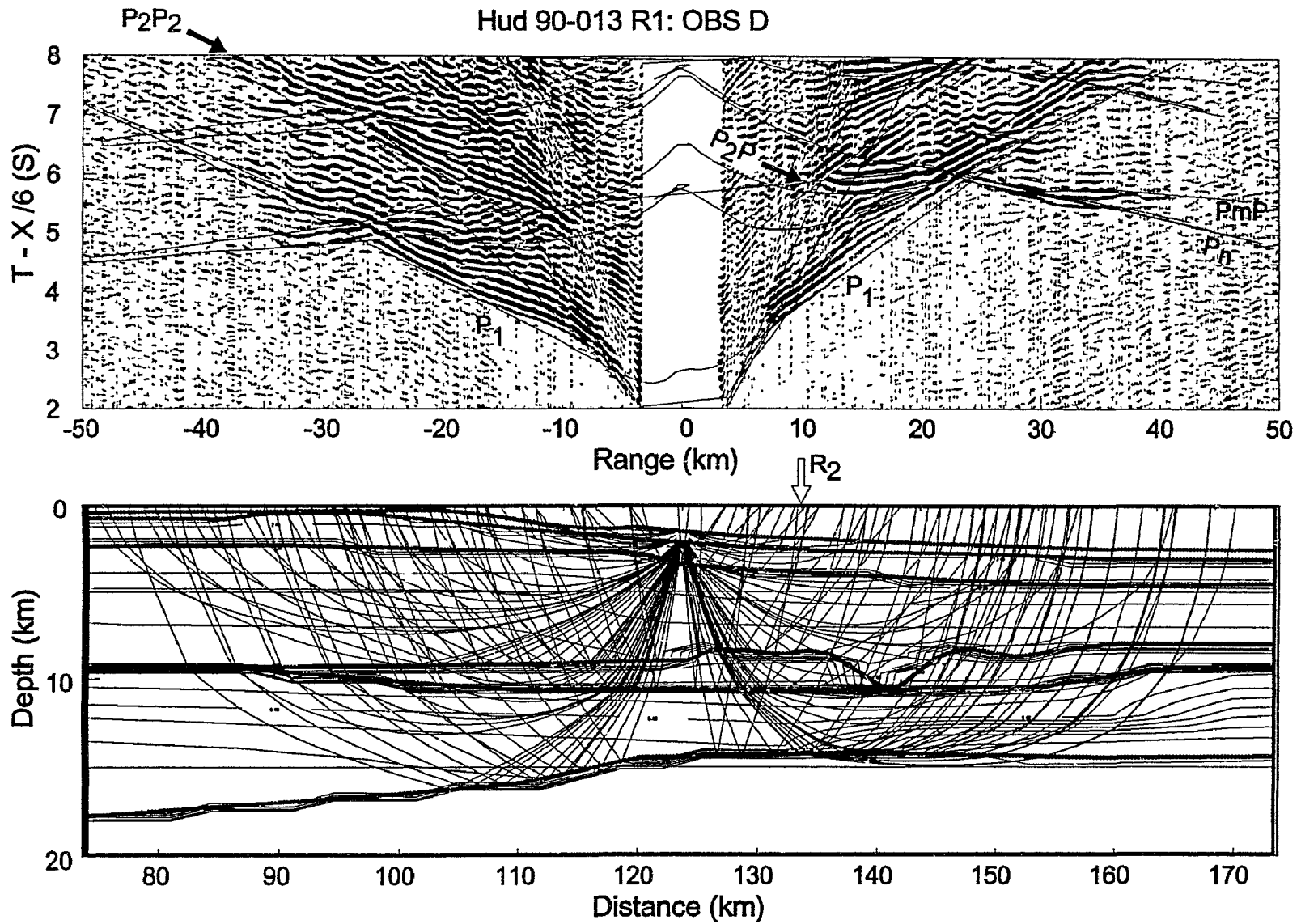


Figure 5.14. Top: Wide-angle profile from OBS D on line 90R1. Bottom: traced rays overlain onto the velocity model.

fortunate that I have good control from the along-strike refraction line 90R2, which is ~10 km to the east of this OBS, and structures of sediment and basement surface from the reflection profile.

Modeling of P1 suggests that a velocity gradient of 3.2-3.8 km/s at 4-8 km for the lower part of the sediment, as obtained from line 90R2, is consistent with the 2-D structure under the continental slope. The alignment of sediment velocity contours is also consistent with this part of the reflection profile where there are strong sub-horizontal reflectors (Figure 5.2).

Consistent with the model for line 90R2, a two-layer structure starts to form in the crust. The reflection from the upper/lower crustal interface, P2P, has well-modeled strong amplitudes that are distinct from other phases at ranges of 10-20 km. Because of influence of large lateral variations in the crust, it is difficult to separate the phases of PmP and Pn. Therefore, in the modeling both of these phases are modeled simultaneously.

#### OBS P

This OBS (Figure 5.15) records very good quality wide-angle data from shots on both sides. A strong sediment phase P1, which is readily recognizable between ranges of -40 km and 40 km, again supports the previously determined sediment velocity structure. For the crust, a two-layer structure, as determined from the nearby refraction line 90R2, is consistent with arrivals on this OBS. This can be seen by first identifying phases P1P, P2, P2P and P3 at positive ranges. The wide-angle reflection from the basement surface, P1P, is visible at 10-20 km range, with a slope which corresponds to a slightly higher apparent velocity than P1. The reflection from the upper/lower crustal interface, P2P, is visible and well modeled at ranges of 8-12 km and 20-30 km. P2P is also visible as a later arrival between -28 km and -10 km.

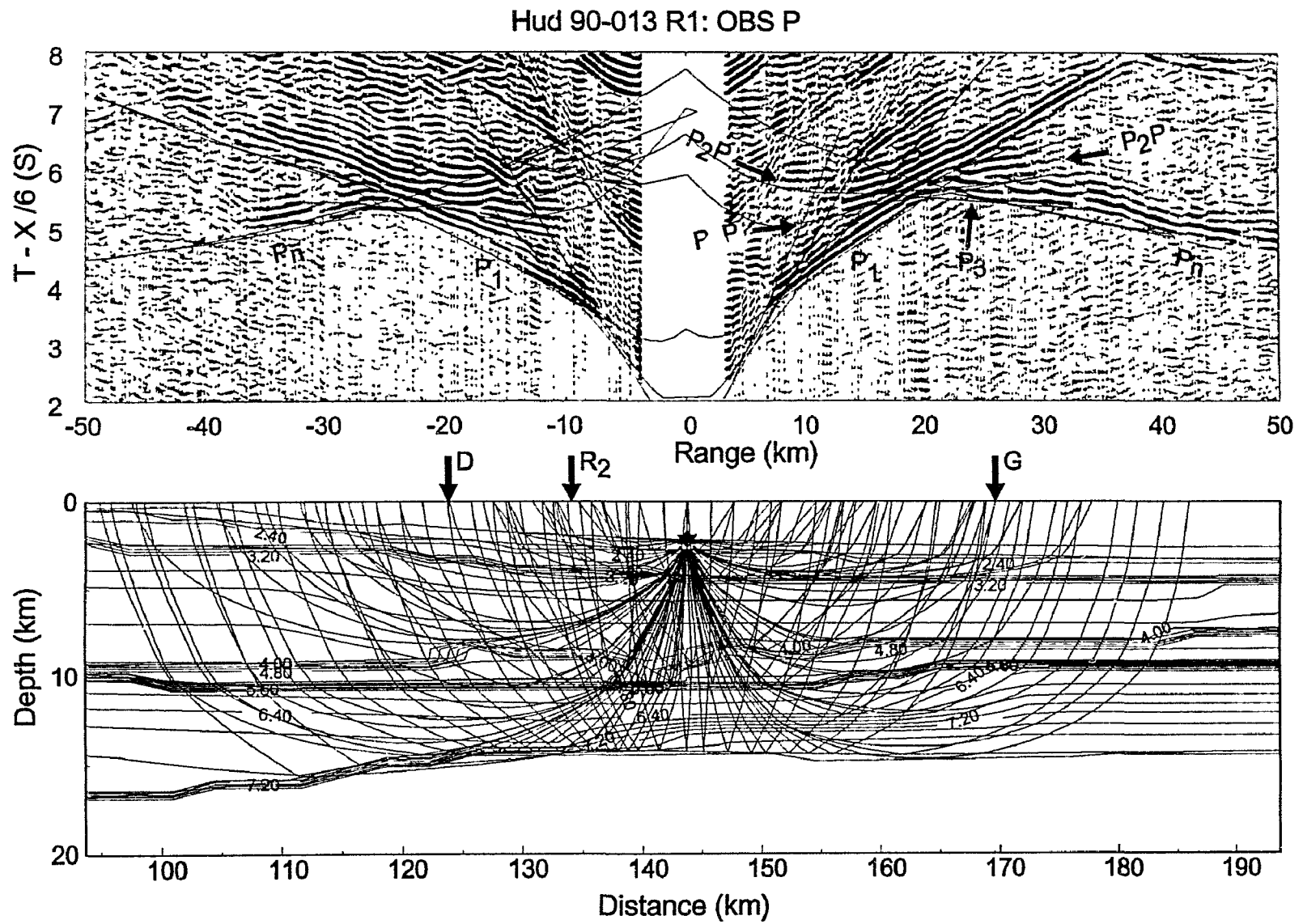


Figure 5.15. Top: Wide-angle profile from OBS P on line 90R1. Bottom: traced rays overlain onto the velocity model.

Modeling of these phases, and similar phases from adjacent OBS on lines 90R1 and 90R2, supports the existence of an upper layer, characterized by a low-velocity of 4.8-5.0 km/s, and a distinct lower layer with a velocity of 6.2-6.9 km/s, extending westward to join the single layer crust beneath the shelf.

PmP at positive ranges is not visible, but replaced by a strong Pn phase which is connected with P3, forming a continuous arrival with a change in slope at 37 km range. This phenomenon also exists for OBS G and A and is attributed to an increased velocity gradient ( $0.1 \text{ s}^{-1}$ ) in the lower crust. This high gradient creates velocities of up to  $\sim 7.7$  km/s at the base of lower crust.

#### OBS G

The low-velocity upper crust still exists near OBS G (Figure 5.16). This can be seen from a strong phase P2P at ranges of 20-26 km. In addition, at ranges of -20 km to -30 km, the computed travel-time curve matches an observed phase P2P. However, another sub-parallel phase, arriving at an earlier time, cannot be modeled. I attribute this mis-fit to local complexities in this region.

Well-defined crustal phases are only observed as water multiples (P32 and Pn2) at eastern ranges of OBS G. These two refracted phases are connected while the PmP2 phase is absent. This is similar to OBS *P* and OBS A.

#### OBS A

Sediment phase P1 (Figure 5.17) is clear and well modeled. Modeling shows that the deep sediments to the east of OBS A have velocities of 3.2-3.8 km/s, similar to under adjacent OBS (G and D). For the sediment to the west of the OBS A, higher velocities of 3.3-3.9 km/s for distances of 185 km and 200 km should be used for generating the correct travel-time for P1. This slight increase of sediment velocity is also compatible

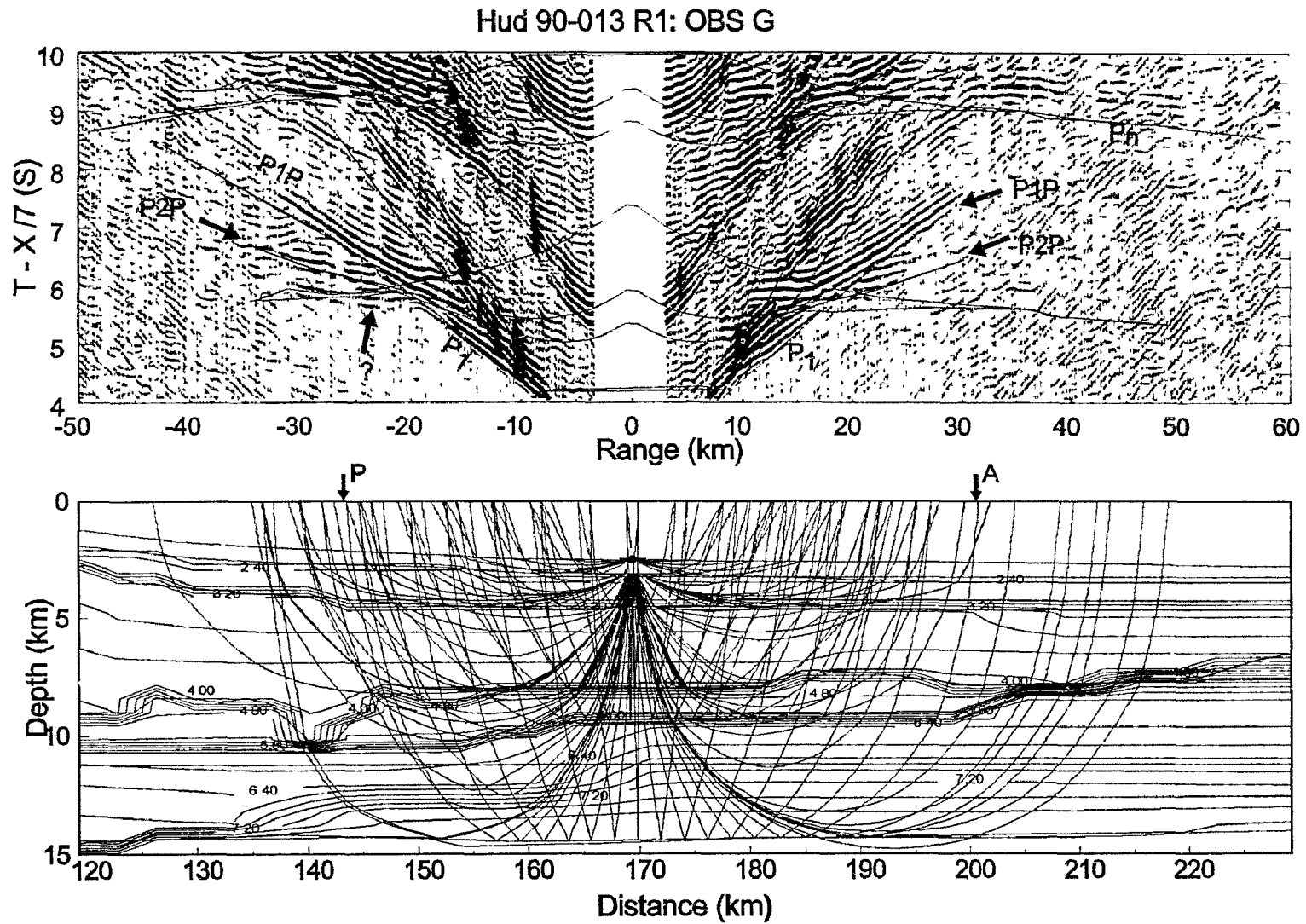


Figure 5.16. Top: Wide-angle profile from OBS G on line 90R1. The number below distance 0 corresponds to the location of the OBS on the 2-D velocity model. Bottom: traced rays overlain onto the velocity model.

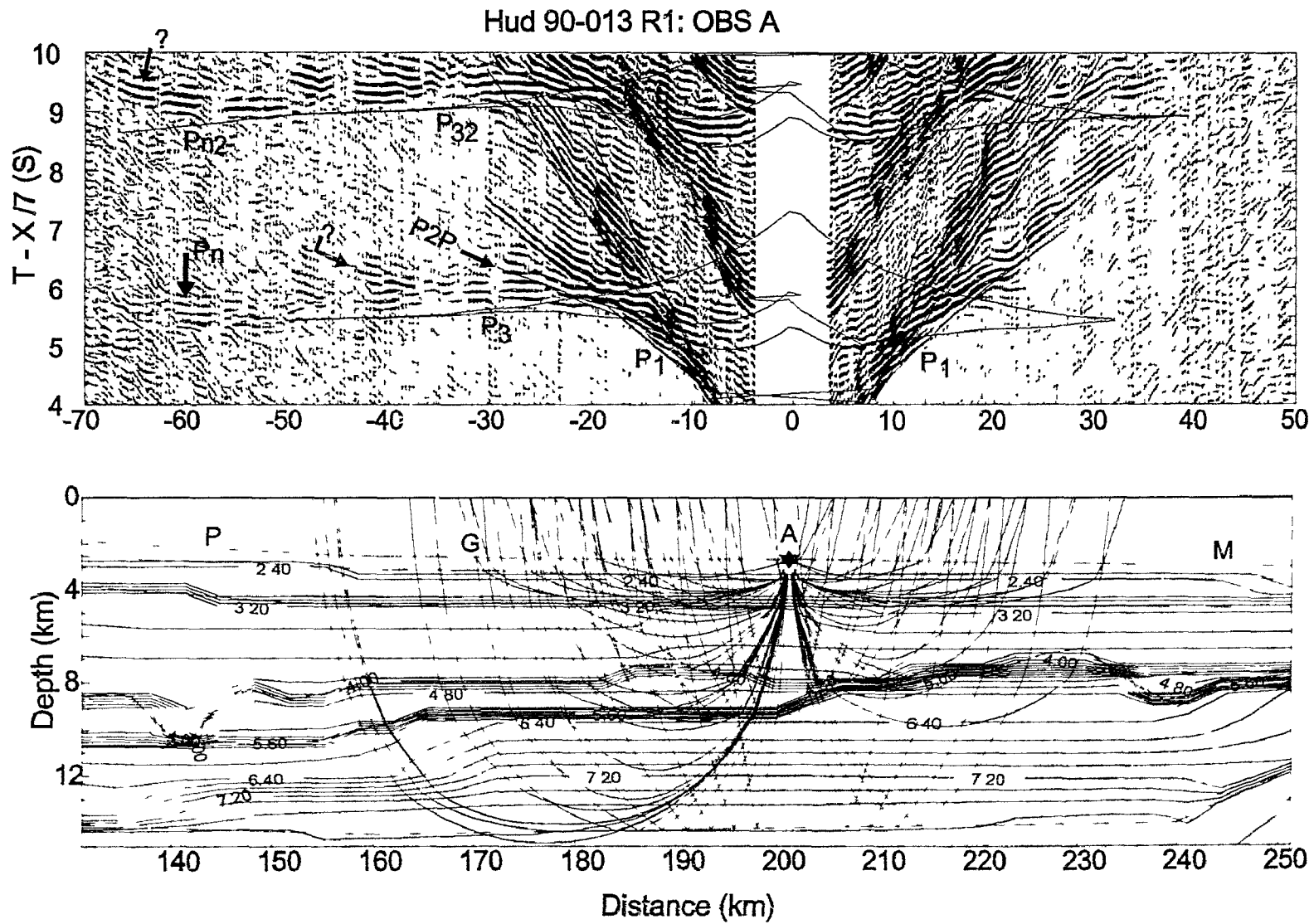


Figure 5.1 Top Wide-angle profile from OBS A on line 90R1. The number below distance 0 corresponds to the location of the OBS on the 2-D velocity model Bottom traced rays overlain onto the velocity model



with the change in reflective pattern at a distance of >180 km in the reflection profile (Figure 5.2).

Crustal phases are only observed at western ranges, where a two-layer crustal structure is still evident. Although confused with the reverberations of P3, P2P can still be recognized as a group of amplitudes at a smaller apparent velocity between ranges of -15 km and -30 km. No clear crustal phases are observed at positive ranges, consistent with the reflection data which show a transparent crust under and to the east of OBS A. Therefore, I conclude that the low-velocity upper crust terminates approximately at 202 km.

P3 is modeled as refracted from a lower crust with a velocity of 6.4 km/s at the top to 7.7 km/s at the seismic Moho. Similar to OBS P and G, P3 joins Pn with no generation of PmP. Meanwhile, the junction of the high-velocity crust with thinned continental crust (Figure 5.17b) has generated diffractions which are especially clear on the multiple of Pn (or Pn2) at ranges of -50 km to -70 km. Another diffraction occurs as a phase with very low apparent velocity around -40 km range. This phase is not modeled.

#### OBS M

OBS M (Figure 5.18) has very noisy data and only P1 and P2P can be modeled. A two layer structure is consistent with the observed phases.

#### OBS K and I

The seismic phases recorded by OBS K and I (Figures 5.19-21) show a pattern different from all previous OBS to the west. The modeling of these phases is relatively easy because the coincident reflection data has a good control on the TWTT for the sediments, crust and the Moho. The modeling of the sediment arrival P1 indicates that the sediments have relatively low velocity which goes from 2.2 km/s at 4 km depth to 2.6

Hud 90-013 R1: OBS M Ch2

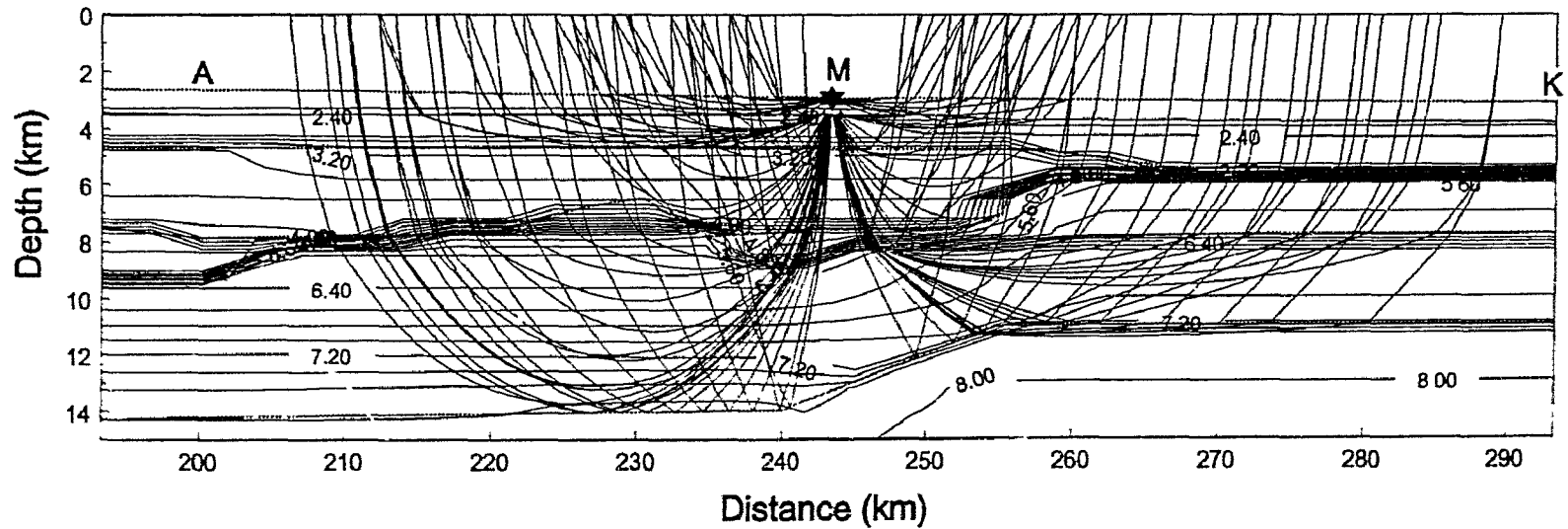
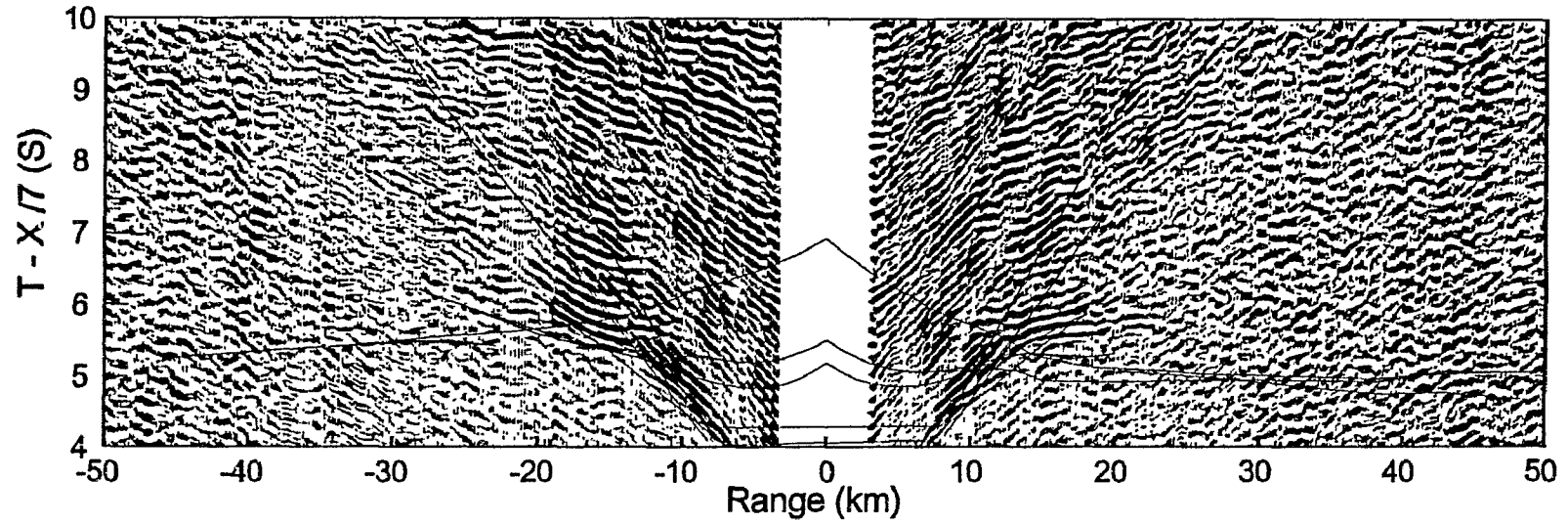


Figure 5.18 Top: Wide-angle profile from OBS M on line 90R1. Bottom: traced rays overlain onto the velocity model.

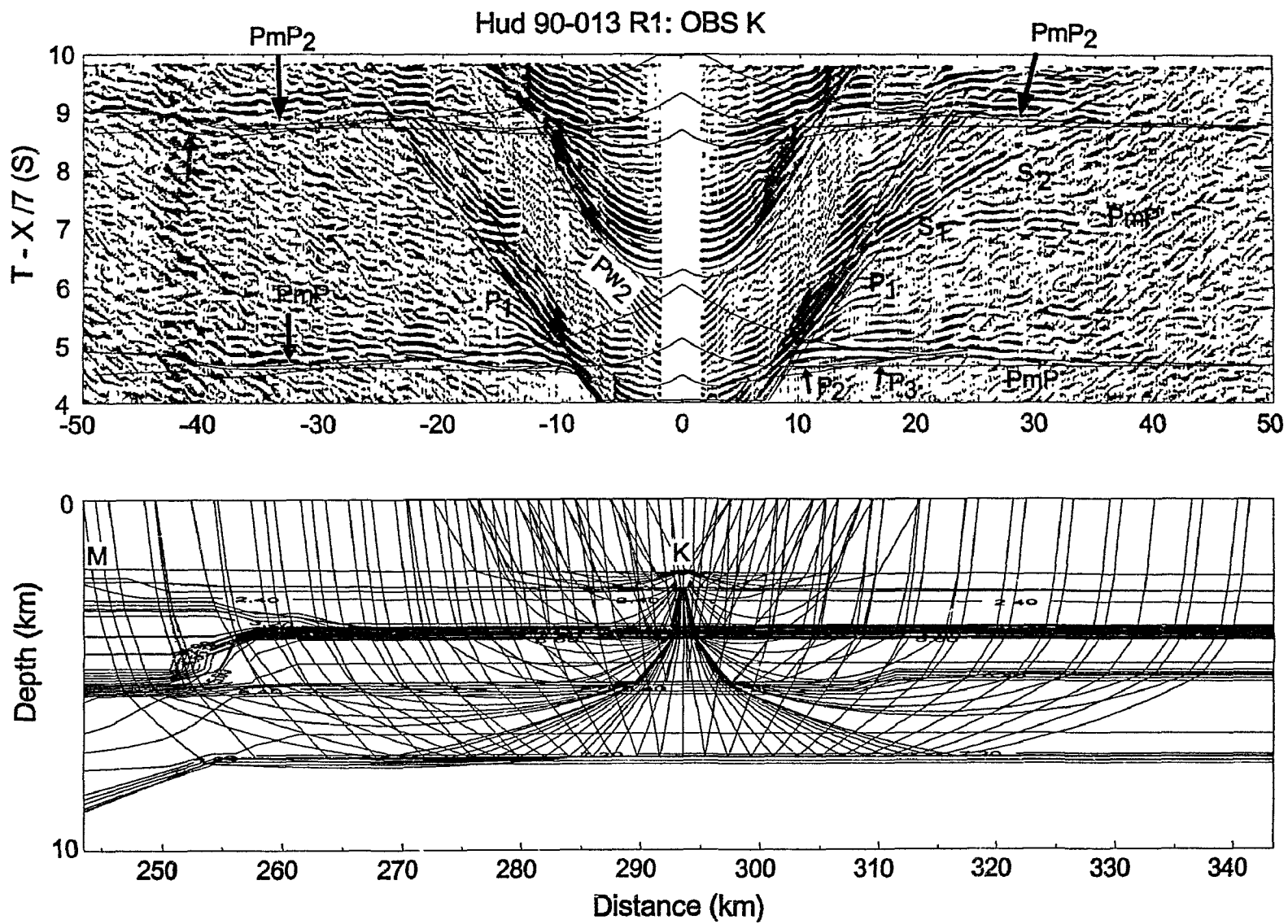


Figure 5.19. Top: Wide-angle profile from OBS K on line 90R1. Bottom: traced rays overlain onto the velocity model.

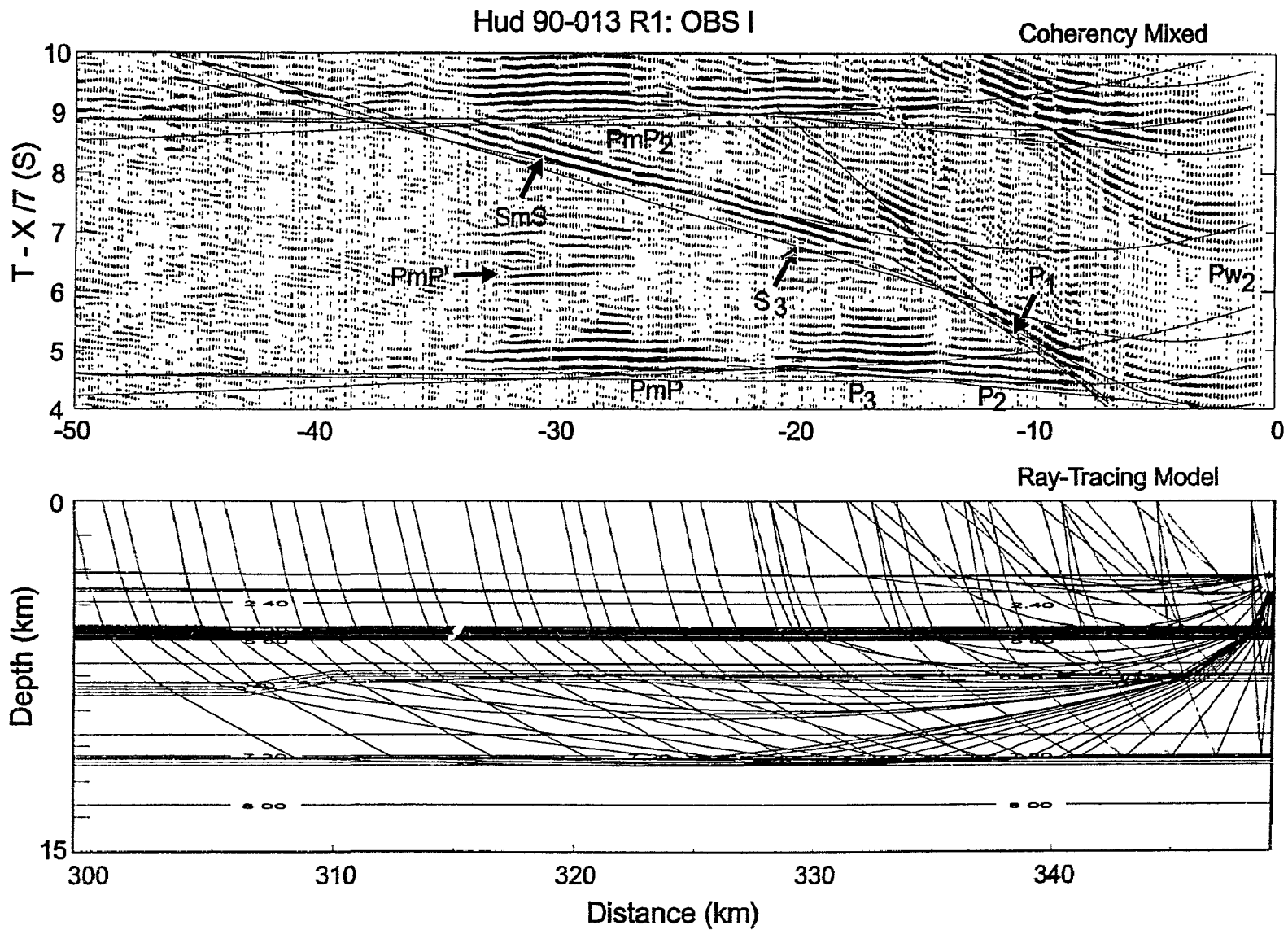


Figure 5.20. Top: Wide-angle profile from OBS I on line 90R1. Bottom: traced rays overlain onto the velocity model.

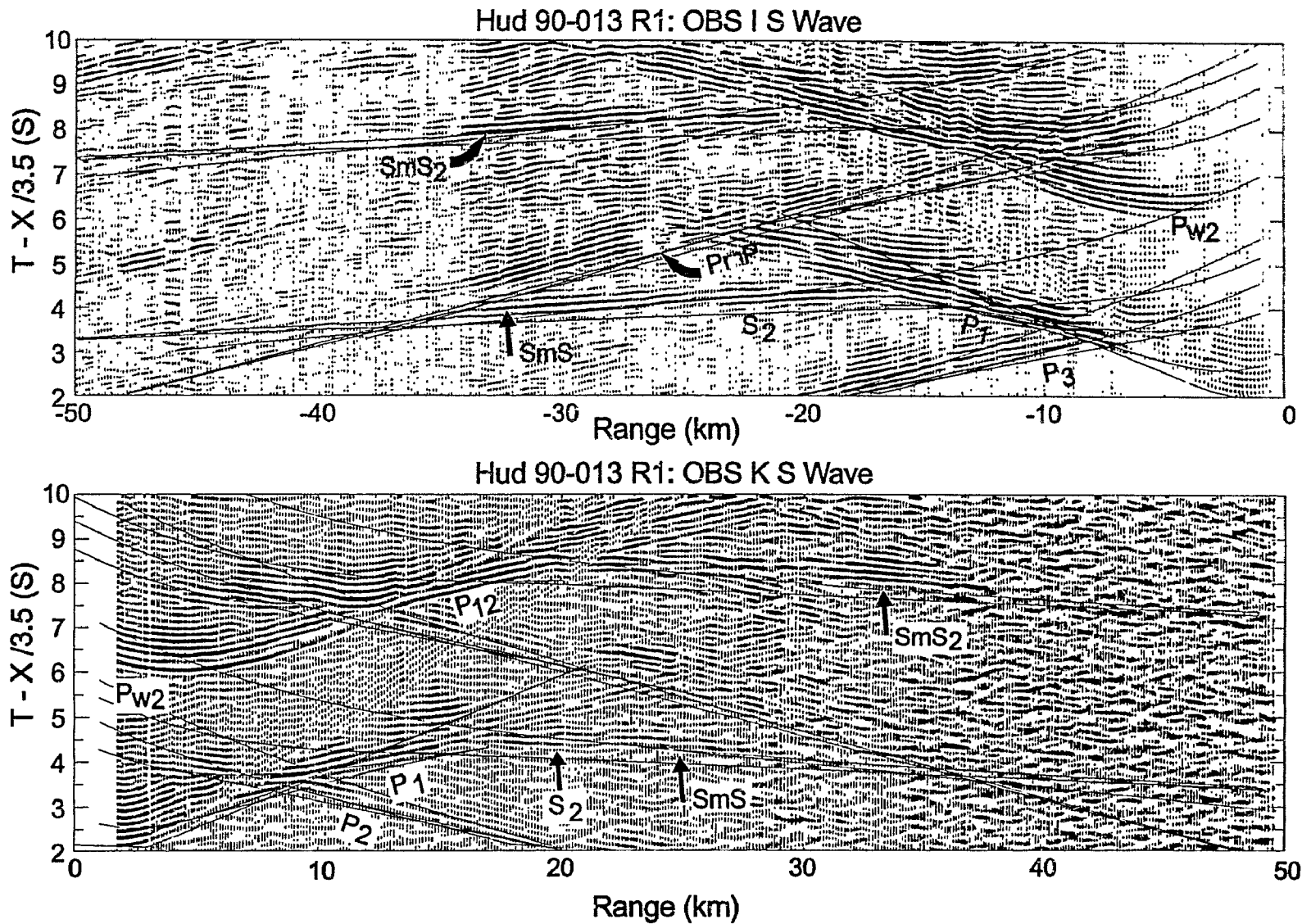


Figure 5.21. Top: Wide-angle profile from OBS K on line R1, plotted at a reducing velocity of 3.5 km/s for emphasizing crustal S waves. PSP is a crustal S refraction generated by double P-S conversion at the sediment/basement interface. Bottom: OBS I plotted in the same format.

km/s at 5.5 km depth. The crust is divided into two layers, which is necessary for modeling the change in slope from P2 to P3 at a range of 12 km. These phases suggest an upper crust with a velocity gradient of 5.6-6.0 km/s and a lower crust with a velocity gradient of 6.8-7.1 km/s. The change in slope from P2 to P3 corresponds to a division between upper and lower crust at approximately 7.5 km depth. The modeling of the water multiples also supports these results.

One importance of OBS K is in that it helps to determine the exact position of the 1-km basement jump in the ambiguous region between 240 and 260 km in the reflection profile. This basement jump is exhibited on the PmP2 phase as a change in slope at -40 km range. Modeling shows that this feature can be re-produced on the synthetic profile if the basement jump occurs at 252 km in the 2-D model.

OBS I is situated at the eastern end of the line, giving high quality data for phases P2, P3, PmP, S3, SmS and their water multiples. The modeling procedure is very similar to OBS K.

Clear *S* waves (S1 and S2) are observed only at OBS K and I (Figures 5.21a and b). These *S* waves are doubly converted at the sediment/basement interface, traveling as *P* waves in the sediment and refracted in the crust as *S* waves. Modeling indicates that the *S* velocities in the crust can be best described by a  $V_p/V_s$  ratio of 1.92.

#### **5.4 Interpretation**

Similar to the zone division convention made for the SW Greenland margin, the cross-section (Figure 5.22) for the Labrador margin can be divided from west to east into 3 zones:

*Zone I* represents a rapid thinning of continental crust. Beginning with a thickness of 27 km at the western end of the model (0 km; based on results of refraction line 90R3), this crust is reduced to a thickness of only 13 km within a distance of 52 km. At this point

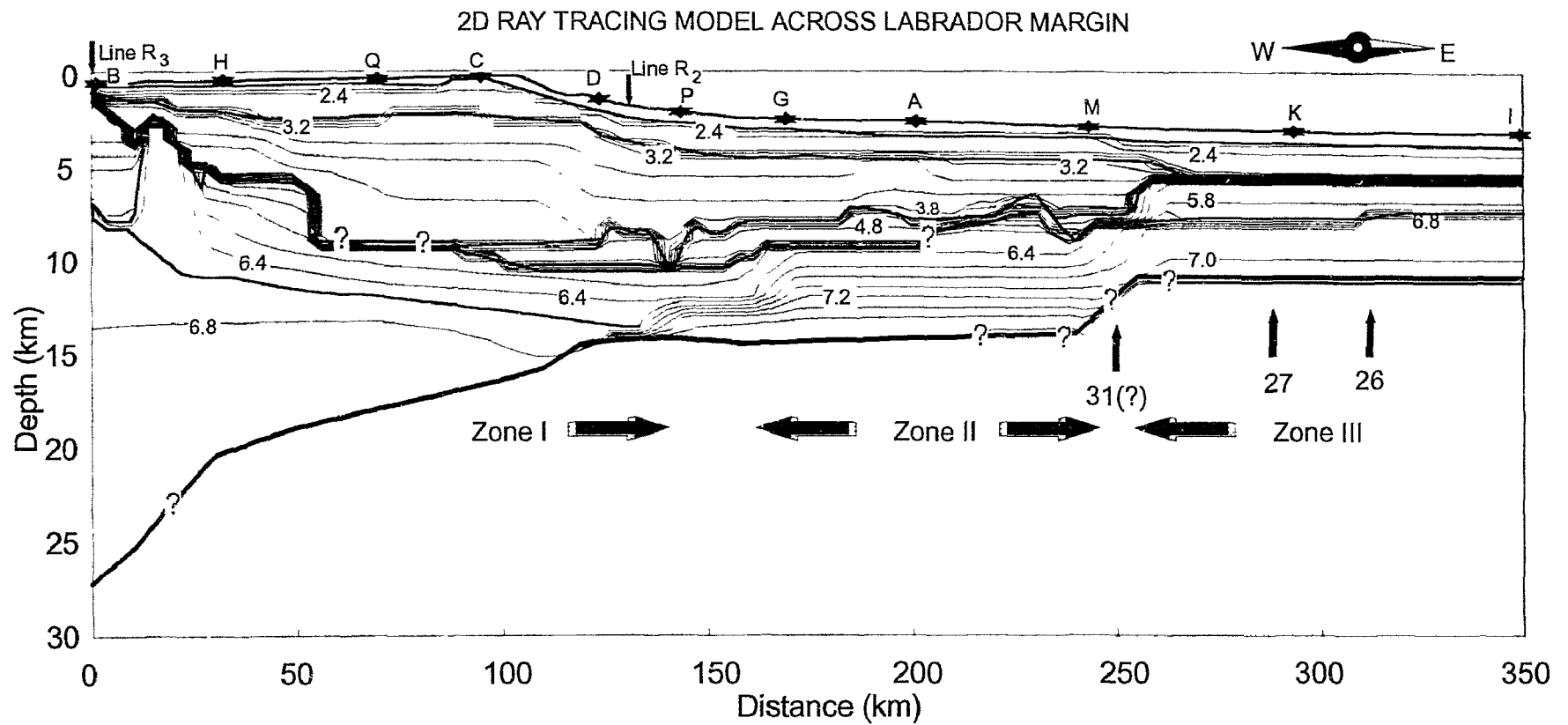


Figure 5.22. Two dimensional velocity model showing contours of  $V_p$  (in km/s) across the Labrador margin. The contour interval is 0.2 km/s. At some significant velocity boundaries (thick lines) contour lines are terminated for clarity. Filled stars indicate positions of OBS. Vertical exaggeration is 3:1.

there exists a sharp 3-km deepening of basement. Further seaward, the thickest (~9 km) sediments are deposited, with the underlying crust best described as a single layer bearing a velocity of 6.0 km/s at the top, increasing linearly to 6.9 km/s near the Moho. From west to east the velocity contours are smooth and slightly tilting towards the east. This velocity structure produces a fit to the arrivals of OBS H, Q, and D.

Therefore, seismic evidence from reflection and refraction profiles suggest that the upper crust terminates at ~52 km. Beyond this point there is only middle to lower continental crust which extends seaward to 140-160 km where it joins Zone II.

*Zone II* is characterized by a distinctive lower crust with anomalous high-velocity of >7.2 km/s. This lower crust is about 5-6 km thick, extending laterally from 160 km to 250 km. The modeling of the wide-angle phases from OBS P, G and A indicates a high velocity gradient from 6.4 km/s at the top (9.5 km depth) to ~7.7 km/s near the seismic Moho (14.5 km depth). The Moho is, therefore, associated with a small velocity contrast which generates poor reflections on wide-angle and vertical-incidence profiles. The same high-velocity layer is also observed offshore in the SW Greenland margin in Chapter 4, where it is interpreted as serpentinized peridotite, although an alternative origin of underplate is also possible. This issue will be more thoroughly discussed in Chapter 6.

Between distances of 100 km and 200 km, a relatively low-velocity (4.8-5.0 km/s) layer forms the crystalline upper crust. The existence of this thin (~1.5 km) layer is well-defined from an along-strike line 90R2 (Figure 5.3) on the continental slope, and from OBS D, P, G and A. The upper boundary of this layer corresponds to a series of very discontinuous reflectors (Figure 5.24) which may be related to a large degree of faulting and fracturing. Because the velocity of this layer is greater than that of the overlying sediment layers and smaller than either the continental or oceanic crust to either side, and



no block faulting patterns are observed which is unlike the SW Greenland margin, the origin of this layer (continental, oceanic, or both) remains unclear.

Zone *III* is characterized by a 5.5-km, two-layer crust with an oceanic character. The division between Zones II and III occurs as a complicated region between 240 and 255 km, associated with a 1-km basement shallowing and 3-km Moho shallowing. East of 260 km, the basement surface becomes more smooth and the velocities and thickness of crust are stabilized with little lateral changes. Here the upper crust is 1.8-2.0 km thick and the *P* velocity is 5.6-5.8 km/s. The lower crust is 3.0-3.5 km thick with normal velocity (6.8-7.0 km/s). The modeling of the well-defined *S* phases indicates a  $V_p/V_s$  ratio of 1.82 or a Poisson's ratio of 0.28 for oceanic layer 2 and layer 3.

## 5.5 Resolution of Results

### 5.5.1 Error Analysis

Error analysis can be used for fine tuning intermediate velocity models, and most importantly serves as an estimate for the resolution of the final model. In doing this, I choose a crustal unit which produces a coherent refracted phase, slightly perturb the velocity and boundary for the unit and calculate the resulting misfit in travel-times for the refracted phase. This method can generate the maximum error estimates of the velocity and boundary. For details of this method, refer to Appendix A.

Figure 5.23 shows the result of the application of the above error analysis method for the P3 phase on OBS A. It can be seen that the velocity for the high-velocity lower crust to the west of OBS A has an error bound of  $\pm 0.07$  km/s while the depth to the top boundary has an error bound of  $\pm 0.3$  km.

It should be noted that when multiple ray paths from different receivers overlap, I will have a better estimate of the velocity structure than the maximum error bounds calculated above. For example, the high-velocity lower crust is sampled not only by the

## Error Analysis for Layer 3 at OBS A

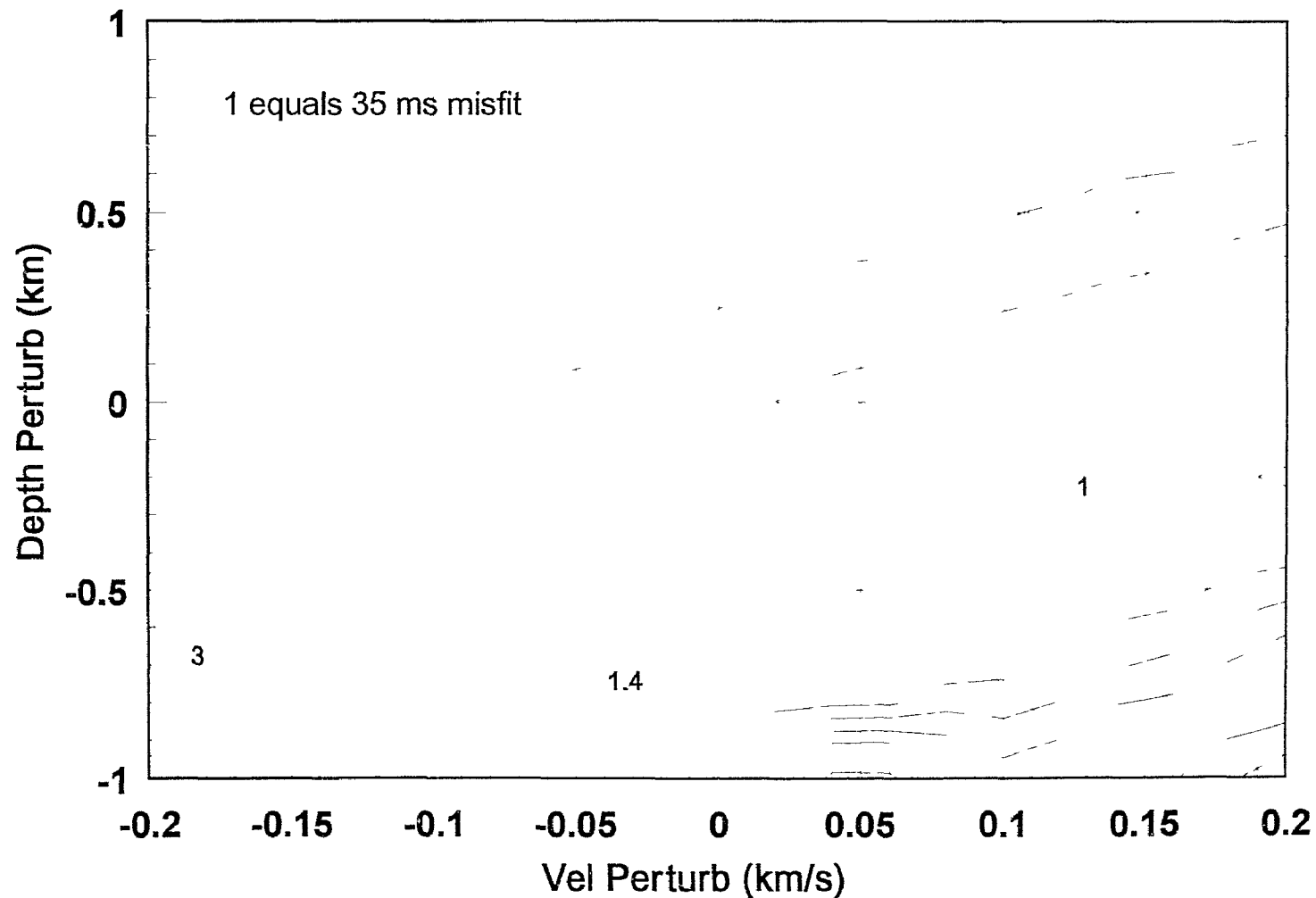


Figure 5.23  $\chi^2$  contour plot for perturbations of velocity and depth for the seismic phase P3 west of OBS A (Fig. 17). The contours are normalized to the travel-time endurance (maximum errors in observed travel-time) of 35 ms. The areas enclosed by  $\chi^2=1$  delimits error bounds for the velocity and depth for the lower crust.

ray paths from OBS A to also from OBS G and P. The densest ray paths occur in the lower crust between 110 km and 150 km, where ray overlapping is contributed from OBS D and P and from four OBS on the crossing line 90R2. However, since this region actually has the most complicated structure, it is not possible to give quantitative error bars for this part of the crust.

There are several regions on the final model through which few or no rays propagate (see question marks in Figure 5.22). Among these regions the most important is probably the basement surface at 52-80 km distance. Modeling of OBS H (Figure 5.11) suggests a 3-km basement deepening at 52 km distance, and modeling of an adjacent OBS (Q; Figure 5.12) shows no indication of upper continental crust at >80 km distance. Therefore, the region in between is thought to be lacking upper continental crust. As can be seen in the following sections, this is supported by comparison with the coincident reflection profile.

### **5.5.2 Comparison with Reflection Data**

The accuracy for the final velocity model can be improved by comparison with the coincident reflection profile. In doing this, it is more suitable to compare with a migrated section in the time domain rather than in the depth domain. This is because the MCS depth section assumes a velocity structure which is different from that obtained from wide-angle modeling. Therefore, I convert the boundaries on the 2-D velocity model into two-way travel-time and overlay them onto the line drawings of the migrated time section (Figure 5.24). In this figure, solid continuous lines represent boundaries used in the final model,

and other discontinuous lines are line-drawings hand-picked from the coincident multi-channel profile (Keen et al. 1993). The solid lines within the sediments are drawn for the purpose of specifying velocity variations and do not necessarily represent geological layer boundaries.

### Deep Multi-Channel Reflection Profile

In 1990, 991 km of deep multi-channel reflection data were collected across the entire Labrador basin. These data comprise three segments, among which line 90-1 and 90-3 cross the complete Labrador margin and its conjugate Greenland margin. Line 90-1 closely follows the track of the refraction line 90R1 on the Labrador margin (Figure 5.1).

Interpretation of line 90-1 (Figure 5.24; Keen et al. 1994b) suggests that the sedimentary section can be divided into syn-rift and post-rift units, separated by a breakup unconformity, "U". This interpretation is tied to the regional seismic stratigraphy based on boreholes which has been established as part of hydrocarbon exploration in the region (Bell 1989). The "U" reflector corresponds to the top of the Bjarni formation of late Albian age (~98 Ma). The syn-rift unit below "U" is discontinuous and occupies structurally low regions between basement blocks. The identification of "U" becomes less certain near the shelf break and below the slope.

Below the sediments, basement ("B") has been dissected by normal faults, some of which also cut the syn-rift sediments (e.g. the basement high between 10-25 km). From 52 km seaward to the shelf break, the depth of basement deepens sharply by <3 km, allowing thick syn-rift sediments to be deposited. Below the continental slope, basement reflections

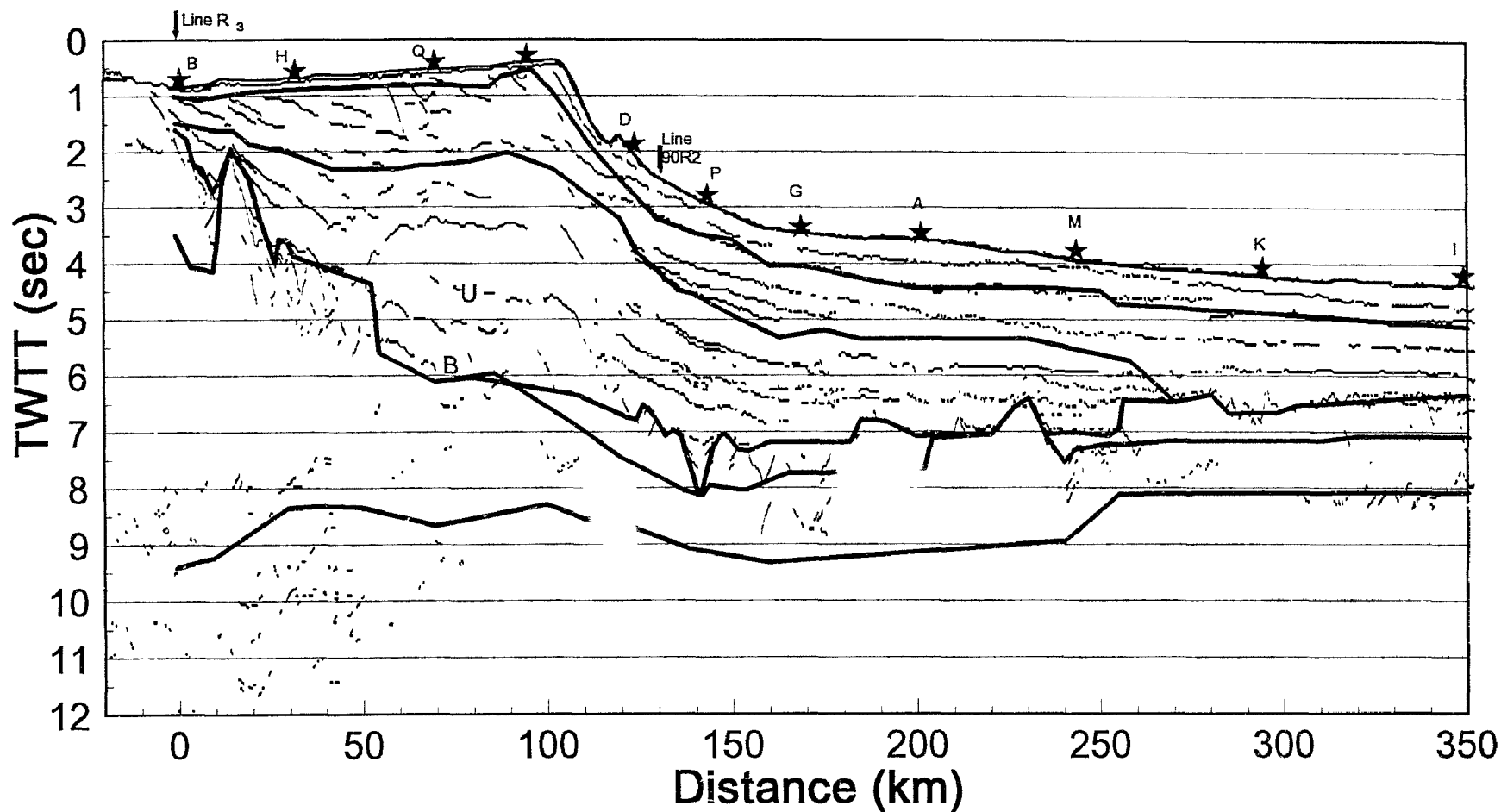


Figure 5.24 Comparison of refraction results with reflection time section. Boundaries (solid lines) of the 2-D velocity model in Figure 5.22 are converted to two-way travel-time (TWTT) using the obtained velocities. The solid lines in the sediments do not necessarily represent geological boundaries.

define a rough surface below a few relatively flat-lying sediments. Between 185 and ~240 km, a "transparent" basement is observed. Further seaward, another reflector bearing a basement character emerges at a depth 1 km shallower, underlain by sub-crustal reflections. The topography of this new basement is smooth compared to the rough basement to the west. This basement continues seaward and remains at ~5.5 km depth toward the end of the line.

Below the basement, Moho reflections are observed at both ends of the line: the inner shelf at <50 km, and the eastern end of the line at >300 km. On the shelf, there are several reflectors at the base of the crust with differences in two-way travel-time of up to 2.5 sec. When converted to depth, this amounts to a difference of 9 km assuming a lower crustal velocity of 6.9 km/s. Therefore, it is difficult from reflections alone to determine which phase corresponds to the Moho.

#### Combined View of Reflection and Refraction Results

From Figure 5.24 it can be seen that effort has been made during the wide-angle modeling to use as much information from the reflection profile as possible. For the basement surface, the closest matching between refraction and reflection results occurs where basement reflections are clearest (e.g. 0-50 km, 120-150 km, and 200-350 km). The termination of the upper continental crust at 52 km is associated with many irregular sub-crustal diffractions between 20 and 52 km. Further seaward, no basement reflection is observed in the reflection profile and the basement depth is determined from refraction profiles. The continental crust near the division between Zones I and II is possibly most

fractured as seen from the velocity contours (Figure 5.22), which explains the occurrence of many basement diffractions at 120-160 km on the reflection profile. A mismatch exists in the reflectively "transparent" crust at 180-230 km. In this region the reflection profile shows no signals from the crust, whereas refraction data suggest a strong mid-crustal velocity boundary extending eastward to at least 200 km.

The refraction Moho matches perfectly with the reflection Moho in Zone III. No reflections are observed from the Moho in Zone II, which is consistent with the absence of the PmP phase in the refraction data (Figures 5.15-17). At distances >70 km in Zone I, the Moho depth is convincingly controlled by refraction data, while no Moho reflections are recorded on the reflection profile. Landward of this region, there is some reflective energy recorded near the refraction Moho. However, this energy is scattered over a wide range of depths, which is a phenomenon difficult to explain.

### **5.5.3 Constraints From Two-dimensional Gravity Modeling**

Having obtained the detailed velocity structure (Figure 5.22) for the Labrador margin, I can perform gravity modeling for this cross-section, assuming a velocity-density relationship which should be consistent with that on the conjugate Greenland margin (Chapter 4). The advantage of this method is that the resulting density model retains the details of the local and regional velocity variations for the both conjugates. This is especially important for the Labrador margin because up to 9 km of sediments are deposited with large 2-D velocity variations within sediment layers near the continental slope. It should be noted, however, that even with this method there are still uncertainties because there is almost no control over the velocity-density relationship for the deep sediments, and yet small changes in density for the thick sediments could produce noticeable changes in the computed gravity curves. It is fortunate that I have arrived at a

reasonable gravity modeling for the SW Greenland margin where only a thin sheet of sediments have been deposited. The extrapolation of the modeling parameters for this margin makes it possible to further reduce unknowns involved in the gravity modeling for the Labrador margin.

Similar to the density values used in the SW Greenland margin (Chapter 4), the water layer and the first two thin sediment layers for the Labrador margin are assigned a density of 1.03, 1.8 and 2.1 g/cm<sup>3</sup>, respectively. To determine the density ( $\rho$ ) for the remaining thick sediments whose velocity ( $v$ ) lies between 3.2 and 4.0 km/s, I use a linear relationship  $\rho = 0.25 v + 1.6$  for  $v \in (3.2, 4.0)$  km/s. When this is coupled with a density of 2.65 g/cm<sup>3</sup> for the low-velocity upper crust (4.0-5.2 km/s), and  $\rho = -.6997 + 2.2302 v - .598 v^2 + .07036 v^3 - .0028311 v^4$  (Ludwig et al. 1971; Chapter 4) for all the remaining crust, an overall fit for Zones I and II is obtained.

In the computation of the gravity anomalies, it is necessary to extend the 2-D density model to infinity. The Moho at the eastern end (Zone III) of the model is well-defined by reflection and refraction data and its 11-km Moho depth is simply extended to infinity to the east. For the western end of the model, one notices that the Moho shallows significantly toward the basin and the 27-km Moho depth at 0 km distance likely represents a thinned continental crust. I find that a good fit of gravity anomaly is obtained by setting the Moho under unstretched continental crust to be 34 km at distances less than -10 km. Because the computed anomaly is very sensitive to changes in depth of the Moho, I rely on this property to obtain the Moho relief between 0 and 70 km where there is little seismic control over the depth of the Moho. As can be seen from the comparison of reflection and refraction results (Figure 5.24), the refraction Moho is shallower than the reflection Moho at 0-70 km distance. In correspondence to this difference, in the gravity modeling of this reflection Moho, Keen et al. (1994b) used higher densities for the



sediments than the sediment density used above. This uncertainty of Moho shallowing does not exist for the SW Greenland margin where there are only thin sediments deposited and the Moho relief is well determined from gravity modeling (Chapter 4).

Assuming that the oceanic mantle at 35 km depth on both sides of the basin is in isostatic equilibrium, I will have the eastern extension of the model for the Labrador being associated with a gravity anomaly which is equal to that for the western extension of the SW Greenland model. Since the latter (-4288 mGal) is already known from Chapter 4, this assumption sets a control for the reference level of the computed gravity curve for the Labrador margin.

Similar to the Zone III for the SW Greenland margin, the computed gravity anomaly near the eastern end on the Labrador margin is >20 mGal higher than observed. This suggests that either the actual density for the oceanic crust in Zone III is lower than computed, or the density in the oceanic lithosphere varies across the margin. This issue is beyond the scope of this thesis.

## **5.6 Correlation with Magnetic Anomalies**

The top diagram of Figure 5.25 shows a plot of observed magnetic anomalies interpolated along the refraction line across the Labrador margin (refer to Keen et al. 1994b). It can be seen that the first clear magnetic anomaly is at Chron 27 inside Zone III. Landward of this anomaly, an anomaly with a smaller amplitude possibly represents Chron 31, which corresponds to the junction between Zones II and III. The magnetic anomalies in Zone II, where the high-velocity lower crust is observed, are characterized by low amplitude oscillations, in a pattern different from that in Zone III. Therefore, similar to the interpretation for the SW Greenland margin (Chapter 4), it is possible that the formation of true oceanic crust was initiated between Chrons 27 and 31, and Zone II represents a wide transition zone from the continent to the ocean.

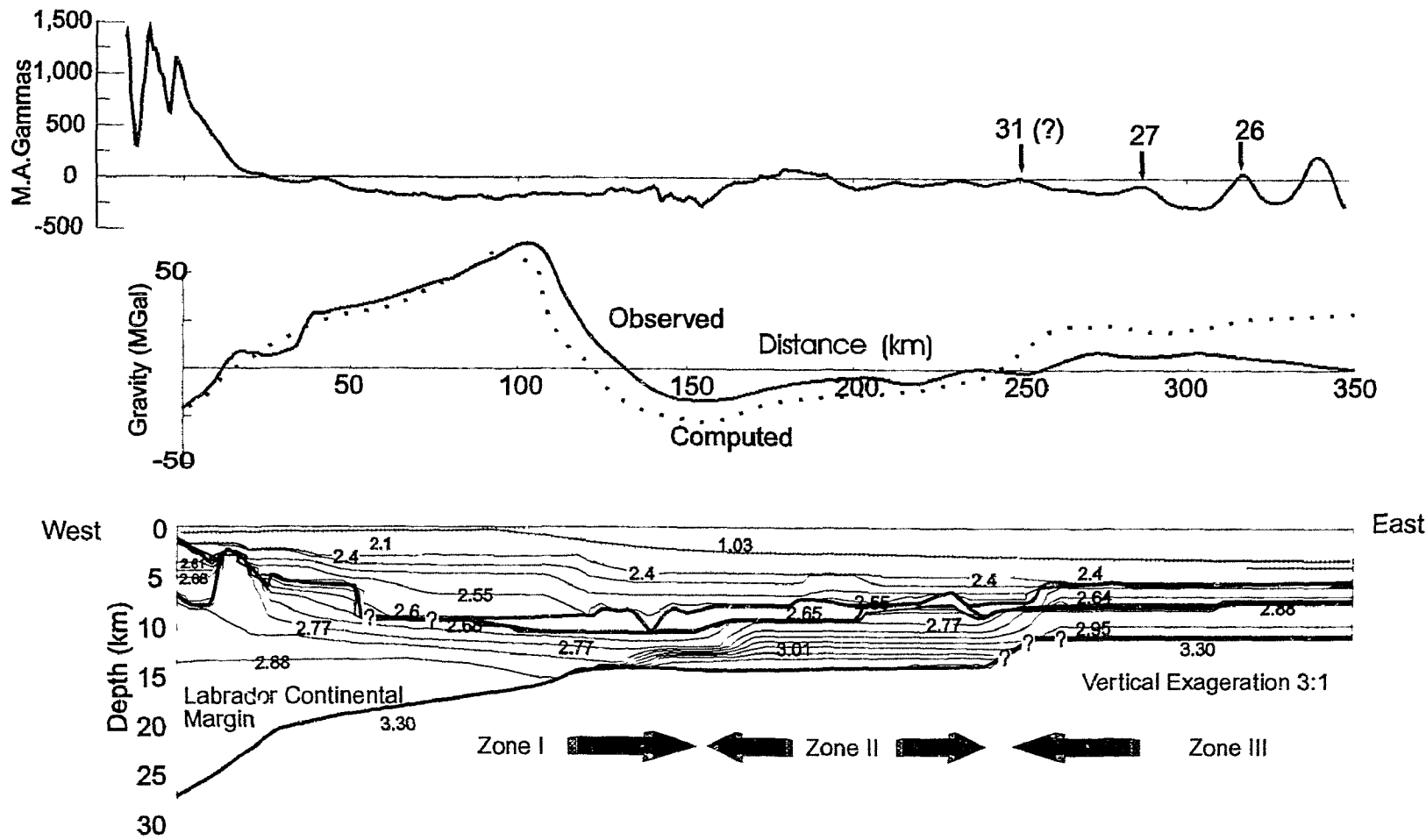


Figure 5.25. The modeling of magnetic and gravity data across the Labrador margin. (a) Top: Observed magnetic data. (b) Middle: Observed free air anomaly (solid line) along with computed gravity profile (dotted line) calculated from the 2-D density model shown in the bottom diagram. (c) Bottom: 2-D density model. The density in the crust is calculated from the 2-D seismic model (Figure 5.22) according to the relationship  $\rho = -.6997 + 2.2302V - .598V^2 + .07036V^3 - .0028311V^4$  (Ludwig et al. 1971). In the figures, a zero gravity anomaly corresponds to  $4279.27 - 29.42 = 4249.9 \sim 4250$  mGal when contributions from materials down to 35 km are considered. The gravity and magnetic anomalies are extracted according to Keen et al. (1994) based on the dense coverage of cruise lines on the Labrador margins (Bell 1989).

## 5.7 Conclusion

(1) A combined wide-angle modeling of three refraction lines and a coincident MCS reflection line reveals the detailed velocity structure for the sediments and crust along a 350-km cross-margin line on the Labrador margin.

(2) The crust can be divided into three distinct zones from west to east. Zone I represents a wide thinning zone of the continental crust. Beginning at a thickness of 27 km at 0 distance, the continental crust is thinned to 10 km at 140 km distance where Zone I ends. The crust in Zone I is dominated by lower continental crust. Upper continental crust terminates at ~52 km, seaward of which only middle to lower crustal velocities are observed.

(3) Zone II is characterized by a lower crust with a high-velocity of 6.4-7.7 km/s. This layer is only 5-6 km thick, extending laterally for 80-90 km. This layer is interpreted as serpentized peridotite, although an alternative interpretation of underplate is also possible.

(4) Zone III is characterized by a 5.5 km, two-layer crust which is typical for an oceanic origin.

(5) Combined gravity modeling for the both margins of the Labrador Sea supports the velocity structure in Zones I and II in Figure 5.22, but results in a computed anomaly higher than observed for Zone III. Normal oceanic crust was first created between Chrons 27 and 31.

## **Chapter 6. Reconstruction of Rift-Stage Crust Across the Conjugate Margins of Labrador Sea**

Chapters 3, 4, and 5 presented detailed velocity sections for the sediments and crust across the SW Greenland and Labrador conjugate continental margins. Three distinct zones have been identified and correlated for each margin. This chapter combines all these seismic results, and tries to arrive at a uniform interpretation which is supported by the available data. This interpretation will consider two fundamental issues common to nonvolcanic continental margins: (a) whether the high-velocity lower crust in Zone II represents underplate or serpentinite; and (b) whether rifting is best described by a mechanism of simple shear, pure shear, or a combination of both types.

### **6.1 Location of Continent-Ocean Boundary**

As discussed in Chapters 4 and 5, there exists a wide (70-80 km) zone of crust with an anomalous high-velocity across both Labrador and Greenland margins. This zone is characterized by velocities as high as 6.4-7.6 km/s in the thin (~5 km thickness) lower crust. Most of the thin (~2 km thickness) upper crust in this zone has a low-velocity of 4-5 km/s which resembles neither the typical continental crust in Zone I nor the oceanic crust in Zone III. As seen in Figure 6.1, Zone II is nearly symmetrically distributed offshore on the conjugate margins of the Labrador Sea. The transitional nature of Zone II must be taken into consideration in determining the continent-ocean boundary (COB).

A similar two-layer transitional crust has been recently reported for several nonvolcanic rifted continental margins, and yet its relation with the position of COB has

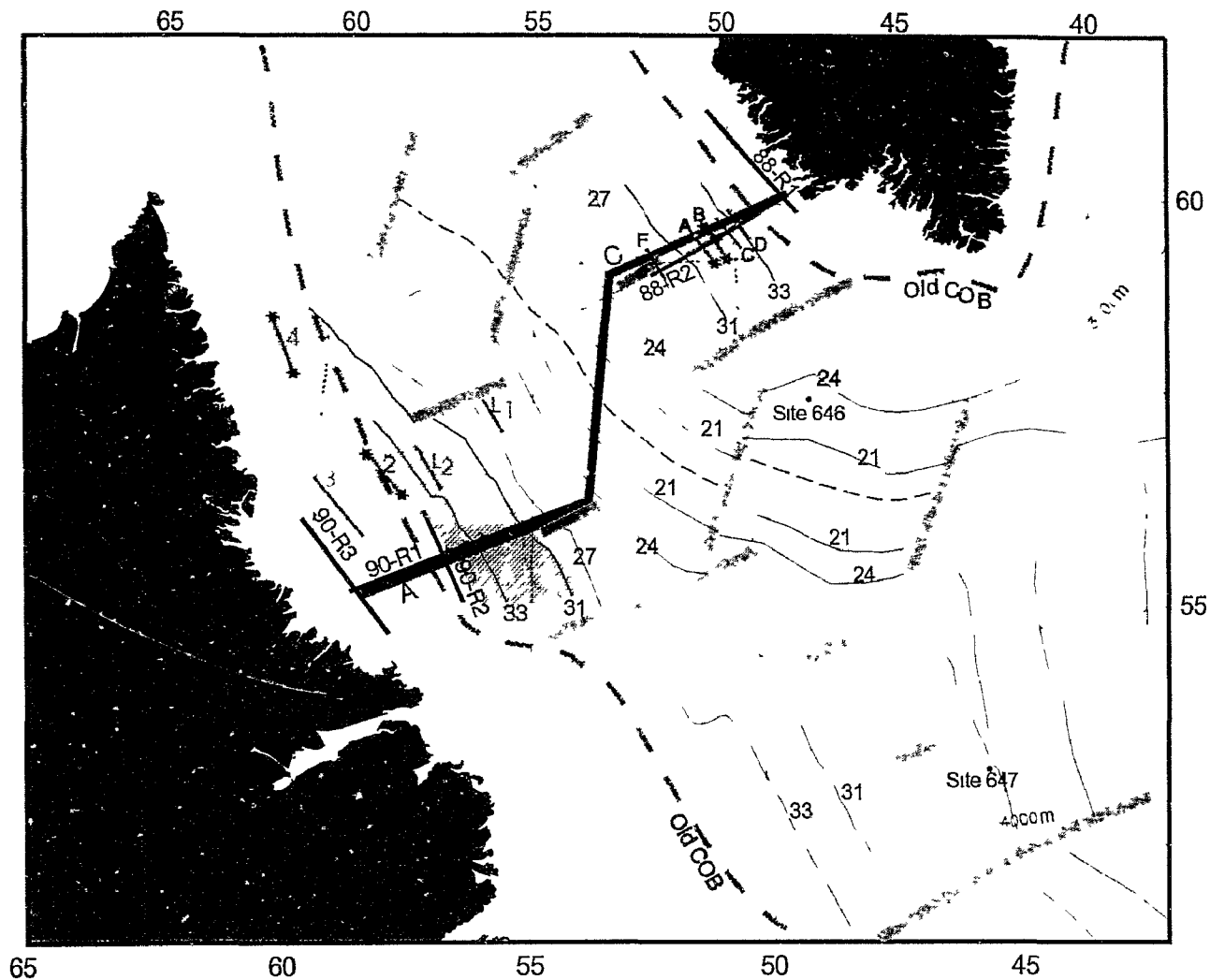


Figure 6.1 Map of the Labrador Sea, showing zones with high-velocity lower crust (light shading). Also shown are refraction lines 88-R1, 88-R2, 90-R1, 90-R2, and 90-R3 (thick solid), cross-basin reflection lines A and C (thick heavy), bathymetric contours (thin dotted), chrons (thin solid), fracture zones (thick grey), and extinct rift axis (thin broken), and old continent-ocean boundary (thick broken).

not been clearly understood. For example, Whitmarsh et al. (1990) observed on the Iberia margin a significant velocity difference between normal oceanic crust and the high-velocity transitional crust and placed the COB at this seaward boundary. On the margins of Newfoundland, however, Todd and Reid (1989), Reid and Keen (1990), and Reid (1994) place the COB at the landward boundary between normal continental crust and the high-velocity crust. Comparing these data with the velocity profiles across the margins of the Labrador Sea (Figures 6.2-3), it can be seen that these proposed positions of the COB approximately correspond to the two boundaries between Zones I, II, and III.

The same two positions of the COB in the Labrador Sea are also suggested by Keen et al. (1994b) from the multi-channel reflection data on lines 90-1 and 90-3, which are coincident or nearly coincident with refraction lines 90-R<sub>1</sub> and 88-R<sub>2</sub>. On both margins, these data exhibit a clear change in basement topography (COB1) close to the junction of Zones I and II, possibly produced by large rotated fault blocks in continental basement to oceanic crust. The alternative to this scenario is that the COB lies further seaward, between Chrons 31 and 27. This location (COB2) is marked by a change in basement reflective character with smoother basement found farther seaward in Zone III on both sides of the basin. This feature is most prominent on the Labrador side, where COB2 is associated with a 1 km change in basement depth and the seaward appearance of a clear intra-crustal reflector. In contrast, landward of COB2 the crust is "transparent" in its reflective character.

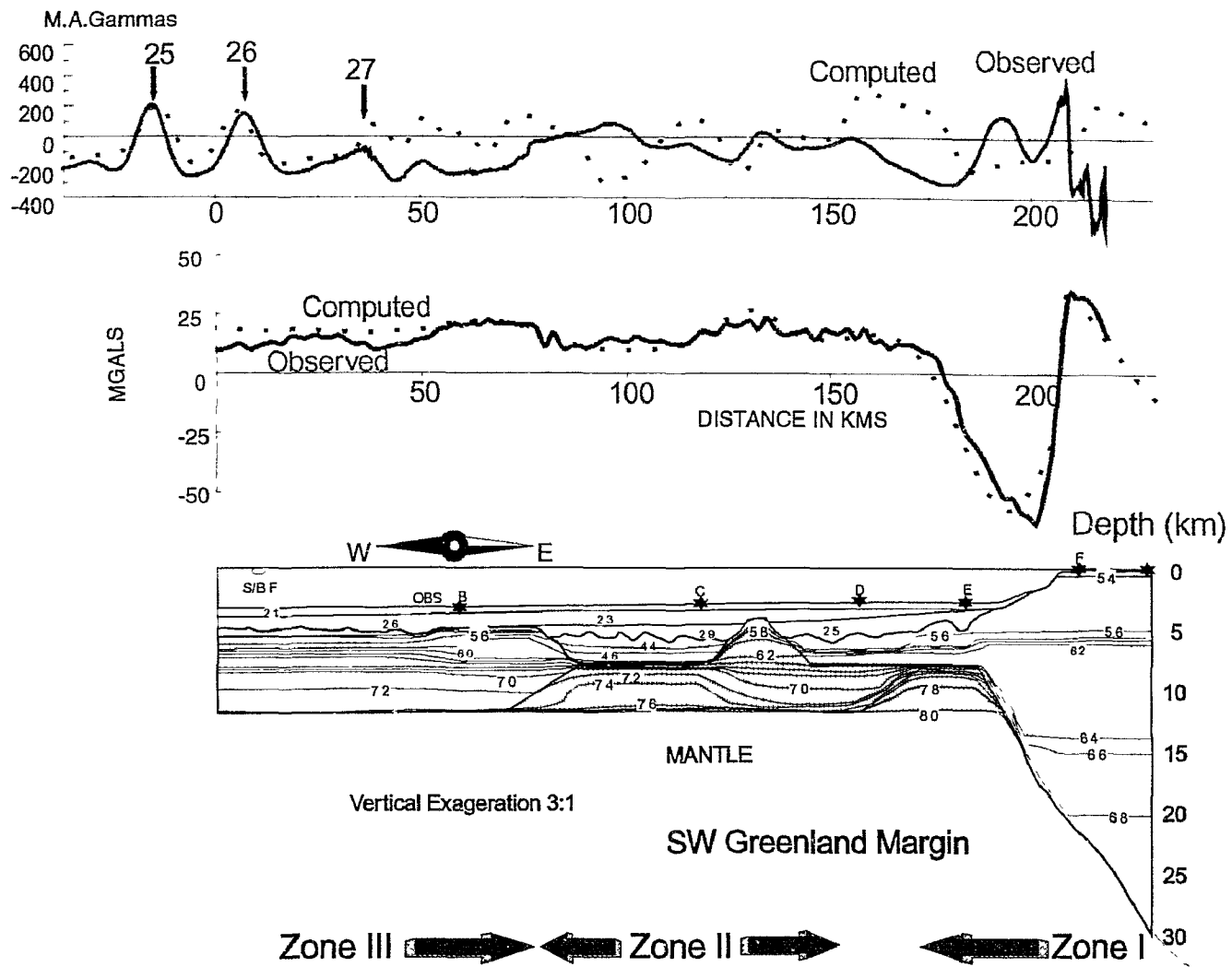


Figure 6.2 Compilation of magnetic (top), gravity (middle), and seismic velocity (bottom) results across the SW Greenland continent margin. The velocity contour interval is 0.2 km/s. For more description of this figure, see captions of Figures 4.10 and 4.12.

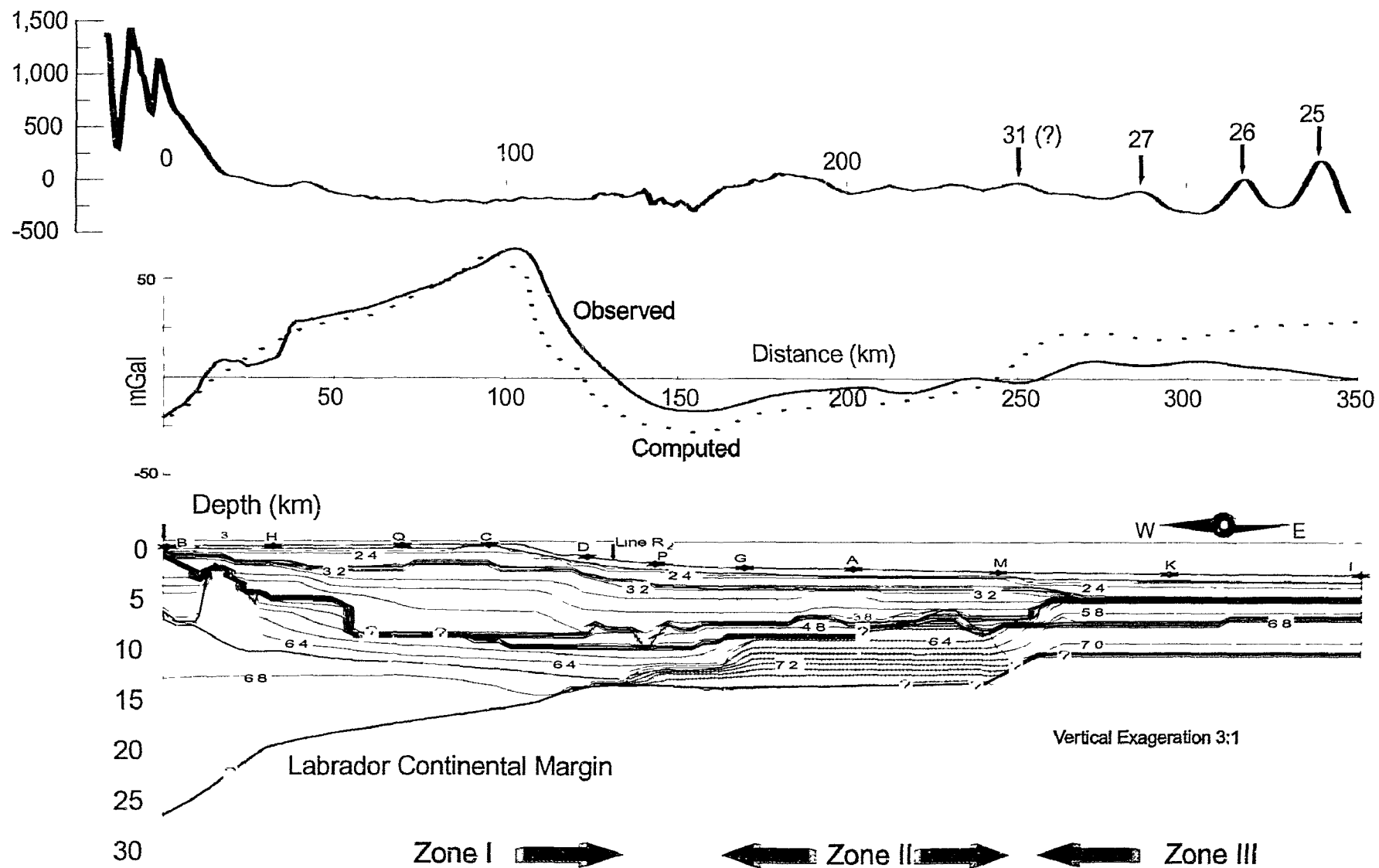


Figure 6.3 Compilation of magnetic (top), gravity (middle), and seismic velocity (bottom) results across the Labrador continent margin. The velocity contour interval is 0.2 km/s. For more description of this figure, see captions of Figures 5.22 and 5.25



I suggest that neither of these two discrete boundaries can represent the true COB on nonvolcanic rifted margins. Similar to the interpretation of the ocean-continent transition on the Iberia margin (Whitmarsh et al. 1993), the actual COB on the conjugate margins of the Labrador Sea is probably best described by the wide area of Zone II, rather than a sharp vertical boundary. The main reason for this interpretation is that the high-velocity nature of Zone II is completely different from either the continental (Zone I) or oceanic crust (Zone III), and a positioning of a sharp COB would imply that the material of Zone II has a predominantly continental or oceanic origin.

Figure 6.1 shows a plan view of the locations of the high-velocity layer (shaded areas) in the Labrador Sea. In this figure I include the results of the new refraction data presented in thesis, and the older wide-angle profiles of Van der Linden (1975) on the northern Labrador margin, and of Stergiopolous (1984) on the SW Greenland margin. Filled stars represent locations of the OBS or sonobuoys which show evidence for a high-velocity lower crust. When the positions of high-velocity material are connected to form a band at each margin, this band approximately follows the northwestern trend of magnetic anomalies and covers crust older than Chron 31. It is interesting to note from Figures 6.2-3 that the magnetic anomalies associated with these bands are of irregular and low amplitudes, a pattern different from the well-defined, high amplitude Anomaly 27 and other younger anomalies. This is suggestive of a different origin for Zone II.

Setting Zone II as a wide region between continental and oceanic crust implies that true seafloor spreading in the Labrador Sea started seaward of this zone at Chrons 27-31.

This is consistent with the interpretation of Chalmers (1991) which is based on reprocessing of some old MCS reflection data across the western Greenland margin. The revised timing for the initiation of oceanic crustal generation is younger than the previously suggested position at Chron 33, based on the identification and modeling of magnetic anomalies in the Labrador Sea (Srivastava and Tapscott 1986).

The above interpretation of a wide zone as ocean-continent transition (OCT) instead of a sharp COB is similar to the suggestion of Whitmarsh et al. (1993) who proposed that an OCT several tens of kilometers wide exists on the Iberia margin. It is likely that this OCT, and the high-velocity zone on the conjugate margin of Newfoundland (Todd and Reid 1989, Reid and Keen 1990, and Reid 1994), are the same layer as Zone II on conjugate margins of the Labrador Sea. A wide zone of transitional crust may be a common feature for nonvolcanic rifted continental margins.

## **6.2 Origin of Transitional Crust**

As summarized in Chapter 4, a high-velocity ( $>7.2$  km/s) transitional crust has been observed on many nonvolcanic rifted margins, and is interpreted as either underplate (i.e. high-Mg mafic gabbro) (Todd and Reid 1989; Reid and Keen 1990; Whitmarsh et al. 1990; Keen et al. 1994b) or undercrusted serpentinized peridotite (Pinheiro et al. 1992; Reid 1992, 1994). It is unfortunate that seismic velocities ( $P$  and  $S$  waves) alone cannot definitely distinguish between these two models as discussed in Chapter 4 (Figure 4.13). In this section, I will try to combine other available observations with the refraction data and discuss the implications of each interpretation.

The concept of magmatic underplating was initially proposed for volcanic rifted margins to explain the existence of seaward-dipping reflectors and an anomalous high-velocity (7.2-7.6 km/s) lower crust (Mutter et al. 1984; White et al. 1987). One explanation for this is that the anomalously high asthenospheric temperature associated with hotspot activity generates excessive partial melting which is responsible for the extrusion of basalt (seaward-dipping reflectors) and the large volume of underplated material (high-velocity lower crust) (White and McKenzie 1989; Campbell and Griffiths 1990). Alternatively, a convective melt model (Buck 1986; Mutter et al. 1988) can also explain the generation of significant volumes of melt without a major thermal anomaly. It is unfortunate that this second model does not provide any mechanism for generating the observed high-velocities. This is partly because this model does not invoke a high asthenospheric temperature, which, in the simple model of White and McKenzie (1989), is required to produce high-Mg and therefore high-velocity mafic gabbro. The results of melt generation on volcanic rifted margins have been extended to nonvolcanic margins to explain the existence of a lower crustal layer which has a high-velocity of >7.2 km/s similar to volcanic margins (Todd and Reid 1989; Reid and Keen 1990; Whitmarsh et al. 1990).

Alternatively, the high-velocity crust in Zone II can represent serpentinized peridotite. Such a model has been developed to explain the ODP drilling results on Galicia Bank and in the Iberia basin, and the geometry of an intra-crustal S-reflector. The S-reflector is observed over the Armorican and Galicia continental margins and has been

interpreted as the seismic signature of a syn-rift detachment fault rooted in the lower crust (Le Pichon and Barbier 1987; Sibuet 1992) or upper mantle (Boillot et al. 1987). Boillot et al. (1992) suggest that the S-reflector correlates with the top of a serpentinite body whose shallow ridges have been partly sampled by ODP drilling (Leg 103; Boillot et al. 1987). These peridotites show strong mylonitization in a normal shear zone before their serpentinization (Girardeau et al. 1988; Beslier et al. 1990). ODP drilling on other peridotite ridges during Leg 149 (Shipboard Scientific Party 1993) in the Iberia basin supports these interpretations. Therefore, the S-reflector may represent the tectonic contact (ductile shear zone) between the continental basement and serpentinized peridotite.

Such a serpentinite body on the Galicia margin is associated with a high-velocity and high gradient from  $\sim 6$  km/s to  $>7.2$  km/s, as suggested by some sonobuoy refraction data (Sibuet et al. 1992). Approximately 120 km southward in the Iberia basin, refraction results of Whitmarsh et al. (1990) reveal a high-velocity (7.3-7.6 km/s) lower crustal layer sitting at a similar position as the drilled serpentinite body. This high-velocity layer is overlain by a thin upper crust bearing a low-velocity of  $\sim 5$  km/s. Assuming that this upper crust has a continental origin which is consistent with the scenario of Boillot et al. (1992), it follows that the upper continental crust atop the S-reflector has a low-velocity compared to normal upper continental crust whose velocity is typically in the range between 5.5 and 6.0 km/s. Surprisingly, this crustal structure has been observed on many nonvolcanic rifted continental margins. For example, refraction data east of

Newfoundland (Reid 1994) show a thin, high-velocity (7.2-7.7 km/s), lower crust interpreted as serpentinite. This layer is overlain by a thin layer with a low-velocity velocity of 4.5-5.0 km/s. A similar velocity structure is also observed on the southern and northern margins of Flemish Cap (Todd and Reid 1989; Reid and Keen 1990). Although at these two locations the high-velocity crust was tentatively interpreted as underplate, it could also be serpentinite. A similar structure is also observed on the Tagus Abyssal Plain, where the 2-km thick 4.4-6.3 km/s upper crust is underlain by 7.6-7.9 km/s material (Pineiro et al. 1992). It should be noted that these profiles do not extend far enough to cover the complete continental, transitional, and oceanic crustal sequence, as do the data for the Labrador and Greenland margins presented in this thesis (Figures 6.2-3).

The success or failure of each of the two models (underplate and serpentinite) is summarized in Table 6.1. In this table, check marks indicate success of a specific model prediction for the observations. Question marks represent uncertainty between predictions and observations, and crosses indicate failure of the predictions. It can be seen that while each of the two models explains some of the features observed on seismic profiles, neither model can unequivocally explain all the phenomena:

(1) Geometry of Crust: In case of the melt model, a higher asthenospheric temperature is invoked to produce the observed high-velocity by enriching the Mg content (Furlong and Fountain 1986; White and McKenzie 1989). However, this high asthenospheric temperature will generate a volume of underplate more than five times thicker than observed on nonvolcanic margins. In the serpentinite model (Sibuet et al.

1992; Boillot et al. 1992), the high-velocity layer is also well explained by partial serpentinization of mantle material (Christensen 1966; Fountain and Christensen 1989). This model requires tectonic denudation and serpentinization of the mantle followed by undercrusting over a wide (70-80 km) area. The difficulty with this model is the absence of any melt along this wide zone where the continental crust is stretched by a factor  $\beta > 10$ .

(2) Location of Crust: Another difficulty with the melt model is that it cannot explain why the underplate is offset by ~80 km seaward of, and does not exist beneath, the thinned continental crust where underplating is typically located. In addition, most of the underplate body is overlain by a thin (~2 km thickness) layer with a low-velocity of 4-5 km/s. In contrast, a general conception for underplated crust is that its landward side is overlain by crust with a typical continental velocity (e.g. Mutter et al. 1984; White et al. 1987; Holbrook et al. 1994). On the other hand, the lateral offset of the high-velocity material is relatively easy to explain with the serpentinite model in which the serpentinites are transported along a rift-related shear zone to the lower crustal level where they become undercrusted. In this model, the low-velocity of the upper crust can be tentatively explained by faulting and interaction with seawater.

The differences in the distribution of high-velocity crust between nonvolcanic and volcanic margins are also seen when comparing profile 88-R<sub>2</sub> on SW Greenland margin with another refraction dataset which is ~500 km north of my study area on the western Greenland shelf (Gohl and Smithson 1993). Here the high-velocity (~7.5 km/s) lower crust is located beneath the shelf or even further inland, thickens northward from 3 km in the

south to 8 km towards Davis Strait, where abundant volcanism occurred at ~Chron 24. Therefore, it is reasonable to interpret this high-velocity layer as the rift-related Mesozoic underplating into the lower continental crust, whereas the high-velocity crust observed in our data is located much farther seaward and was formed before Chron 31 time (see Figure 6.1).

(3) Absence of extrusives and appearance of a possible S-reflector: Seaward-dipping reflectors are a typical feature of volcanic margins and may represent subaerial basalt flows (Hinz 1981; Eldholm et al. 1986). The absence of seaward-dipping reflectors and other geophysical (Balkwill 1987) signatures of rift-related extrusive melt indicates absence of such extrusive products. An example is the SW Greenland margin where a basement high is located on top of the high-velocity layer (Figure 6.2). The melt model would predict that this high is associated with a high-amplitude magnetic anomaly, but this is not observed. In contrast, a smaller amplitude would be produced if this is an extrusion of serpentinite (Schouten and Denham 1979). To explain the existence of an intra-crustal reflector (Keen et al. 1994b) in Zone II on the SW Greenland margin, the melt model would treat it as a possible crust/magma boundary similar to the case in de Voogt (1988). This reflector fits well into the serpentinite model, interpreted as an S-reflector acting as the seismic signature of a syn-rift detachment fault and is similar to observations from the Bay of Biscay and Galicia Bank margins (Le Pichon and Barbier 1987; Boillot et al. 1987; Sibuet 1992).

**Table 6. 1 Comparison Between Observations and Predictions of Melt and Serpentinite Models**

Observations	Melt Model	Serpentinite Model
$V_p = 7.2-7.7$ km/s	High $T_a$ (asthenospheric temperature) $\rightarrow$ High Mg ratio $\rightarrow$ High $V_p$ $\checkmark$	Partial serpentinization of mantle $\rightarrow$ High $V_p$ $\checkmark$
$h$ (thickness) = 3-5 km	High $T_a \rightarrow h > 15$ km $\times$	Requires large stretching without melt for 80 km $\times$
$W$ (width) $\sim 75$ km $\gg h$	Observed $W \sim 20-60$ km $\checkmark$	Requires exposed mantle over a wide area ?
High-velocity lower crust offset seaward from slope by $>50$ km	Underplate beneath slope $\times$	Requires undercrusting of serpentinites, transported and emplaced along the shear zone $\checkmark$
No magmatism in the overlying crust and sediments	Presence of dipping reflectors $\times$	Not required $\checkmark$
Strong intra-crustal reflector (SW Greenland); basement feature non-magnetic	Possible crust/magma boundary; Volcanic basement $\rightarrow$ magnetic ?	S Reflector; Serpentinized crust less magnetic $\checkmark$



From the above analysis, I conclude that the crustal structure on the conjugate margins of the Labrador Sea supports a serpentinite model more than a melt model for the formation of the ocean-continent transition in Zone II.

### **6.3 Nature of the Thinned Upper Crust**

This section reviews seismic evidence for the determination of the geometry and physical properties of the upper crust in Zones I and II, and discusses the nature of the thinned preexisting continental crust on the conjugate margins of the Labrador Sea. This discussion is important because it affects the reconstruction of pre-breakup continental crust, and has important implications for the model of rifting.

The upper crust in Zone II on the SW Greenland margin is characterized by a low-velocity layer of 4-5 km/s, as defined by OBS C on refraction line 88-R<sub>2</sub>. This low-velocity forms a strong velocity contrast with the underlying high-velocity layer, producing a clear intra-crustal reflector (called quasi S-reflector in this thesis) on the MCS reflection profile 90-3 (Keen et al. 1994b; Figure 6.4a, see insert back cover). Similar to the *S* reflector on the Galicia margin (Hoffman 1991), this quasi S-reflector extends nearly continuously through Zone II and disappears beneath the continental slope. The crust above this reflector appears to be highly faulted (Figure 4.2) and its low-velocity is compatible with the 4.2 km/s velocity for the upper continental crust above the S-reflector on the Galicia margin (Sibuet 1992). This layer is interpreted in Chapter 4 as tilted fault blocks of upper continental crust thinned by a factor of 2-3. The reduction of the velocity in this layer with respect to the velocity (5.5-5.6 km/s) for normal upper continental crust on the shelf of

SW Greenland (Chapter 4) and Labrador (Reid 1994) can be interpreted to be a result of stretching and faulting.

If the upper crust of Zone II on the SW Greenland margin is thinned upper continental crust, its seaward end would probably correspond to an observed interruption of the upper continental crust in the mid-shelf at ~52 km on the Labrador profile (Figure 6.3). Since the sediment close to this point is very thick (6-9 km), and the basement surface exhibits large relief, care is needed to properly model the crustal structure in this area.

1. Reflection data show a pattern change around 52 km distance, from steep-dipping, irregular events on the left side to flat continuous events on the right side (Figure 6.4b, see insert back cover).
2. On refraction profiles (Table 6.2), the modeled termination of upper continental crust at ~52 km produces a match in travel-time to a clear concave-shaped phase ( $P_2$ ) at OBS H (Figure 5.11) which can not otherwise be modeled. A deeper phase  $P_3$  is refracted from crust with a velocity of 6.2-6.9 km/s which represents middle and lower continental crust.
3. The adoption of the upper crustal termination at 52 km distance also enables proper modeling of a travel-time 'pull-down' of >0.5 sec for crustal phases  $P_2$  and  $P_3$  at western ranges of OBS Q (Figure 5.12). At eastern ranges of this OBS, modeling of phase  $P_3$  supports the determination of a one-layer crust with velocity of 6.2-6.9 km/s seaward of the termination point.

4. The termination of upper crust at 52 km is also exhibited in the travel-time ‘pull-down’ of  $\sim 0.5$  sec around  $\sim 40$  km range for  $P_3$  of OBS C (Figure 5.13).
5. The one-layer structure is compatible with the crustal structure at 100-160 km distance where there exists a dense ray coverage from OBS D and  $P$  (Figures 5.14-15), and refraction line 90-R<sub>2</sub> (Figures 5.5-8).

Seaward from the point at 100 km distance on the Labrador margin, an extra, highly faulted, upper crust starts to appear on top of the lower continental crust. This upper layer has a small thickness of  $< 2$  km and a low-velocity of 4.6-5.0 km/s (OBS D, P and A on 90-R<sub>1</sub>, Figures 5.14-15, 5.17; and the four OBS on line 90-R<sub>2</sub>, Figures 5.5-8). This layer extends seaward at least half-way through Zone II to 200 km distance where the crustal column is ‘transparent’ on MCS reflection profiles (Figure 6.4b, see insert back cover). Therefore, there is no clear-cut boundary separating the low-velocity upper crust and the high-velocity lower crust, implying a high velocity gradient within the crustal column. I suggest that this low-velocity upper layer was formed by a process in which fractured continental crust or upper mantle interacts with seawater. This also explains why this upper layer extends over both continental crust and the high-velocity region. For the SW Greenland margin, however, the upper crust is possibly more brittle due its continental nature, which results in a sharp boundary with the underlying high velocity lower crust rather than in a large vertical velocity gradient as on its conjugate Labrador margin.

It should be noted that the above interpretation for the low-velocity upper crust as thinned continental crust overlying a quasi S-reflector on the SW Greenland margin is by

no means definitive. The corresponding termination of the upper crust on the Labrador margin is interpreted based on reflection and refraction data in the presence of thick sediments. However, this interpretation does provide an overall fit to the existing reflection and refraction data and its important implications for the initial rifting, which will be discussed in the next section, can be tested when more data become available.

#### **6.4 Reconstruction of Pre-breakup Crust and Rifting Model**

In the previous chapters I presented a detailed velocity profile across the conjugate margins of the Labrador Sea. The combination of these results with coincident multi-channel reflection, gravity, and magnetic data (Figures 6.2-4) provides an opportunity to re-connect crust that has been separated due to subsequent seafloor spreading. This reconstruction leads us to visualize the pre-breakup crustal structure and provides a basis for building a balanced cross-section and for developing a model for rifting.

Figure 6.5 shows a reconstruction of the seismic data at Chron 27 (69 Ma) which is the first clearly defined magnetic anomaly. In doing this I have removed most of the oceanic crust in Zone III. It can be seen that the high-velocity layer of Zone II on both margins is still not completely joined. As discussed in Chapters 4 and 5, structural complications exist between anomalies 27 and 31, the latter of which marks the end of the transition region (Zone II) and the beginning of true oceanic crust (Zone III).

To proceed to a cross-section of rifted continental crust for the Labrador Sea, let us move the crustal velocity structure closer to each other. Since there is a clear asymmetry in the sediment thickness on both margins, I remove the complete water and

**Table 6. 2 Supporting Refraction Observations for the Upper-Continental**

**Termination on the Labrador Margin**

OBS	Seismic Phases	OBS Ranges or Model Distance	Comments
H (Figure 5.11)	P <sub>2</sub>	(20, 30) km ranges	Clear concave-shape of travel-time due to the sharp basement topography at ~52 km
H (Figure 5.11)	P <sub>3</sub>	(37, 50) km ranges	Crust with V <sub>p</sub> = 6.2-6.9 km/s seaward of 52 km
Q (Figure 5.12)	P <sub>2</sub> , P <sub>3</sub>	(-50, -22) km ranges	Possible travel-time pull-down by >0.5 sec from P <sub>2</sub> to P <sub>3</sub> due to basement topography at 52 km
Q (Figure 5.12)	P <sub>3</sub>	(28, 40) km ranges	Supports one-layer crust seaward of 52 km
C (Figure 5.13)	P <sub>3</sub>	(-60, -30) km ranges	Possible travel-time jump of ~0.5 sec around -40 km range due to the basement topography
D, P (Figures 5.14-15), and Line 90-R2 (Figures 5-8)	P <sub>2</sub> , P <sub>3</sub>	100-160 km model distance	Dense ray coverage; velocity structure compatible with the one-layer model landward of 100 km

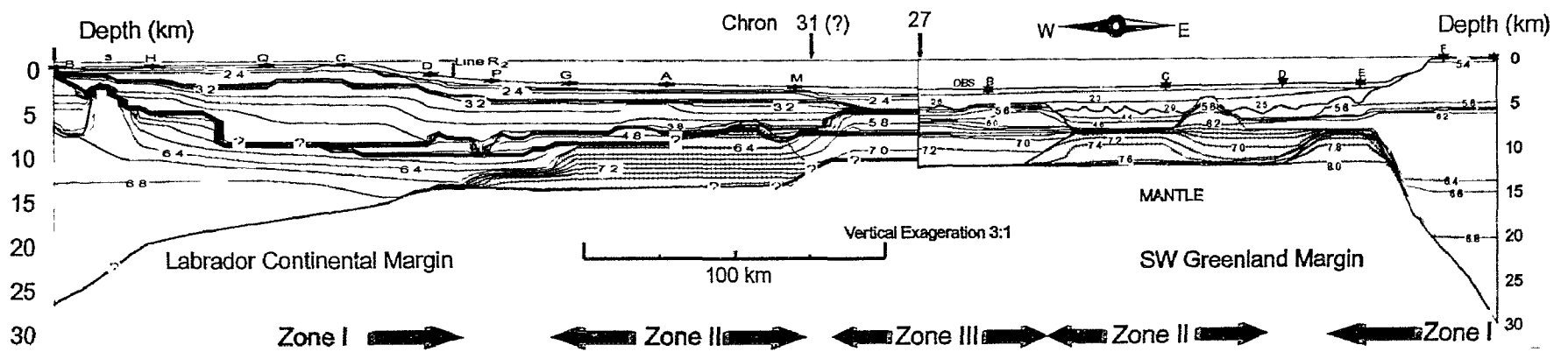


Figure 6.5 Reconstruction to chron 27 for velocity contour profiles for crust transecting the conjugate margins of the Labrador Sea.

sediment column to emphasize the balanced crustal structure. Assuming local isostatic adjustment, I take the crustal models for both margins and calculate the corrected basement depth after removing the sediments and water. In doing this, the density contours obtained from gravity modeling are used for calculating the sediment load.

Figure 6.6a shows such a cross section reconstructed at Anomaly 31. Zone III is completely removed from this section. It can be seen that the basement surface and the Moho in Zone II for both margins are at a similar depth. The high-velocity crust in Zone II extends for almost equal distance on either side of Chron 31. Figure 6.6b shows the same cross-section with the high-velocity material removed. A rather thin (<2 km) crust appears over a wide (~160 km) area. This is an unusual crustal configuration and it is clear that its explanation must include a proper description of the high-velocity material underneath. If one assumes that the crustal cross-section shown in Figure 6.6b cannot exist by itself, it follows that this high-velocity material was formed before Chron 31.

The initial crustal configuration at the time of the final crustal separation is determined by removing Zone II. As discussed in Section 6.3, the seaward termination of the upper crust on the Labrador margin matches the seaward termination of the upper crust from the conjugate Greenland margin. Therefore, in this reconstruction, the thin upper crust above the quasi S-reflector on the SW Greenland margin is retained and assumed to move together with Zone I. To avoid overlapping of crust, the Moho at each point is adjusted vertically by an amount equal to the thickness of the thinned upper crust

contributed from SW Greenland. The low-velocity upper crust on the Labrador margin (yellow area in Figure 6.6c) is removed in this reconstruction.

The geometry and velocity structure of the stretched, preexisting continental crust at the time of the breakup is reconstructed in Figure 6.6c. It can be seen that at this time there was a zone of continental crust thinned by a factor  $\beta > 3$  extending for over 100 km within the rift zone. Assuming that the Moho is 34 km at 20 km to either side of the reconstructed model, the overall thinned crust totals 3830 km<sup>2</sup>. When divided by the crustal thickness (34 km), this gives 113 km. Therefore, assuming mass conservation during stretching, an initial 113-km wide preexisting crust was stretched to a width of 242 km as seen on the reconstructed cross section. This gives an overall stretching factor of 2.1. Interestingly, this number is similar to the stretching factor of 2-3 calculated from the tilted blocks off SW Greenland (Chapter 4), suggesting that the upper and lower crust were stretched by a similar amount before breakup.

The overall appearance of the reconstructed rift zone crust (Figure 6.6c) is that immediately before the final crustal separation. The stretching event had affected crust over a 200 km distance on the cross-section, with more stretching occurring close to the eastern end of the rift. If I define the lower crust by a velocity of 6.2-6.9 km/s, I see that the lower crust was broken up (or rifted) at the eastern end of the rift zone, causing all the stretched lower crust to move together with the Labrador margin, and the lower crust on the Greenland side is basically unmodified. Therefore, the location of the lower crustal separation is compatible with the location of the thinnest continental crust.



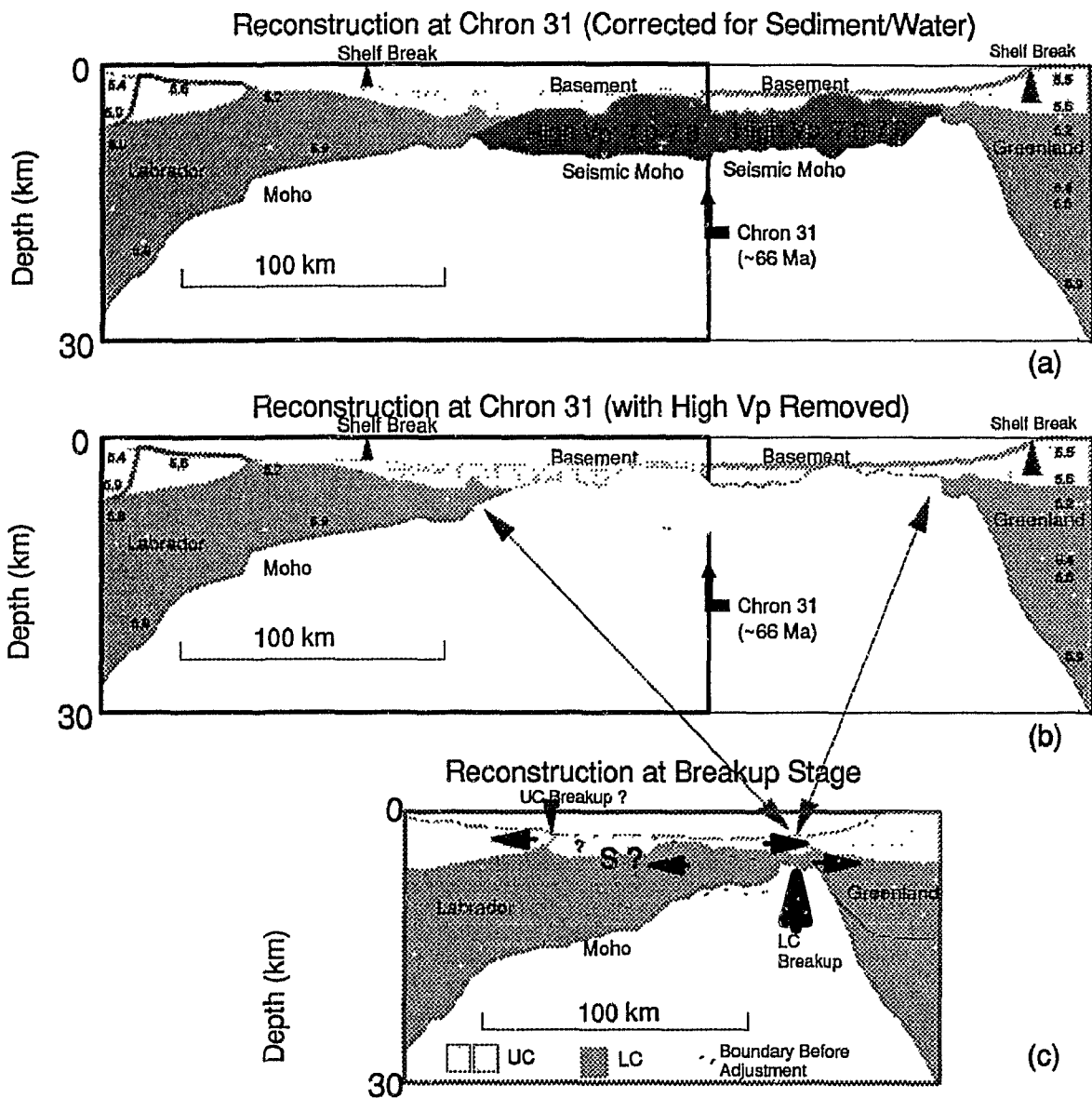


Figure 6.6 Reconstruction of crust from both margins. Water and sediment are stripped off assuming isostatic adjustment. (a) Crustal reconstruction to Chron 31 (68 Ma). The high-velocity regions are joined. (b) The same cross-section as (a) but with the high-velocity crust removed, showing a wide (~160 km) zone of thin upper crust. (c) Seaward ends of lower crust for both margins are joined to show the balanced cross-section at the time of the final breakup. Slight vertical adjustment of basement surface and the Moho is performed to eliminate overlap of crust contributed from the SW Greenland margin. For comparison, dotted lines represent positions of the basement surface and the Moho before this adjustment.

If I move both margins further towards each other, overlapping of the lower crust will occur. Similar to the method for the upper crustal overlap, I assume that during the stretching the masses of the upper and lower crust are respectively conserved and the deformation of overlapped areas occurs ductilely. I start from the crustal structure at the time of the final crustal separation (Figure 6.6c), move the both margins closer to each other until the thinnest crust near the lower crustal rifting point disappears. The resulting overlapped areas are shifted to their nearest locations where no overlapping would occur. This re-shaping results in an intermediate stretching stage as shown in Figure 6.7b. Figure 6.7a shows such a reconstruction at the time of the onset of continental stretching assuming an initial Moho depth of 34 km which is based on gravity modeling. It can be seen that at the early stage the continental stretching was symmetric, which generated a symmetric rift zone with a similar stretching factor in the upper and lower crust. This conforms to a pure shear scenario. At the late stage of the stretching of crust, however, more stretching started to build up locally towards the eastern side, which led to a final breakup of the lower crust at the eastern end of the rift zone.

The position of breakup of the brittle upper crust may differ from that of the ductile lower crust. The two possible positions for the upper crustal breakup are indicated in Figure 6.7c as Rift 1 and Rift 2. Rift 1 is at a similar position as the COB1 proposed by Keen et al. (1994b) to explain the reflective character of tilted fault blocks for the SW Greenland margin. Rift 2 is my favored position for the upper crustal breakup. This is supported by seismic refraction and reflection evidence (see Section 6.3), which shows the

existence of an upper crustal termination point under the shelf of the Labrador margin (Table 6.2), and the existence of a wide zone of thin faulted crust atop a quasi S-reflector (Figure 6.4a, see insert back cover) on the Greenland margin. Only when this interpreted upper continental crust of the Greenland margin is included in the reconstruction can the upper crust from both margins be connected and the reconstructed profile be completed with continuous upper and lower crustal layering.

Therefore, I suggest that while the final rifting cut through the lower crust vertically at the Greenland end of the rift zone, the breakup of the upper crust occurred toward the Labrador side of this zone. As a result, two thirds of the thinned continental crust on the Labrador margin is not covered by upper continental crust. This missing part of the upper crust moved with the Greenland continent, and was later underlain by high-velocity material which is probably partially serpentinized peridotite (Section 6.2). The undercrusting of these serpentinites possibly started as soon as the upper and lower crust became detached. This enables the undercrusted serpentinites to be emplaced seaward of thinned continental crust on the Labrador margin. This serpentinization process evidently ceased at Chrons 27-31, when oceanic seafloor spreading was initiated to produce normal oceanic crust (Figures 6.2-3). Assuming a continental separation rate of 2 cm/yr which is calculated from the distance between Chrons 25 and 27, I get 8 m.yr. for the period of serpentinization. During this period, undercrusting of serpentinites occurred without melt generation. One way to explain this is that the continental lithosphere was still not thinned enough to allow melt generation. This implies that crustal separation predates the final

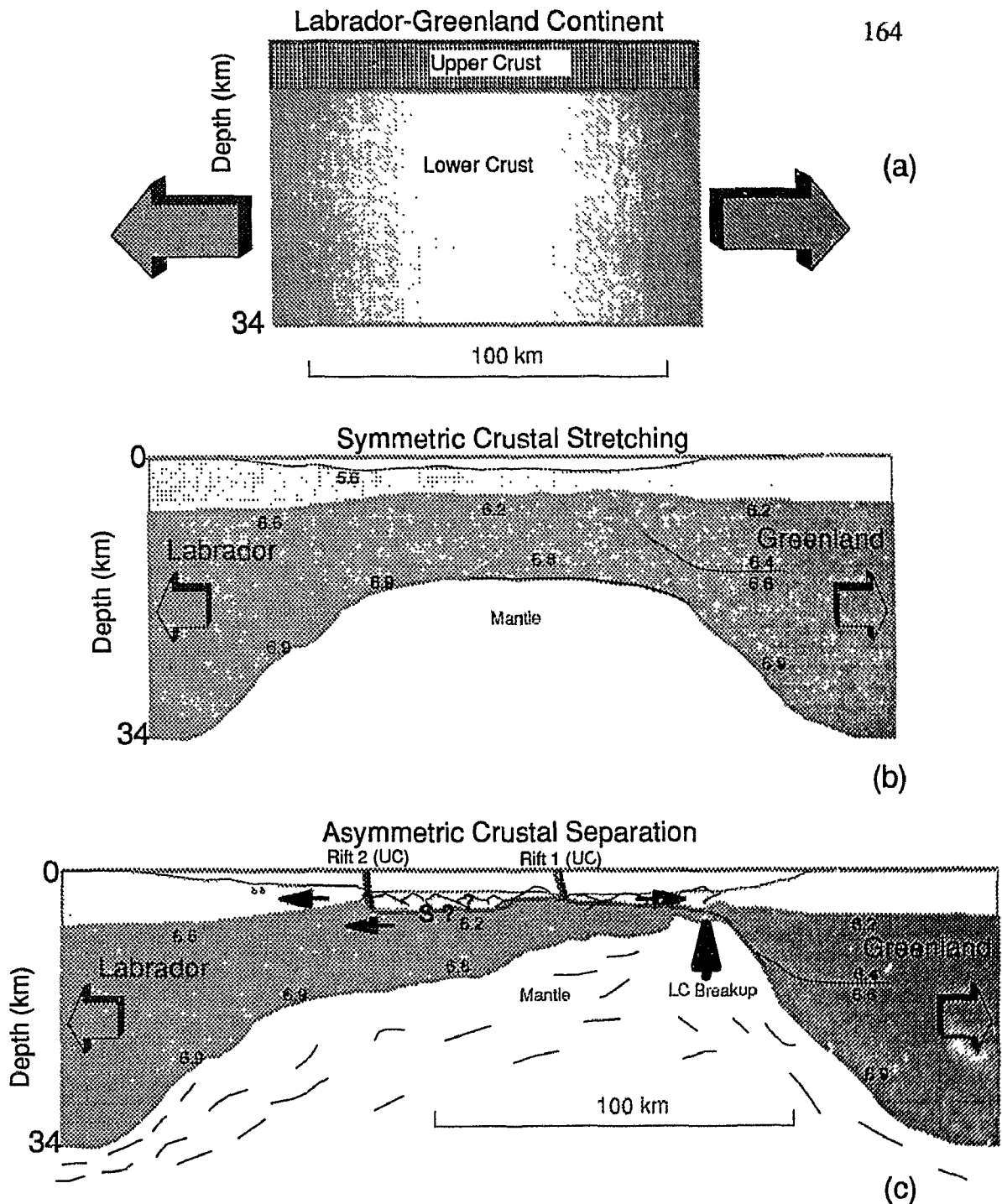


Figure 6.7 (a) Pre-stretching crust of the Labrador-Greenland continent. The area is obtained assuming conservation of the total crustal area during the stretching. This total area is obtained assuming no modification of crust 20 km to either side of the model in Figure 6.7c. (b) Restored cross-section with the asymmetry close to the point of lower crustal breakup removed. (c) Rift zone crust at the time of rifting according to Figure 6.6c. Rift 2 indicates the position for the interpreted upper crustal breakup. Rift 1 indicates another possible position for rifting of upper crust where the boundary between zones I and II is located.

necking of the lithosphere, which is the key factor for generating a wide zone of serpentinites without melt.

Some of the major steps in the proposed model for evolution of the margins of the Labrador basin are summarized below:

1. Stretching of the Canada-Greenland continent started at about 120-160 Ma (Watt 1969) with small-scale injection of dikes and asthenospheric upwelling, symmetric stretching of the continental lithosphere, the ductile lower crust, and the brittle upper crust.
2. Breakup of the lower crust at the eastern end of the rift zone at ~76 Ma; Breakup of the upper crust toward the western side of this zone. All the thinned lower crust moved with the Labrador continent; most of the thinned upper crust moves with the Greenland continent.
3. As a result of the crustal separation, water penetration into the upper mantle, generating high-velocity serpentinites which were subsequently uplifted to fill the ever-widening gap in the lower crust. No melt was generated while the necking of the lithosphere continued for approximately another 8 m.yr. before melt production.
4. After the crustal breakup, an extra 160 km of continental separation occurred before seafloor spreading was initiated at 62-68 Ma.

### **6.5 Comparison with Other Models**

The model proposed above (Figure 6.7) differs in a number of ways from the two competing models of Boillot et al. (1992) (Figure 6.8) and of Sibuet (1992) (Figure 6.8)

which are proposed for explaining the observed S-reflector and drilled serpentinite peridotite ridge on the Iberia margin:

1. The model of Boillot et al. (1989b) follows a simple shear scheme in which the low-angle master fault (S-reflector) cut the crust and upper mantle, and serpentinite peridotites are emplaced and undercrusted through the tectonic denudation process. In this model, the S-reflector forms the lower boundary of the faulted upper continental crust which is well observed by MCS reflection data (e.g. Le Pichon and Barbier 1987; Keen et al. 1989; Hoffmann 1991). This model provides a mechanism for the formation of peridotite ridges, the drilling results of which show strong mylonitization in a shearing environment. More importantly, this tectonic denudation model implies that the crust beneath the S-reflector is serpentinite, compatible with the high-velocity values observed on the Galicia and many other nonvolcanic rifted continental margins (e.g. Whitmarsh et al. 1990; Sibuet 1992; Reid 1994; Chapters 4 and 5). On the other hand, because the observed detachment surface does not cut the upper mantle (Le Pichon and Barbier 1987; Radel and Melosh 1987; Keen et al. 1989), and because earthquake foci in regions of active continental extension are always confined to the upper seismogenic continental crust (Jackson and White 1989), the mechanism of mantle denudation is dynamically not appropriate (Sibuet 1992).
2. Avoiding the introduction of a shear zone cutting across the upper mantle, Sibuet (1992) proposed a composite pure and simple shear model for the formation of the

Galicia and the southeastern Flemish Cap margins: pure shear for the whole continental lithosphere and simple shear for the final crustal breakup (Figure 6.9). In this model, the crust below the S-reflector is stretched lower continental crust, which is in conflict with the observed high-velocity for the lower crust on many nonvolcanic margins. In addition, the serpentinized peridotite is formed by seawater circulation at the end of the rifting phase at places where the crust is particularly thinned. This cannot explain the presence of serpentinites over a wide (70-80 km) zone. This model suggests that the crust seaward of the serpentinite ridge is oceanic, which is again in conflict with observation on the margins of the Labrador Sea, where the high-velocity lower crust exists far seaward of the thinnest continental crust.

3. The model proposed in this thesis is in part a combination of the models of Boillot et al. (1989b) and Sibuet (1992), and yet overcomes the difficulties encountered in these two existing models. Similar to Sibuet's model, the new model is a composite pure and simple shear model in which the mantle and crust were stretched symmetrically while the final crustal separation occurred asymmetrically by simple shear. The key factors for the success of this model are first, that all the rift-zone lower crust moved with the western margin and second, that the necking of the lithosphere continued after crustal separation (Figure 6.7). Serpentinites were produced during this later necking period, which ends with the initiation of seafloor spreading at 62-68 Ma. The concept of mantle denudation which is the foundation

of the model of Boillot et al. (1989b) is not required for producing the observed high-velocity serpentinites because in my model the serpentinites are undercrusted within the widening gap of the lower crust. As a result, the serpentinites are found seaward of the thinned continental crust on the Labrador margin, and yet on the SW Greenland margin underlying an S-reflector which bottoms the thinned upper continental crust. The initiation of seafloor spreading occurred with a significant change in crustal velocities, reflective patterns, and gravity and magnetic anomalies on each side of the basin (Figures 6.2-4).

The new extension model presented in this thesis as a whole is consistent with the MCS reflection data of Keen et al. (1989) for the conjugate Flemish Cap and Goban Spur margins. This restored cross-section shows a nearly symmetric extension with the final breakup occurring at the western side of the rift zone. This is similar to the restored cross-section for the conjugate margin pair of the Labrador Sea where the extension is nearly symmetric and the final breakup occurred at the eastern side of the rift zone. A difference between these two datasets is that on the Flemish Cap and Goban Spur margins the continent-ocean boundary appears to be a sharp boundary and no clear intra-crustal reflector that may represent an S-reflector is observed. Recent refraction data on the Goban Spur margin support these interpretations (Horsefield et al. 1994). Therefore, while the composite pure and simple shear mode may represent some rifted continental margin pairs such as that of the Labrador and Greenland, Iberia and Newfoundland, the final



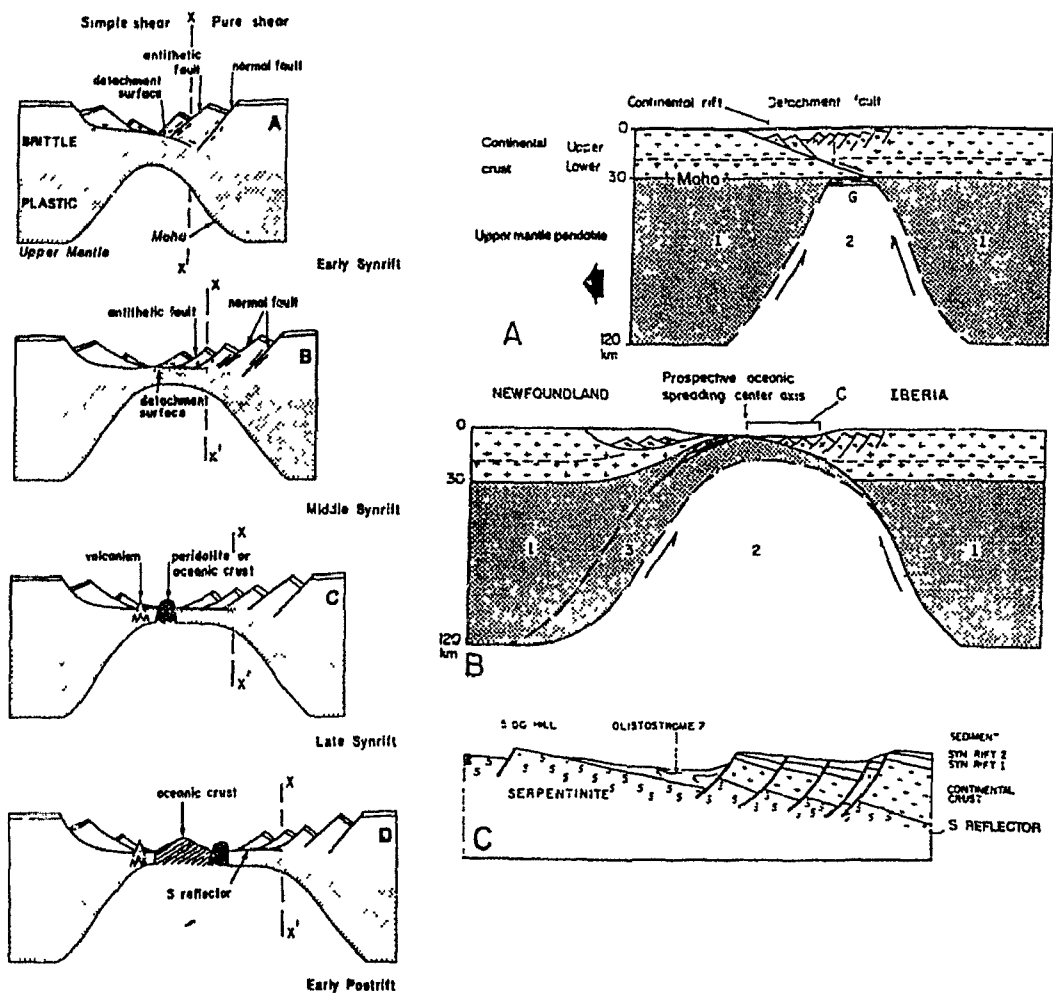


Figure 6.8 (left) Sibuet's rifting model; (right) Boillot's rifting model.

crustal separation may also take place in a pure shear mode, as on the conjugate margins of Flemish Cap and Goban Spur

## 6.6 Conclusions

In the above discussions I have analyzed the newly obtained crustal velocity structures across the conjugate margins of the Labrador Sea. These results are interpreted in combination with coincident multi-channel reflection, gravity, and magnetic data. This is the most extensive dataset for analyzing the crustal structure across nonvolcanic rifted conjugate margins. Comparison with datasets on similar margins show consistent results which suggest:

1. The conjugate margins of the Labrador Sea are divided on each side by three distinct zones according to crustal velocities. Zone I represents stretched continental crust, much wider on the Labrador margin than on its conjugate SW Greenland margin. Seaward of this zone, Zone II is characterized by existence of a high-velocity ( $<7.7$  km/s) lower crust, nearly symmetrically distributed over 50-80 km distance. The continent-ocean transition is best described by this wide zone rather than a sharp boundary. Further seaward, Zone III has typical oceanic crustal velocity, and its age is younger than Chrons 27-31 (62-68 Ma). A three zone division of this kind may also be applicable to several other nonvolcanic rifted margins such as Iberia and Newfoundland margins.
2. The high-velocity crust in this zone is more likely to be serpentinite than underplate.

3. A really balanced reconstruction of observed cross-sections for both margins suggests that the east-west stretching of the Labrador-Greenland continent started symmetrically. At the later stage of stretching, more thinning occurred in the crust towards the eastern side of the rift zone, leading to a final breakup of the lower continental crust at the point immediately next to unmodified Greenland continent. The data shown in this thesis suggest that the upper crust was rifted towards the Labrador side of the rift zone.
4. A composite pure and simple shear model is favored for the crustal rifting for the conjugate margins of the Labrador Sea. This model can easily incorporate the serpentinite model for the formation of the wide Zone II sitting symmetrically on both margins. In this scenario, the intra-crustal reflector on the SW Greenland side is an S-reflector, separating the stretched upper continental crust from underlying serpentinites, while on the Labrador margin the serpentinites were undercrusted seaward of the continental crust without producing an S type reflector.
5. For a proper modeling and interpretation of the detailed two-dimensional velocity contours for crustal structures across rifted continental margins, it is important to incorporate results from coincident MCS reflection profiles, especially when there is a thick sediment cover.

## Chapter 7. Summary and Future Work

### 7.1 Summary

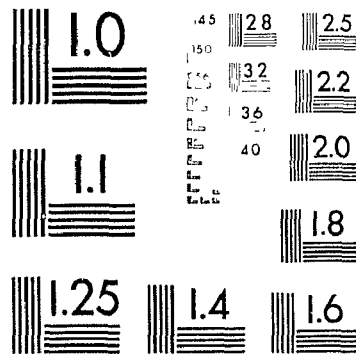
1. This thesis includes processing, modeling, and interpretation of four wide-angle seismic lines across the complete conjugate margins of the Labrador Sea. These data, coupled with coincident multi-channel and single-channel reflection, and gravity and magnetic data, reveal a clear picture of how the continental crust varies seaward to join the oceanic crust on both margins.
2. Wide-angle seismic signals from a total of 29 recording instruments (ocean bottom seismometers and sonobuoys) are analyzed in this thesis. These data are modeled using one-dimensional reflectivity and WKBJ, and two-dimensional ray-tracing methods wherever appropriate. For some profiles, *S* waves are also recorded and modeled. Error analyses are performed for selected crustal layers.
3. The crust across both margins can be divided on each side by three distinct zones according to crustal velocities. From the continent seaward, **Zone I** represents stretched preexisting continental crust, much wider on the Labrador margin than on the southwestern Greenland margin. Seaward of this zone, **Zone II** is characterized by high velocity gradient of up to 7.2-7.7 km/s in the lower crust. The crust in this zone is transitional and its high-velocity lower crust is nearly symmetrically distributed over 50-80 km distance. The continent-ocean transition is best described by this wide zone rather than a sharp boundary. **Zone III** has typical oceanic crustal

3

OF/DE

3

PM-1 3½"x4" PHOTOGRAPHIC MICROCOPY TARGET  
NBS 1010a ANSI/ISO #2 EQUIVALENT



PRECISION<sup>SM</sup> RESOLUTION TARGETS

velocity, and is associated with clear magnetic anomaly patterns younger than Chrons 27-31 (62-68 Ma).

4. A synthesis of these data suggests that creation of normal oceanic crust did not start until 62-68 Ma in the Labrador Sea. Landward of this oceanic crust, the high-velocity lower crust in Zone II is likely mantle-derived serpentinite rather than underplated mafic rocks.
5. The new cross-sections obtained in this thesis are used for restoring the history of continental rifting. The reconstructed profile shows the initial crustal cross-section at the time of the final crustal separation. It is seen that after this separation all the thinned lower crust moved together with the western margin (Labrador). Existing data cannot exclusively determine if most of the thinned upper crust moved with the eastern margin (southwestern Greenland), although this is suggested by some data.
6. A composite pure and simple shear model is proposed for nonvolcanic conjugate margins of Labrador and southwestern Greenland. In this model, stretching started symmetrically. At the later stage of the stretching, more crustal thinning occurred towards the eastern end of the rift zone, inducing breakup of lower crust near this area. The upper crust, however, was separated towards the western side of the rift zone. Subsequent water penetration into the upper mantle induced undercrusting of mantle-derived serpentinite in the lower crust of Zone II. Lithospheric necking continued after the crustal breakup for a period of time until normal oceanic crust started to be produced at 62-68 Ma.

## 7.2 Major Contribution

1. This thesis presents the most extensive dataset to date for analyzing crustal velocity structures across nonvolcanic rifted conjugate margins.
2. Three distinct zones are recognized and described in detail for each of the conjugate margins of the Labrador Sea. This division is essential for a proper explanation of continent-ocean transitions across many nonvolcanic rifted margins.
3. This thesis provides strong evidence to suggest that normal oceanic crust started to be created no sooner than 62-68 m.yr. This is much younger than a previously suggested time of ~80 m.yr for initiation of seafloor spreading.
4. This thesis compiles extensive datasets to suggest that the continent-ocean transition of the Labrador Sea margin is best described by a wide zone instead of a sharp boundary.
5. This thesis defines, for the first time, the detailed geometrical and physical properties of a wide, high-velocity lower crustal layer across both nonvolcanic rifted conjugate margins. Interpretation shows that this layer likely represents serpentinized upper mantle rather than underplated mafic rocks.
6. This thesis proposes a new composite pure and simple shear model for the initial continental stretching and rifting. This model overcomes the difficulties of existing rifting models, and explains all the major observations for nonvolcanic rifted continental margins.

7. These results can be applicable to many similar cases worldwide. Their important implications are much more far-reaching than can be counted here.

### 7.3 Future Work

1. Knowing crustal extension factor ( $\beta$ ) across the conjugate margins, I can utilize existing seismic stratigraphy for these margins and compute the extension factor ( $\delta$ ) for the lower lithosphere.  $\delta$  differs from  $\beta$  because data suggest that there was a period when the crust was already separated and the lower lithosphere was still being stretched. This is consistent with the depth-dependent model of Issler and Beaumont (1987) who suggest  $\delta > \beta$  on the Labrador margin. On the other hand, if the low-angle shear zone as seen in the upper crust on the SW Greenland margin continues into the lower lithosphere, which is the extreme case of Wernicke's simple shear model, the lower plate Labrador margin would exhibit  $\delta < \beta$  which is contrary to my model suggestions. Therefore, in terms of rifting mechanisms, what is observed in the upper crust may not represent what happened in the lower crust and lower lithosphere. A complete understanding of the relationship between  $\delta$  and  $\beta$  would help explain the significant asymmetry in sediment thickness for the conjugate margins of the Labrador Sea.
2. It is interesting to note that on free-air gravity profiles the initiation of normal oceanic crust is associated with an increase in gravity anomaly in Zone III. This property may be used to delineate the distribution of the high-velocity crust based on a gravity map of the Labrador Sea.



3. As discussed in Section 5.7, the computed gravity anomaly in Zone III is  $>20$  mGals higher than observed, which may be attributed to lateral variations in the thickness of the lithosphere. A self-consistent hypothesis is that because the oceanic lithosphere is still young ( $<68$  Ma), it has not reached its thermal steady state and therefore has a thinner lithosphere than the preexisting continents of Labrador and southern Greenland. The resulting reduction of lithospheric mass in Zone III can reduce the excessive gravity anomaly in the computation. This may explain the anomalously shallow seafloor and basement depths (Hyndman 1973; Srivastava and Arthur 1989) compared to the world average depths
4. The reflections beneath the refraction Moho landward of 80 km distance on Figure 6.4b (see insert back cover) may represent traces of the initial stretching in the upper mantle (see schematic lines within the upper mantle in Figure 6.7c). These reflections do not correspond to any bulk velocity changes. Their reflection coefficient can be enhanced due to existence of (1) water saturation within fractures; (2) shearing; (3) basalts (Warner 1990).
5. ODP drilling to determine the nature of the shallowest basement high as observed on line 88-R2 on SW Greenland margin; or drilling through the thin sediments in Zone II on SW Greenland margin into the low-velocity, upper crust to determine its origin, which is useful for confirming the predictions of the model.
6. Reflection and refraction profiling should be conducted simultaneously for studying deep crustal structures. Structures that are of great interest are sometimes not

clearly seen on reflection profiles and yet are sometimes able to be determined by refraction modeling. In addition, at greater depth where velocities are high, depths obtained from two-way travel-times have a much lower resolution than from refraction profiling.

7. A major problem of presenting refraction results is that observed seismic data cannot be overlain onto the complicated 2-D velocity model. This is different from reflection profiles where the match between seismic data and geological interpretations can be judged visually with the same figure. As a result, the quality of refraction results can only be partly shown by separate figures by the density of ray coverage at each location. To solve this problem, 2-D migration of wide-angle reflections has been proposed which can image strong reflectors such as the Moho (Holbrook et al. 1992b). This method ought to be modified to include refractions because in many cases crustal refractions appear more frequently than crustal reflections. Zelt and Smith (1992) proposed a travel-time inversion and modeling scheme in which the parameters of velocity structure are perturbed to give error estimates. It is unfortunate that this method does not work well where ray coverage is not dense and for complicated structures the number of model parameters is increased which makes modeling and error estimation difficult. In this thesis, and the thesis of Osler (1993), a simplified method is used in which error estimates are conducted only for a single crustal unit and a single OBS. This simplification

evidently gives the maximum error bars for major model parameters and a better method ought to be developed in this aspect.

## Appendix A. Error Analysis of the Seismic Velocity Model

In this section let us investigate the errors of velocity and depth obtained from the two-dimensional seismic modeling. I proceed by choosing a single layer, assuming that all the model parameters above this layer are accurate. I then perturb the depth and velocity for the top boundary of the layer by  $dZ_0$  and  $dV_0$  and perturb the depth and velocity gradient for the bottom boundary by  $dZ_1$  and  $dg$ . It is clear that the refracted phase mainly controls  $dZ_0$  and  $dV_0$  and that the wide-angle reflection from the bottom boundary mainly controls  $dZ_1$  and  $dg$ . Almost all the seismic travel time information about this layer is included in these two seismic phases. The exact travel time error analysis for the layer parameters is thus five dimensional ( $dZ_0$ ,  $dZ_1$ ,  $dV_0$ ,  $dg$ , and the root-mean-square travel time misfit,  $T_{rms}$ ). To simplify things, I performed the error analysis for one phase at a time, that is, a ( $dZ_0$ ,  $dV_0$  and  $T_{rms}$ ) contour plot for the refracted (diving) phase within the layer (omitting the less sensitive parameter  $dg$ ) and a ( $dZ_1$ ,  $dg$  and  $T_{rms}$ ) contour plot for wide-angle reflections from the bottom of the layer (assuming  $V_0$  is accurate and therefore  $dV_0=0$ ).

To quantify the error bounds of model parameters, a  $\chi^2$  misfit is used instead of  $T_{rms}$ , where

$$\chi^2 = \frac{T_{rms}}{U_0} = \frac{1}{U_0} \left( \frac{1}{n} \sum_{i=1}^n (T_{o_i} - T_{c_i})^2 \right)^{1/2}.$$

$To_i$  and  $Tc_i$  are the observed and calculated travel times at selected points ( $i=1, 2, \dots, n$ ) of a specific seismic phase whose travel time pick has an uncertainty of  $Uo$  (assumed to be constant for all  $i$ ). For values of  $\chi^2 \leq 1$ , the computed and observed arrivals agree within the observed uncertainties of the travel times. This criterion may be used for defining error bounds of velocity, depth, and gradients. The bounds might be reduced further when consistent amplitude patterns are modeled in addition to travel times and where multiple ray paths from different receivers overlap.

In the implementation of the error analysis for the refracted phase, the perturbation of  $Z_0$  is set to be uniform along the top boundary so that for all iterations the boundary relief is kept the same. The perturbation of  $V_0$  is constant throughout the layer so that there is no gradient change during iterations. The errors of the gradient can be estimated by the second approach for wide-angle reflections in which  $g$  and  $Z_1$  are varied. Figure A1 shows a  $\chi^2$  contour plot for the phase  $P_3$  which is refracted from the high-velocity, lower crust for the final model in Figure 10a.

A similar approach can be used for the error analysis of  $S$  waves such as the PSP phase which is doubly converted at the sediment/basement interface. For PSS phases, with only a single  $P$ - $S$  conversion, the method for error analysis is different because an extra unknown  $V_{sed}$ , the  $S$  velocity in the sediments, is introduced. In this instance, I replace the less sensitive variable, the depth perturbation  $dZ_0$ , with a perturbation of  $V_s$  in the sediment. Figure A2 shows a  $\chi^2$  contour plot of  $d(V_p/V_s)$  for the lower crust and  $d(V_p/V_s)$  for the topmost sediments. Here I use the ratio  $d(V_p/V_s)$  instead of  $V_s$  alone for model

iterations in order to retain the model variations obtained from the generally better resolved  $P$  waves. However, this method results in minimum  $\chi^2$  values of  $\sim 4$ , indicating that strict adherence to the  $P$  wave model and a uniform  $V_p/V_s$  ratio within each layer does not result in calculated  $S$  wave travel times that are able to fit the observations within their estimated uncertainties. This suggests either that the estimated uncertainties in the observed travel times are too low or that the  $V_p/V_s$  ratio varies within the layers, increasing the uncertainty in  $V_s$ .

Knowing the errors of  $V_p$  and  $V_s$ , the errors of Poisson's ratio  $\sigma$  can be estimated.

Differentiating

$$\sigma = \frac{1}{2} - \frac{1}{2} \frac{V_s^2}{V_p^2 - V_s^2},$$

yields

$$|d\sigma| = \frac{|V_p V_s^2 dV_p - V_s V_p^2 dV_s|}{(V_p^2 - V_s^2)^2} \leq \frac{V_p V_s^2 / dV_p + V_s V_p^2 / dV_s}{(V_p^2 - V_s^2)^2}.$$

If  $V_p=7.5$  km/s,  $dV_p = \pm 0.1$  km/s,  $V_s=4.0$  km/s, and  $dV_s = \pm 0.2$  km/s, the above formula gives  $\sigma = 0.30 \pm 0.03$ .

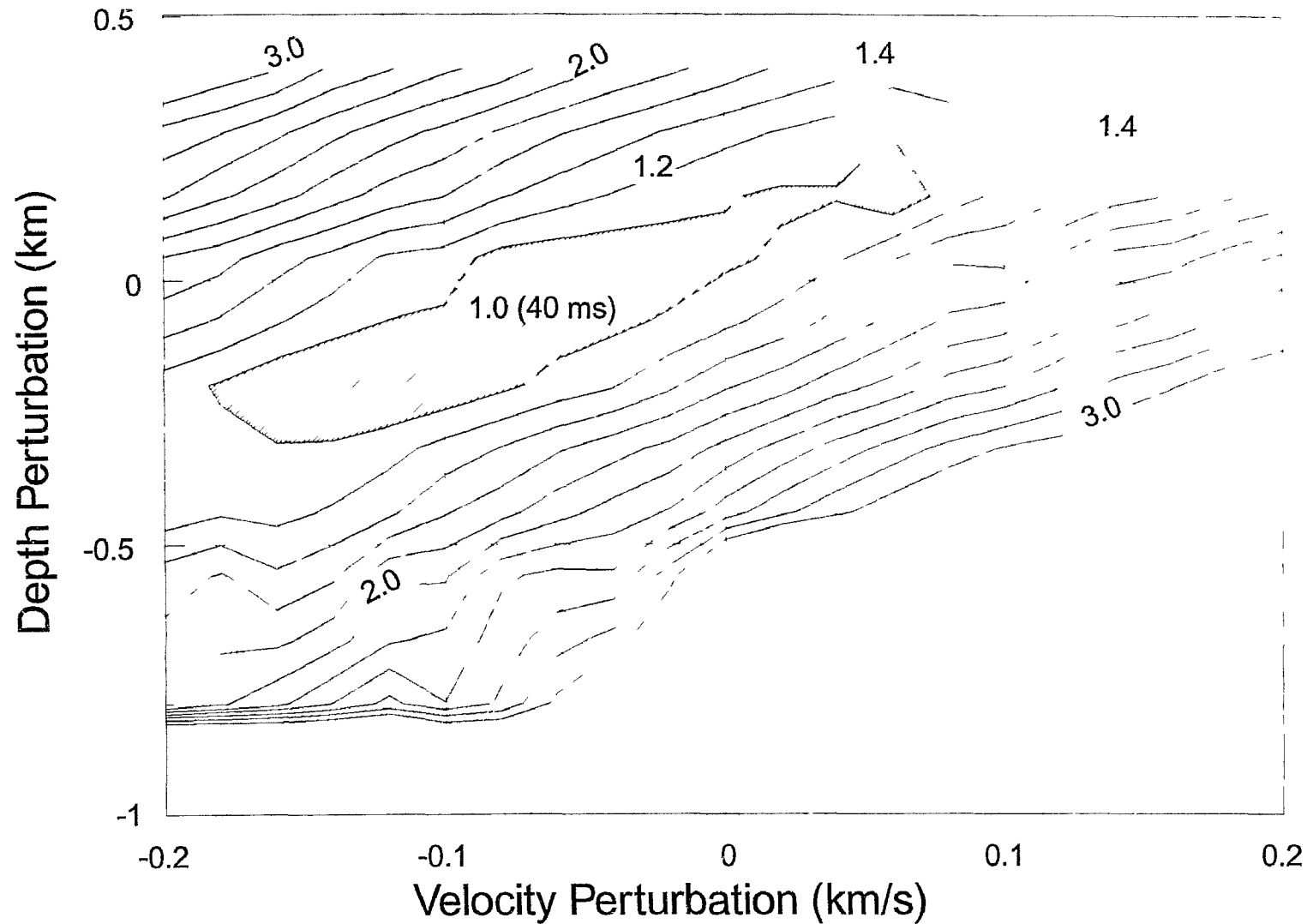


Figure A1  $\chi^2$  contour plot for perturbations of velocity and depth for the seismic phase P3 west of OBS C (Figure 4.6). The contours are normalized to the travel time endurance (maximum errors in observed travel time) of 40 ms. The area enclosed by  $\chi^2=1$  delimits error bounds for the velocity and depth for the lower crust

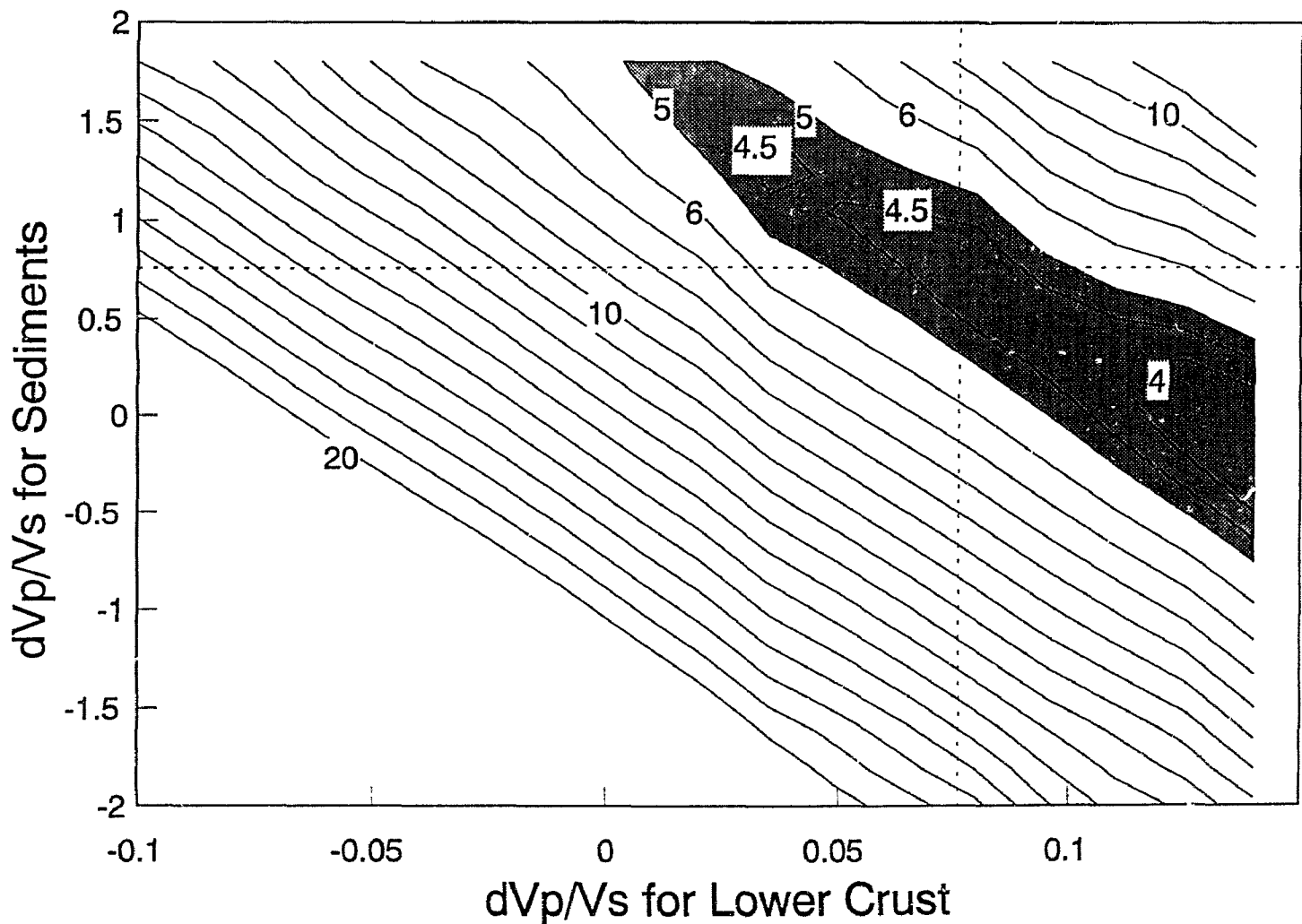


Figure A2.  $\chi^2$  contour plot for perturbations of  $V_p/V_s$  ratios in the lower crust and in the topmost sediment. The seismic phase for this error analysis is S3 for the western ranges of OBS C (Figure 4.11b). The starting model has  $V_p/V_s$  ratios of 1.83 for the lower crust and 4.5 for the top sediment layer, respectively. No S waves can be generated for  $d(V_p/V_s) > 0.14$ . The contours are normalized to 35 ms. This plot indicates that the preferred ratio for  $V_p/V_s$  is  $1.91 \pm 0.10$ . The larger values of  $\chi^2$  suggest a further uncertainty due to limitations in the modeling procedure (see discussion in text).



## **Appendix B. Suppression of Time Code Cross-talk Disturbances in Signal Channels of Ocean Bottom Seismometers in Seismic Refractions**

### **B1 Introduction**

By far most of the information about the structure of the Earth crust comes from seismic reflection and seismic refraction techniques. While the former gives the detailed layering of the crust, the latter, which is to be concerned here, is very efficient in revealing the seismic velocities at different layers in the whole Earth crust. Seismic refraction technique is based on the simple relationship that, in plane layer cases, the slope of each refraction event in T-X profiles is just the reciprocal of the velocity at which the refracted wave travels. This renders refraction technique to have more uniqueness in determining the structure of the crust compared to other geophysical methods such as gravitation and magnetics.

One of the most successful instruments in seismic refraction is in the use of Ocean Bottom Seismometer (OBS) receivers. Before shooting a refraction line, several OBS are deployed along the line in the ocean floor, and begin to record every vibration that reaches the instrument. An airgun installed in a ship then shoots all the way through the line at a certain time interval, typically every one minute. The reflected and refracted signals from the boundaries of the sediment and crust are recorded by the OBS. After released from the floor and brought back, the recordings are digitized, processed, and plotted by computers. Finally interpretations are made and configurations of the structure of the sediment and crust are obtained. The advantages of using OBS in seismic

... is in the facts that 1) the ocean floor is typically a quieter environment for detecting low amplitude seismic energy, a particular case at large source-receiver separations; and 2) shear waves only travel through geological structures and are not able to travel in the water column, so the only way to record direct shear waves is to detect them on the ocean floor.

OBS has four channels. Channel 1 is usually the internal time clock of the OBS, or, as I call it in this project, time codes. The other three channels are hydrophone (recording signals in the water column), vertical geophone and horizontal geophone (recording vertical and horizontal displacement of the vibration).

In the summer of 1988, two seismic refraction lines were shot in the Western Greenland Margins (Figure B1.1). Most of the OBS data along line 88R1 has already been interpreted. But some OBS such as R1J and R1H have channels mixed with time codes. These time code disturbances usually have stronger amplitudes than actually signals which makes seismic signals very hard to pick up (see Figure B1.2). This project tries to suppress these time codes in the signal channels. It turns out that unlike the time codes in channel 1 which are perfectly lined up along X-axis, the time codes in signal channels are only roughly lined up, which seems to be randomly distributed around the straight line (Figure 2.1). I will first investigate the spectral characteristics of the whole time code cross-talked signal channel and then apply an iterative time code suppressing technique to enhance the signal to noise ratio in the profile.

## B2 Brief Description of Data

Seismic signals arrive at receivers at some specific time. If I repeat a seismic event for a number of times, and treat each record as one realization of a random process, I can calculate the expected value and variance. I soon find that these values change with time. So seismic processes, such as the seismic refraction profiles to be presented in this project, are not stationary random process. A reference on this topic can be found in John Osler's last year's project report for the course of Time Series Analysis.

In plotting the seismic refraction profiles, the OBS is usually put at the origin (Figure B1.2). For convenience of interpretation, the data is plotted at a certain reducing velocity  $V_r$  (typically 6, or 8 km/sec), i.e. the time indicated on the profile is equal to the actual time- $X/V_r$ . In Figure B1.2 it can be seen that the time code has very strong amplitudes compared to the signal. The time code disturbances are from channel 1 whose profile is shown in Figure B1.3.

In the following some diagrams are labelled along x and y axes by the number of their data points. The conversion to the actual values is easy. In all my data in this project, the sampling rate is 72 samples per second in time and the distance interval of adjacent traces is approximately 0.15 km. So the Nyquist (or maximum) frequency is  $1/(2*dt)=36$  Hz; and the maximum wavenumber is  $1/(2*dx)=3.3$  /km. The frequency interval is then 36 Hz divided by half the maximum number of data points in time, and wavenumber increment can be calculated the same way.

For the purpose of using Matlab software to investigate the behaviour of time code noise, I choose 16 traces at -45 km and output channel 1 and channel 2 data from 5 to 10 seconds(actual time) to a file for the use of Matlab. No reducing velocity is applied in writing these data. Figure B2.1 and Figure B2.2 show the data in channel 2 and channel 1, respectively.

It is not difficult to see that the time codes in channel 1 is perfectly lined up, while channel 2 is the data channel contaminated with time codes. These cross-talked time codes approximately forms straight lines with some randomly valued positive or negative time lags. This random timing of T.C. cross-talks is caused by 1) that the OBS did not record the four channels with exactly the same speed; and 2) that in digitization of the data of the four channels the speed of playing the tape cassettes shifts across the traverse section of the tape. In Figure B2.1 there are some signals at data point numbers above 200, but they are severely mixed up with time codes. How to suppress these time code disturbances?

### **B3 Spectral Analysis**

Figures B3.1 shows the frequency response of channel 2 and channel 1 of the 5th trace (counting from below) in Figures B2.1 and B2.2. As can be seen that time codes get their strongest energy from 7.75 Hz to 12.5 Hz. The seismic signals usually covers the frequency band of 2 Hz to 12 Hz, as is shown in another channel that is not influenced by time codes (Figure B3.2). So a single filtration at a narrow frequency band of 2 Hz to 7.75 Hz would be able to filter all the time codes out from the signal channel. This is

really the case. Figure B3.3 shows the same data as in Figure B1.2 but filtered at frequency bands of 2 Hz to 7.75 Hz. The time codes almost disappear except there are only some weak lines tracing the original time code positions. But by doing so, I lost those abundant energy of signals spanning from 7.75 Hz to 12 Hz.

Considering a straight line (defined by  $dx/dt=V_a$ ,  $V_a$  is called apparent velocity) in  $t-x$  domain corresponds also to a straight line in its 2-D Fourier domain ( $f/k=V_a$ ), I tried the possibility of filtering the time codes in frequency-wavenumber space. Figure B3.4 shows that the time code energy in channel 1 forms a straight line  $k=0$  in  $f-k$  space, a result reasonable in the sense that all time codes in channel 1 are perfectly lined up in  $t-x$  space. But the time code cross-talk in channel 2 has different characters; it spreads at various slopes (or velocities). Figure B3.6 is a contour map of the absolute value of the 2-D Fourier transform. As I mentioned before, the main time code energy is not only distributed along  $f$ -axis, but along some other discrete velocity values, with frequency all above 7.7 Hz. Since there are no signals whose arrival time decreases with distance, when expressed in  $f-k$  space this means that there is no energy in the first and the fourth quadrants of Figure B3.6, I can certainly null this space to avoid some noise. Figure B3.7 shows the transform only in the second and the third quadrants, while energy along the  $f$ -axis is removed. By applying an inverse transform, I get seismograms as shown in Figure B3.8. It can be seen that time codes are suppressed while signals remain the same. In addition to this cut of energy in  $f-k$  domain, I can delete those energy at frequencies above 7.7 Hz, the resulting seismogram is

shown in Figure B3.9. As one can see, while T.C. energy is highly suppressed, signals are also attenuated. The remaining time code energy in f-k domain mainly comes from the four spots as numbered from 7 to 10 in Figure B3.6. As an example, if I only retain the two spots numbered 9 and 10 as the Fourier transform, I get the inverse transform as shown in Figure B3.10 which is purely time codes.

In summary for this section, T.C. cross-talk in signal channels are difficult to remove by directly using filtration technique either in f-k space or in f-x space. The reason is that the cross-talk energy is spread not only along the f-axis but at other wavenumbers (or k) with frequencies above 7.75 Hz. There are several peaks of the T.C. energy all lined up in f-k space at certain apparent velocities.

#### **B4 Time code suppression in T-X space**

As seen in the above section, the suppression of time codes disturbances in signal channels is hindered by the wide band of frequency overlap with signals. Here I try to a method of time code suppression in T-X space. This method is based on the simple idea that by computing the average value along the straight lines of time codes I get an estimate of T.C. disturbances which does not include signals because signals never line up the same way. I can subtract this value from each T.C. contaminated trace and hence suppress the T.C.. In case of T.C. deviated from the straight lines I can compare the T.C. channel (channel 1) and signal channel (channel 2) and estimate the time lag of T.C. crosstalks in the signal channel with respect to the T.C. in channel 1. I then

average along the curved line defined by these time lags to get the T.C. estimates and perform the subtraction.

In the above an assumption was made that the T.C. cross-talk in a certain trace has a constant time lag with respect channel 1 for the whole trace. This is only accurate within a short time window (see Figure B2.1). For long traces a moving time window should be used for calculating the time lag, which would change according to different time windows.

#### **B4.1 Computing Time Lags**

One way to calculate the time lag is first to calculate the correlation of channel 2 and channel 1. The time lag should correspond to the maximum of correlation between the two. Figure B4.1 shows two typical cases of correlation of the two channels. While the bottom diagram reveals a maximum correlation at a correct time lag, the top diagram shows a maximum correlation at an incorrect lag time. To avoid mistakes in computer's decision-making, a further constraint is necessary. For my data the time lag of T.C. in signal channels is mostly smaller than 1 period of its main frequency, which spans 7 data points for a 10 Hz time code; this serves as another constraint to the calculation of time lags.

Figure B4.2 shows the same profile as in Figure B2.1 but each trace is shifted toward the straight line of T.C. in channel 1 by the estimated time lags. The T.C.'s are now better lined up. Figure B4.3 shows the T.C. suppressing processing applied to the 5th trace from our example profile. The T.C. was estimated by averaging along the

16 traces at the same time point(i.e. with no time lag). After applying the time lag estimation (Figure B4.4), the estimated time codes are better resolved. After subtracting the estimated T.C. from the original trace, the resulting trace is more improved.

#### **B4.2 Time Code Suppression to Field Data**

By using the correlation of channel 2 and channel 1, I get for each trace an estimate of time lags of the T.C. cross-talks in channel 2 with respect to the T.C. in channel 1. I can then average across different traces along the curved line defined by these lags, allowing them to change between (-6, 6) data points. This average trace is then subtracted from all the involved traces along the same curved lines as in the preceding averaging process. Figure B 4.5 shows the process applied to the refraction profile in Figure B1.2. T.C. cross-talks are suppressed while signals remain the same.

It is soon noted that the T.C. still dominate the whole profile. The idea follows that it is no harm to repeat this process as many times as to one's satisfaction. Figure B4.6 shows the same profile after 7th iteration of this T.C. suppression processing. The time codes are more suppressed; It is especially so in the middle of the profile, leaving the ends and corners less affected by the processing. This may be caused by the fact that for the 10 seconds records the T.C. time lag of each trace is not constant. By assuming a constant time lag its corresponding lag estimates tend to approximate the inner parts of the whole record and the contribution of data close to both ends becomes less significant.



### **B4.3 Improving Time Lag Estimates**

An accurate estimate of T.C. time lags in channel 2 is essential for the effectiveness of the processing. However, due to irregularity of the shape of T.C. and some other noise in channel 2, the lag estimate is sometimes quite unstable. One way to improve it is that in computing correlations I only use a frequency band of 7.75 Hz to 12 Hz, over which T.C. dominates. This consideration is very easy to implement if I perform the convolution in frequency domain. After FFT channel 2 and channel 1, null those points that correspond to frequencies outside the band (7.75, 12) Hz, and then inverse FFT to the time domain to get the correlation. The time lags estimated in this way better represent the actual lags of T.C. cross-talks in channel 2.

Figure B4.7 shows the result. Comparing to Figure B4.5 it is apparent that the T.C. cross-talks are more suppressed. A 3rd iteration of this processing ( Figure B4.8) almost reaches the same effect as in the 7th iteration of the original processing (Figure B4.6).

### **B4.4 Time Windows**

As mentioned in section 4.2, time lags of T.C. cross-talk in signal channels with respect to T.C. in the clock channel changes along the whole 10 seconds of records. But, as one can see from Figure B2.1, the lag is fairly constant for a shorter time period, say, 2 seconds. I can then divide the record into several time windows, say, 5. The above processing is hence done in each window separately. Figure B4.9 shows a resulting profile of this processing. The whole record was divided by 5 windows;

separate processing were made in each window while a narrow band correlation is applied. Apparently, more suppressions of T.C. were achieved.

Figure B4.10 shows the result by the same processing procedure but all the time windows were half overlapped. Even though only the first iteration was made the T.C. energy are more suppressed than the profile with 7 iterations in Figure B4.6.

Figure B4.11 shows the profile processed with 10 time windows with no overlap. It became worse. So time windows should not be too short or too long. I am quite confident with the 5 divisions for the 10 seconds of records.

Combining all the discussions in this section, I applied 5 half-overlapped time windows to the 10 seconds of records. The correlation of channel 2 and channel 1 is performed in the narrow frequency band from 7.75 Hz to 12.00 Hz. The time lags are confined to the range from -6 to 6 data points. After 3 iterations the profile comes out as shown in Figure B4.12. By comparing it with the original profile Figure B1.2, it is evident that all the signals remain the same while time code disturbances are highly suppressed.

## **B5 Conclusions**

Seismic refraction profiles do not represent stationary random processes. However, many ideas and programs of data processing based on stationary random processes can be directly used here. For example, In stead of using window closing methods I just set  $M=N$  in applying the program of cross-spectral analysis to seismic data and the result is also quite reasonable.

The time code disturbances cross-talked from channel 1 to other signal channels during OBS recording are very significant in amplitudes compared to signals. Spectral analysis indicates that these time codes occupies mainly in the frequency band of 7.75 Hz to 12.5 Hz which is just part of the seismic signal band ranging from 2 Hz to 12 Hz. A filtration from 2 Hz to 7.7 Hz is able to filter almost all the time codes out but at the same time half of the signals are lost in terms of frequencies. Unlike the time codes in channel 1, the energy of time codes in channel 2 spread not only along f-axis (infinite apparent velocity) but along some other velocities as well. So a 2-D filtration can not filter them out.

Once proper factors are taken into account and related parameters are chosen well, the time codes can be greatly suppressed by an iterative suppressing method as presented in section 4. The result is promising but further developments are clearly necessary. The crucial point is at the estimation of accurate time lags. A possible way for further improvement is the combination of both f-k domain filtration and t-x domain iteration. It has been indicated in the spectral analysis in this project that after taking away energy in the first and third quadrants in the f-k transform, the time codes show more regularity. This may make maximum correlation point more stable, and hence enhance the signal to noise ratio.

## **B6 Acknowledgements for Appendix B**

This appendix is based a term project for the course of Spectral Analysis instructed by Keith Thompson. Personal communications and discussions with John Osler

about the methods and results was very useful in the course of the project. I thank Ian Reid in Bedford Institute of Oceanography for his suggestion of averaging across different traces to get time code estimates.

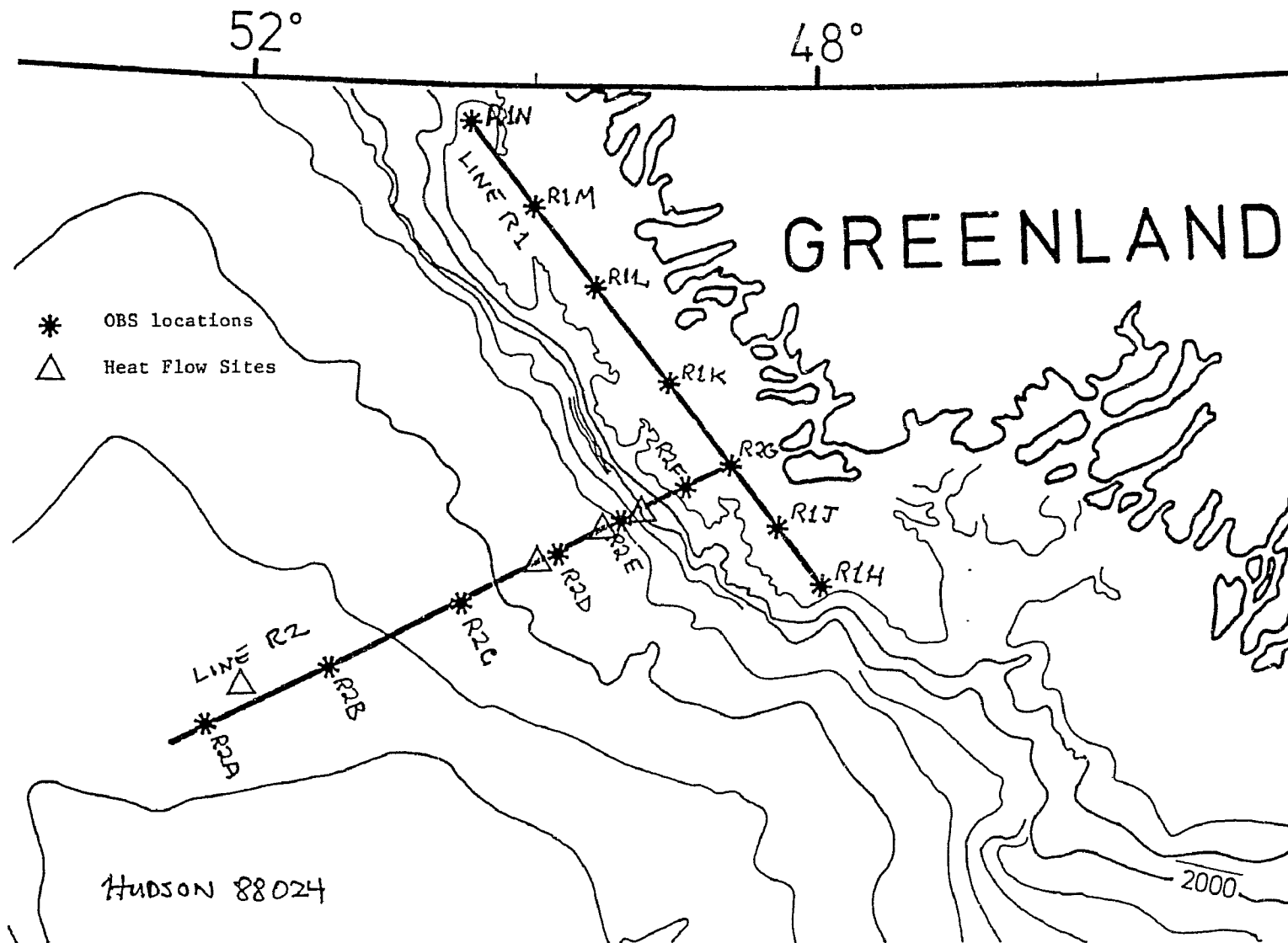


Figure B1.1 Cruise line positions of the Hudson 88R1 and 88R2.

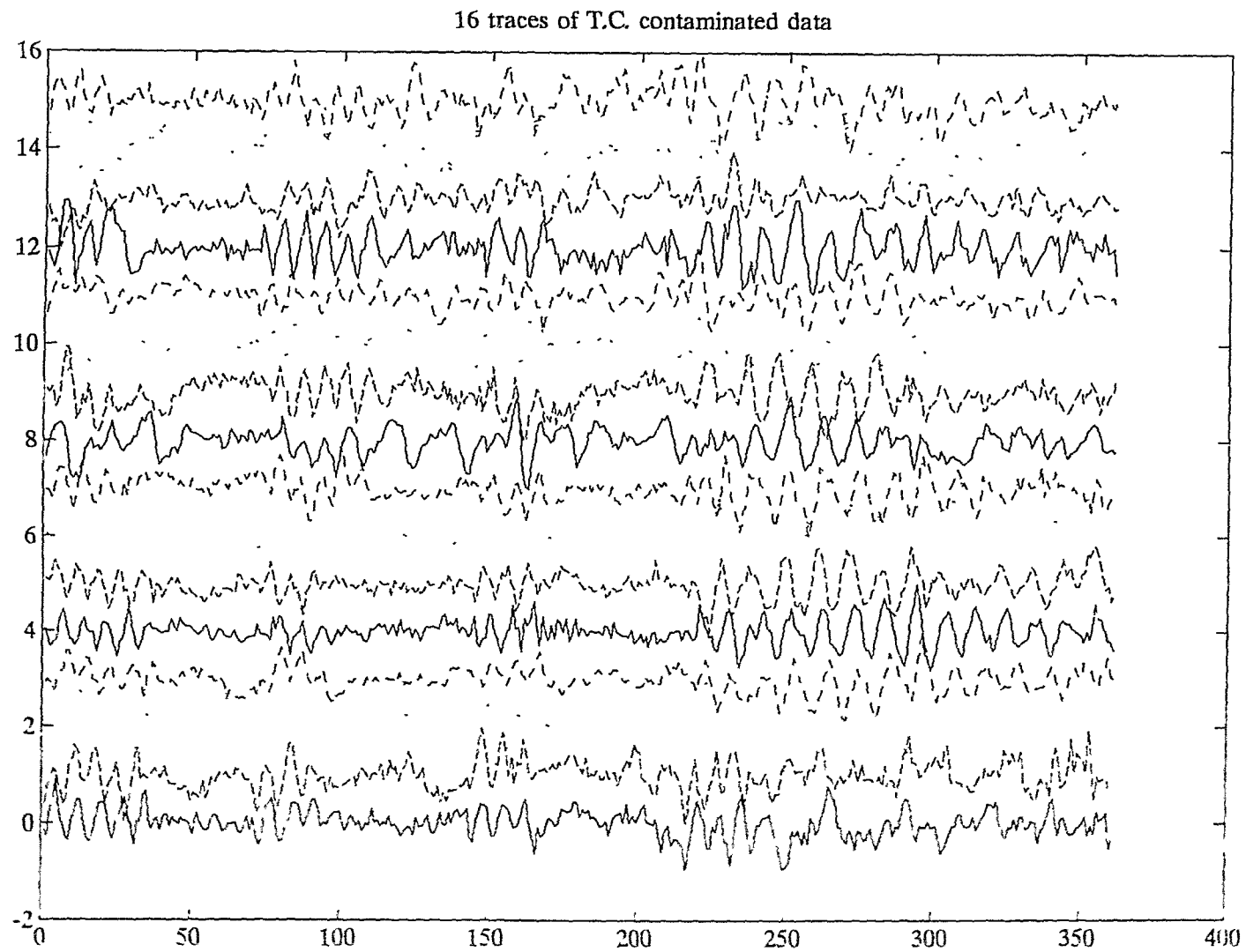


Figure B1 2 Channel 2 (hydrophone) data of OBS R1J. Time code cross-talks cover most of the profile, making signal arrival pickup difficult.

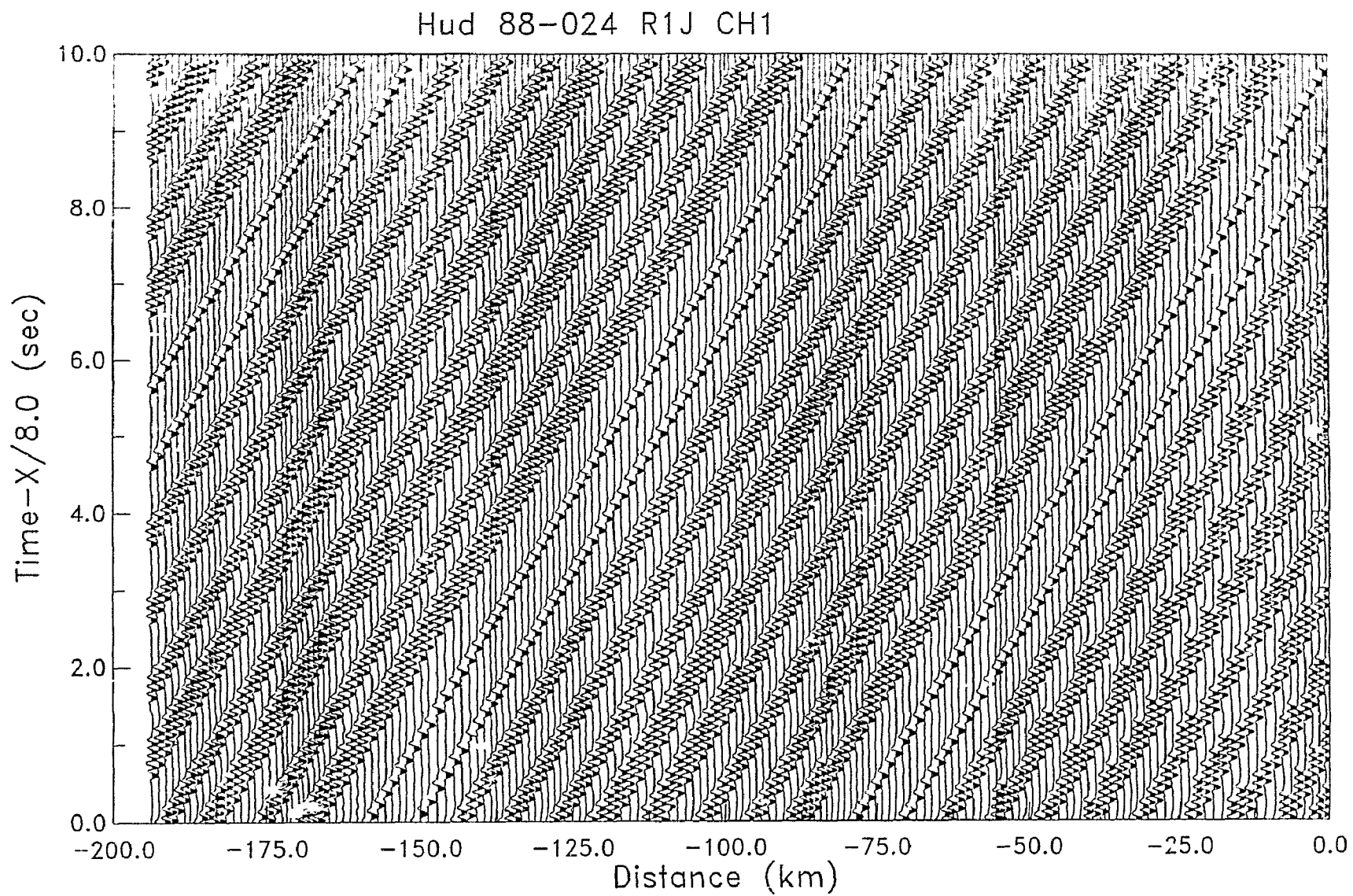


Figure B1.3 Channel 1 time codes of OBS R1J. These time codes were cross-talked to channel 2 when the OBS were working on the ocean floor (c.f. Figure B1.2).

Hud 88-024 R1J CH2

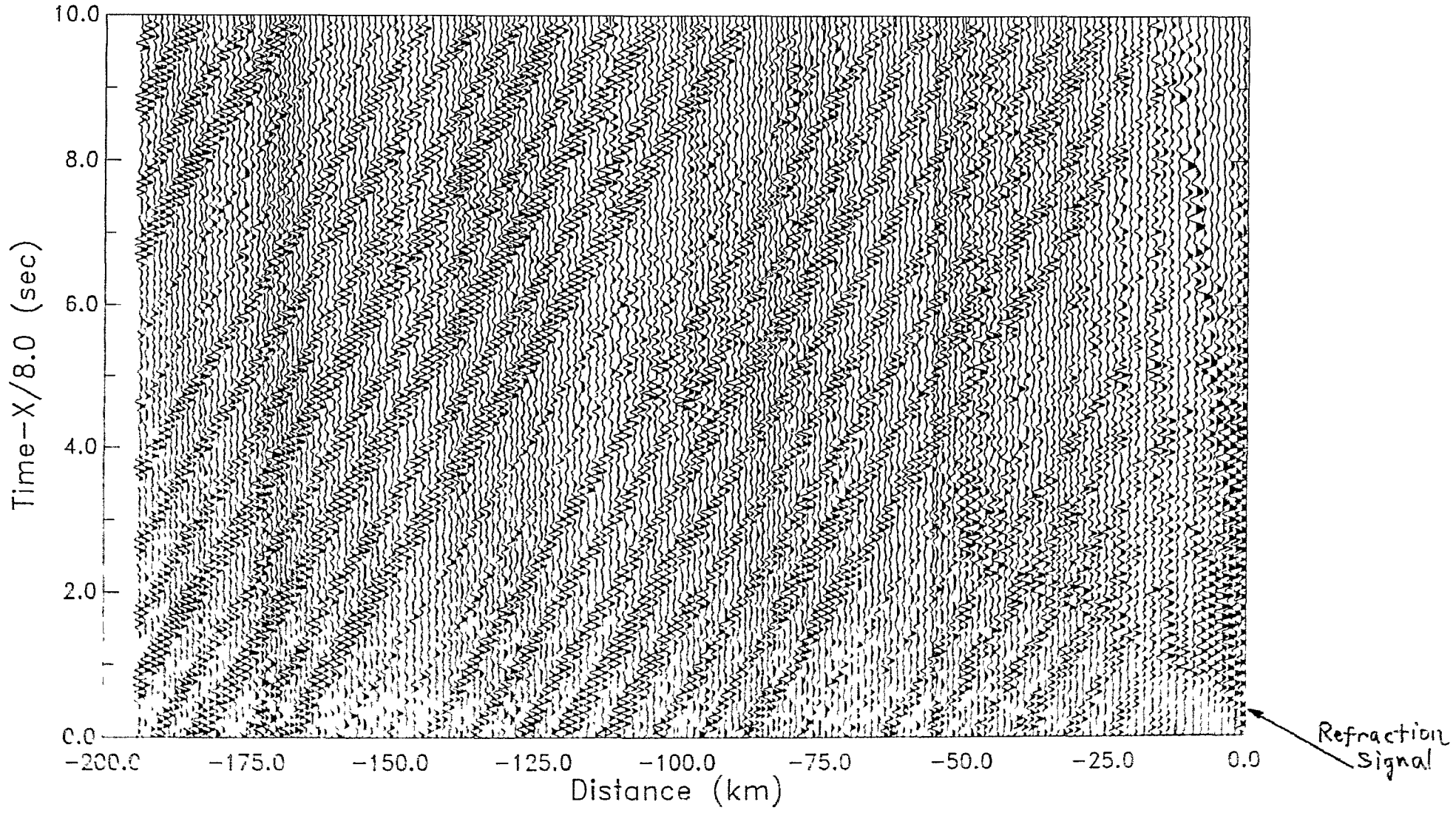


Figure B2.1 16 traces from the channel 2 of OBS R1J at 45 km from OBS position. This is output for use in Matlab. X axis is in sample numbers with a sample interval dt=1.72



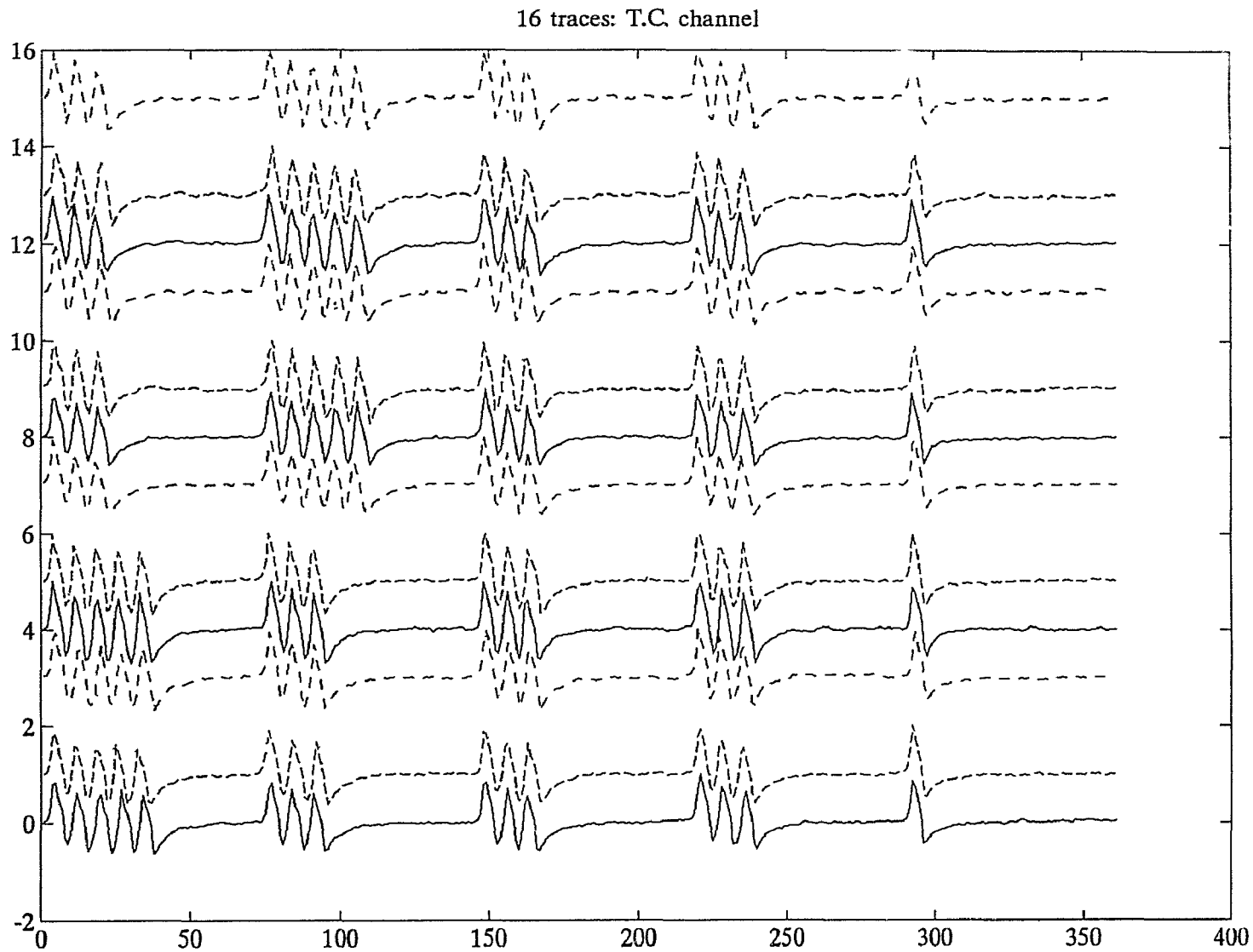


Figure B2.2 16 traces from channel 1 of OBS R1J at 45 km from OBS position. This is output for use in Matlab. X axis is in sample numbers with a sample interval  $dt=1/72$ .

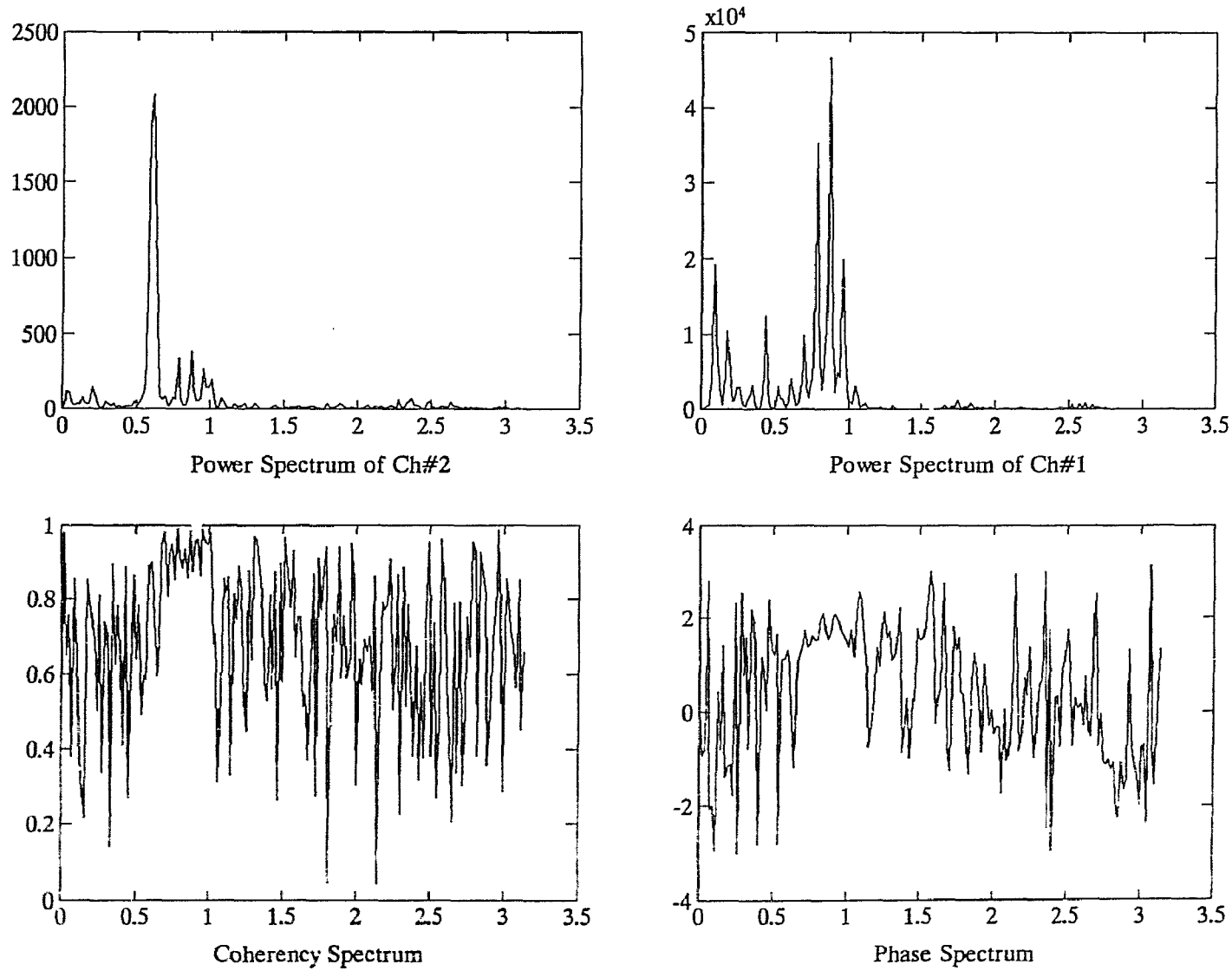


Figure B3.1 Power spectrums of the 5th trace ( counting from below in Figs. B2.1 and B2.2) of channels 2 and 1 of OBS R1J at 45 km from OBS position. Also shown are the coherency and phase spectrums of the two channels. X axis is the actual angular frequency multiplied by  $dt=1/72$ .

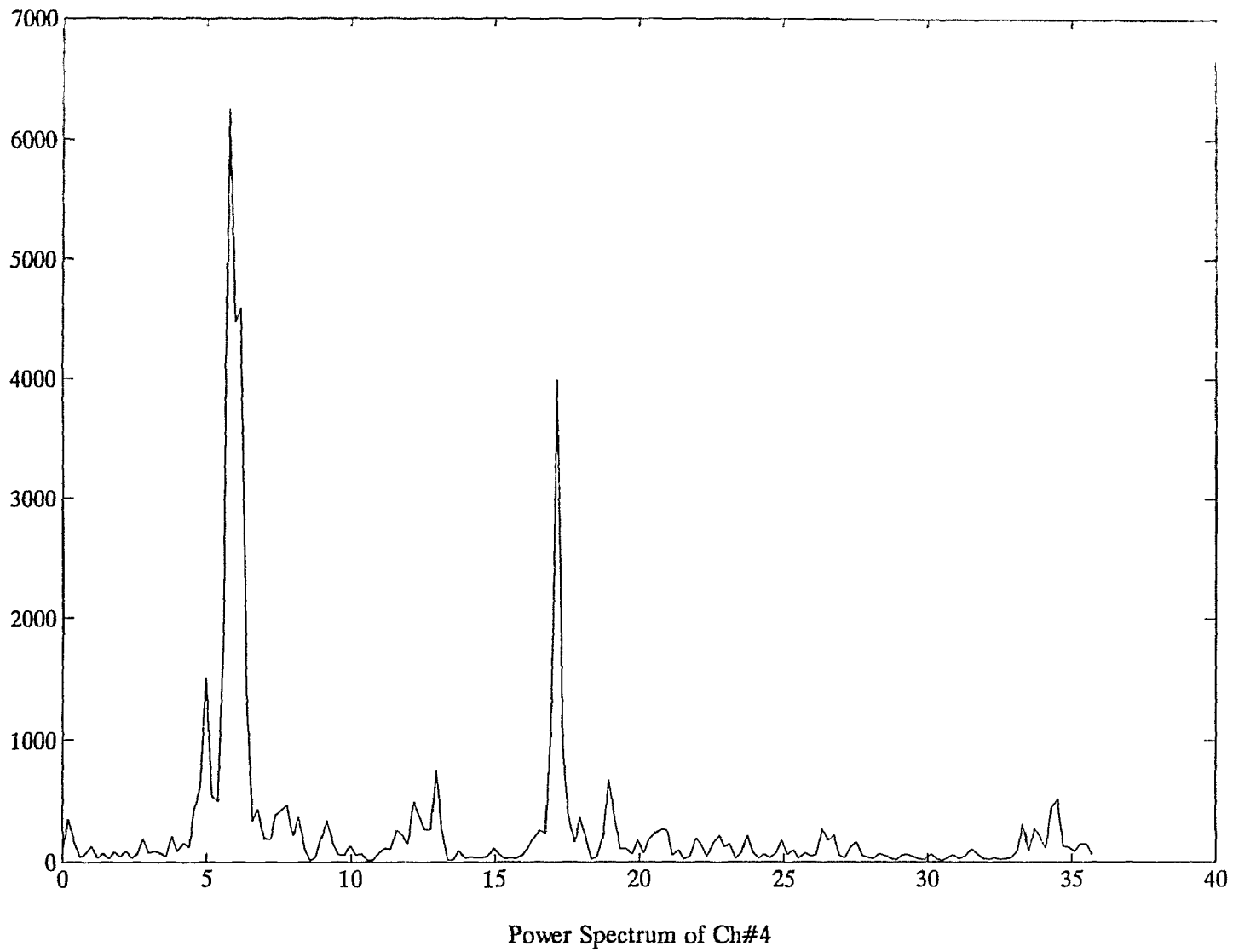


Figure B3.2 Power spectrum of channel 4 (vertical geophone) data of OBS R1J at 50 km from OBS position. This channel is not influenced by time code disturbances. X axis is in Hz.

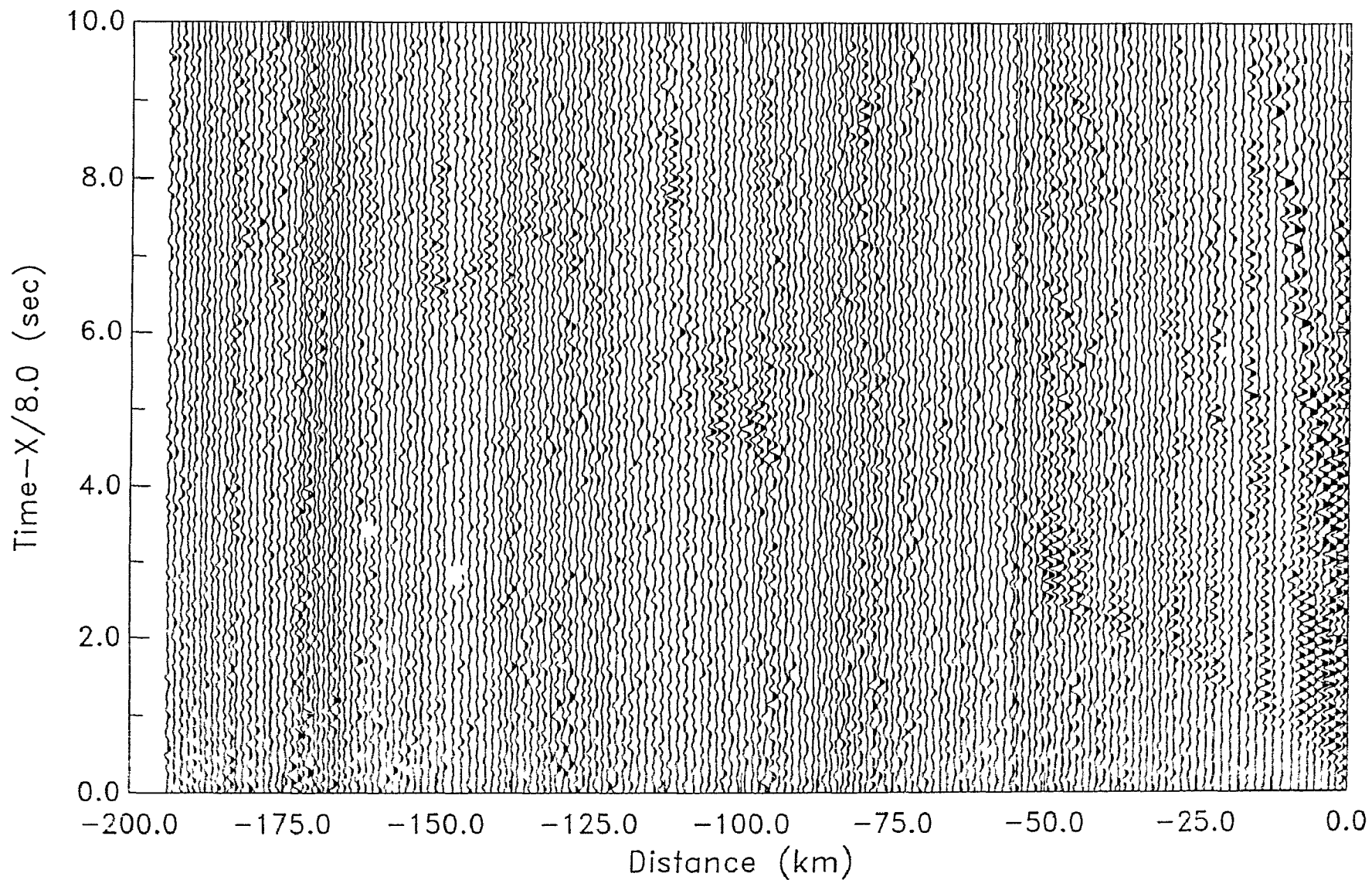


Figure B3.3 Channel 2 data of OBS R1J. Frequencies above 7.75 Hz are rejected by an 8-point Butterworth regression filter. Time code disturbances are mostly suppressed, while signals are also attenuated.

F-k display of the 16 traces

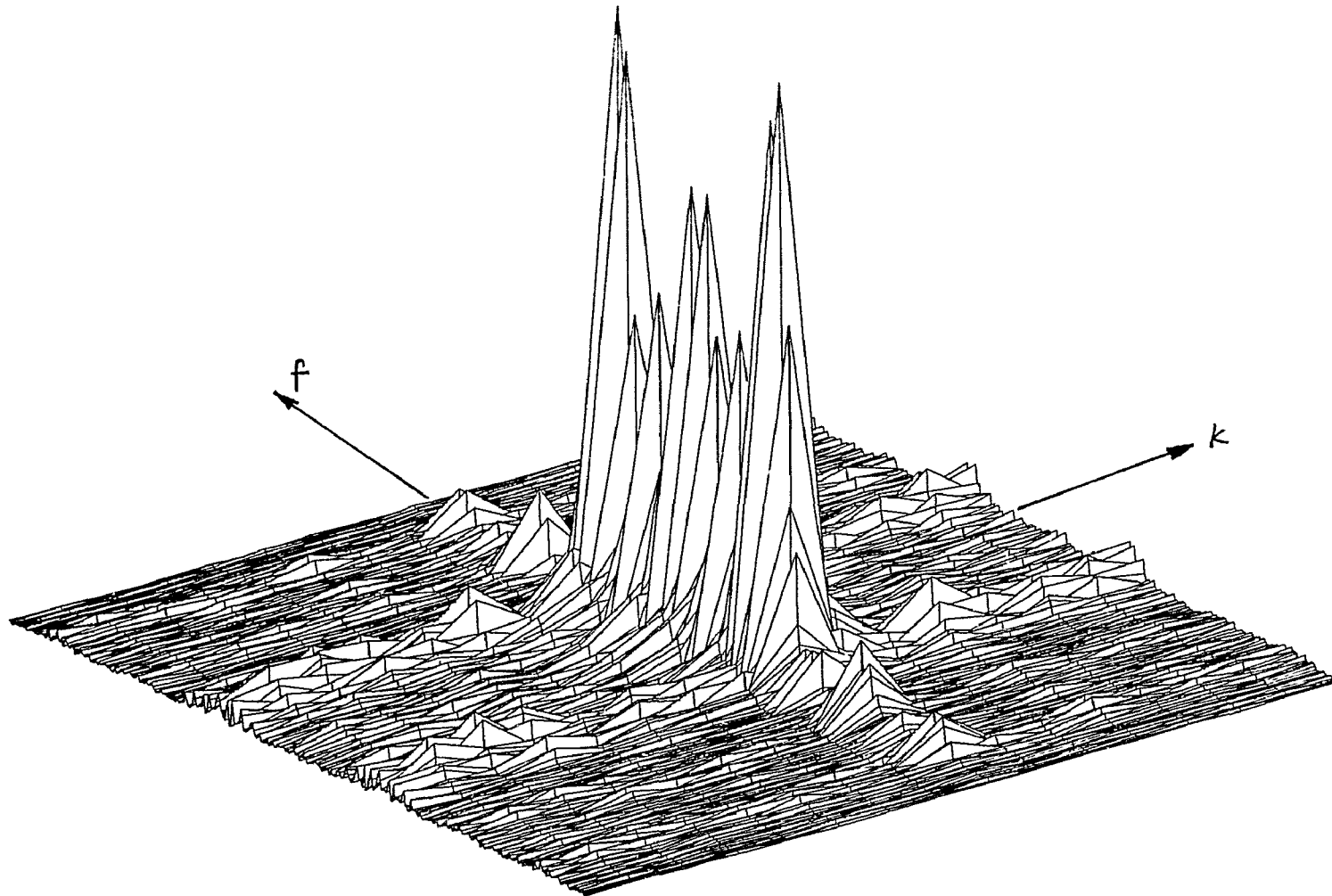


Figure B3.4 Channel 1 (time code channel) in f-k domain. Number of points in f-axis is 361. Number of points in k-axis is 16. The diagram has been FFT-SHIFTed so the origin is in the middle.

F-k display of the 16 traces

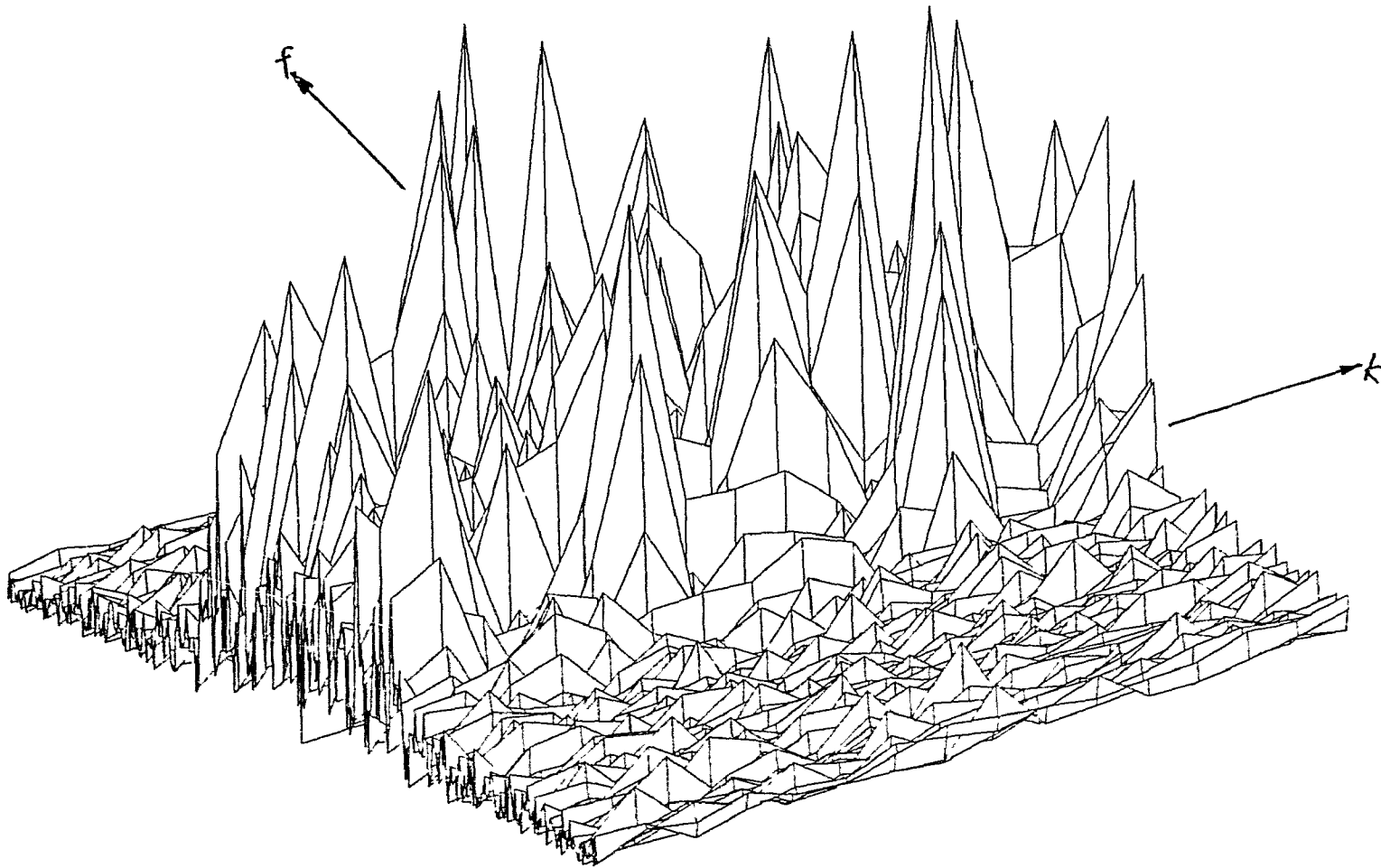


Figure B3 5 Channel 2 in f-k domain. Number of points in f-axis is 361. Number of points in k-axis is 16. The diagram has been FFT-SHIFTed so the origin is in the middle.

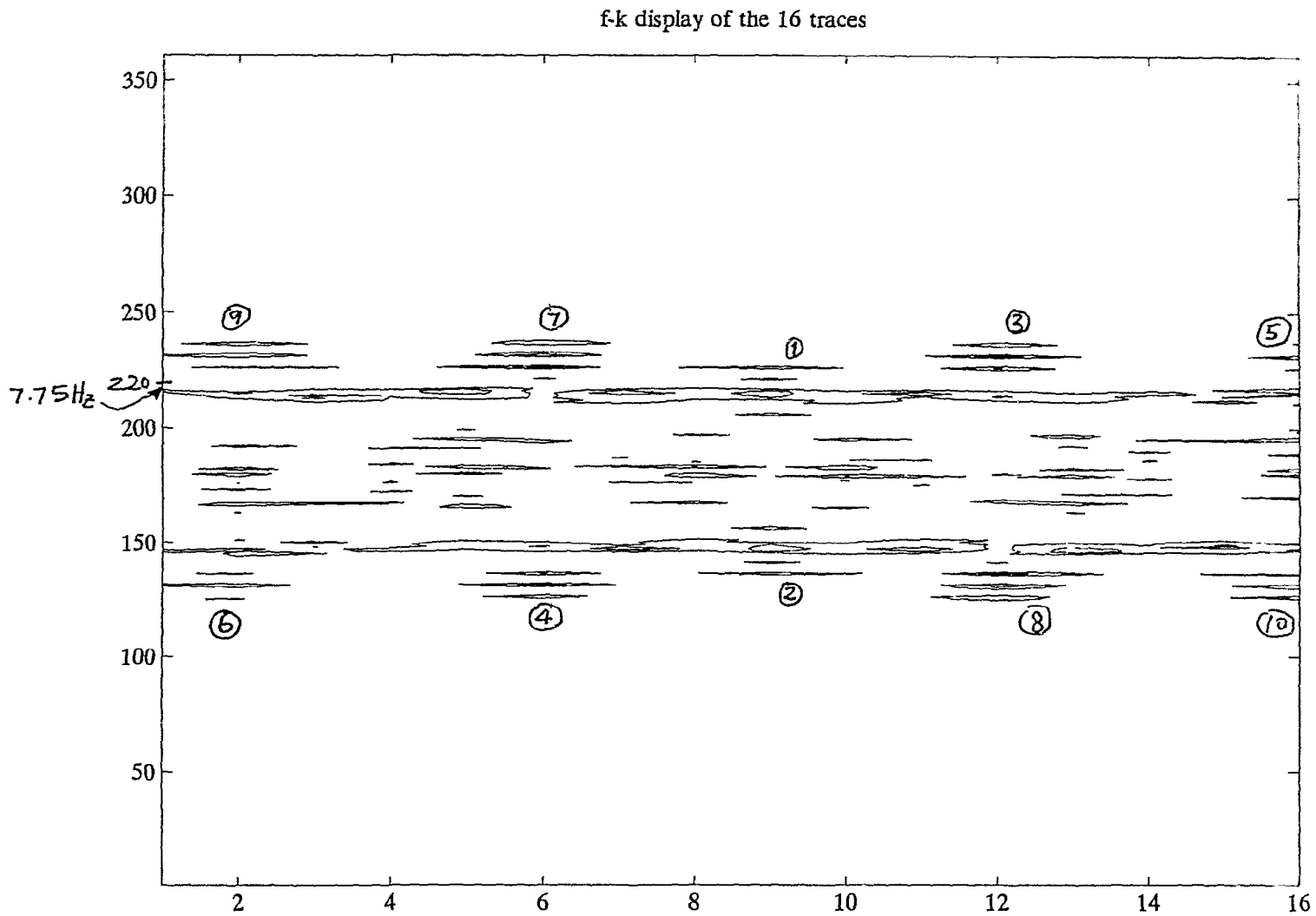


Figure B3.6 Contour map of channel 2 in f-k domain. Number of points in f-axis is 361. Number of points in k-axis is 16. The diagram has been FFT-SHIFTed so the origin is in the middle. The numbered groups within the diagram show energy concentrations of time code disturbances cross-talked from channel 1.

f-k display of the 16 traces

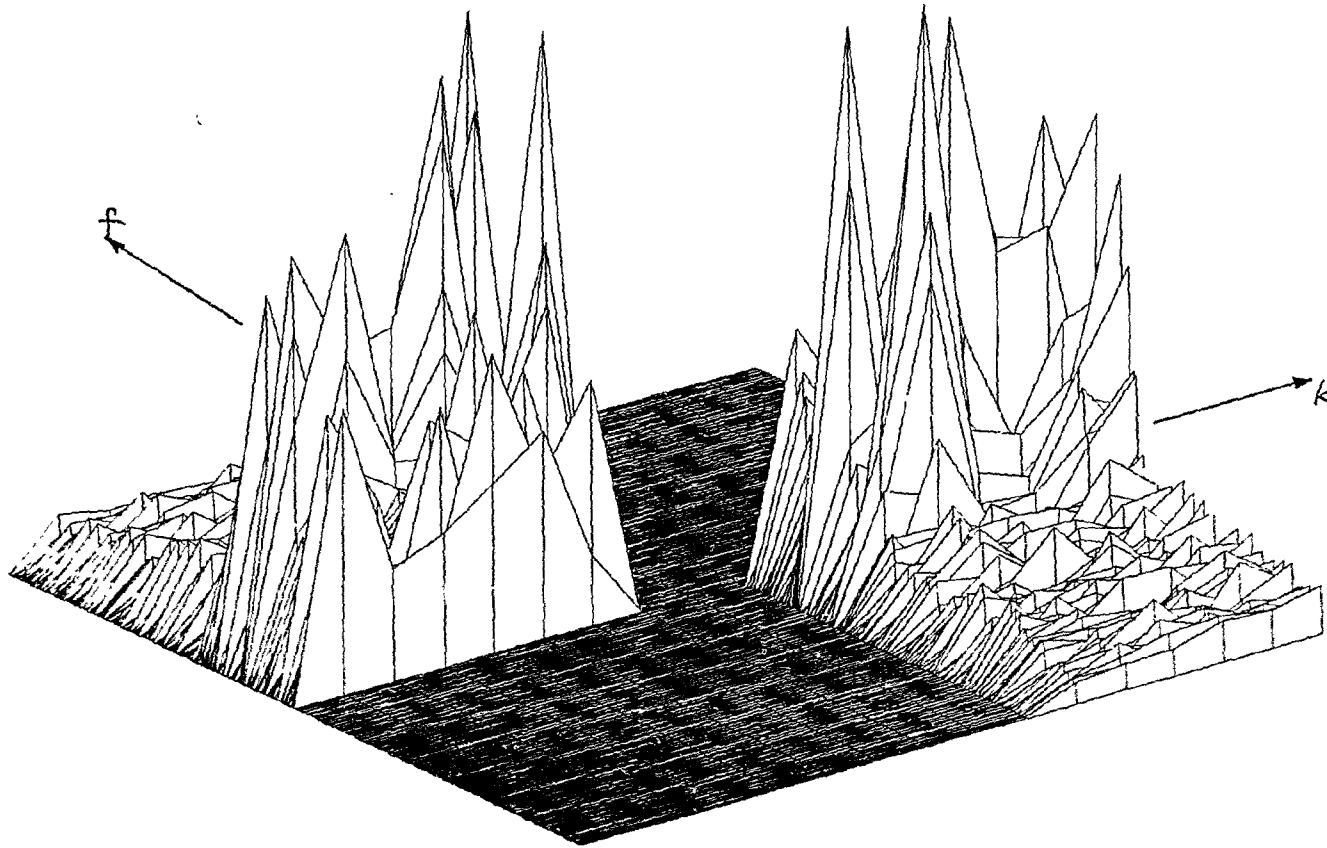


Figure B3.7 Mesh display of channel 2 data in f-k domain with the first and the third quadrants removed of their energy (c.f. Figure B3.5).



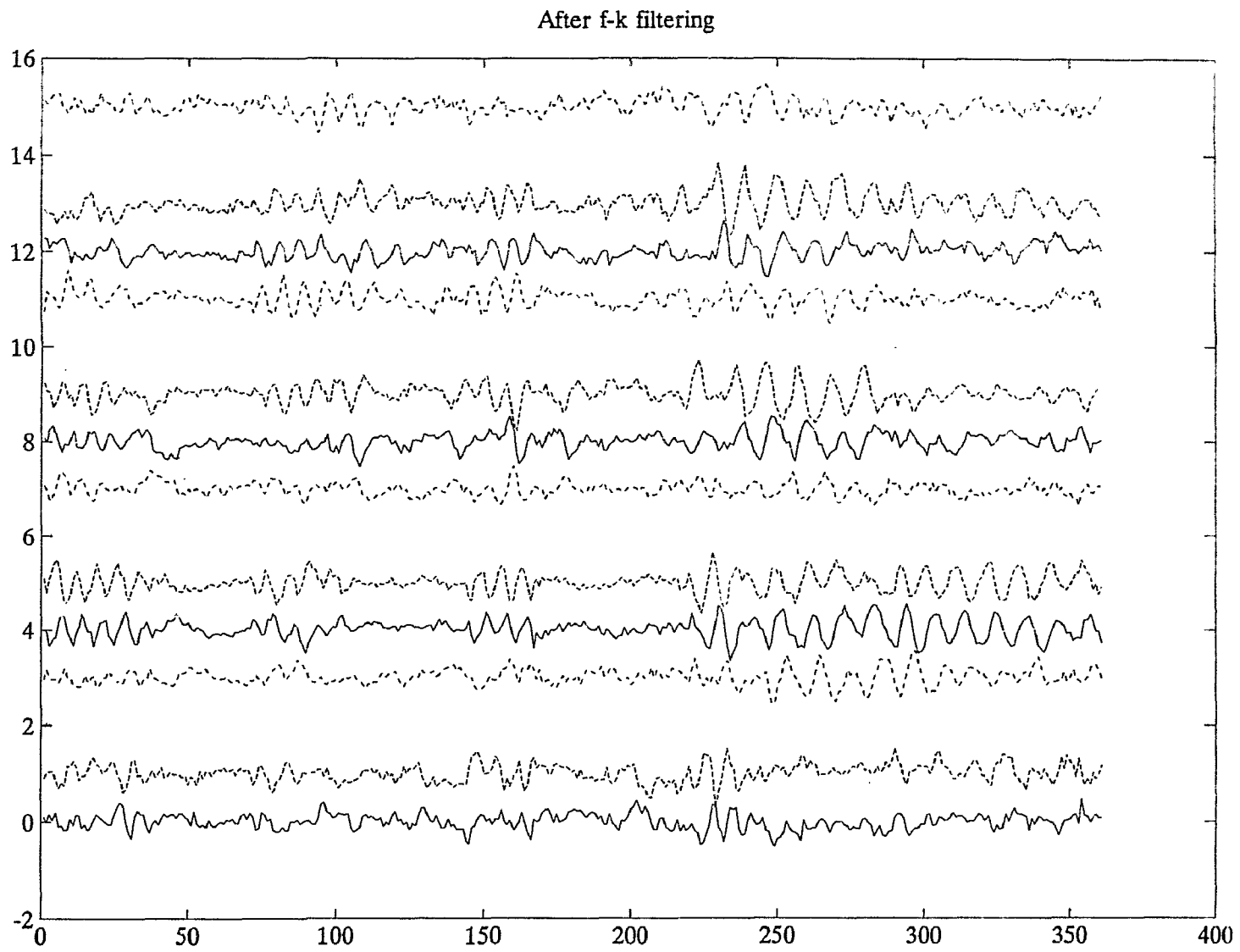


Figure B3.8 Seismograms generated by inverse Fourier transform the modified f-k response function as shown in Figure B3.7.

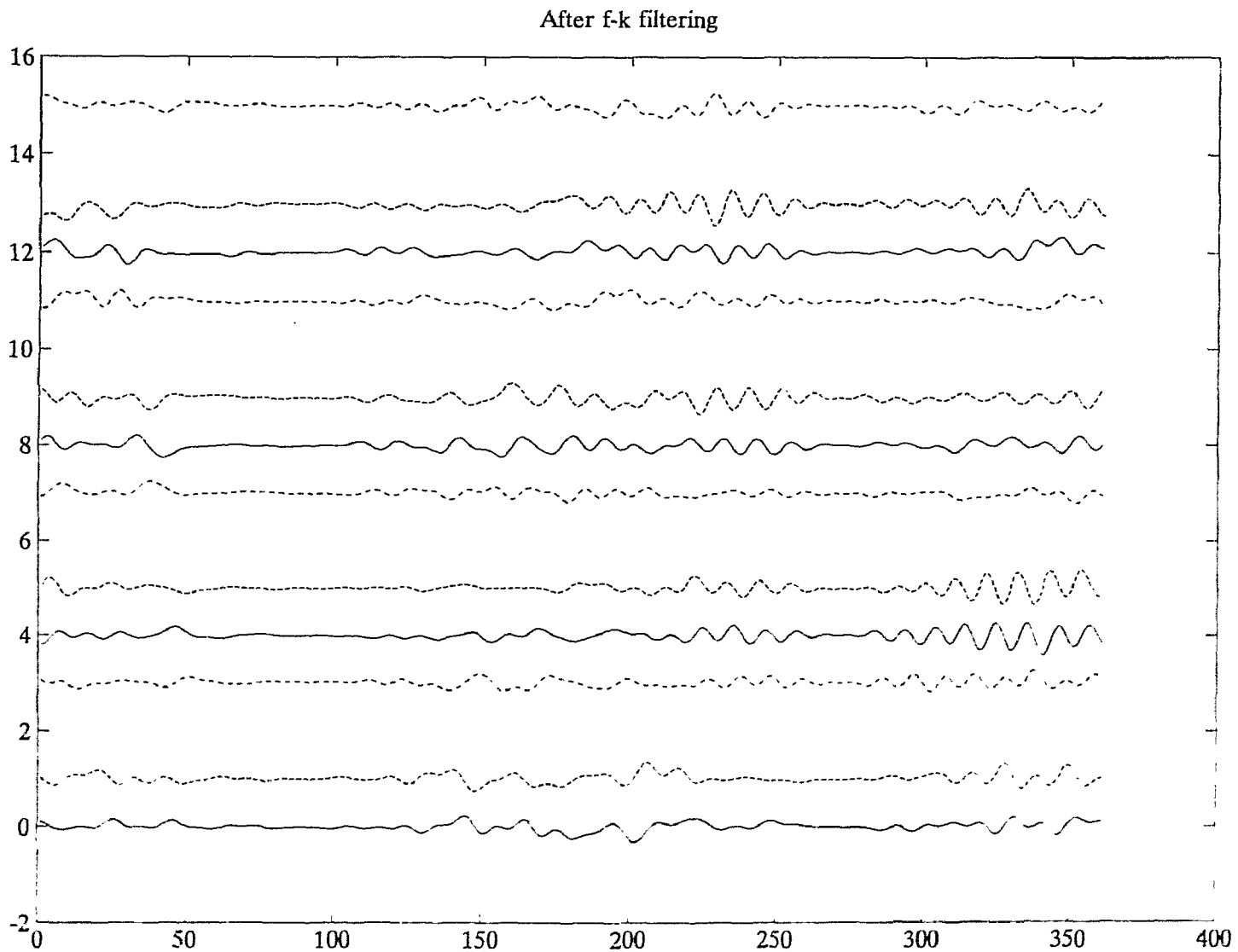


Figure B3.9 Seismograms generated by inverse Fourier transform the f-k response function of channel 2 after removing all the numbered energy concentrations in Figure B3.6. While time codes are highly suppressed, signals are also attenuated.

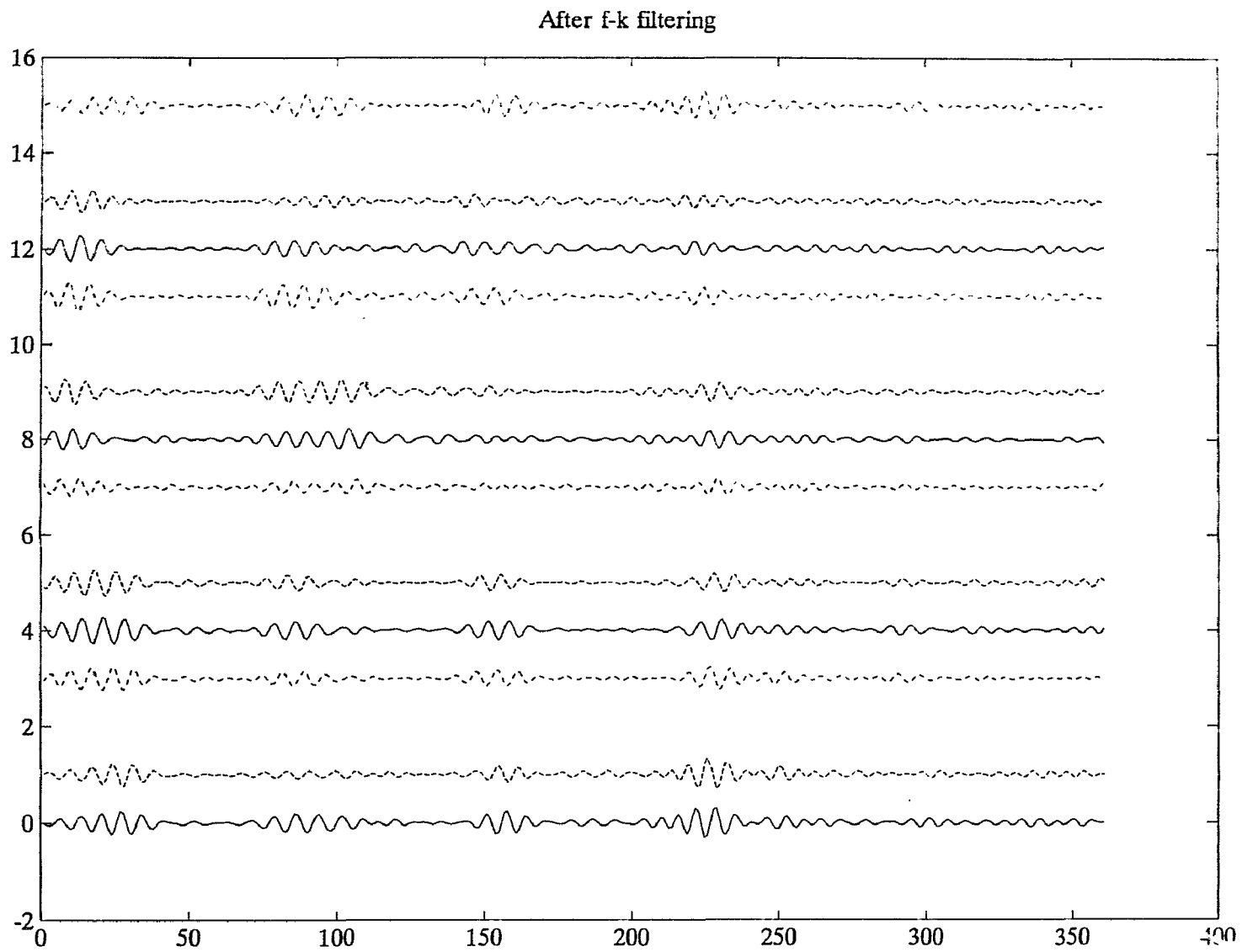


Figure B3.10 Seismograms generated by inverse Fourier transform the f-k response function that includes only the energy concentrations numbered 9 and 10 in Figure B3.6. These are purely time codes.

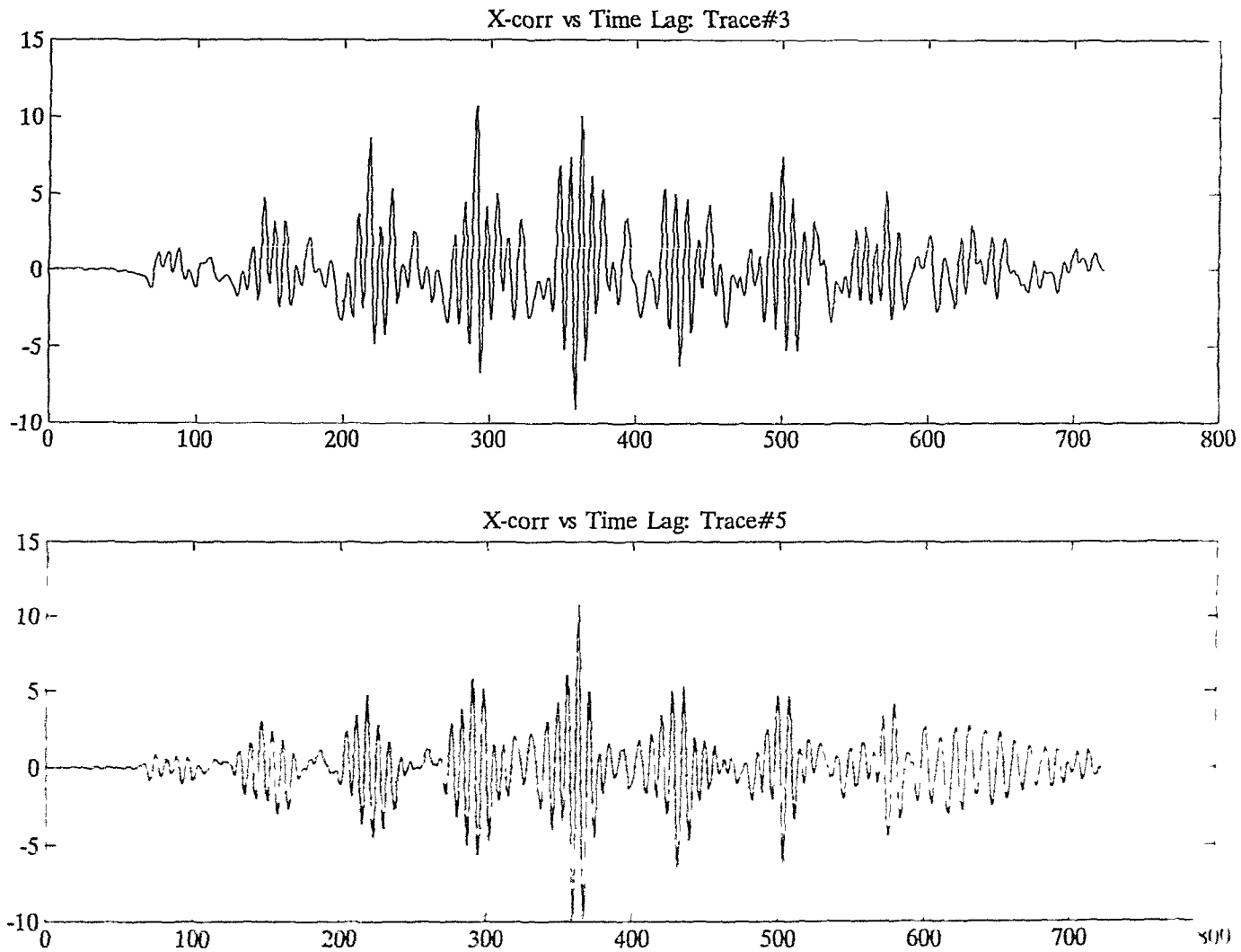


Figure B4.1 Estimating time lags by matching the maximum correlation between channel 2 and channel 1. X axis is labelled by the sequential number of sample points. 0 time lag is at point number 361.

16 traces of T.C. contaminated data

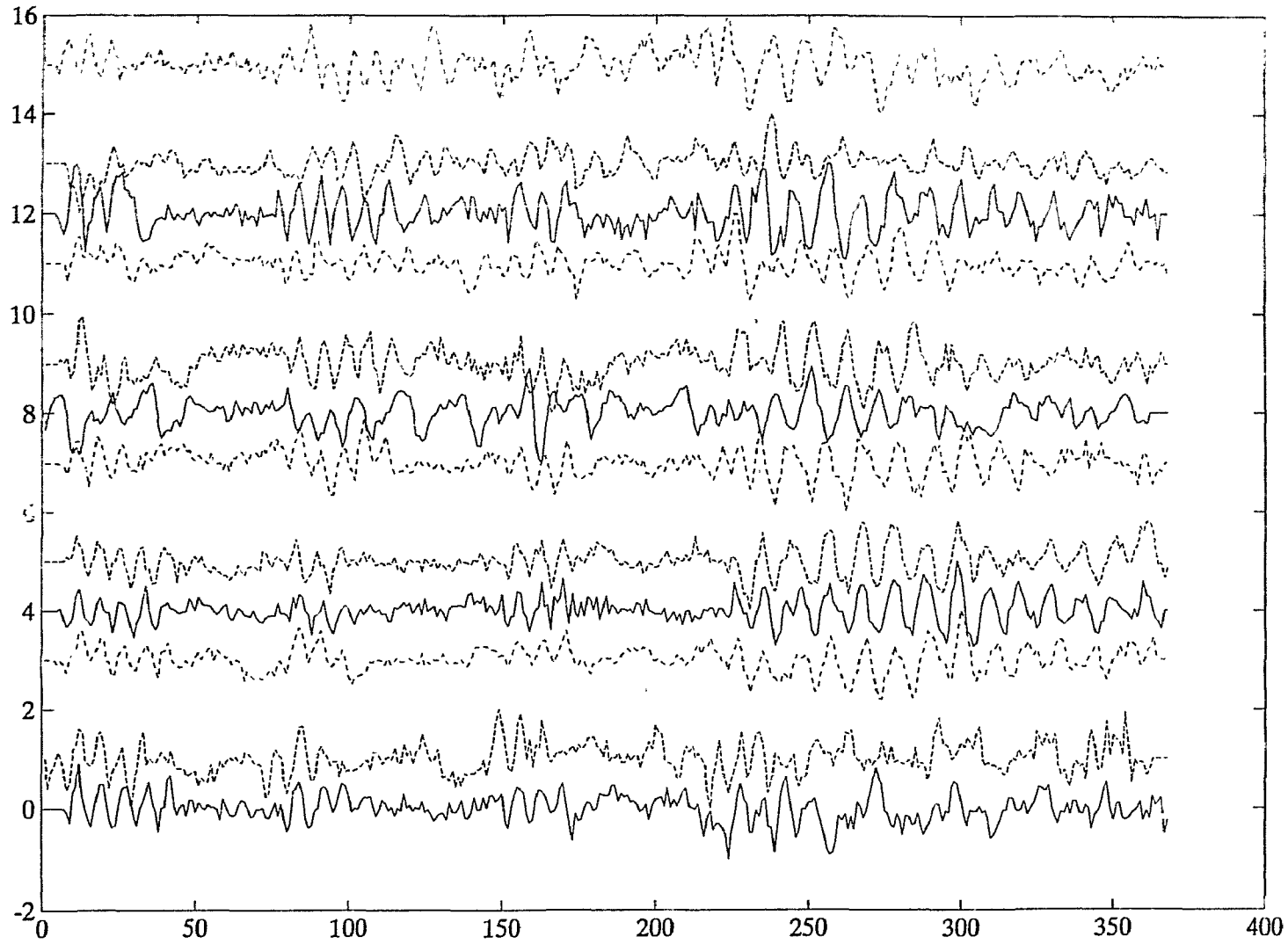


Figure B4.2 After time code line-up, the time codes in channel 2 is better lined up than the original traces as shown in Figure B2.1.

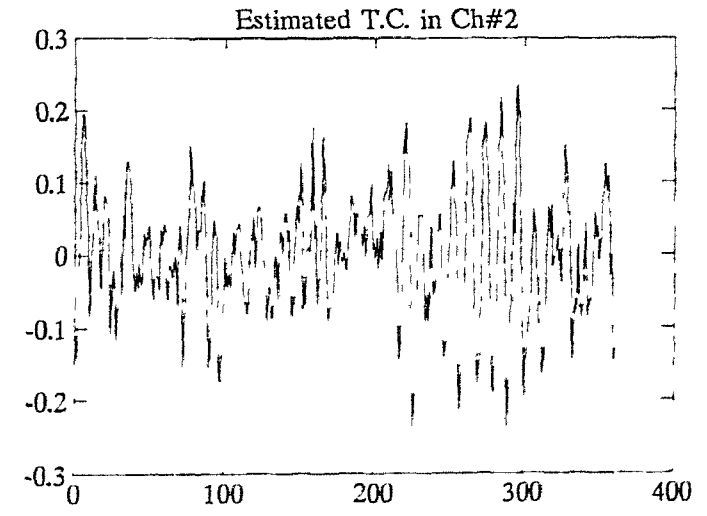
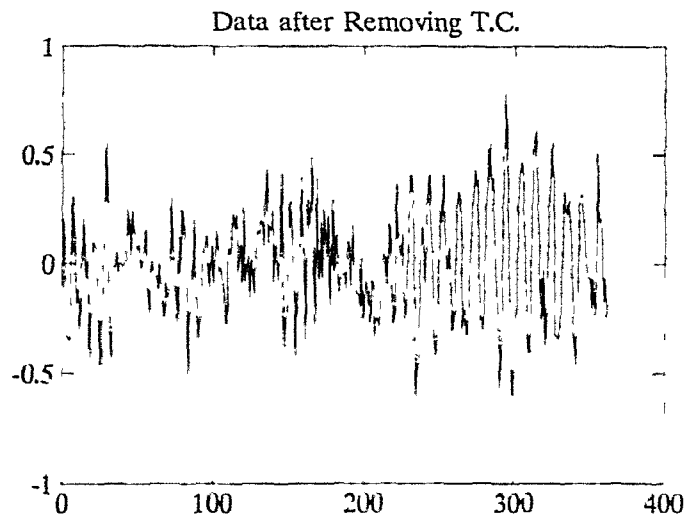
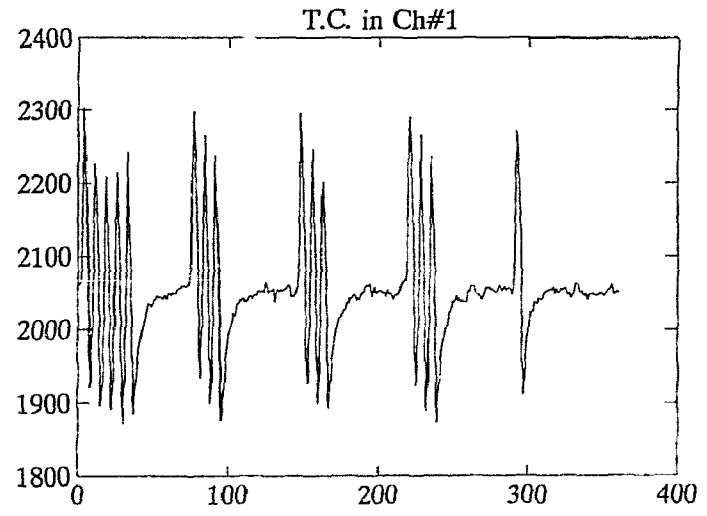
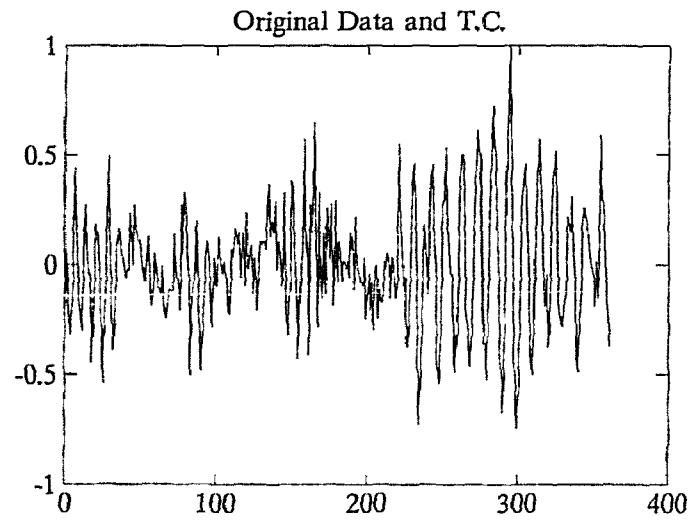


Figure B4 3 Before time code line-up the estimated time code in channel 2 (by averaging along straight lines across different traces) is less resolved. Subtracting the estimates from the data gives the lower left diagram.

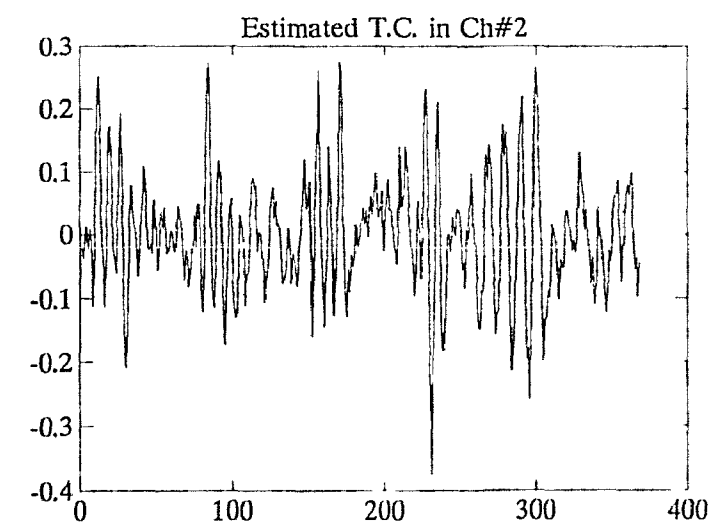
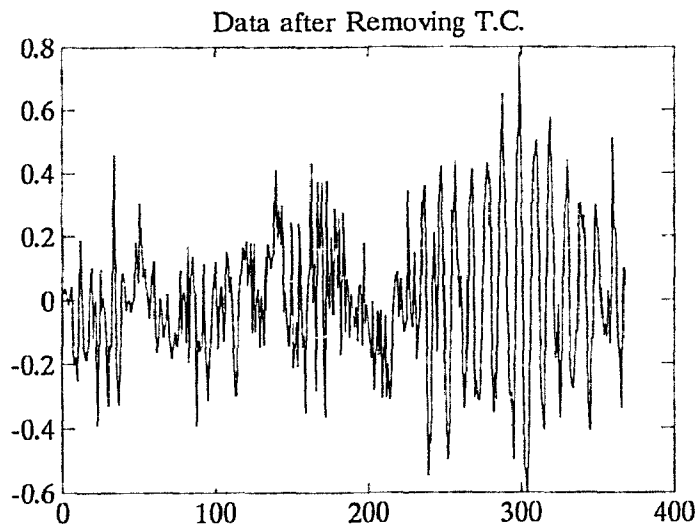
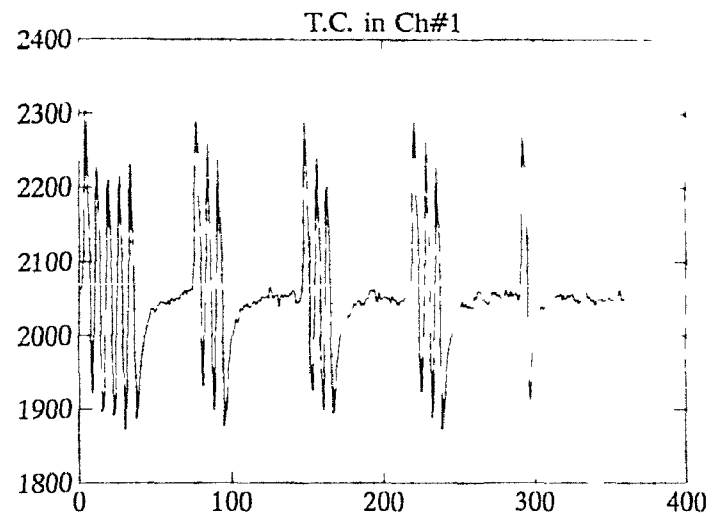
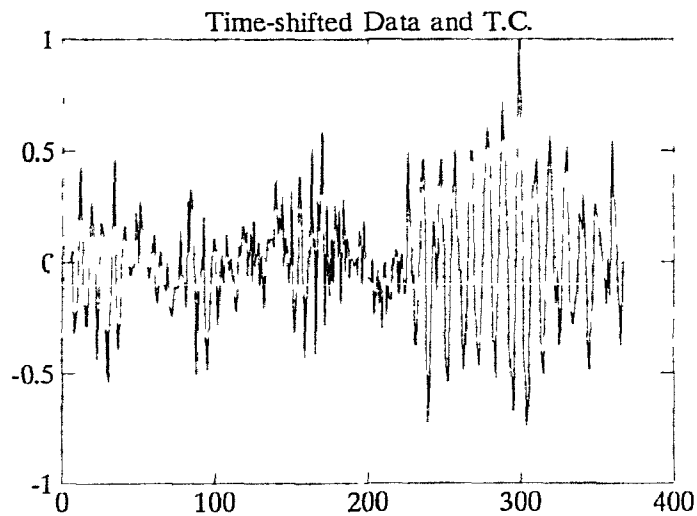


Figure B4.4 After time code line-up the estimated time code in channel 2 (by averaging along curved lines across different traces defined by the estimated time lags) is better resolved. Subtracting the estimates from the data gives the lower left diagram.

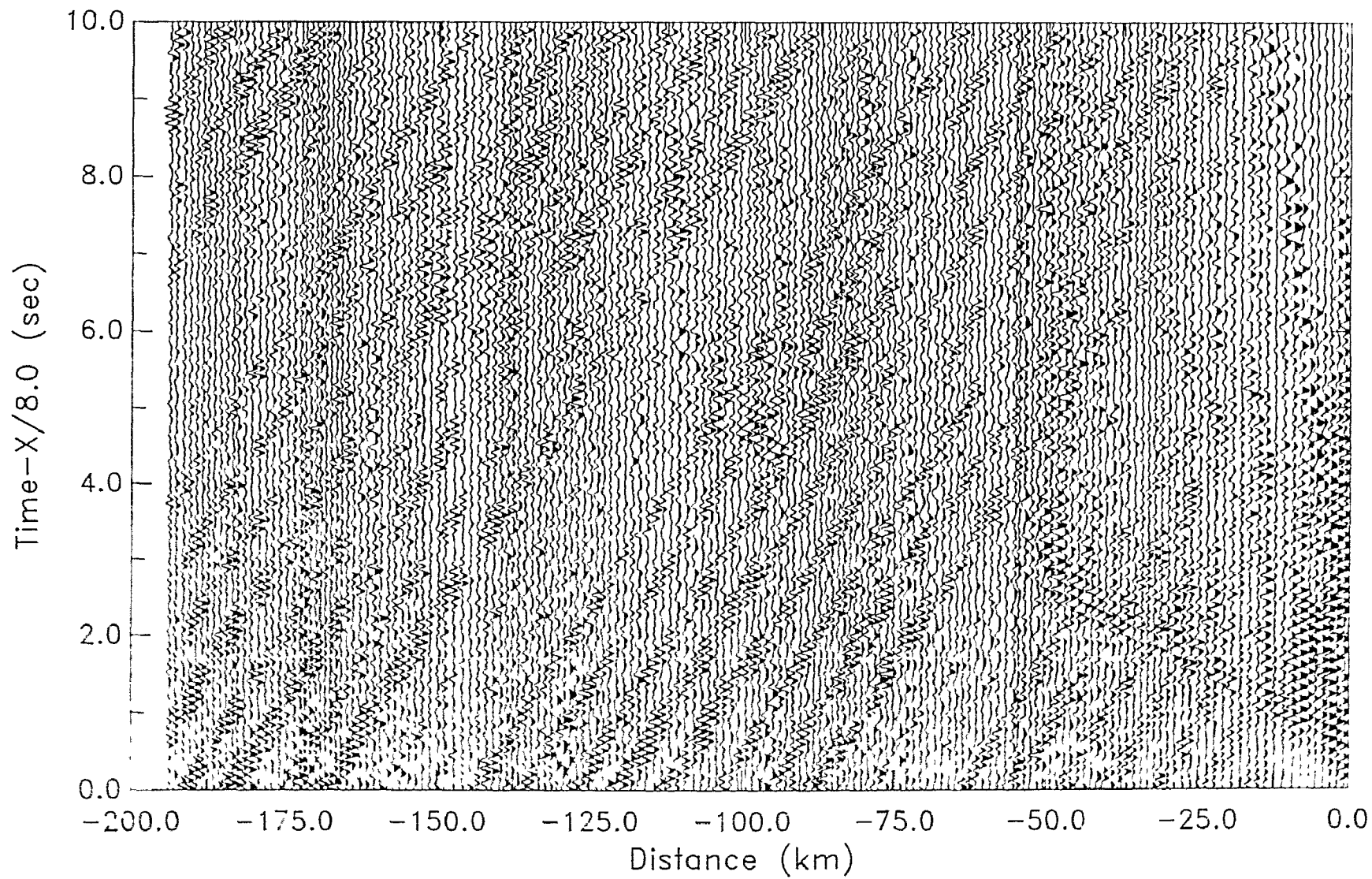


Figure B4.5 First iteration of time code removing processing.



Hud 88-024 R1J CH2

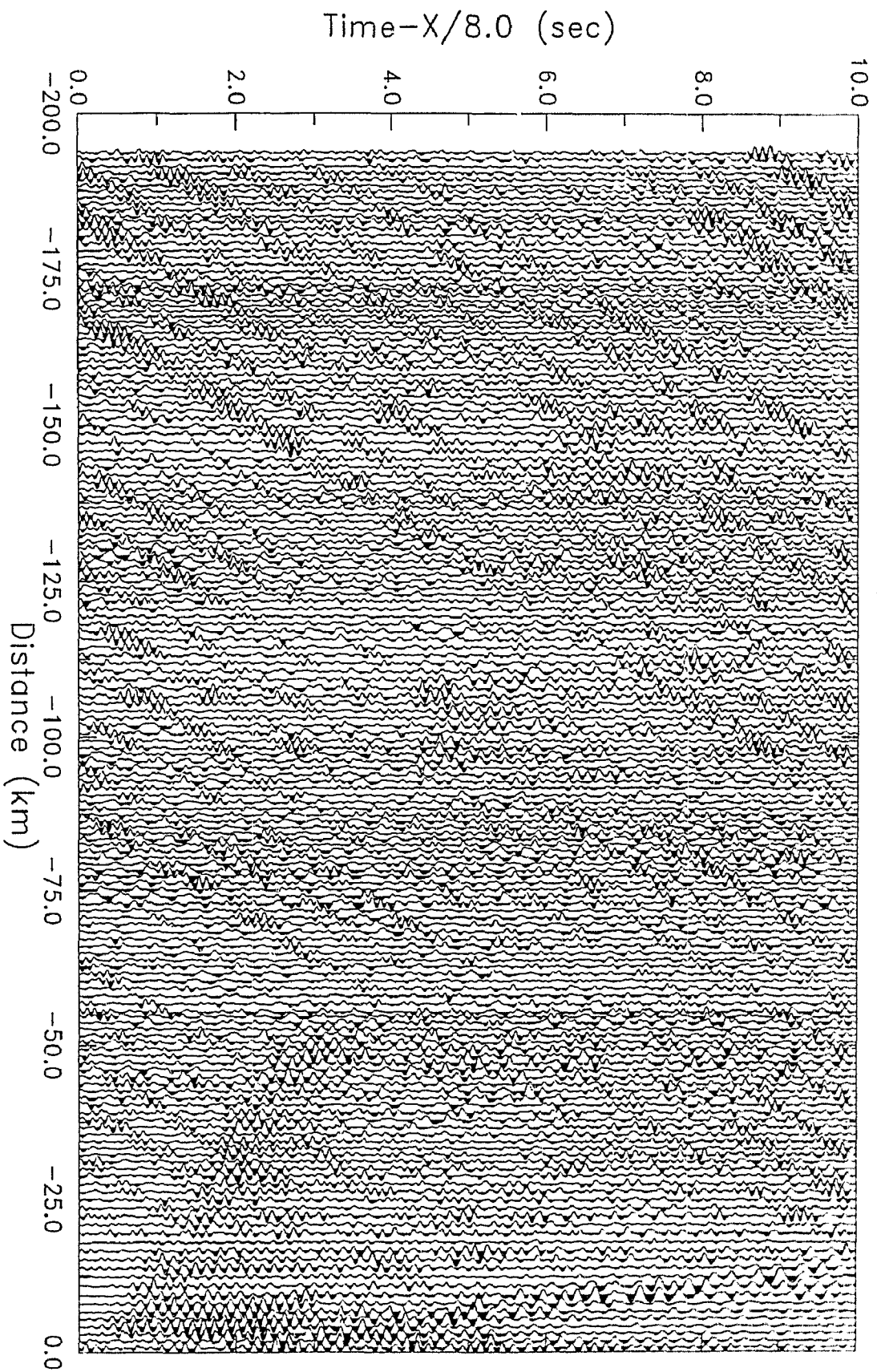


Figure B4.6 7th iteration of time code removing processing.

Hud 88-024 R1J CH2

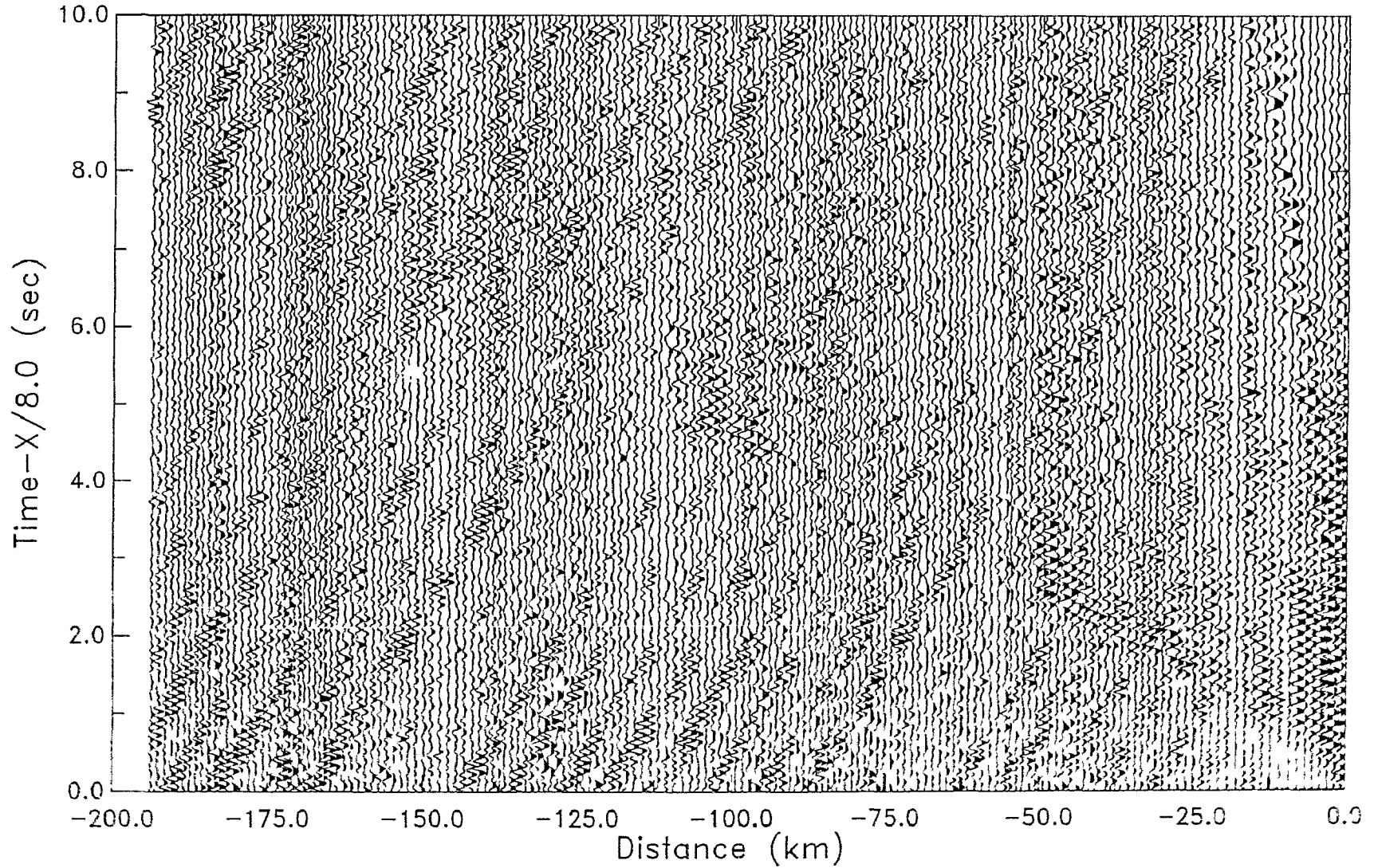


Figure B4.7 First iteration of time code removing processing with correlation performed at a narrow frequency band from 7.75 to 12 Hz

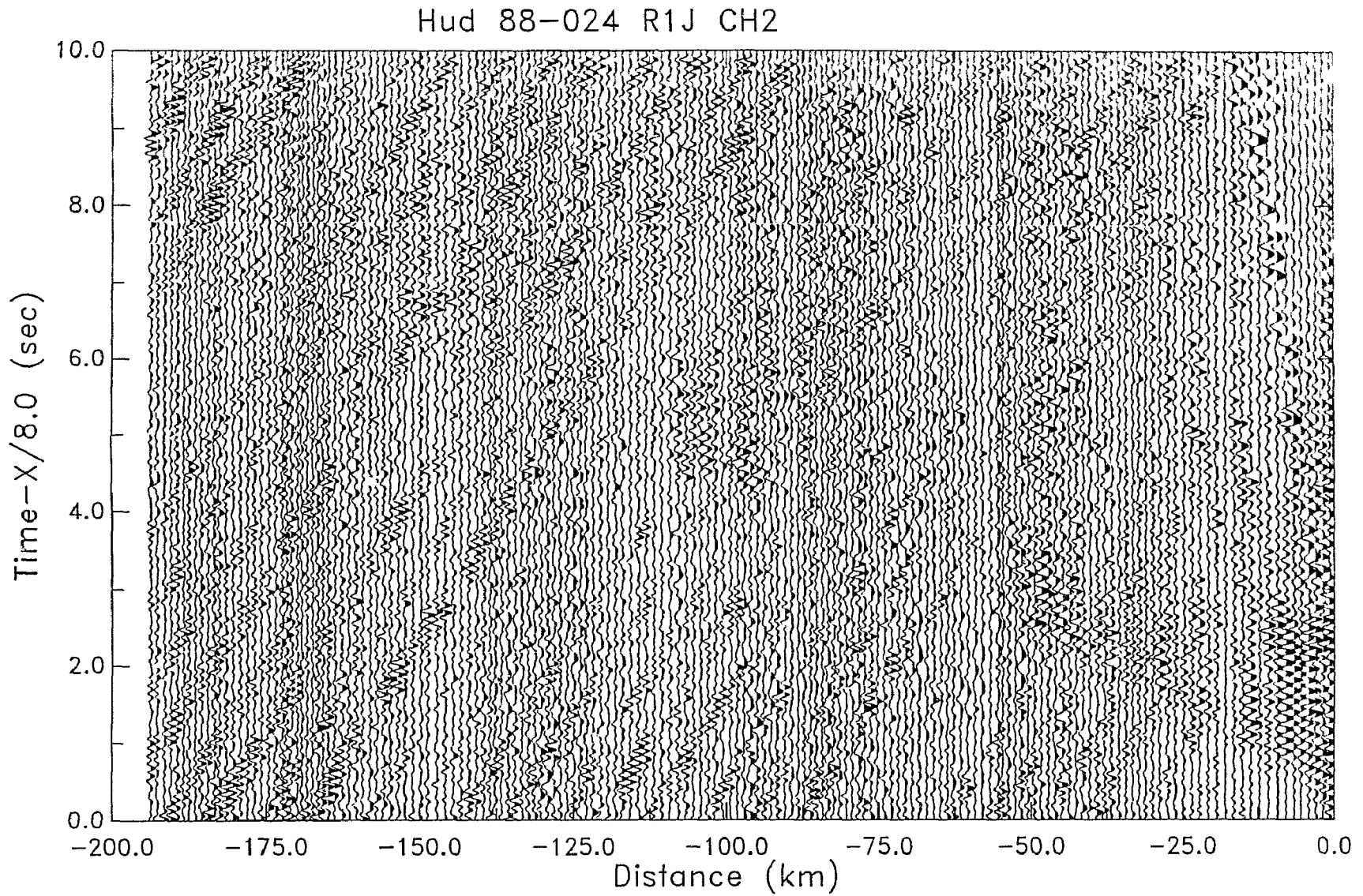


Figure B4.8 third iteration of time code removing processing with correlation performed at a narrow frequency band from 7.75 to 12 Hz.

Hud 88-024 R1J CH2

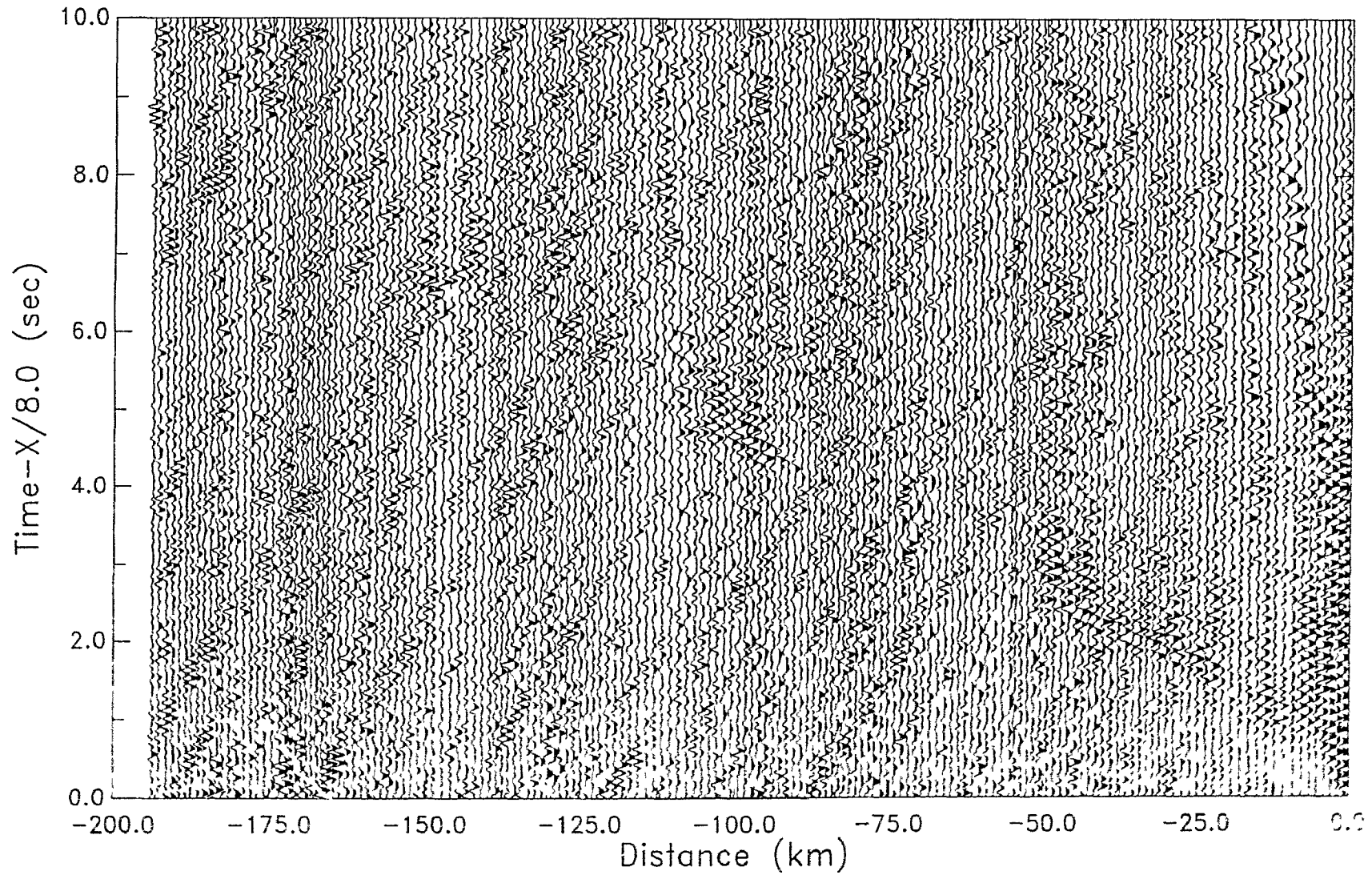


Figure B4.9 Time code removing processing with correlation performed at a narrow frequency band from 7.75 to 12 Hz. 5 time windows were used.

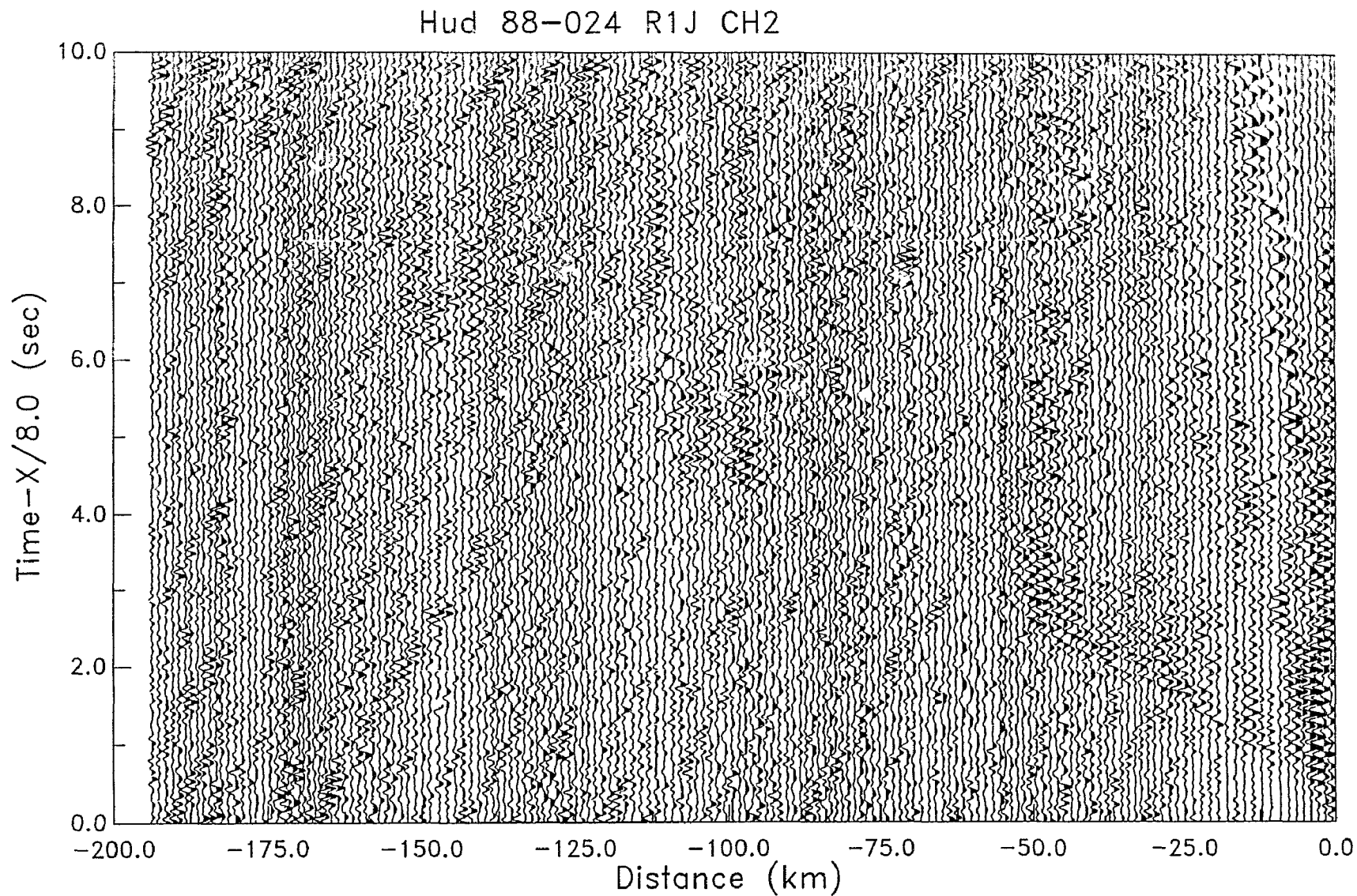


Figure B4.10 Time code removing processing with correlation performed at a narrow frequency band from 7.75 to 12 Hz. 5 time windows were used with half of each overlapped.

Hud 88-024 R1J CH2

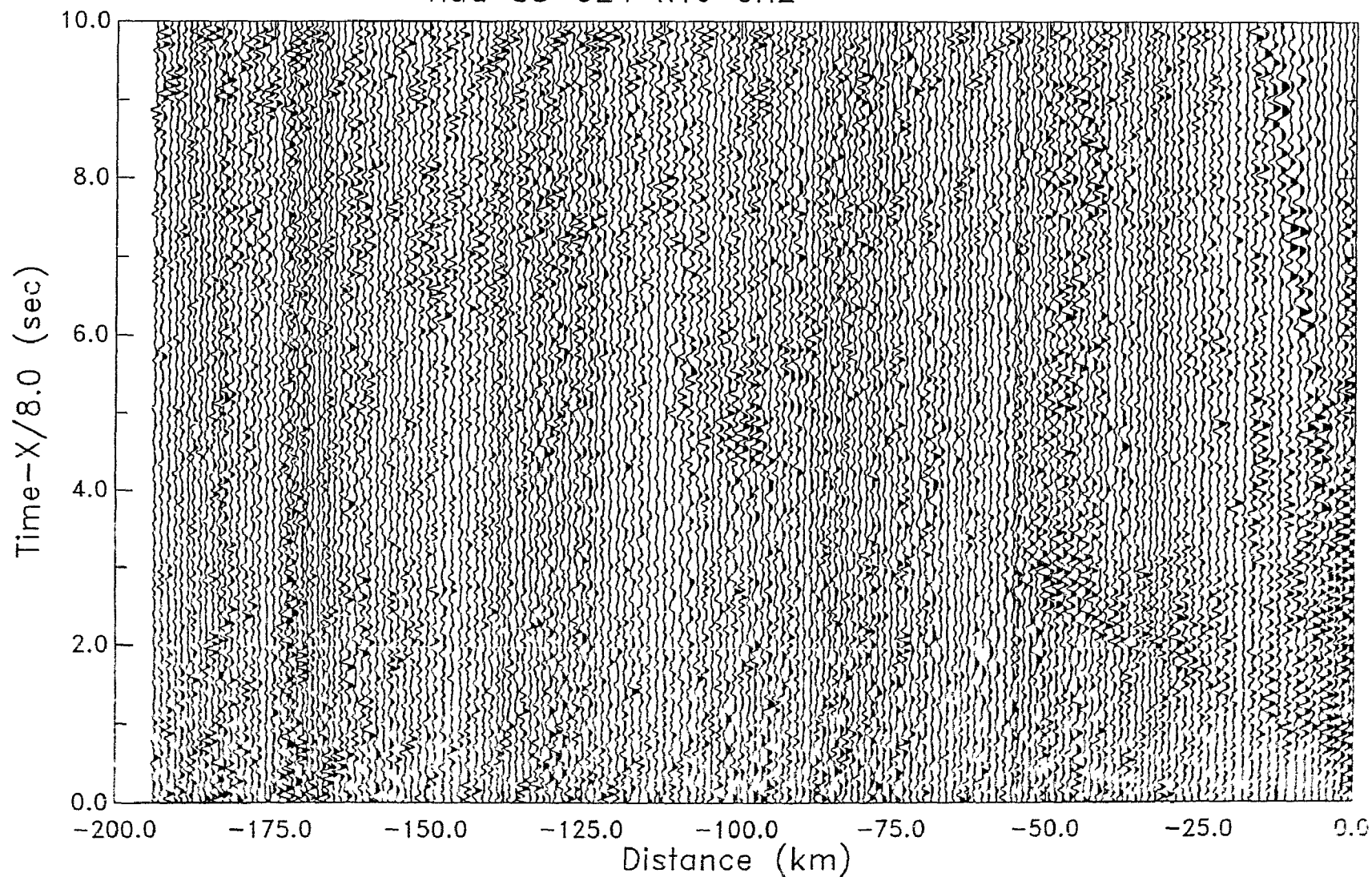


Figure B4 11 3rd iteration of time code removing processing with correlation performed at a narrow frequency band from 7.75 to 12 Hz. 5 time windows were used with half of each overlapped.

Hud 88-024 R1J CH2 STACK

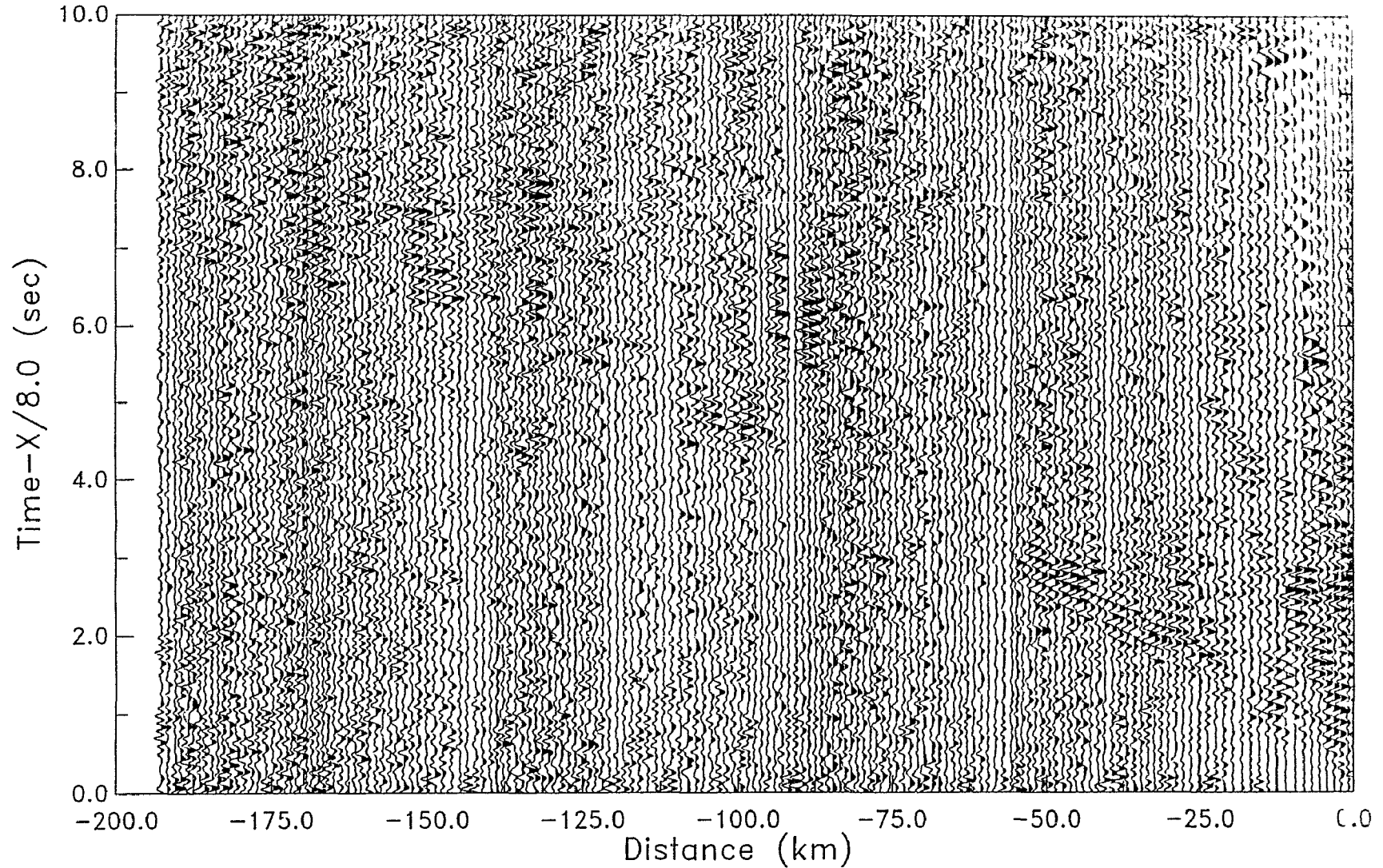


Figure B4.12 3rd iteration of time code removing processing with correlation performed at a narrow frequency band from 7.75 to 12 Hz. 5 time windows were used with half of each overlapped. The resulting traces are stacked by 12.

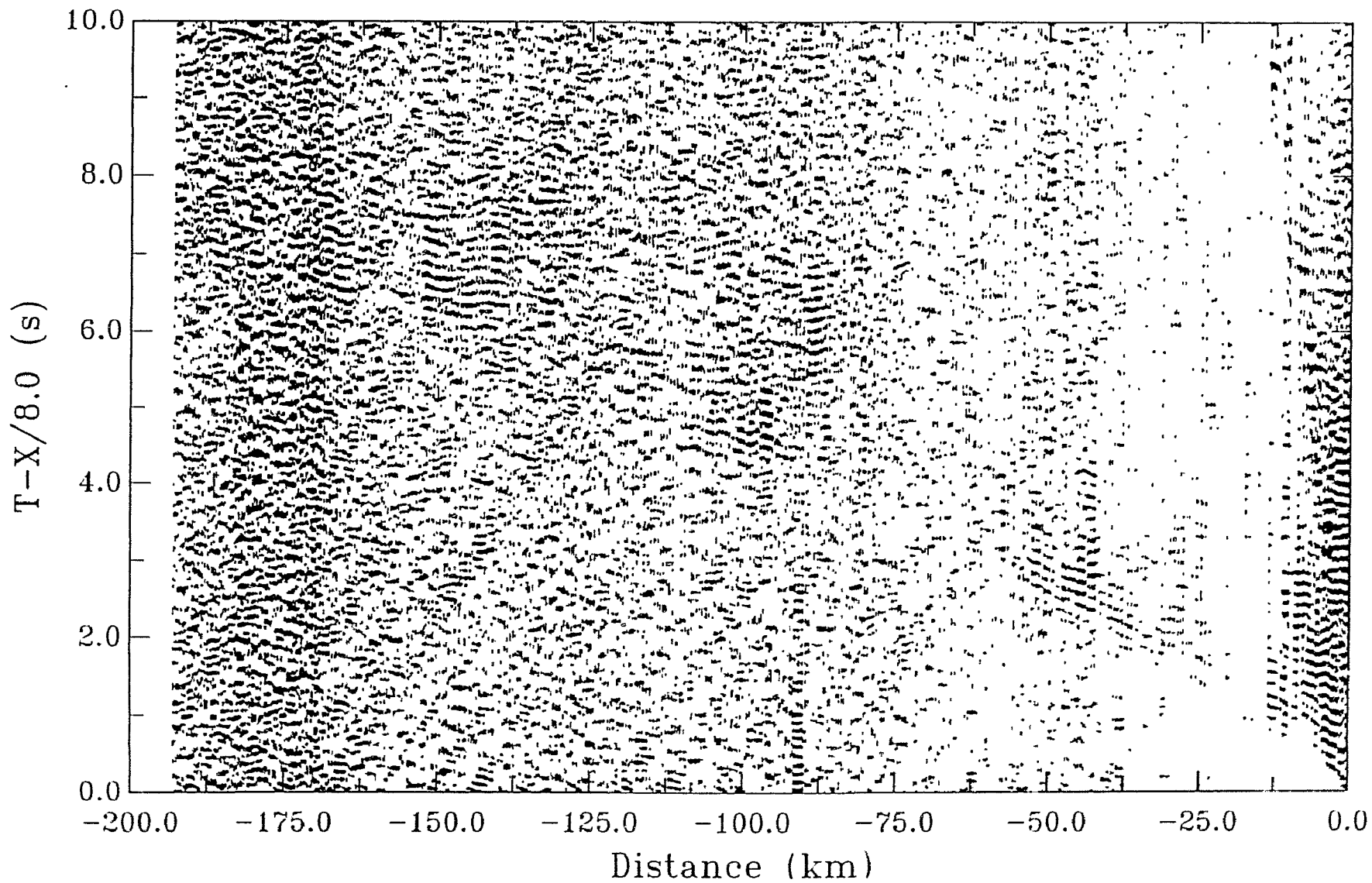


Figure B4.13 First iteration of time code removing processing with correlation performed at a narrow frequency band from 7.75 to 12 Hz. 5 time windows were used with half of each overlapped. The resulting traces are stacked by 12 and every one trace is displayed.



### Appendix C. OBS Locations

**Table C. 1 OBS Locations for the 1990 refraction lines 90R1, 90R2, and 90R3**

R1	Latitude (°N)	Longitude (°W)	R2	Latitude (°N)	Longitude (°W)	R3	Latitude (°N)	Longitude (°W)
B	55.82602	59.06638	K	56.56388	57.23703	C	56.39167	59.8321
H	55.92533	58.60108	Q	56.44065	57.13085	I	56.14083	59.41533
Q	56.05452	58.06693	C	56.19792	56.92156	B	55.86798	58.9889
C	56.14527	57.66815	I	56.07311	56.81334	K	55.59511	58.5749
D	56.24962	57.24698				Q	55.32183	58.1643
P	56.31985	56.94953						
G	56.41250	56.56757						
A	56.51962	56.08620						
M	56.66775	55.45270						
K	56.84732	54.69673						
I	57.04228	53.85013						

## Bibliography

- Allaart, H., Ketilidian mobile belt in South Greenland, in *Geology of Greenland*, edited by A. Escher and W. S. Watt, Geological Survey of Greenland. Copenhagen, Denmark, 121-151, 1976.
- Balkwill, H. R., Labrador Basin: structural and stratigraphy style, in *Sedimentary basins and basin-forming mechanisms*, edited by C. Beaumont and A. J. Tankard, Canadian Society of Petroleum Geologists, Memoir 12, 17-43, 1987.
- Beaumont, C., C.E. Keen, and R. Boutilier, On the evolution of rifted continental margins: composition of models and observations for the Nova Scotia margin, *Geophysical Journal of Royal astronomical Society*, 70, 667-715, 1982.
- Bell, J.S. (Coordinator), *East Coast Basin Atlas Series, Labrador Sea*, Atlantic Geoscience Centre, Geological Survey of Canada, Dartmouth, Nova Scotia, 1989.
- Berry M. J., and Fuchs, K., Crustal structure of the Superior and Grenville Provinces of the Northeastern Canadian shield, *Seismological Society of America Bulletin*, 63, 1393-1432, 1973.
- Beslier, M.O., J. Girardeau, and G. Boillot, Kinematics of peridotite emplacement during North Atlantic continental rifting, Galicia, NW Spain, *Tectonophysics*, 184, 321-343, 1990.
- Boillot, G., J., M.O. Beslier, and M. Comas, Seismic image of undercrusted serpentinite beneath a rifted margin, *Terra Nova*, 4, 25-33, 1992.
- Boillot, G., J., G. Feraud, M. Recq and J. Girardeau, "Undercrusting" by serpentinite beneath rifted margins: the examples of the west Galicia margin (Spain), *Nature*, 341, 523-525, 1989a.
- Boillot, G., J. Girardeau, and J. Kornprobst, Rifting of the Galicia Margin: crustal thinning and emplacement of mantle rocks on the seafloor, *Proceedings of Ocean Drilling Program, Scientific Results*, 103, 741-756, 1988.
- Boillot, G., D. Mougnot, J. Girardeau and E.L. Winterer, Rifting processes on the west Galicia margin, Spain, in *Extensional Tectonics and Stratigraphy of the North Atlantic Margins*, Memoir 46, edited by A.J. Tankard and H.R. Balkwill, American Association of Petrologic Geology, Tulsa, OK, 363-377, 1989b.
- Braun, J., and C. Beaumont, Dynamic models of the role of crustal shear zones in asymmetric continental extension, *Earth and Planetary Science Letters*, 93, 405-423, 1989.
- Bridgwater, D., Escher, A., and Watterson, J., Tectonic displacements and thermal activity in two contrasting Proterozoic mobile belts from Greenland. *Royal Society of London, Philosophical Transactions*, A273, 513-533, 1973.
- Bridgwater, D., Keto, L., McGregor, V. R., and Myers, J. S. Archean gneiss complex of Greenland. in *Geology of Greenland*, edited by A. Escher and W. S. Watt, Geological Survey of Greenland, Copenhagen, Denmark, 19-75, 1976.
- Buck, W.R., Small-scale convection induced by passive rifting: The cause for uplift of rift shoulders, *Earth and Planetary Science Letters*, 77, 362-372, 1986.
- Burke, M. M. Reflectivity of highly deformed terranes based on laboratory and in situ velocity measurements from the Grenville front tectonic zone, Central Ontario, Canada, Ph.D. thesis, Dalhousie University, Halifax, Nova Scotia, 1990.

- Campbell, I.H., and R.W. Griffiths, Implications of mantle plume structure for the evolution of flood basalts, *Earth and Planetary Science Letters*, 99, 79-93, 1990.
- Cerveny, V., I.A. Molotkov, and I. Psencik, *Ray Method in Seismology*, 214 pp., University of Karlova, Prague, 1977.
- Chalmers, J.A., New evidence on the structure of the Labrador Sea/Greenland continental margin, *Journal of Geological Sciences*, London, 148, 899-908, 1991.
- Chalmers, J.A., T.C.R. Pulvertaft, F.G. Christiansen, H.C. Larsen, K.H. Laursen, and T.G. Ottesen, The southern West Greenland continental margin: rifting history, basin development, and petroleum potential, in *Petroleum Geology of Northwest Europe*, in Proceedings of the 4th Conference, edited by J.R. Parker, *Petroleum Geology '86 Ltd.*, The Geological Society, London, 915-931, 1993.
- Chapman, C. H. A new method for computing synthetic seismograms, *Geophysical Journal of the Royal Astronomical Society*, 54, 481-518, 1978.
- Chapman, C. H., and Drummond, R., Body-wave seismograms in inhomogeneous media using Maslov asymptotic ray theory, *Seismological Society of America Bulletin*, 72, S277-S317, 1982.
- Chenet, P.-Y., L. Montadert, H. Gairaud, and D. Robert, Extension ratio measurements on the Galicia, Portugal and northern Biscay continental margins: implications for evolutionary models of passive continental margins, in *Studies in Continental Margin Geology*, edited by J.S. Watkins and C.L. Drake, *American Association Petrological Geology, Memoir 34*, Tulsa, OK, 703-715, 1983.
- Chian, D. and Louden, K.E., The structure of Archean/Ketilidian crust along the continental shelf of southwestern Greenland from a seismic refraction profile, *Canadian Journal of Earth Sciences*, 29, 301-313, 1992.
- Chian, D. and Louden, K.E., The continent-ocean crustal transition across the southwest Greenland margin, *Journal of Geophysical Research*, in press, 1994.
- Christensen, N.I., Elasticity of ultramafic rocks, *Journal of Geophysical Research*, 71, 5921-5931, 1966.
- Christensen, N.I., Ophiolites, seismic velocities and oceanic crustal structure, *Tectonophysics*, 47, 131-157, 1978.
- Christensen, N.I., Seismic velocities, in *Practical Handbook of Physical Properties of Rocks and Minerals*, edited by R.S. Carmichael, CRC Press, Boca Raton, FL, 429-546, 1989.
- Christensen, N. I., and Fountain, D. M., Constitution of the lower continental crust based on experimental studies of seismic velocities in granulite, *Geological Society of America Bulletin*, 20, 227-236, 1975.
- Christensen, N.I., and J.D. Smewing, Geology and seismic structure of the northern section of the Oman Ophiolite, *Journal of Geophysical Research*, 86, 2545-2555, 1981.
- Clarke, D. B., Cameron, B. I., Muecke, G. K., and Bates, J. L., Early Tertiary basalts from the Labrador Sea floor and Davis Strait region, *Canadian Journal of Earth Sciences*, 26, 956-968, 1988.
- Clarke, D.B., and B.G.J. Upton, Tertiary basalts of Baffin Island: Field relations and tectonic setting, *Canadian Journal of Earth Sciences*, 8, 248-258, 1971.

- de Voogd, B., L. Serpa, and L. Brown, Crustal extension and magmatic processes COCORP profiles from Death Valley and the Rio Grande rift, *Geological Society of America Bulletin*, 100, 1550-1567, 1988.
- Dunbar, J.A., and D.S. Sawyer, Implications of continental crust extension for plate reconstruction: An example from the gulf of Mexico, *Tectonics*, 6, 739-755, 1989.
- Eldholm, O., J. Thiede, and ODP Leg 104 Scientific Party, Formation of the Norwegian Sea, *Nature*, 319, 360-361, 1986.
- Fountain, D.M., and N.I. Christensen, Composition of the continental crust and upper mantle; A review, in *Geophysical Framework of the Continental United States*, Boulder, Colorado, edited by L.C. Pakiser, and W.D. Mooney, Geological Society of America Memoir, 172, Boulder, CO, pp. 711-742, 1989.
- Friend, C. R. L., A. P. Nutman, and V. R. McGregor, Late Archean terrain accretion in the Godthab region, south West Greenland, *Nature*, 335, 535-538, 1988.
- Furlong, K. P., and Fountain, D. M. 1986, Continental crustal underplating thermal considerations and seismic-petrologic consequences. *Journal of Geophysical Research*, 91, 8285-8294.
- Ginzburg, A., R.B. Whitmarsh, D.G. Roberts, L. Montadert, A. Camus and F. Avedik, The deep seismic structure of the northern continental margin of the Bay of Biscay, *Annales Geophysicae*, 3, 499-510, 1985.
- Girardeau, J., C.A. Evans, and M.O. Beslier, Structural analysis of plagioclase-bearing peridotites emplaced at the end of continental rifting: hole 637A, ODP leg 103 on the Galicia margin, in *Proceedings of Ocean Drilling Program, Scientific Results*, 103, edited by G. Boillot, E.L. Winterer et al., 209-223, Ocean Drilling Program, College Station, TX, 1988.
- Gohl, K., and S.B. Smithson, Structure of Archean crust and passive margin of Southwest Greenland from seismic wide-angle data, *Journal of Geophysical Research*, 98, 6623-6638, 1993.
- Hall, J., Physical properties of Lewisian rocks: implications for deep crustal structure in *Evolution of the Lewisian and comparable Precambrian high grade terrains*, edited by R. G. Park and J. Tarney. Geological Society Special Publication No 27, 185-192, 1987
- Hall, J., and F. M. Al-Haddad, Variation of effective seismic velocities of minerals with pressure and its use in velocity prediction, *Geophysical Journal of Royal Astronomical Society*, 57, 107-118, 1979.
- Hall, J., and G. Simmons, Seismic velocities of Lewisian metamorphic rocks at pressures to 8 kbar: relationship to crustal layering in North Britain, *Geophysical Journal of Royal Astronomical Society*, 58, 337-347, 1979.
- Hinz, K., J. C. Mutter, C. M. Zehnder, and the NGT Study Group, Symmetric conjugation of continent-ocean boundary structures along the Norwegian and east Greenland margins, *Marine and Petrological Geology*, 4, 166-181, 1987
- Hinz, K., Schluter, H.-U., Grant, A. C., Srivastava, S. P., Umpleby, D., and Woodside, J. 1979. Geophysical transects of the Labrador Sea: Labrador to southwest Greenland *Tectonophysics*, 59, 151-183, 1979

- Hoffmann, J., Pre-tectonic depth migration on the *S* reflector off Galicia, D.E.A. Univ. Bretagne Occidentale, Brest, 53 p., 1991.
- Holbrook, W. S., D. Gajewski, A. Krammer, and C. Prodehl, An interpretation of wide-angle compressional and shear wave data in southwest Germany: Poisson's ratio and petrological implications, *Journal of Geophysical Research*, 93, 12081-12106, 1988.
- Holbrook, W.S. and P.B. Keleman, Large igneous province on the U.S. Atlantic margin and implications for magmatism during continental breakup, *Nature*, 364, 433-436, 1993.
- Holbrook, W.S., W.D. Mooney, and N.I. Christensen, The seismic velocity structure of the deep continental crust, in *Continental Lower Crust*, edited by D.M. Fountain, R. Arculus, and R. Kay, Elsevier, Amsterdam, 1-43, 1992.
- Holbrook, W.S., E.C. Reiter, G.M. Purdy, and M.N. Toksöz, Image of the Moho across the continent-ocean transition, U.S. east coast, *Geology*, 20, 203-206, 1992b.
- Holbrook, W.S., E.C. Reiter, G.M. Purdy, D. Sawyer, P.L. Stoffa, J.A. Austin Jr., J. Oh and J. Makris, Deep structure of the U.S. Atlantic continental margin, offshore South Carolina, from coincident ocean-bottom and multichannel seismic data, *Journal of Geophysical Research*, 99, 9155-9178, 1994.
- Horsefield, S.J., R.B. Whitmarsh, R.S. White and J.-C. Sibuet, Crustal structure of the Goban Spur passive continental margin results of a detailed seismic refraction survey, *Geophysical Journal of International*, 1994 (in press).
- Hyndman, R. D., Evolution of the Labrador Sea, *Canadian Journal of Earth Sciences*, 10, 637-644, 1973.
- Issler, D. R. The thermal and subsidence history of the Labrador margin, Ph.D. thesis, Dalhousie University, Halifax, Nova Scotia, 1987.
- Issler, D.R., and Beaumont, C., Thermal and subsidence history of the Labrador and West Greenland continental margins. in *Sedimentary basins and basin-forming mechanisms*, edited by C. Beaumont and A. J. Tankard, Canadian Society of Petroleum Geologists, Memoir 12, 45-69, 1987.
- Issler, D.R., H. McQueen, and C. Beaumont, Thermal and isostatic consequences of simple shear extension of the continental lithosphere, *Earth and Planetary Science Letters*, 91, 341-358, 1989.
- Jackson, J.A., and N.J. and White, Normal faulting in the upper continental crust: Observations from regions of active extension, *Journal of Structural Geology*, 11, 15-36, 1989.
- Jarrard, R.D., K.A. Dadey, and W.B. Busch, Velocity and density of sediments of Eirik Ridge, Labrador Sea: control by porosity and mineralogy, *Proceedings Ocean Drilling Program, Scientific Results*, 105, 811-835, 1989.
- Kalsbeek, F., and Taylor, P. N., Pb-isotopic studies of Proterozoic igneous rocks, West Greenland, with implications on the evolution of the Greenland shield, in *The deep Proterozoic crust in the North Atlantic provinces*, edited by A. C. Tobi and J. L. R. Touret. D. Reidel Publishing Company, Hingham, MA., 237-245, 1985a.
- Isotopic and chemical variation in granites across a Proterozoic continental margin—the Ketilidian mobile belt of South Greenland, *Earth and Planetary Science Letters*, 73, 65-80, 1985b.

- Keen, C.E., and B. de Voogd, The continent-ocean boundary at the rifted margin off eastern Canada: new results from deep seismic reflection studies, *Tectonics*, 7, 107-124, 1988.
- Keen, C.E., C. Peddy, B. de Voogd, and D. Matthews, Conjugate margins of Canada and Europe: results from deep reflection profiling, *Geology*, 17, 173-176, 1989.
- Keen, C.E., R.C. Courtney, S.A. Dehler, M.-C. Williamson, Decompression melting at rifted margins: comparison of model predictions with the distribution of igneous rocks on the eastern Canadian margin, *Earth and Planetary Science Letters*, 121, 403-416, 1994a.
- Keen, C.E., P. Potter, and S.P. Srivastava, Deep seismic reflection data across the conjugate margins of the Labrador Sea, *Canadian Journal of Earth Sciences*, in press, 1994b.
- Kent, D V, and Gradstein, F.M., A Jurassic to recent chronology, in *The Western North Atlantic Region*, edited by P.R. Vogt and B.E. Tucholke, *The Geology of North America*, Vol. M, Geological Society of America, Boulder, CO, pp. 379-404, 1986.
- Korstgård, J., Ryan, B., and Wardle, R., The boundary between Proterozoic and Archean crustal blocks in central West Greenland and northern Labrador, in *Evolution of the Lewisian and comparable Precambrian high grade terrains*, edited by R. G. Park and J. Tarney, Geological Society, Special Publication 27, 247-259, 1987.
- Le Pichon, X., and F. Barbier, Passive margin formation by low-angle faulting with the upper crust: the northern Bay of Biscay margin, *Tectonics*, 6, 133-150, 1987.
- Lewis, B, and McClain, J., Converted shear waves as seen by ocean bottom seismometers and surface buoys, *Seismological Society of America Bulletin*, 67, 1291-1302, 1977.
- Lister, G.S., M.A. Ethridge and P.A. Symonds, Detachment faulting and the evolution of passive continental margins, *Geology*, 14, 246-250, 1986.
- Louden, K. E., Dadey, K. A., and Srivastava, S. P., Heat flow measurements at ODP Site 646, in *Proceedings of Ocean Drilling Program, part B, scientific results*, edited by S. P. Srivastava and M. A. Arthur, Ocean Drilling Program, 105B, 923-931, 1989.
- Ludwig, W.J., J.E. Nafe, and C.L. Drake, Seismic refraction, in *The Sea*, Vol. 4, edited by A.E. Maxwell, Interscience Publishers, New York, pp. 53-84, 1971.
- McKenzie, D.P., Some remarks on the development of sedimentary basins, *Earth and Planetary Science Letters* 40, 25-32, 1978.
- Meissner, R., Th. Wever, and P. Sadowiak, Continental collisions and seismic signature, *Geophysical Journal International*, 105, 15-23, 1991.
- Mutter, J.C., M. Talwani and P.L. Stoffa, Evidence for a thick oceanic crust adjacent to the Norwegian margin, *Journal of Geophysical Research*, 89, 483-502, 1984.
- Mutter, J.C., W.R. Buck, and C.M. Zehnder, Convective partial melting: A model for the formation of thick basaltic sequences during the initiation of spreading, *Journal of Geophysical Research*, 93, 1031-1048, 1988.
- Osler, J.C., Crustal Structure of the Extinct Spreading Centre in the Labrador Sea: Implications for Dynamic Models of Flow beneath Mid-Ocean Ridges, Ph.D. Thesis, Dalhousie University, Halifax, NS, 200 pp., 1993.

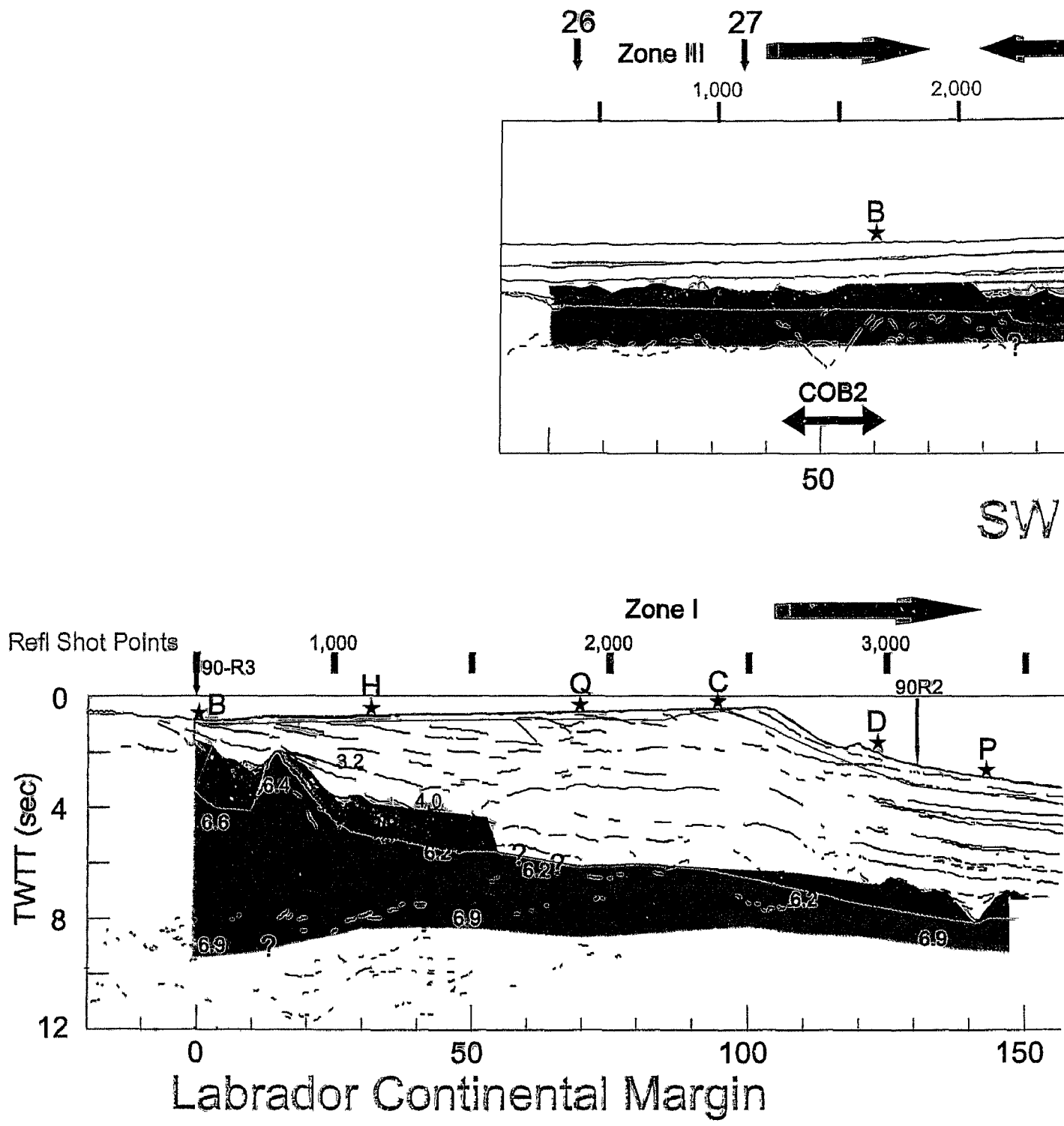
- Osler, J.C., and K.E. Loudon, Crustal structure of an extinct rift axis in the Labrador Sea: preliminary results from a seismic refraction survey, *Earth and Planetary Science Letters*, 108, 243-258, 1992.
- Osler, J.C., and K.E. Loudon, The extinct spreading centre in the Labrador Sea: I - crustal structure from a 2-D seismic refraction velocity model, submitted to *Journal of Geophysical Research*, 1994.
- Patchett, P. J., and Bridgewater, D. Origin of continental crust of 1.9-1.7 Ga age defined by Nd isotopes in the Ketilidian terrain of South Greenland, *Contributions to Mineralogy and Petrology*, 87, 311-318, 1984.
- Peddy, C., B. Pinet, D. Masson, R. Scrutton, J.-C. Sibuet, M.R. Warner, J.-P. Lefort and I.J. Shroeder, Crustal structure of the Goban Spur continental margin, Northeast Atlantic, from deep seismic reflection profiling, *Journal of Geological Society, London*, 146, 427-437, 1989.
- Pinheiro, L.M., R.B. Whitmarsh and P.R. Miles, The ocean-continent boundary off the western continental margin of Iberia Part II. Crustal structure in the Tagus Abyssal Plain, *Geophysical Journal of International*, 109, 106-124, 1992.
- Radel, G., and H.J. Melosh, A mechanical basis for low-angle normal faulting in the Basin Range, *EOS*, 68, 1449, 1987.
- Reid, I.D., Crustal structure of a nonvolcanic rifted margin east of Newfoundland, submitted to *Journal of Geophysical Research*, 1994.
- Reid, I.D. and C.E. Keen, High seismic velocities associated with reflections from within the lower oceanic crust near the continental margins of eastern Canada, *Earth and Planetary Science Letters*, 99, 118-126, 1990.
- Roest, W.R., and S. P. Srivastava, Sea-floor spreading in the Labrador Sea: a new reconstruction, *Geology*, 17, 1000-1003, 1989.
- Rolle, F., Late Cretaceous-Tertiary sediments offshore central West Greenland: lithostratigraphy, sedimentary evolution and petroleum potential, *Canadian Journal of Earth Sciences*, 22, 1001-1019, 1985.
- Royden, L., and Keen, C. E., Rifting process and thermal evolution of the continental margin of eastern Canada determined from subsidence curves, *Earth and Planetary Science Letters*, 51, 343-361, 1980.
- Sawyer, D.S., B.A. Swift, J.G. Sclater, and M.N. Toksoz, Extensional model for the subsidence of the northern United States Atlantic continental margin, *Geology*, Boulder, 10, 134-140, 1982.
- Schärer, U., and Gower, C. F., Crustal evolution in eastern Labrador: constraints from precise U-Pb ages, *Precambrian Research*, 38, 405-421, 1988.
- Schouten, H., and C.R. Denham, Modeling the oceanic magnetic source layer, in *Deep Drilling Results in the Atlantic Ocean: Ocean Crust*, edited by M. Talwani, C.G. Harrison, and D.E. Hayes, American Geophysical Union, Washington, D.C., 151-159, 1979.
- Sclater, J.G., and P.A.F. Christie, Continental Stretching: an explanation of the post-Cretaceous subsidence of the central North Sea basin, *Journal of Geophysical Research*, 85, 3711-3739, 1980.

- Sibuet, J.-C., Formation of non-volcanic passive margins: a composite model applied to the conjugate Galicia and southeastern Flemish Cap margins, *Geophysical Research Letters*, 19, 769-772, 1992.
- Shipboard Scientific Party, ODP drills the west Iberia rifted margin, *EOS*, 74, 454-455, 1993.
- Spudich, P., and J. Orcutt, A new look at the seismic velocity structure of the oceanic crust, *Review Geophysical Space Physics*, 18, 627-645, 1980a.
- Spudich, P., and J. Orcutt, Petrology and porosity of an oceanic crustal site: results from wave form modeling of seismic refraction data, *Journal of Geophysical Research* 85, 1409-1433, 1980b.
- Srivastava, S.P., Evolution of the Labrador Sea and its bearing on the early evolution of the North Atlantic, *Geophysical Journal of Royal astronomical Society*, 52, 313-357, 1978.
- Srivastava, S.P., Davis Strait: structures, origin and evolution, in *Structure and Development of the Greenland-Scotland Ridge*, edited by Bott, Saxov, Talwany, and Thiede, 159-189, 1983.
- Srivastava, S.P., and M.A. Arthur, Tectonic evolution of the Labrador Sea and Baffin Bay: constraints imposed by regional geophysics and drilling results from LEG 105, in *Baffin Bay and 646 and 647 in the Labrador Sea*, *Proceedings of Ocean Drilling Program, Scientific Results*, 105, 1989.
- Srivastava, S. P., Falconer, R. K. H., and MacLean, B., Labrador Sea, Davis Strait, Baffin Bay geology and geophysics--a review, in *Geology of the North Atlantic Borderlands*, edited by J.W. Kerr, A. J. Fergusson, and L. C. Machan, *Canadian Society of Petroleum Geologists, Memoir 7*, 333-398, 1981.
- Srivastava, S.P., K. E. Loudon, S. Chough, D. Mosher, B. D. Loncarevic, P. Mudie, A. de Vernal, and B. Maclean, Results of detailed geological and geophysical measurements at ODP sites 645, in *Baffin Bay and 646 and 647 in the Labrador Sea*, *Proceedings of Ocean Drilling Program, Scientific Results*, 105, 891-922, 1989.
- Srivastava, S.P., and C.R. Tapscott, Plate kinematics of the North Atlantic, in *The Geology of North America: The Western Atlantic Region*, Boulder, DNAG Series, Volume M., Special Publication, 589-404, 1986.
- Steckler, M.S., and A.B. Watts, Subsidence history and tectonic evolution of Atlantic-type continental margins, in *Dynamics of Passive Continental Margins -- Geodynamic Series*, edited by R.A. Sclaton, American Geophysical Union, Washington, 184-196, 1982.
- Stergiopolous, A.B., *Geophysical Crustal Studies off the Southwest Greenland Margin*, M.Sc. Thesis, Dalhousie University, Halifax, NS, 250 pp, 1984.
- Todd, B.J. and I. Reid, The continent-ocean boundary south of Flemish Cap: constraints from seismic refraction and gravity, *Canadian Journal of Earth Sciences*, 26, 1392-1407, 1989.
- Tucholke, B., Sediment distribution, in *Geophysical Atlas of the North Atlantic between 50° to 72° N and 0° to 65° W*, edited by S.P. Srivastava, D. Voppel and B. Tucholke, Deutsches Hydrographisches Institut, Hamburg, 9-12, 1988.
- Tucholke, B., and V.A. Fry, Maps of sediment thickness and depth to basement in the northwest Atlantic ocean basin, Tulsa, OK (AAPG), 1985.



- Van Breemen, O., Aftalion, M., and Allaart, J. H., Isotopic and geochronologic studies on granites from the Ketilidian mobile belt of South Greenland, *Geological Society of America Bulletin*, 85, 403-412, 1974.
- Van der Linden, W.J.M., Crustal attenuation and sea-floor spreading in the Labrador Sea, *Earth and Planetary Science Letters*, 27, 409-423, 1975
- Voorhoeve, H., and G. Houseman, The thermal evolution of lithosphere extending on a low-angle detachment zone, *Basin Research*, 1-9, 1988.
- Voppel, D., R. Rudloff, J. Schulz-Ohlberg, S.P. Srivastava, K.G. Shih, P.D. Rabinowitz, and W. Jung, Free Air Gravity Anomalies, in *Geophysical Atlas of the North Atlantic between 50° to 72° N and 0° to 65° W*, edited by S.P. Srivastava, D. Voppel and B. Tucholke, Deutsches Hydrographisches Institut, Hamburg, pp. 5-8, 1988.
- Warner, M. 1990. Basalts, water, or shear zones in the lower continental crust? *Tectonophysics*, 173, 163-174.
- Watt, W.S., The coast-parallel dike swarm of southwest Greenland in relation to the opening of the Labrador Sea, *Canadian Journal of Earth Sciences*, 6, 1320-1321, 1969
- Watterson, J., Proterozoic intraplate deformation in the light of southeast Asia neotectonics, *Nature*, 273, 636-640, 1978.
- Wernicke, B., Uniform-sense normal simple shear of the continental lithosphere, *Canadian Journal of Earth Sciences*, 22, 108-125, 1985.
- Wernicke, B. and P. G. Tilke, Extensional tectonic framework of the U.S. Central Atlantic passive margin, in *Extensional Tectonics and Stratigraphy of the North Atlantic Margins*, edited by A.J. Tankard and H.R. Balkwill, Memoir 46, American Association of Petrological Geology, Tulsa, OK, 7-21, 1989.
- White, R. and D. McKenzie, Magmatism at rift zones the generation of volcanic continental margins and flood basalts, *Journal of Geophysical Research*, 94, 7685-7729, 1989.
- White, R. S., Spence, G. S., Fowler, S. R., McKenzie, D. P., Westbrook, G. K., and Bowen, A. N. Magmatism at rifted continental margins, *Nature*, 330, 439-444, 1987
- Whitmarsh, R. B., F. Avedik, and M.R. Saunders, The seismic structure of thinned continental crust in the northern Bay of Biscay, *Geophysical Journal of Royal Astronomical Society*, 86, 589-602, 1986.
- Whitmarsh, R. B., and Miles, P. R., Seismic structure of a seaward-dipping reflector sequence southwest of Rockall Plateau, *Geophysical Journal of Royal Astronomical Society*, 90, 731-739, 1987.
- Whitmarsh, R.B., P.R. Miles, and A. Mauffret, The ocean-continent boundary off the western continental margin of Iberia. Crustal structure at 40°30'N, *Geophysical Journal of International*, 103, 509-531, 1990.
- Whitmarsh, R.B., L.M. Pinheiro, P.R. Miles, M. Recq, and J.-C. Sibuet, Thin crust at the western Iberia ocean-continent transition and ophiolites, *Tectonics*, 12, 1230-1239, 1993.
- Woodside, J., Gravity anomaly in Labrador Sea. in *Labrador Sea Atlas*, edited by J. S. Bell, East Coast Basin Atlas Series, Geological Survey of Canada, Dartmouth, NS, pp. 94-95, 1989.

- Woodside, J., and Verhoef, J., Geological and tectonic framework of eastern Canada as interpreted from potential field imaginary, Geological Survey of Canada, Paper 88-26, 1989.
- Zelt, C.A., and R.B. Smith, Seismic travelttime inversion for 2-D crustal velocity structure, Geophysical Journal International, 108, 16-34, 1992.
- Ziegler, P.A., Evolution of the North Atlantic -- an overview, in Extensional Tectonics and Stratigraphy of the North Atlantic Margins, edited by A.J. Tankard and H.R. Balkwill, AAPG Memoir 46, 111-129, 1989.



6.4 Time domain line drawings (Keen et al., 1994) of the coincident MCS and 90-1 for the Labrador margin (bottom) overlain with boundaries of reflection and refraction profiles are at a slight angle to each other (see Fig. 6.4 profile according to the positions of Chron 27 and the shelf break.